BLANKET PERFORMANCE AND RADIOACTIVE WASTE OF FUSION REACTORS: A NEUTRONICS APPROACH

Bethany R. Colling

MEng. Nuclear Engineering (Hons)

This thesis is submitted with the requirements of Lancaster University for the degree of Doctor of Philosophy

September 2016

ABSTRACT

Fusion energy for use in power plants is a continually developing area and many of the related parameters are not yet fixed. The investigation of fusion neutronics and development of computational approaches for assessment is imperative in the road to commercial realisation of fusion power. This research has explored blanket performance, including tritium breeding and the shielding requirements, and assessed radioactive waste, utilising the 3-D Monte Carlo transport code MCNP, and the activation inventory code FISPACT.

The performance of some solid and liquid breeder materials has been compared with regards to tritium breeding, energy production and shielding. In the case of novel spherical tokamak concepts, that make use of high temperature superconducting magnets and have no inboard blanket, scoping studies have been performed to investigate the impact of shielding requirements on how small the tokamak can be.

Fusion power plants will not produce high level waste, as seen in nuclear fission plants, however the components and structures will become active as a result of interactions with high energy neutrons. A suitable radioactive waste management plan will be required in order to deal with this material appropriately, with an aim to recycle or clear from regulatory control all materials 100 years after shutdown. The study indicates that through suitable material selection and the use of component dismantling the requirement could potentially be satisfied.

In terms of computational methods, the neutron flux averaging has been assessed throughout the work and has shown in neutronics estimates to produce some substantial differences. The recently developed unstructured mesh approach to neutronics modelling has been explored and the potential use for more accurate radioactive waste inventory calculations. Although the analysis and comparison shows promising results, it still requires significant development and improvement in the work flow to create a robust neutronic analysis method.

DECLARATION

I, Bethany R. Colling, herby certify that this dissertation is the result of my own work (or clearly acknowledged) and has not been previously submitted, in part or whole, to any university or institution for any degree, diploma, or other qualification.

ACKNOWLEDGEMENTS

This research was supported, both technically and financially by the Lancaster University Engineering Department and the Culham Centre for Fusion Energy (CCFE). Additional funding support was provided by the European Union's Horizon 2020 research and innovation programme. Further funding support was provided by RCUK Energy Programme [grant number EP/1501045] and Fusion-4-Energy [grant FPA-168.02] primarily for work presented in Appendix 6.

The author would like to thank supervisors, Prof. Malcolm J. Joyce, Dr. Shanliang Zheng and Lee W. Packer for their scientific support, valuable comment and guidance. Further thanks to Dr. Mark Gilbert for running his FISPACT radioactive waste classification script and providing the output data for comparison with the alternative methods used within this thesis.

The author would also like to thank EUROfusion for providing the Generic DEMO models, as referenced within the text. And the Princeton Plasma Physics Laboratory for providing the preliminary CAD and radial build of the ST-FNSF.

Further thanks to the following people for their valuable discussions and guidance, Prof. Laila El Guebaly, Dr. Tim Hender, Dr. Jon Menard, Dr. Stephen Monk and Tom Todd.

Past and present colleagues at Lancaster University and CCFE are also thanked, including Tim, Andy, Jon N, Michael, Jon S, Steve, Lee M, Sarah, Jamie and Mark for their continued encouragement, motivation and neutronics and nuclear data guidance.

CONTENTS

LIST OF TABLES

LIST OF FIGURES

LIST OF ABBREVIATIONS AND ACRONYMS

ADVANTG	automated variance reduction parameter generator
ANDRA	French national agency for radioactive waste management
BSCCO	bismuth - strontium - calcium - copper - oxygen
BSSD	basic safety standards directive
CAD	computer aided design
CCFE	Culham Centre for Fusion Energy
CLAFM	China low activation ferritic martenistic
CSA	centre de stockage de l'Aube
CSG	constructive solid geometry
DBTT	brittle ductile transition temperature
DCLL	dual coolant lithium lead
DEMO	DEMOnstration fusion power reactor
DFLL	dual functional lithium lead
EFDA	European fusion development agreement
EU	European Union
EUROFER	An EU reduced activation ferritic/martensitic reference steel for fusion
FENDL	fusion evaluated nuclear data library
FPY	full power year
GVR	global variance reduction
HCLL	helium cooled lithium lead
HCPB	helium cooled pebble bed
HLW	high level waste
HTS	high temperature superconductor
HTS-ST	high temperature superconducting - spherical tokamak
IAEA	International Atomic Energy Agency

ILW	intermediate level waste
IRAS	indice radiologique d’acceptabilite de stockage index
ITER	Latin for 'the way' (originally an acronym for the international thermonuclear experimental reactor)
LLW	low level waste
LTS	low temperature superconductor
MTS	medium temperature superconductor
MCNP	Monte Carlo neutron particle transport code
ODS	oxide dispersion strengthened
ONR	Office for Nuclear Regulation
PPCS	European power plant conceptual studies
RAFM	reduced activation ferritic/martensitic
ReBCO	rare earth - barium - copper oxide
SiCf/SiC	silicon carbide fibre-reinforced matrix composites
TBR	tritium breeding ratio
US	United States
VLLW	very low level waste
WCCB	water cooled ceramic/beryllium blanket
YBCO	yttrium - barium - copper oxide

LIST OF APPENDICES

1 INTRODUCTION

1.1 Neutronics analysis for fusion power plants

Fusion power has the potential to provide a substantial amount of energy for use on earth with inherently safe and environmentally favourable features. The fuels required for a fusion reaction are deuterium and tritium; this is known as the D-T reaction. Deuterium can be extracted from water, with relative ease. Tritium, however, is of low abundance and volatile, thus resulting in a requirement to produce a self-sufficient tritium supply within a fusion reactor. An important part of the European magnetic confinement fusion research programme focuses on tritium breeding using a lithium based blanket on the reactor walls. The work presented in this thesis focuses on the DEMOnstration (DEMO) facility, which is to form the main stage between the fusion research reactor, ITER, and commercial fusion power plants, with the aim of proving the economic feasibility and tritium self-sufficiency of fusion power.

Conceptual studies of DEMO reactors have been carried out throughout Europe as part of the European Union (EU) fusion power plant research programme, and internationally, such as in China, Japan, the US and Korea. The designs are all based on the magnetically confined ‘tokamak’, similar to ITER, but differ mainly in the design of the divertor and breeder blanket. A measure of the fusion tokamak performance is the beta value (β); a ratio of plasma pressure to the magnetic field. A higher β is more efficient and requires less magnetic material, it therefore has the potential to be less expensive. A limiting factor in improving β is the size of the magnets. The physical dimensions of the rings mean that the hole in the torus can only

be reduced so far before the windings of the coil are touching. This limits the reduction in the aspect ratio of conventional tokamaks to about 2.5. Spherical tokamak designs place the toroidal field coils closer to the plasma and often make use of a single centre column conductor allowing for a lower aspect ratio (as low as approximately 1.2). Spherical tokamaks hold the fusion plasma in a tighter magnetic field than a conventional large aspect ratio tokamak resulting in a more compact device. This, coupled with the use of high temperature superconducting (HTS) magnets, has the potential for a more economical and efficient method to fusion power, and is particularly attractive for component test devices and fusion neutron source facilities.

The first wall (plasma-facing region) of a magnetically confined nuclear fusion reactor will be used to produce the tritium fuel and convert the fusion energy into heat that can be extracted for electricity generation. This wall, known as the blanket, will need to contain a lithium compound and a neutron multiplying material to ensure that the tritium breeding ratio (TBR) is greater than or equal to unity. In the case of a spherical tokamak, there is no space for this blanket on the inboard side, i.e. the inner radius of the tokamak, due to the tight aspect ratio. A dedicated neutron shield is required to protect the magnets.

The neutrons not only cause damage to the magnets but will also cause materials to become ‘activated’, generating radioactive wastes. Investigating the waste arising and the activation products is crucial to the development of a suitable waste management plan for any future power plant.

There has been significant research on the breeding capabilities of candidate blanket designs for test modules to be placed in ITER. In recent years the focus has shifted towards the performance of breeding materials in a fusion power plant environment, typically increased power and operational life, and the available methods for simulating the reactor neutronics of a fusion power plant using 3-D geometry.

Typically neutronics analysis with 3-D geometry is conducted using simulation software, such as the Monte Carlo Neutron Particle transport code (MCNP), that simulates the neutron behaviour as described by the Boltzmann transport equation. Analysis with MCNP uses a cell-based geometry, however, estimating neutron flux with this geometry type assumes the flux to be uniform through the entire cell. In the

case of activation and radioactive waste calculations this flux averaging can result in an over-estimation of the levels of radioactive waste which will impact on the disposal options available and associated costs.

The use of a superimposed structured mesh with MCNP allows the neutron flux to be ‘tallied’ (recorded) in a finer resolution without having to rebuild the MCNP geometry. This method has been used extensively in neutron flux and activation analysis for shutdown dose rate calculations, though not for radioactive waste assessments. These methods, along with a recent development from MCNP regarding the use of an unstructured mesh representation of the geometry, were investigated as part of the research presented in this thesis.

The capabilities of some proposed breeder blanket and neutron shield materials, and the shielding requirements for centre column magnets in novel spherical tokamak concepts are also investigated.

1.2 Thesis outline

The research conducting over the PhD period is presented in this thesis and draws on some published and unpublished works. A summary of the chapters and related presentations and publications is given here.

Background

- The background chapter assumes the reader may have little knowledge of fusion energy and the associated ITER facility and DEMO concepts. Fusion power is introduced along with a brief history within the research area. The current status on the path towards fusion and the European roadmap is described. The main components of a fusion reactor are presented with a focus on superconducting magnets and blanket technology.

Neutronics analysis

- This chapter introduces, defines and explains the terms and parameters used within the work regarding neutronics analysis. The particle transport code MCNP is described along with the material activation and inventory code FISPACT.

Blanket performance; tritium breeding, energy multiplication and shielding

- Investigations into the neutronic assessment of blanket capabilities is performed and presented. The research includes the effect of material composition of breeder blankets and optimisation potential for tritium breeding performance. A comparison of some proposed solid and liquid breeding materials has been performed, drawing on peer-reviewed published investigations:

Development of fusion blanket technology for the DEMO reactor, Bethany R. Colling, S D. Monk, Applied Radiation and Isotopes, Volume 70, Issue 7, July 2012

- The shielding requirements of novel spherical tokamaks with high temperature superconducting magnets are investigated through a parametric scoping study. The neutronics assessment of blanket performance, shielding capabilities and activation considerations is presented for a spherical tokamak model based on the Princeton Plasma Physics Laboratory fusion nuclear science facility concept. Initial results were presented at the 18th international spherical torus workshop. Further results were included in the collaborative paper by J. Menard published in Nuclear Fusion.

Neutronics Analysis of HTS-ST, Bethany Colling, T. Brown, M. J. Joyce, J. Menard, L. W. Packer, The 18th International Spherical Torus Workshop (ISTW-2015), Princeton University, November 3-6, 2015.

J. E. Menard, T. Brown, M. Boyer, L. El-Guebaly, J. Canik, B. Colling, R. Raman, Z. Wang, Y. Zhai, P. Buxton, et.al., "Fusion Nuclear Science Facilities and Pilot Plants Based on the Spherical Tokamak," Nucl. Fusion, vol. 56, 2016.

Radioactive waste assessment of DEMO

- Conventional methods for calculating radioactive waste from fusion reactors are compared with the novel unstructured mesh based analysis through the use of recent developments in the MCNP6 code and adaptations to the MCR2S particle transport and activation coupling code. The radioactive waste assessment is performed on the 2015 generic EU DEMO model using an assumed homogeneous mix of breeding material based on the EU helium cooled pebble bed (HCPB) blanket concept.

Final remarks

- Final comments and areas to be considered for further work are presented.

Other related publication contributions during the PhD period include:

Neutronics experiments and analyses in preparation of DT operations at JET, R. Villari, P. Batistoni, M. Angelone, J.P. Catalan, B. Colling, D. Croft, U. Fischer, D. Flammini, A. Klix, S. Loreti, S. Lilley, F. Moro, J. Naish, L. Packer, P. Pereslavtsev, S. Popovichev, P. Sauvan, B. Syme, Fusion Engineering and Design, In Press, February 2016

- Benchmarking MCR2S with other Rigorous-Two Step approaches, a Direct-One Step tool and experimental data from the JET 2012–2013 D-D shutdown experiments.

Neutronics analysis for integration of ITER diagnostics port EP10, Bethany Colling, T. Eade, M J. Joyce, R. Pampin, F. Seyvetc, A. Turner, V. Udintsevd, Fusion Engineering and Design, In Press, January 2016

- Shielding analysis of the ITER nuclear facility's equatorial port 10. This included investigations of the activation of the port when integrated into the ITER C-lite neutronics model and the contribution to shutdown dose rated from neighbouring ports.

Proposal to characterise legacy Sellafield ponds using SONAR and RadLine™, Sarah D. Reddy, S D. Monk, D W. Nye, B R Colling, S J. Stanley, Applied Radiation and Isotopes, Volume 70, Issue 7, July 2012

- Gamma radiation through a theoretical tank of water was evaluated using MCNP (MCNPX v2.70). This was used to investigate the intensity of gamma radiation as a function of depth and the suitability of proposed detection systems using RadLine™ for eventual characterisation of legacy ponds at Sellafield.

2 BACKGROUND

2.1 Fusion reactions

The mass of an atomic nucleus is not the sum of the component parts, i.e. the protons and the neutrons, there is a mass defect (Equation 1 & 2).

$$\sum m_n + \sum m_p < m_A \qquad (1)$$

$$Mass\ Defect\ \Delta m = \sum m_n + \sum m_p - m_A \qquad (2)$$

where, m_n is the mass of the neutrons, m_p is the mass of the protons and m_A is the atom mass.

This mass defect can be thought of as the energy required to bind the nucleus together, or the energy that would be required to break the nucleus apart, and is known as the 'binding energy'. The mass difference from the fusing of two light nuclei to form a heavier nucleus is released as kinetic energy according to Einstein's formula (Equation 3, where E is the kinetic energy of the reaction products, Δm is the mass defect, and c the speed of light).

$$E = (\Delta m)c^2 \qquad (3)$$

For a fusion reaction to take place the two light nuclei must overcome the long-range Coulomb repulsion force to allow them to be close enough for the short-range nuclear force to take effect. Energies in the order of 10 keV to 100 keV [1] are required to

overcome the Coulomb force. This corresponds to temperatures of 10^8 K[1] to 10^9 K, at which light nuclei are stripped of their electrons creating a plasma.

The fusion reactions of interest are:

$$D + D \rightarrow \begin{cases} {}^3H\ (1.011\ MeV) + p\ (3.022\ MeV) \\ {}^3He\ (0.820\ MeV) + n\ (2.449\ MeV) \end{cases} \quad (4)$$

$$D + T \rightarrow {}^4He\ (3.261\ MeV) + n(14.029\ MeV) \quad (5)$$

$$D + {}^3He \rightarrow {}^4He\ (3.712\ \text{MeV}) + p\ (14.641\ \text{MeV}) \quad (6)$$

The D-T reaction for energy production is the main focus of fusion research world-wide due to the lower temperature requirements to initiate the fusion reaction (Figure 2.1) [2]–[4].

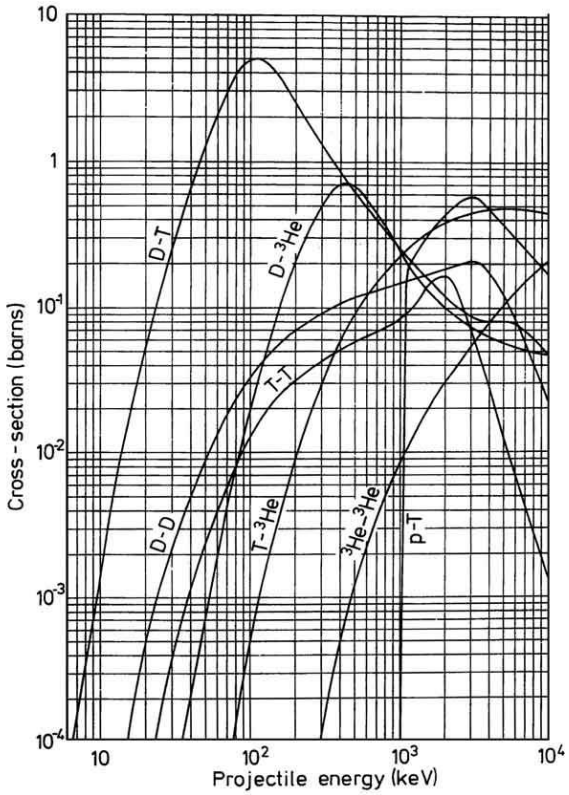

Figure 2.1 - The cross-section (barns) of some key fusion reactions as a function of projectile energy (keV). (Reproduced with permission, Kaye & Laby Online [4].)

[1] A Kelvin (K) is the standard international unit of thermodynamic temperature, beginning its scale at absolute zero (-273.15 ºC). Both the Kelvin and degrees Centigrade (ºC) are used within this thesis.

2.2 Using fusion energy for power generation

A power plant using fusion could potentially provide a large amount of power for little fuel when compared with other energy sources; just 1 kilogram of fusion fuel could produce the equivalent amount of energy as 10 million kilograms of fossil fuel [5]. In order to sustain the D-T plasma and 'hold' it away from the surfaces of a reactor vessel, a form of confinement is required. Without confinement the plasma would rapidly cool due to interactions with the wall. The most developed fusion confinement technologies are magnetic confinement and inertial confinement. The focus of this research is the use of magnetic confinement for a demonstration reactor and future fusion power plants. Magnetic confinement uses magnetic pressure to hold the plasma at the required temperature and density away from the surrounding walls; as opposed to the use of kinetic pressure in the case of inertial confinement. The most common magnetic confinement configuration is that of the 'tokamak', where the plasma is held in a torus shaped chamber (Figure 2.2).

Figure 2.2 - A computerised image of a fusion tokamak with a plasma superimposed. (Reproduced with permission, EUROfusion [6].)

2.3 Main components of magnetic confinement reactors

The main components of a magnetic confinement reactor are: the magnets to create the magnetic fields to hold the plasma, blankets for tritium fuel, heat production and shielding of surrounding magnets, the divertor to remove fusion reaction products from the plasma, and the vacuum vessel to maintain the vacuum conditions for sustaining the plasma. The main components are described in further detail in the following sections, making reference to the ITER design for examples. A DEMO

fusion power plant will have similar main components, though will differ in size, material and final design.

2.3.1 The magnets

Magnetic forces are used to confine the hot plasma and prevent the high temperature particles touching containment walls. The most developed magnetic confinement system is the tokamak. Tokamaks have, in general, three main magnet systems in order to produce the confinement and fusion conditions. These are the poloidal field coils, toroidal field coils, and the ohmic heating central solenoid. Correction coils may also be used for stability.

The toroidal field coils create the primary confining toroidal field and the poloidal field coil system is used for plasma shaping, stability and position control. The plasma current is induced by a transformer, with the ohmic heating central solenoid acting as the primary winding and the plasma as the secondary winding. Many reactor designs make use of superconducting magnets to reduce the power dissipation and minimise recirculating power. Superconducting magnets and their use in fusion power are discussed in further detail in Section 2.4.

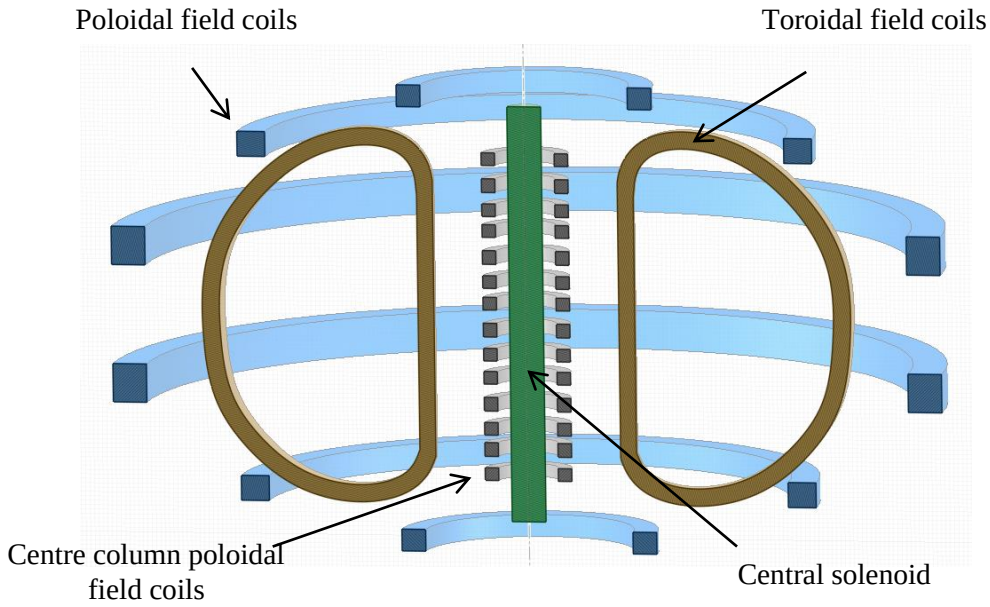

Figure 2.3 - An illustrative diagram of the magnetic coil configuration used for fusion magnetic confinement.

2.3.2 The breeder blanket

The blanket surrounding the fusion plasma will be required to fulfil three main neutronics criteria. Firstly it must provide a self-sufficient supply of tritium which can be recovered for use as new fuel. Secondly, it will extract the heat energy from the particle interactions to produce useable power. And thirdly it will need to provide shielding to personnel and the superconducting magnets which are required to provide the plasma confinement. Some blanket concepts will be tested in the ITER fusion test facility, currently under construction in the South of France. (A computer representation of a test blanket module is given in Figure 2.4.) The blankets are discussed in further detail in Section 2.5.

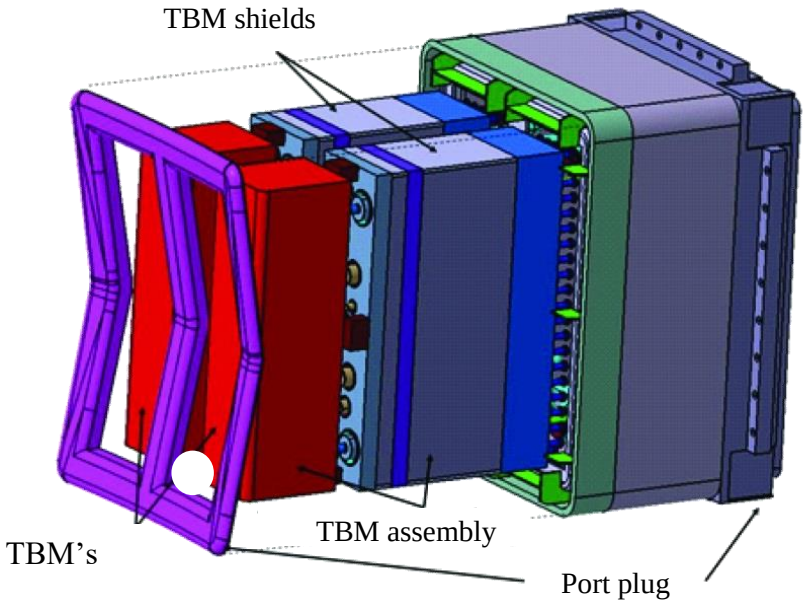

Figure 2.4 - A computer image of a tritium breeding test blanket module (TBM) for ITER. (Reproduced with permission, © ITER Organisation [7].)

2.3.3 The divertor

The divertor region is formed at the edge of the plasma confinement and is designed to 'divert' impurities and helium (resulting from the D-T fusion reaction) away from the plasma to minimise contamination. The divertor, a plasma facing component, will receive very high heat loads and as a result a large amount of research is on-going with regards to possible materials that could withstand such conditions. The most viable materials currently under consideration for the critical plasma facing

components are beryllium, tungsten, and carbon fibre-reinforced carbon composite. Materials are tested in facilities such as the Joint European Tokamak (JET) located in the UK, and further materials information will be gained from the ITER facility once available.

To ease the process of replacement or repair, the divertor is split into sections, referred to as divertor cassettes. In ITER 54 divertor cassette assemblies will be used, each with supporting stainless steel structure and three plasma-facing components: the inner and outer vertical targets and the dome. The target tiles will be positioned at an angle so as to increase the effective area, reducing the power density. In ITER the divertor will make use of carbon fibre-reinforced carbon composite in the initial phase of ITER operation, moving to tungsten plasma facing components for D-T operations. (A computerised image of a divertor cassette for ITER is shown in Figure 2.5.)

Due to the high temperatures and heat fluxes received by the divertor, it will need to be replaced during the lifetime of a fusion power plant. In ITER this is anticipated to take place at least once, and will require sophisticated remote handling.

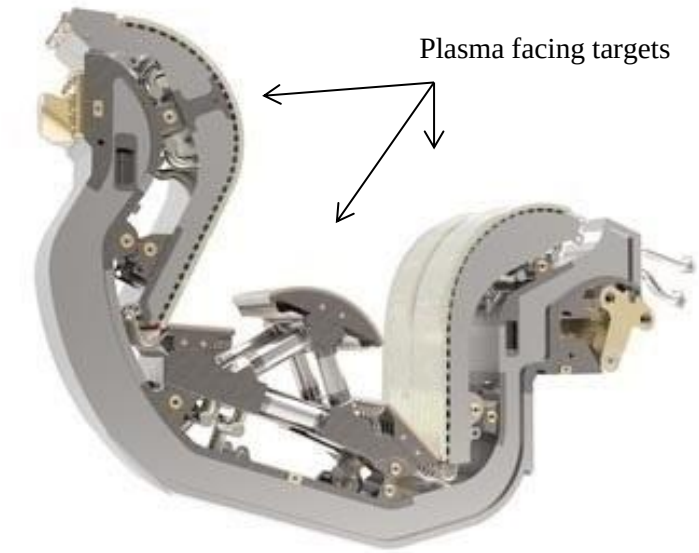

Figure 2.5 - Illustration of an ITER divertor cassette. (Reproduced with permission, © ITER Organisation [7].)

2.3.4 The vacuum vessel

The vacuum vessel is the airtight container that provides a high-vacuum environment for the fusion plasma and acts as the first safety barrier for radioactivity. It also

provides support for the in-vessel components, such as the blanket and divertor. Within the ITER design, the vacuum vessel will have forty-four ports to provide access for remote handling and diagnostic systems. In ITER the vacuum vessel (Figure 2.6) will measure 19.4 m across and 11.4 m high, weighing approximately 5200 tonnes (t).

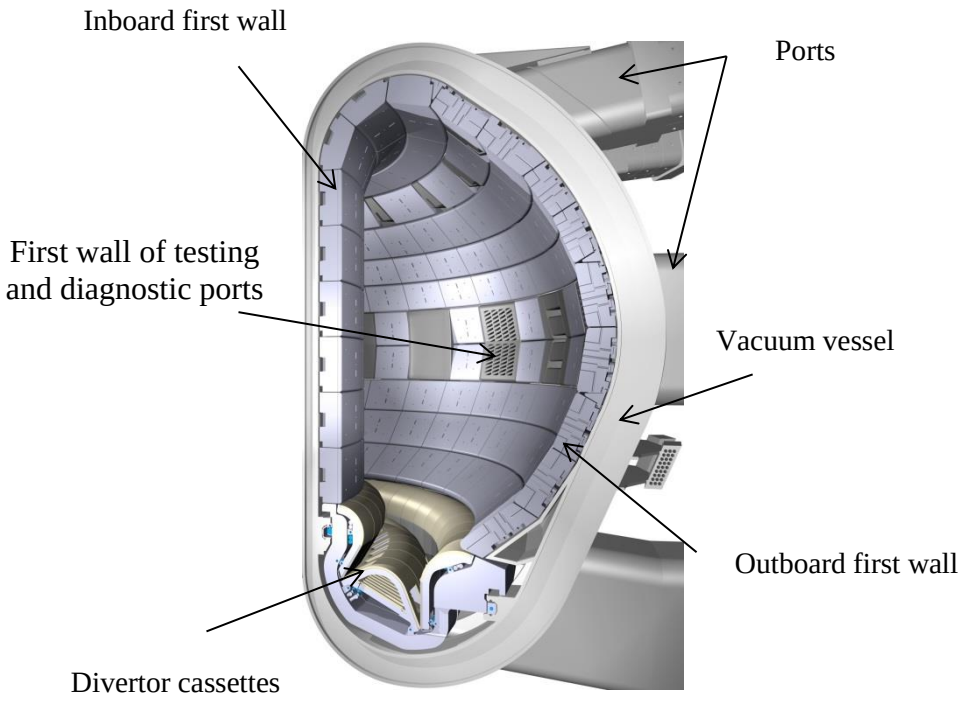

Figure 2.6 - Computer illustration of the ITER vacuum vessel, also showing the location of the divertor cassette from Figure 2.5. (Reproduced with permission, © ITER Organisation [7].)

2.4 Superconducting magnets

Superconducting materials exhibit a phenomenon of zero electrical resistance to low applied currents and expulsion of magnetic fields when cooled below a characteristic critical temperature. The complete expulsion of magnetic field lines from the inside of a superconductor is characterised by the Meissner effect [8]. A superconductor with little or no magnetic field within it is said to be in the Meissner state; this state breaks down when the applied magnetic field is too large. Superconducting materials can be categorised as type 1 or type 2 superconductors according to how this break down occurs. Type 1 superconductors have one critical field, above which all

superconductivity is lost. Type 2 superconductors have two critical fields, having perfect superconductivity up to the first critical field, partial penetration of the magnetic field between the two critical fields and then losing all superconductivity above the second critical field. Most pure elemental superconductors, except niobium and carbon nanotubes, are type 1, while the majority of the impure and compound superconductors are type 2.

Characteristics of superconductivity appear when the temperature is lowered below a critical temperature. Conventional low temperature superconductors (LTS) usually have critical temperatures ranging from around 30 K to < 1 K. The highest critical temperature found for a conventional superconductor is 39 K for magnesium diboride (MgB_2) which is sometimes referred to as a medium temperature superconducting (MTS) material [9]. A superconductor is generally considered a high temperature superconducting (HTS) material if it reaches superconductivity when cooled using liquid nitrogen, i.e. critical temperature > 77 K, or low temperature if more aggressive cooling is required to achieve superconductivity; critical temperature < 77 K. High temperature superconductors have a number of advantages, most notably that it allows liquid nitrogen to be used as a refrigerant replacing the need for the more expensive liquid helium. The higher temperatures also help to avoid some of the problems associated with liquid helium temperatures, such as the formation of plugs of frozen air that can block cryogenic lines and cause pressure build-up.

There have been significant developments in HTS materials in recent years, primarily lead by the commercial electric power transmission sector [10]. The HTS materials can be classified into two groups, BSCCO (bismuth - strontium - calcium - copper - oxygen) first generation materials and ReBCO (rare earth - barium - copper oxide) second generation superconductors. First generation HTS wire has been commercially available since 1990, with kilometre lengths of tape available from 2000 [11]. Uses in power devices include transmission cables, transformers, motors and generators, etc. [12]–[14].

A comparison of the critical current density achieved, for an applied magnetic field, for some superconducting materials is shown in Figure 2.7.

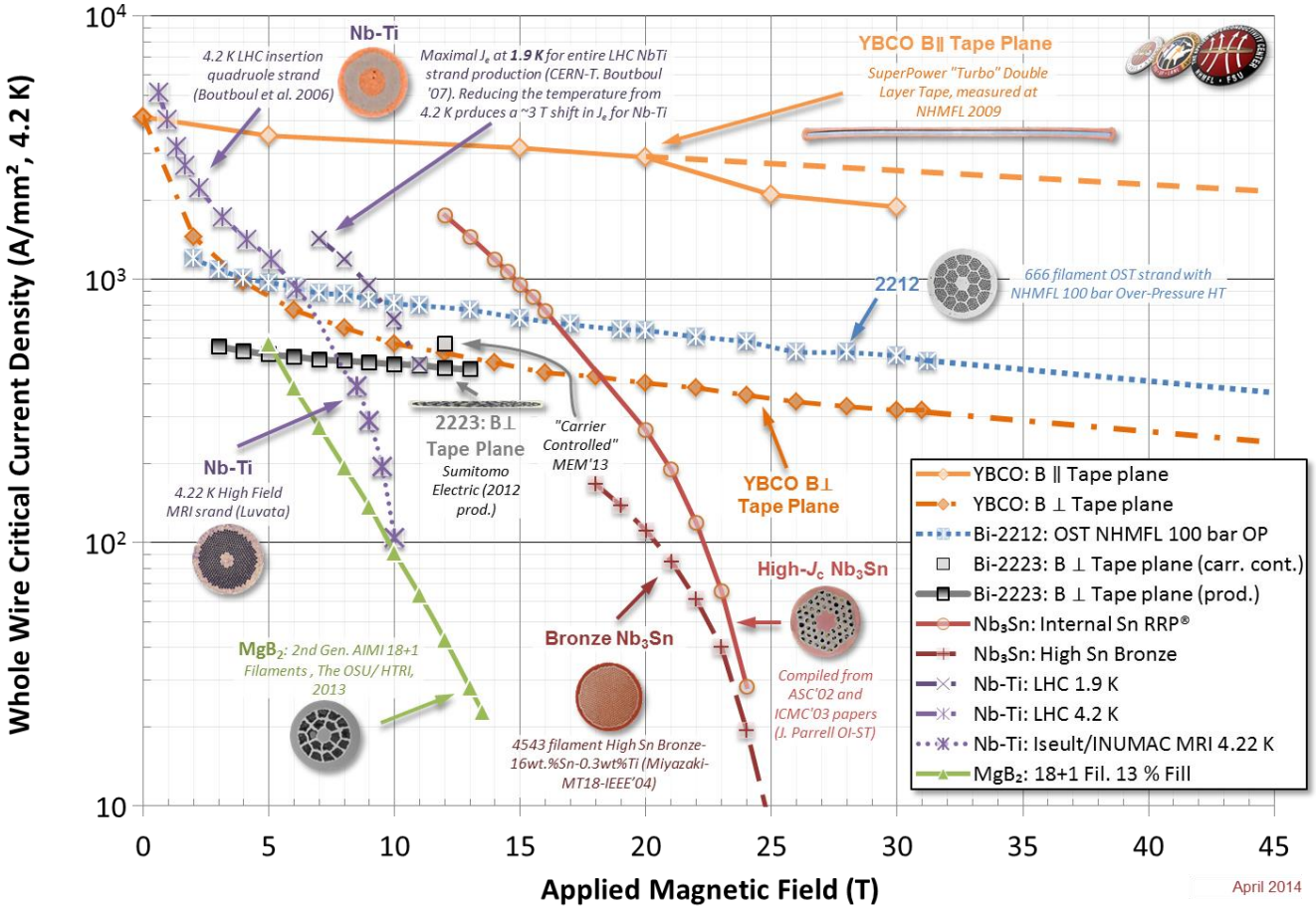

Figure 2.7 - Critical current density as a function of the local magnetic field for some typical superconducting materials. Reproduced with permission, The National High Magnetic Field Laboratory, P. Lee (see https://nationalmaglab.org/magnet-development/applied-superconductivity-centre/plots for further details and a list of references for the data).

2.4.1 Use in fusion magnets

Second generation HTS magnets have the potential for use in magnetic confinement fusion devices. A ReBCO HTS could be operated at 77 K, however significantly higher current densities (as required to reach the magnetic fields required for fusion applications) can be achieved by operating the HTS at lower temperature. Options for cooling the magnets to such temperatures include the use of subcooled nitrogen (~65 K), a eutectic mixture of nitrogen and oxygen (~55 K) or high pressure helium gas (down to approximately 4 K) [15]. A further advantage of the HTS materials, is their possible use in remountable (can be mounted and demounted repeatedly) magnets with mechanical or electrical joints [16]. This is not possible with LTS due to the joule heating at the joint (leading to quenching) and the large power required for cooling the joints.

Although significant information has been gained through the development of HTS for use in power transmission, there are a number of important differences:

(1) the higher cryogenic efficiency of the superconductor arranged in coils, will allow operation of the HTS at lower temperatures, achieving significantly higher critical current densities than observed in power transmission cables,
(2) the use of HTS in demountable coils results in the longest continuous section of HTS tape to be metres as opposed to kilometres [17], avoiding the limitations present in longer sections of tape as used in power transmission, and ,
(3) there is a need to operate the HTS in high magnetic fields which can affect the achievable critical current density.

A HTS with the rare earth element yttrium (YBCO) has particular advantages over the use of conventional LTS materials, such as NbTi or Nb_3Sn. YBCO materials have a larger tolerance in operating temperature and the ability to deal with higher resistive loads. The required cooling to reach the necessary critical current density is significantly reduced and high magnetic fields can be achieved (Figure 2.7). The commercial availability and reducing cost of YBCO tape makes the material even more attractive for near-term feasibility, though significant research will be required before engineering a full scale toroidal field system.

2.4.2 YBCO tapes

The performance of the HTS tape is a strong function of the thickness; the thinner the tape, the higher the current density [18]. Commercial YBCO tape is currently available in widths of between 4 mm and 12 mm and at a thickness of less than 100 μm [19]. A typical tape consists of a nickel-based hastelloy structural layer, a buffer/insulator, a superconducting layer and a silver layer (see Figure 2.8) [11]. The structural and buffer layers of the tape act as electrical insulators necessitating an electrical connection on the silver side of the tape in order to transfer current into the YBCO layer. A copper stabilising layer maybe used for protection against flux-jumping (a thermomagnetic instability to changes in temperature and electromagnetic fields that can result in quenching). Stabilising layers are only required for operation at temperatures below 20 K as above this HTS materials do not suffer flux-jumping due to the very high thermal capacity.

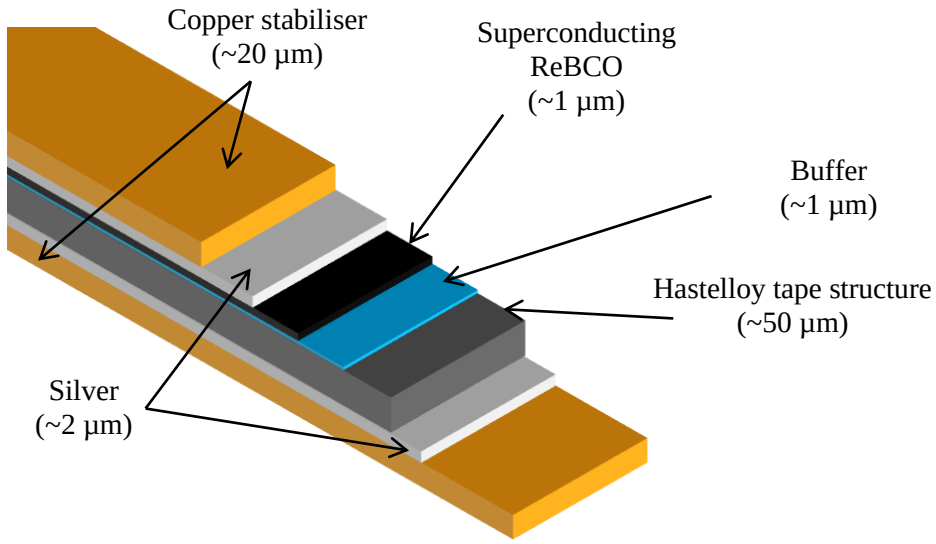

Figure 2.8 - Illustration of a typical ReBCO tape. (Not to scale)

2.4.3 Conventional tokamaks

A measure of the fusion tokamak performance is the beta value (β); a ratio of plasma pressure to the magnetic field. A higher β requires less magnets and therefore has the potential to be less expensive. A limiting factor in improving β is the size of the magnets. The physical dimensions of the rings mean that the hole in the torus can only be reduced so far before the windings of the coil are touching. This limits the reduction in the aspect ratio of tokamaks to about 2.5.

Conceptual studies of DEMO reactors have been carried out throughout Europe and internationally. The studies tend to focus on designs based on tokamaks with an aspect ratio around 2.5 - 4, similar to that of ITER. The DEMO concepts differ mainly in the design of the divertor and blanket. The European power plant conceptual studies [20], [21] produced a number of conceptual designs for commercial power plants. It focuses on five plant models A, B, AB, C and D all based on the tokamak concept with approximately the same net electric power output of 1500 MW(e). These designs illustrate a wider range of possibilities and span from relatively near-term concepts, A & B, based on limited technology and plasma physics extrapolations, to the more complex and advanced designs of C & D.

2.4.4 Spherical tokamaks

Spherical tokamak designs place the toroidal field coils closer to the plasma and often make use of a single centre column conductor [22] allowing for a lower aspect ratio (as low as approximately 1.2). The single solid centre column or centre post is often referred to as the Peng–Hicks as a result of their novel concept [23]. Spherical tokamaks hold the fusion plasma in a tighter magnetic field than a conventional large aspect ratio tokamak, resulting in a more compact device. Coupled with the use of HTS magnets, spherical tokamaks have the potential to be a more economical and efficient method for fusion power and are particularly attractive for component test facilities and fusion neutron sources.

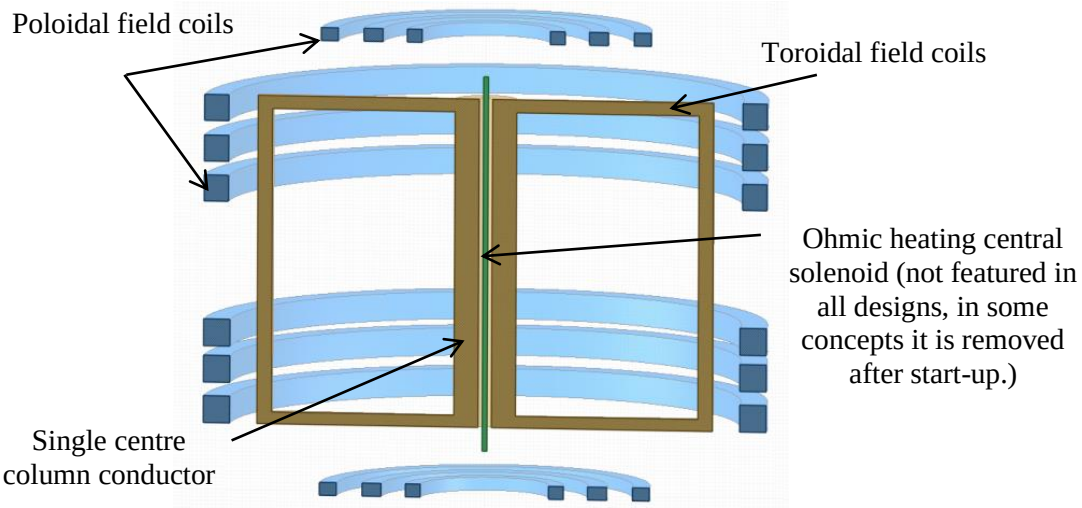

Figure 2.9 - An illustrative diagram of a magnetic coil configuration for a low aspect ratio spherical tokamak.

2.5 Blanket technology

2.5.1 Tritium fuel breeding

The fuels required for the D-T fusion reaction are deuterium and tritium; the former is abundant as it is relatively easily extracted from heavy water [24]. Tritium, however, is a volatile and radioactive substance. With a half-life of 12.3 years there are no substantial quantities of naturally occurring tritium on earth. A D-T fusion power plant operating at 1 GW fusion power will consume approximately 56 kg of tritium per year [25].

This tritium could be bred in the reactors first wall (the blanket) via neutron interactions (n, t) with a suitable material. If each neutron were to produce one tritium atom then the reaction would be sustainable, however there will be losses. A material to produce more neutrons, such as lead or beryllium (Equation 7 and Figure 2.10), is also required to ensure sufficient (n, t) reactions can take place.

$$^{208}Pb + n \rightarrow {}^{207}Pb + 2n$$
$$^{9}Be + n \rightarrow {}^{8}Be + 2n \qquad (7)$$

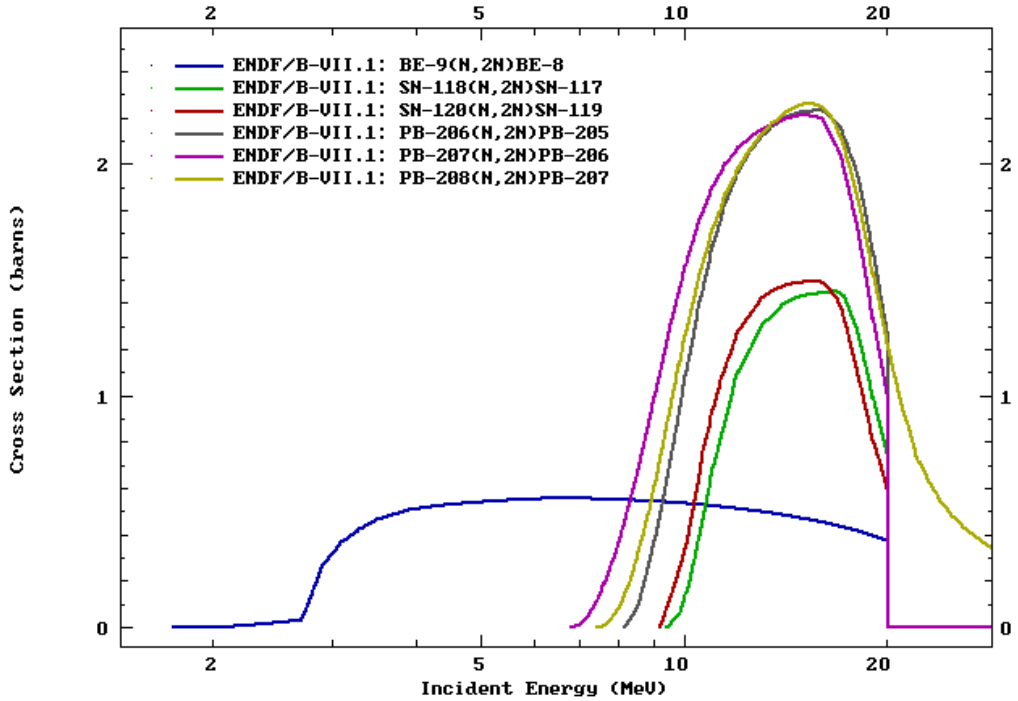

Figure 2.10 - Cross-section (ENDF/B.VII.1) data for some neutron multiplying materials. (Plot produced using www-nds.iaea.org - Project: "Multi-platform EXFOR-CINDA-ENDF", V.Zerkin, IAEA-NDS, 1999-2016)

A lithium compound is the ideal material for tritium breeding as both ^{6}Li and ^{7}Li isotopes produce tritium (Equation 8 and Figure 2.11). The ^{7}Li reaction requires fast neutrons and is harder to initiate than the ^{6}Li reaction making an enrichment of the ^{6}Li isotope favourable in some cases. Although lithium is the dominant tritium producer there are other pathways, such as via beryllium [25].

$$^{6}Li + n(slow) \rightarrow {}^{4}He + {}^{3}H + 4.8\,MeV$$
$$^{7}Li + n(fast) \rightarrow {}^{4}He + {}^{3}H + n - 2.5\,MeV \qquad (8)$$

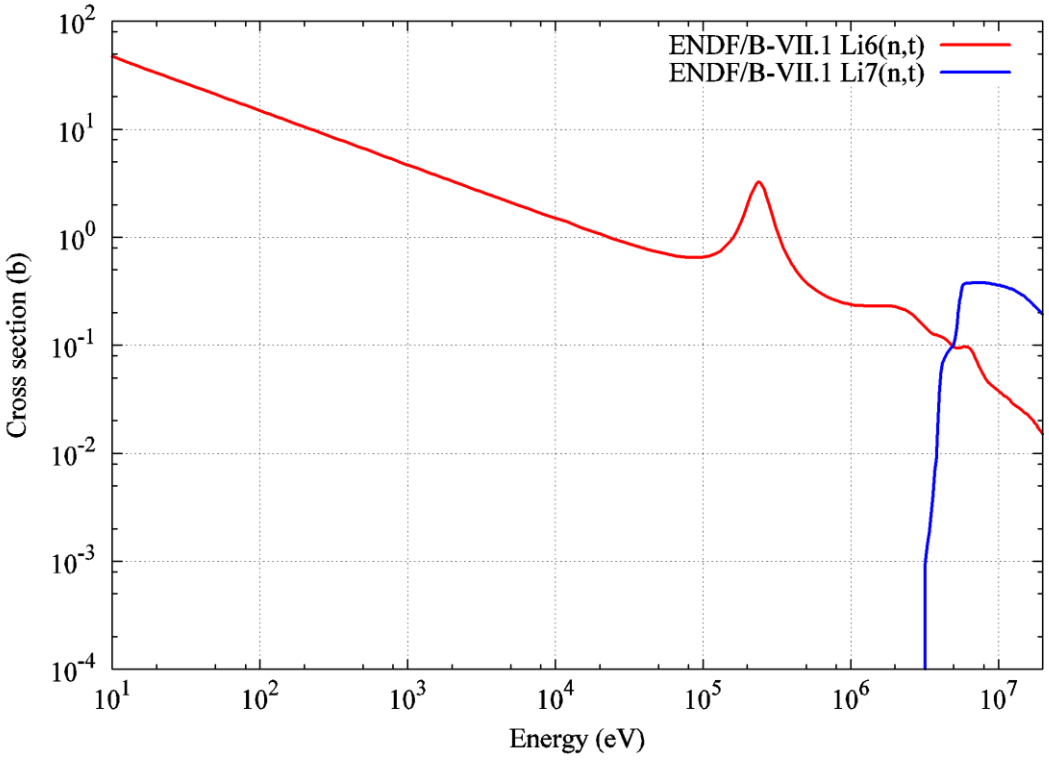

Figure 2.11 - Tritium production cross-sections (ENDF B VII.I) for lithium-6 and lithium-7 isotopes. (Plot courtesy of M.Fleming)

2.5.2 Tritium self- sufficiency and the breeding ratio

The self-sufficiency of a tritium supply can be determined by the tritium breeding ratio (TBR); the rate of tritium production per tritium burnt in the fusion plasma (Equation 9).

$$TBR = N^{+}/N^{-} \qquad (9)$$

where N^{+} is the rate of tritium production in the system and N^{-} is the rate of tritium burning in the plasma.

The required TBR needs to exceed unity by a margin to ensure a self-sufficient tritium supply compensating for losses. The margin required is a function of many reactor parameters, as described by Abdou [26], and can vary depending on design. A margin has been given [27] as 0.1, requiring a TBR of:

$$TBR \geq 1.1 \qquad (10)$$

The supply of tritium needs to be self-sufficient for the whole reactor blanket's lifetime. Not all of the produced tritium will be extracted into the tritium processing system. To reduce the inventory of tritium that remains in the reactor structure, materials with low tritium retention properties are required [28]. If the lithium material is in a liquid form it is conceptually planned that the lithium could be replenished and reprocessed continuously ensuring that the tritium supply will be sustained. However, if a solid form is used the TBR will reduce as the lithium is burnt. The self-sufficiency time of the lithium blanket (the time in which the TBR is greater than or equal to 1.1) needs to exceed the engineered design lifetime of the blanket which will be determined by the structural integrity of the materials used [25].

Neutronics analysis can be used to analyse the tritium breeding capabilities of blanket designs and materials using various different computational approaches. The data can also be evaluated via experimental procedures, these are either direct tritium production measurements or via the decay products.

2.5.3 Test blanket modules for ITER

ITER will be a test facility and will not have one continuous breeding blanket. Instead test blanket modules (TBM) will be placed into ports (numbers 2, 18 and 16) within the tokamak wall. This will allow a number of different blanket designs to be tested. It is presently planned, according to the 2012 overview of the ITER TBM program [29], that 6 breeder blankets and auxiliary systems will be assessed within the facility (see Table 2.1).

The TBMs will be required to conform to a set of boundaries: they must be recessed by 50 mm from the nominal surface of the ITER shielding blanket first wall in order to reduce plasma-wall interaction effects, have a maximum disruption energy load of 0.55 MJ/m^2 and have a 2 mm beryllium protection layer on the first wall [30]. Inside each of the test ports the TBMs will be contained in a water-cooled steel frame, of thickness 20 cm, to provide a standardised interface with the ITER structure and

ensure thermal insulation of the machine. This leaves a maximum space of 1.35 m wide and 1.80 m high available for testing.

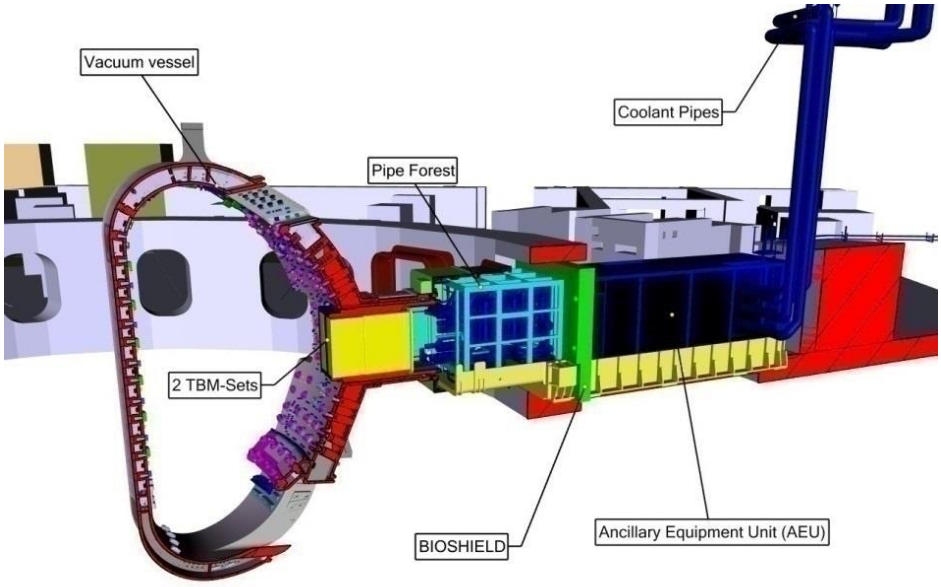

Figure 2.12 - A computer illustration of an example of ITER test blanket setup. (Reproduced with permission, © ITER Organisation [5].)

Table 2.1 - A summary of the 6 independent tritium breeder blanket systems for ITER testing [29].

TBM type	Structural material	Breeder material	Multiplier	Coolant
Helium-cooled lithium lead (HCLL) EU Members	EUROFER	LiPb (90% ^{6}Li)		Helium
Helium-cooled pebble bed (HCPB) EU Members	EUROFER	Li_4SiO_4 or Li_2TiO_3 (30% ^{6}Li)	Beryllium	Helium
Water-cooled ceramic breeder (WCCB) Japan	F82H	Li_2TiO_3 (30% ^{6}Li)	Beryllium	Water
Duel-cooled lithium lead (DCLL) US & Korea	F82H	LiPb (90% ^{6}Li)		LiPb & Helium
Helium-cooled ceramic breeder (HCCB) China	RAFM	Li_4SiO_4 (80% ^{6}Li)	Beryllium	Helium
Lithium lead ceramic breeder (LLCB) India & Russian Federation	RAFM	Li_2TiO_3 (30-60% ^{6}Li) &/or LiPb (90% ^{6}Li)		Helium &/or LiPb

2.5.4 The EU fusion road map and a demonstration plant

The European fusion development agreement (EFDA) set out an ambitious roadmap to the realisation of a supply of fusion electricity to the grid by 2050 through a goal-oriented approach [31]. The critical aspects surrounding fusion power have been transformed into eight key missions over three time periods; the Horizon 2020 research and innovation programme (covering 2014 - 2020), the years 2021 - 2030, and 2031 - 2050. A summary of the main objectives, as provided in the 2012 EFDA roadmap, are given in Table 2.2.

Table 2.2 - A summary of the three phases of the EFDA roadmap to fusion power [31].

Phase	Main objectives
2014 - 2020	Five overarching objectives: 1 Construct ITER within scope, schedule and cost; 2 Secure the success of future ITER operation; 3 Prepare the ITER generation of scientists, engineers and operators; 4 Lay the foundation of the fusion power plant; 5 Promote innovation and EU industry competitiveness.
2021 - 2030	Focused on maximising ITER explorations and the preparation of DEMO power plant construction. The majority of the eight key missions need to be accomplished in order to progress onto the third DEMO focused phase.
2031 - 2050	Construct and operate a DEMO facility proving the ability to produce net electricity from fusion power.

The European power plant conceptual studies, as previously mentioned, explored the conceptual designs for commercial fusion power plants and a DEMO reactor. It focused on four main models, named A to D. The models range from relatively near term concepts, based on limited technology and plasma physics extrapolations to more advanced concepts. The designs differ from one another in size (see Figure 2.13), fusion power and material compositions leading to differences in economic performance and environmental impacts [20]. The near term models A and B have a plasma physics scenario which represents parameters around 30 % better than the design basis of ITER [32]. The DEMO concepts C and D are based on improvements in plasma shaping and stability, limiting density and minimising divertor loads without constraining the core plasma conditions. The models are described in more detail in the following text.

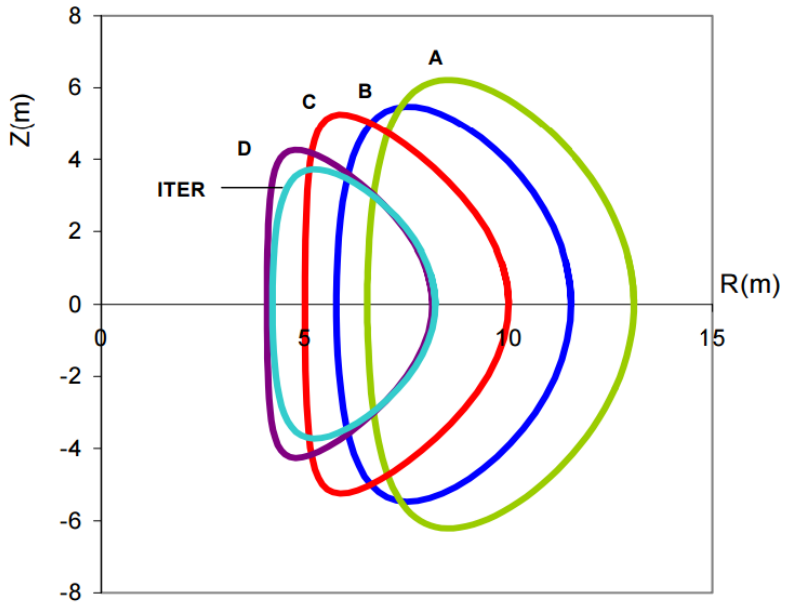

Figure 2.13 - Illustration of the size (major radius, R, height, z) and shape of the models arising from the power plant conceptual studies [18].

Model A is based on the WCLL DEMO blanket concept, which has been in development for some time, and the water-cooled ITER divertor. This concept uses a liquid LiPb blanket with lithium to generate tritium and lead as a neutron moderator. The structural material is the reduced-activation ferritic-martensitic steel EUROFER. Both the in-vessel shield and vacuum vessel are made of water-cooled steel. The average pressure and temperature of the cooling water in the blanket modules is similar to those used in fission pressurised water reactors at 15 MPa and 300 °C respectively. With a net electrical power of 1500 MW(e) the power conversion system is based heavily on the qualified technology of fission pressurised water reactors. This reactor model requires the smallest extrapolation from present-day knowledge in terms of both the physical and technological aspects.

Model B is based on the long developed European reference concept, the helium cooled pebble bed (HCPB) reactor. Studies [21], [33] have shown that with only moderate extrapolation of progress in terms of plasma physics and technology this concept can be realised. The conceptual design was originally to produce a net electrical output of 1500 MW(e), as with model A, but changes in the electrical power needed for heating and current drive have resulted in the calculated power being short by 170 MW(e). The blanket uses a ceramic breeder with beryllium pebbles for

neutron multiplication. The use of beryllium creates an issue with regards to water and therefore a helium coolant is used.

The model C design is based on a dual coolant blanket concept using a self-cooled LiPb breeding zone and a helium cooled structure and divertor. The structure is made of EUROFER steel with flow channel inserts in the LiPb channels made of silicon carbide composites. This concept requires greater assumptions in the extrapolation of technological and physical issues allowing higher plant efficiency. The liquid-metal breeder also serves as a coolant with a maximised outlet temperature to increase efficiencies. The coolant enters the modules at 460 °C and leaves them at 700 °C. This is above the maximum permissible temperature for steel and so the LiPb channels have to be thermally insulated.

The most advanced design, Model D, is based on a self-cooled LiPb blanket concept. This concept is the most attractive in terms of efficiency but comes with a much higher development risk. This model requires the most developments to be made in technological and physical terms but is included in the conceptual analysis to show how fusion power could be used in the future. The blanket is formed by only two materials; silicon carbide composite structures and LiPb breeder, moderator and coolant. This design is based on the principle of coaxial flow which allows the LiPb to have a maximum temperature of 1100 °C without exceeding the limit of 1000 °C for the silicon carbide composites [34].

Hybrid Models

Following revisions of the conceptual study, a fifth model was conceived; a hybrid of model A and B, referred to as model ‘AB’. Similar to A and B this is a near term model based on a helium cooled lithium lead concept and has similar performance levels.

Since the power plant conceptual studies, more focus has been on assessing technology readiness [35], [36] and identifying requirements for technology research and development.

2.5.5 The Power Plant Physics and Technology programme

The European Power Plant Physics and Technology programme, organised within the EUROfusion Consortium, aims at developing a conceptual design of a DEMO reactor

within the time period of the Horizon 2020 roadmap. To ensure some design flexibility in the early stages of EU DEMO design, the systems code PROCESS [37] is being used to develop self-consistent design points, enabling some flexibility whilst identifying key design drivers and constraints with regards to the four main variants; referred to as HCPB, HCLL, WCLL, DCLL. The most recent performance issues based on the 2014 blanket designs is given in [38]. The design of the blankets under the European Power Plant Physics and Technology programme is conducted by different teams:

- HCPB - Germany's Karlsruhe Institute of Technology (KIT),
- HCLL - the French Alternative Energies & Atomic Energy Commission (CEA),
- WCLL - the Italian National Agency for New Technologies, Energy and Sustainable Economic Development (ENEA) and,
- DCLL - Spain's Centre for Energy, Environment and Technology Research (CIEMAT).

The consistency of the analyses is ensured by a common methodological approach specified in the neutronic guidelines [39] for DEMO nuclear analyses. An essential feature of this approach is the mandatory use of a generic DEMO model which is consistent with the DEMO design configuration and individually adapted to the different blanket concepts. The generic EU DEMO 2015 model [40] is used in the radioactive waste assessment of this thesis (Section 5).

2.5.6 Summary of materials for a fusion breeder blanket

Numerous materials are mentioned throughout the literature with varying advantages and disadvantages. For the tritium breeding it is clear that a lithium compound of some kind must be used but several other options are available for the neutron multiplier, moderation and heat extraction; a summary of some materials and key references are given in Table 2.3. These breeding materials are assessed further within the research documented in this thesis, see Section 4.

Table 2.3 - Summary of a selection of proposed tritium breeding materials within literature.

Breeding material	Key references	Main material considerations
		Molten lithium
Li	[41]	• Very chemically active, needs to be made stable. • High melting point, though can be reduced through the addiction of BeF_2.
		Molten lithium mixtures
LiPb	[41]–[48]	• Activation issues: Bi, Po, Tl and Hg will need to be removed via a purification process. • Could be used as coolant, however, high performance tritium permeation barriers, such as SiC/SiC flow channel inserts , between LiPb and structural material for electrical and thermal insulation to reduce magnetohydrodynamics (MHD) effects.
LiSn	[49]–[52]	• Could be used as coolant. • Better thermal conductivity than LiPb. • Due to its low vapour pressure, higher operating temperatures can be used.
		Molten lithium salts
LiBeF, LiFNaK, LiBeFNa	[41], [49], [53]–[55]	• Stable salts of lithium. • Resistivity up to four orders of magnitude greater than that of LiPb.
		Ceramic lithium
Li_2O (lithium oxide)	[27], [41], [56]	• Require a neutron multiplier; beryllium. • Difficulty in using water as a coolant as it is highly reactive with beryllium. • Fabrication and manufacturing methods defined. • No long-term radioactive concerns for Li_2O, Li_4SiO_4, Li_2TiO_3 and $LiAlO_2$.
Li_4SiO_4 (lithium orthosilicate)	[25], [27], [41], [56]–[58]	
Li_2TiO_3 (lithium metatitanate)	[25], [27], [41], [56]–[58]	
Li_2ZrO_3 (lithium zirconate)	[41]	
$LiAlO_2$ (lithium aluminate)	[41]	
Li_8PbO_6	[59], [60]	• Neutron multiplication in lead could minimise or avoid the use of beryllium. • Li_8PbO_6 has been shown to have high tritium diffusivity.

2.5.6.1 Structural materials

The development of structural materials for use in nuclear fusion (in reactors, test facilities and individual components) has been driven by several objectives with regards to economic success and social acceptance. For economic success the requirement is to have a material that can reach as high as possible temperature with a large operating window for increased thermal efficiency. However, for social acceptance the material needs to exhibit low activation and be either recycled or disposed of as only low level waste [61].

Different parts of the reactor will be subject to different radiation intensities, originating from the D-T reaction, with the in-vessel components and first wall having the most exposure. The materials need to be radiation and corrosion resistant to reduce the degradation, satisfying both the maintenance and safety requirements [33].

The reactor will also undergo various temperature changes with which the materials will need to withstand. The blanket will see temperatures of approximately 250 °C to 650 °C and the divertor 600 °C to 1200 °C [62]. The thermo-physical properties of the materials used needs to be well established. The neutrons produced by the plasma reactions will have approximately 14.1 MeV of energy and will cause damage to materials via displacement cascades and transmutation products [61]. The point defects and transmutations will change the microstructure of the material and so in turn alter the properties.

In DEMO designs the materials should meet the following requirements:

- good physical properties (e.g. thermal conductivity),
- good mechanical properties (such as tensile strength, creep strength and fracture toughness), high radiation resistance (of approximately 80-150 dpa[2]),
- be a low activation material (with a good compatibility with other materials such as the coolant media) and,
- have as wide a temperature window as high as possible to increase the thermal efficiency [61], [62].

[2] A common quantity for assessing damage to materials is the displacement per atom (dpa).

2.5.6.2 Reduced activation steels

The most developed and characterised materials, requiring the lowest amount of extrapolation for use in DEMO, are the reduced activation ferritic/martensitic (RAFM) steels [61] such as F82H. These steels, however, are limited to an upper temperature of approximately 540 °C in breeder blanket applications and they require further validation in a fusion environment. Another commonly used material, such as in the HCPB and WCLL [63] concept, is the RAFM steel EUROFER. Compatibility with Li_4SiO_4, Li_2TiO_3 and Be is good until approximately 550 °C due to the creep strength [64]. The lower limit is 300 °C due to the brittle ductile transition temperature under irradiation [64]. These limits determine the temperature limits for the coolant inlet and outlet and therefore the thermal efficiency. The use of steels such as EUROFER can also cause some problems when it forms a barrier between the breeding material LiPb and helium coolant in the HCLL design. Coatings can be used to protect the EUROFER from direct LiPb exposure and mitigate corrosion problems whilst optimising the tritium recovery process [27].

Another cause for concern with the use of steel materials is the high temperature helium embrittlement. During the life time of the reactor, ~30 years, a large amount of helium will be produced by the (n,α) reactions in the first wall which will accumulate in the steel. As the solubility of helium in a metallic structure is zero [65] the helium will stay in the material causing a concern for embrittlement and limiting the life of the material under the thermal fatigue experienced on the first wall.

2.5.6.3 Oxide dispersion strengthened steels

Further developments with steel have led to the oxide dispersion strengthened (ODS) steel group. These steels have the ability to increase the operating temperature window and the RAFM variants, also known as nano-composite ferritic steels, can increase this temperature further (up to a possible 640 °C [61]). The nano-structure of the ODS steel is capable of distributing the accumulated helium into small bubbles by nucleating them on the surfaces of Ti-Y-O complexes [65]. These complexes are introduced into the steel in large numbers through the attrition of powdered steel with nano yttrium and hot extrusion or HIPing of the milled mixture. In the ODS RAFM steels the yttrium particles are refined to sizes less than 3 nm in diameter.

2.5.6.4 Silicon carbide composites

In more advanced concepts, such as the self-cooled LiPb breeder, potential materials are SiC-f/SiC composites. These composites have the potential to increase the thermal efficiency allowing operating temperatures of 600 °C to 1100 °C. They also have low activation characteristics and good thermal shock resistances. The SiC-f/SiC composites also have a lower neutron absorption cross-section [64] than EUROFER allowing for more neutrons to take part in tritium production. There are, however, some drawbacks: an increased helium production due to nuclear transmutation, radiation induced degradation of the thermal conductivity and reduced strength to radiation exposure. Though studied in many research centres and forming part of numerous reactor concepts, a lot more work is required in improving fibre processing methods and the surround technologies.

2.5.6.5 Refractory alloys

For high heat flux components, such as the divertor and first wall, refractory alloy materials are considered as these have a much higher operating temperature and neutron wall loading capability than ferritic steels and SiC-f/SiC [49]. The proposed refractory alloys are niobium, tantalum, chromium, molybdenum, and tungsten with the most favourable being tungsten for its very high melting point, high creep resistance, high thermal conductivity, low vapour pressure and high erosion resistance. The use of tungsten has been linked with the EU helium cooled divertor concepts but with numerous drawbacks (brittle at low temperatures, low fracture toughness, DBTT well above room temperature, low oxidation resistances above 400 °C and ductility decrease through re-crystallisation) the application of the material has been limited.

2.6 Radioactive waste considerations of a fusion power plant

A fusion reactor device will become radioactive during operation as a result of irradiation from the neutrons generated in the D-T reaction and through tritium activation from the fuel and tritium breeding in blankets. A fusion power plant will typically receive 1 x 10^{21} neutrons per second during full power pulses. Consequently radioactive waste will be produced, however, only a limited amount of long-lived radioactive waste is generated and no waste requiring significant active cooling. This is in contrast to high heat generating waste products arising from fission plants where the thermal output can be 2 - 20 kW/m^3 [66]–[68].

The radioactivity is expected to be ~10^4 times lower than levels arising in fission after only a few decades. Consequently after a relatively short interim decay period of 50-100 years it is possible that the majority of material could be either recycled or cleared from regulatory control. The disposal of waste produced as a result of a fusion power plant, will be dependent on the location and available repositories, and a method needs to be selected that will ensure safe isolation from biological systems. There is also a need to reduce the amount of permanent radioactive waste; an important issue with regards to public acceptance of fusion power. The classification of radioactive waste and issues related to storage and/or disposal are described in further detail in Section 4.6.3.

3 NEUTRONICS ANALYSIS

3.1 Introduction

Particle transport codes can be used to assess neutron flux distributions and related tritium production rates in a fusion reactor, whilst activation codes can be used to investigate time dependence, lithium burn-up rates and nuclide inventory. Particle transport codes use either a deterministic or stochastic approach for ‘solving’ the Boltzmann transport equation for a specific problem. Deterministic methods allow for a result to be determined at any location (all mesh points of the geometry) and give a specific solution, compared with a probabilistic indication of the result calculated using stochastic means. In deterministic methods the problem is approximated, i.e. the energy, time, space and angle are discretised whereas stochastic methods use an ‘exact’ geometrical and transport representation. The stochastic approach in the Monte Carlo (random walk) method, utilised in the Monte Carlo Neutron Particle transport code (MCNP) code, uses probabilities given by the nuclear cross-section data. MCNP is the standard transport code used in ITER, DEMO and EUROfusion analysis with a long history of development and benchmarking.

3.2 Computational codes

3.2.1 MCNP

The Monte Carlo approach [69]–[71] is used in the Monte Carlo Neutron Particle transport code (MCNP) [72], [73] and indirectly ‘solves’ the Boltzmann transport

equation. An example of this equation is given in Equation 11, representing the integral emergent particle density equation.

$$\Psi(r,v) = \int \left[\int \Psi(r',v') C\left(v' \rightarrow v, r'\right) dv' + Q(r',v) \right] T\left(r' \rightarrow r, v\right) dr' \qquad (11)$$

where $\Psi(r,v)$ is the particle collision, $Q(r',v)$ is the density of particles generated by a source, $C\left(v' \rightarrow v, r'\right)$ is the collision kernel, and $T\left(r' \rightarrow r, v\right)$ is the transport kernel [74]. Position and velocity are denoted by r and v respectively.

Solving this equation requires integration over many variables. This same process is estimated in MCNP using a theorem that assumes the model is static, time-independent, Markovian (the next event depends only on the current one, not the previous events) and the material properties are not affected by particle reactions. (This is detailed further in [72], [74].) The solution to the problem is found by simulating many particle 'histories' and inferring the result from the average of each individual history. Many particle histories are required in order to adequately sample a problem; within ITER port plug analysis for example typically a minimum of 1 billion particle histories are simulated.

In MCNP, a particle history begins when a particle is emitted from the source. It is then tracked from its life to its eventual death, through absorption for example. Before its death, the particle may split into several tracks, for instance due to splitting or $(n, 2n)$ reactions, and each track is followed and terminated individually. Probability distributions are randomly sampled using nuclear data to determine the outcome at each interaction. The history ends when all tracks have been terminated.

Due to its dependence on random sampling, the Monte Carlo method suffers from stochastic uncertainty, usually expressed in terms of the variance. Further discussion regarding the uncertainties is provided in Appendix 7.

3.2.2 FISPACT

Activation codes, such as FISPACT [75], solve the rate equations for nuclide production and decay to determine nuclide inventory, decay heat, contact dose etc. FISPACT is an enhanced multiphysics platform that was originally developed for neutron, deuteron and proton induced activation calculations for materials in fusion devices. The recent FISPACT-II release [76], [77] has a range of uses within the

nuclear science and technology sector, and has extended physical models and improved numerical algorithms. It includes features such as self-shielding factors, broad temperature dependence, thin/thick target yields and robust pathway analysis.

FISPACT undertakes four main tasks:

(1) library data preparation - the nuclear and radiological data is extracted, reduced and stored,
(2) inventory calculation - the prepared library data provides the cross-sections and decay constants required to construct the coefficients for the rate equations describing the transmutation of the initial inventory, this is followed by
(3) irradiation steps - as described in the user input file, and computation of the summary output data, and finally
(4) subsidiary calculations - such as a list of the dominant nuclides or pathway analysis.

For neutron irradiation, FISPACT-II follows the evolution of the inventory of nuclides in a target material that is irradiated by a time-dependent neutron flux. The material is homogeneous, infinite and infinitely dilute, and the description of the evolution of the nuclide numbers is reduced to the stiff ordinary differential set of rate equations [78].

3.2.3 MCR2S for shutdown dose rate calculations

The MCR2S, Monte Carlo Rigorous-2-Step, code [79] was developed to implement the Rigorous-2-Step (R2S) method [80] for shutdown dose rate calculations. This implementation of the R2S method couples MCNP 3-D neutron mesh tally data with the inventory code FISPACT-II.

A prominent issue surrounding ITER neutronics is the calculation of dose rates after reactor shutdown. ITER Project Requirements [81] call for a design that ensures the shutdown dose rate, in areas where in-situ maintenance activities are foreseen, be as low as reasonably achievable (ALARA) and shall not exceed 100 μSv/h at 10^6 s after shutdown without formal project approval [PR1782-R]. This has proved to be particularly difficult and calculations have been performed using MCR2S and other implementations of the R2S or Direct One-Step (D1S) method [82]–[84]. Rigorous benchmarking has also been performed with MCR2S, including recent studies comparing results of MCR2S against other shutdown dose rate calculation methods and experimental results from the JET 2012-2013 campaign [85].

In order to compute the shutdown dose rate, three main stages are required: calculation of the neutron flux, activation of material and finally transport of the delayed gammas. There are two main options available; a R2S method or a Direct One-Step (D1S). The R2S method requires two separate MCNP transport calculations, one for neutrons and one for delayed gammas; the method can be simplified as:

- calculate neutron spectrum in multiple locations (either within geometry cells or mesh elements),
- for each location perform an activation calculation,
- from these results derive a shutdown photon source for the decay time of interest,
- collate the individual photon sources into a 3-D MCNP decay photon source definition for each decay time,
- finally, use the derived shutdown source in a subsequent photon transport calculation to determine the shutdown dose rate.

The R2S method enables a full activation calculation to be performed, including multi-step reactions. The method does result, however, in a distortion of the spatial distribution of the activation due to the averaging of the flux over each cell or voxel; this effect is reduced by a finer resolution mesh.

The D1S method uses a coupled neutron-photon calculation (hence the one, single step) where the photons are created exactly where the neutrons collide. This method requires modification to MCNP and the data libraries in order to handle more than just prompt gammas. The D1S method also makes use of pseudo-time bins to separate the contributions from different radioactive nuclides. The D1S method avoids the discretisation error, however it requires the activation to be directly proportional to the neutron flux, so multi-step reactions or depletion effects cannot be taken into account.

3.3 Neutronics modelling

Historically models used for neutronics calculations using the Monte Carlo particle transport code MCNP were built by hand. The computer aided design (CAD) model or design drawings were simplified by the analyst and written in the MCNP geometry

definition as constructive solid geometry (CSG). This process is time consuming and as such meant that complex models had to be simplified considerably.

3.3.1 Solid geometry conversion

Tools, such as the FDS MCAM software [86], have since been developed to convert CAD models into geometry suitable for use with MCNP, making solid geometry conversion much faster. There are limitations with these tools, however, and there is often a large amount of time required to prepare the models for conversion, check the model for conversion errors and to create the 'void' region required for MCNP. The CAD models have become more complex and so typically require some simplification, defeaturing and often splitting to enable successful conversion. The simplification and conversion is usually a time consuming iterative process using some CAD tool such as CUBIT [87] or the SpaceClaim module of the ANSYS® package [88], [89].

3.3.2 Direct Accelerated Geometry Monte Carlo tool

A tool currently in development by the University of Wisconsin-Madison looks to automate some of the pre-processing required for conversion and in some cases the analysis also. The Direct Accelerated Geometry Monte Carlo (DAG-MC) tool [90]–[92] uses a CAD geometry of the model and runs a modified version of MCNP, transporting particles through a geometry defined by the automatically produced facet file. An implicit void is assumed, removing the requirement to manually define. There is still however some pre-processing required, including the creation of a 'graveyard' and the defining of boundary conditions. The graveyard is a shell surrounding the geometry, into which all particles will be killed on entering. The work flow of DAG-MC relies on the CUBIT [93] toolkit developed and distributed through Sandia National Laboratories [94].

3.3.3 Unstructured mesh geometry

The most recent release of MCNP, version 6 [95], [96], allows for a new method of describing the geometry using an unstructured mesh[3] [97], [98]. Using a suitable

[3] The term 'unstructured mesh' is used to differentiate from the 'structured' rectangular or cylindrical mesh types used in MCNP for superimposed tallying or variance reduction.

meshing tool a CAD model can be described using a tetrahedral, pentahedral or hexahedral mesh elements and embedded into the CSG definition within the MCNP input file.

Models created for neutronics assessment through solid geometry conversion are often specific to the analysis being performed. The use of unstructured mesh geometry has the potential to reduce the build time of models, reduce inaccuracies introduced through flux averaging over components and material mixing, and produce models that can be used in other analysis, such as thermal stress. The potential advantages of an unstructured mesh approach to calculations and some of the current limitations and development needs are discussed in further detail in Section 5.11.

3.4 Nuclear data

Nuclear data is of fundamental importance in the study of fusion technology and must cover a wide range of general and specific purposes. Simulation codes such as MCNP require a large amount of nuclear data. As such there are a number of projects underway regarding the development of fusion relevant nuclear data libraries. Some examples include the US evaluated nuclear data file (ENDF-VII) [99], the Japanese Evaluated Nuclear Data Library (JENDL-4.0) [100], the Joint Evaluated Fission and Fusion File (JEFF-3.2) [101] and the TALYS-based Evaluated Nuclear Data Library (TENDL) [102]. An international effort was initiated by the International Atomic Energy Agency (IAEA), launching the Fusion Evaluated Nuclear Data Library project, producing the FENDL data library and subsequent versions 2 [103] and 3 [104]. FENDL-2 is currently considered the standard nuclear data library for fusion application, such as ITER analysis.

A number of photon cross-section data libraries are available for use with MCNP for photon transport/heating calculations. MCNP also has a number of physics options available, including the ability to perform Doppler broadening to incorporate the effect of bound electrons on photon scattering [105], [106]. Appendix 4 provides a summary of investigations into the observed differences by an end user from the use of the various libraries. The photon flux through a simple spherical model was modelled and compared, along with the effect of the known Doppler broadening bug [107]. Comparisons are also made between the implementation of different libraries on a fusion relevant model. The overall conclusion was that the photon library PLIB

04/84 is the most reliable photon data library for use with MCNP6, and that in the case of MCNP5 the PLIB 84 must be used [108].

The FISPACT [75] activation code has been designed to use the European Activation File (EAF -2010) [109]. The FISPACT-II [77] release can also handle other data libraries, such as TENDL, ENDF or JEFF. EAF-2010 was developed as part of an on-going European and world-wide collaboration project and is the standard used in EUROfusion [6] and ITER fusion neutronics and activation calculations with FISPACT.

The nuclear data and codes used in research presented in this thesis are shown in Table 3.1.

Table 3.1 - Summary of the nuclear data and codes used in this work.

Calculation	Chapter/work	Code and libraries
Particle transport, TBR, flux and heating	Chapter 4, Section 4.1	MCNPv5 with ENDF-VI and PLIB04[4]
Particle transport, TBR, flux and heating	All work other than (Chapter 4, Section 4.1)	MCNPv6 with ENDF-VII and PLIB84
Material activation	All activation calculations	FISPACT-II with EAF-2010

3.5 Variance reduction

The simplest Monte Carlo model for particle transport problems is the analog model that uses the natural probabilities that events, such as capture, collision etc., occur. The particles are followed from event to event with the next event always sampled, using the random number generator, from a number of next event possibilities according to the natural event probabilities. This method is directly analogous to the naturally occurring transport. This transport model, however, only works well when a significant number of the particle histories contribute to the final tally, to give a reasonable statistical uncertainty.

[4] There is a known bug in the use of PLIB04 with MCNP5, further detail is given in Appendix 4, where this effect has been investigated. A comparison has also been performed between the two versions of MCNP, MCNP5 and MCNP6, to validate the use of the different versions through the work comprising this PhD thesis.

In order to increase the contribution to a tally, to reduce the statistical uncertainty, non-analog transport is required. Transport models that make use of non-analog transport are known as variance reduction techniques. These techniques make use of particle weighting in order to prevent biasing the result, whilst implementing methods to 'encourage' more particle histories to be tallied in the region of interest.

The four classes of variance reduction techniques are:

(1) Truncation methods - through the use of modified geometry, i.e. removing geometry that will not significantly impact on the final tally, and/or through MCNP options such as the energy cutoff and time cutoff.
(2) Population control - through the use of particle splitting and Russian roulette to control the number of samples taken in different regions of the model. This is implemented through importance mapping and setting particle weight bounds.
(3) Modified sampling - through the use of methods such as exponential transforms, implicit capture, forced collision and source biasing.
(4) Partially deterministic methods - in MCNP these include point detectors, DXTRAN spheres and correlated sampling. These methods should be used with increased caution and require a deep understanding of the problem to ensure unwanted and unintentional biasing to the result is not introduced.

Variance reduction may be considered as either 'local' or 'global' depending on the problem and tally of interest. Variance reduction to increase sampling at a particular point would be considered local, whereas variance reduction techniques that aim to increase statistical uncertainty throughout the phase-space are considered global (GVR).

The use of weight windows for population control is often considered to be the most powerful technique. The weights can be generated automatically through MCNP over a superimposed mesh, however an initial 'guess' is required, and the overall effectiveness of the resulting weight window will be based upon the initial parameters. Iterative approaches to calculating weight windows have been developed, including the WWiter code that sets the weight range based on previous flux values, as per the work of the Cooper and Larsen method [110].

Recently released variance reduction software from Oakridge National Laboratory, uses a deterministic approach to generating a weight window. The Automated

Variance Reduction Parameter Generator (ADVANTG) [111], [112] software automates the process of generating variance reduction parameters for use with MCNP, generating space and energy dependent mesh-based weight window bounds and biased source distributions using 3-D discrete ordinates (SN) solutions of the adjoint transport equation that are calculated by the Denovo package. The lower weight windows are provided in a format that can be used with MCNP as the weight window input file. As ADVANTG employs a deterministic transport solver the user effort and computational time are reduced, though for challenging problems, multiple iterations may be required for refinement to obtain high-quality variance reduction parameters.

Within this work, a number of variance reduction techniques were used, including truncation through the energy and time cutoff values on the CUT card, population control through cell importance mapping and weight windows. Automated processes were used to generate the weight window, including the WWiter code and ADVANTG. A summary of the variance reduction used in the neutronics analysis is given in Table 3.2.

Table 3.2 - Summary of main variance reduction techniques used within this research.

Calculation	Chapter/work	Main VR technique
Particle transport, TBR, flux and heating	Chapter 4, Section 4.1 & 4.2	Energy and time cutoff
Particle transport, flux and heating	Chapter 4, Section 4.4 & 4.5	Cell importance mapping for LVR in the centre column
Particle transport, TBR, flux and heating	Chapter 4, Section 4.6	GVR with weight window generated using WWiter
Particle transport, flux	Chapter 5	The VR used for each method within chapter 5 is detailed further in Section 5.8. For all methods, apart from the use of unstructured mesh, GVR through weight window and source biasing generated with ADVANTG were used.

3.6 Definition of parameters

In assessing the blanket performance and material activation/waste considerations, the following parameters have been used:

On-load performance

- Tritium breeding potential - estimated through the tritium breeding ratio (TBR). This is the ratio of tritium breed per source neutron (i.e. the ratio of

tritium produced to that which is burnt). The TBR has been estimated using the F4 neutron cell averaged flux tally with the MT 205 reaction number.

- Energy production - defined as the ratio of nuclear heating in the blanket per input energy (~14.1 MeV per source neutron), referred to as the energy multiplication and determined through the F6 cell averaged energy deposition tally.
- Shielding - measured as the percentage of incident fast flux reaching the back of the blanket (see Figure 3.1) and through the peak heating of the inboard magnets. The fast flux was calculated with MCNP using an F2 surface tally and considering only neutron flux with E_n > 0.1 MeV. The peak heating was determined using the F6 energy deposition tally.

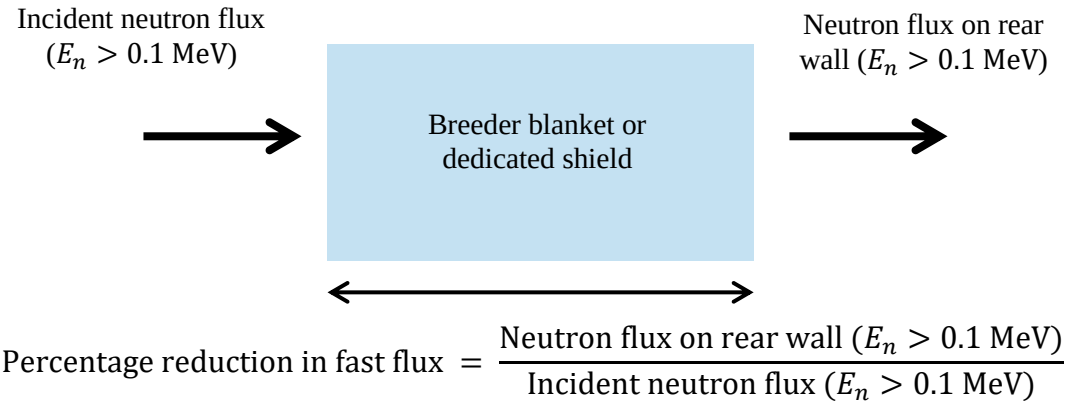

$$\text{Percentage reduction in fast flux} = \frac{\text{Neutron flux on rear wall } (E_n > 0.1 \text{ MeV})}{\text{Incident neutron flux } (E_n > 0.1 \text{ MeV})}$$

Figure 3.1 - Schematic representation of shielding performance quantity.

- Neutron wall loading - the neutron wall loading in this work was calculated as the uncollided neutron flux incident on the first wall. This was tallied in MCNP using the F1 surface current tally with materials void and importance zero to avoid tallying as a result of collisions within first wall material.
- Neutron flux map- the neutron flux was calculated using MCNP on a 3-D superimposed mesh tally. The neutron flux was tallied in 175 energy group structure for use in activation calculations.
- Heating map - heating throughout the reactor geometry has been estimated using 3-D superimposed mesh tally with the corresponding tally multiplier (FM card) relating to the neutron or photon heating.

Activation and waste

- Activation - the total activity per volume irradiated was taken from the FISPACT-II output file, along with the specific activity of some radionuclides.
- Contact dose rate - the FISPACT-II calculated contact dose rate, measured in Sieverts per hour (Sv/hr), was used in determining the quantity of radioactive waste material that could be considered for recycling routes.
- Dominant nuclides - the nuclides that dominate the total activation in some specified locations within the model were extracted from the output files of FISPACT-II.
- Pathway analysis - using the pathways keyword within FISPACT-II, the pathways have been analysed in some locations of the neutronics model used.

The MCNP tallies and normalised units are summarised in Table 3.3.

Table 3.3 - On-load neutronics performance parameters and tallies used.

	MCNP tally	Normalised units
Neutron flux map	FMESH card	Neutrons/cm^2/source particle
Nuclear heating map	FMESH card with reaction numbers for neutron and photon heating	kW
Tritium breeding ratio	F4 cell tally with reaction number for tritium production	Ratio
Peak heating	F6 cell energy deposition tally, renormalised to fusion power for heating in kW	kW or kW/m^3
Peak fast flux	F2 surface flux tally	Neutrons/s/m^2
Neutron wall loading	F1 surface current tally with materials void and centre column importance zero- to tally the uncollided neutron power	MW/m^2

3.7 State of the art in neutronics analysis with regards to blanket technology performance and radioactive waste assessment

3.7.1 Tritium breeding in the ITER test blanket modules

Comprehensive studies have been performed in support of the ITER test blanket module programme. These include extensive neutronics calculations, both with 1-D and 3-D codes, assessing the capabilities for tritium breeding. An example of the work

is given in [113], using detailed 3-D neutronics calculations with the US DCLL test blanket module. The calculations were performed directly in the CAD model using the DAG-MC code; allowing preservation of the geometric detail. Detailed high-resolution, high-fidelity profiles of the nuclear parameters were generated using fine mesh tallies. These included tritium production, nuclear heating, and radiation damage. The test blanket module heterogeneity, exact source profile, and inclusion of the surrounding frame and other in-vessel components result in lower test blanket module nuclear parameters compared to previous 1-D predictions. The work demonstrates the importance of preserving geometrical details in nuclear analyses of geometrically complex components in fusion systems.

More recent 3-D neutronics calculations have been performed, using MCNP, on the supercritical-water cooled solid breeder test blanket module developed by India. This test blanket module uses supercritical water as the coolant, Li_4SiO_4 ceramic pebbles as a breeder, and beryllium pebbles as a neutron multiplier. The results of neutronics, thermo-hydraulic and thermo-mechanical analysis are presented in [114]. The neutronics calculations show that the proposed test blanket module has a suitable TBR of 1.17.

3.7.2 Blanket performance of DEMO

ITER, as already discussed, will be a testing facility. Conversely DEMO is expected to be a fusion device nearer to commercial power plants. There is currently not one specific DEMO design selected and detailed operation conditions are still in development. However it is expected that unlike ITER, DEMO will operate either in long-pulsed or steady-state mode. DEMO will also need to show that tritium self-sufficiency is achievable, and consequently will have a full set of breeder blankets. This is in contrast to the test blanket modules designed for ITER. As described in Section 2.5.5, there are four main blanket concepts being pursued as part of the EU fusion research programme.

Recent research presented in [115] uses neutronic analysis to assess the variations in TBR for the different DEMO blanket concepts; HCPB, HCLL, WCLL and DCLL. This work included recent modifications of the blanket configuration. A dedicated automated procedure was developed to fill the breeding modules in the common generic model in correspondence to the different concepts. The TBR calculations were

carried out using MCNP5. It was determined that one of the most critical issues regarding the blanket material for tritium breeding is the content of steel. The considered variations of the steel content showed a very strong effect on the TBR performance for all DEMO blanket concepts, though the HCPB was shown to be the most sensitivity.

The use of beryllium as a multiplier is a feature of many blanket concepts and is used in the solid breeder HCPB EU DEMO design. Beryllium is however a valuable resource and estimates of beryllium requirements and available resource suggest that this could represent a major supply difficulty for solid-type blanket concepts. Reducing the quantity of beryllium required by breeder blankets would help to alleviate the problem to some extent. It is important though that any reduction in the beryllium quantity within a blanket does not diminish the blanket's performance. Research presented in [116] proposes the use of a mixed pebble bed design with varying fraction of multiplier. This aims to make the most optimum use of the beryllium $(n, 2n)$ reaction by careful positioning. A neutronics study using MCNP (version 6) with the 2013 EU DEMO model investigates linear variations of the multiplier fraction in relation to blanket depth. It was concluded that blankets with a uniform multiplier fraction showed little scope for reduction in beryllium mass. Blankets with varying multiplier fractions were able to use 10% less beryllium whilst increasing the energy multiplication by 1%, and maintaining a sufficient TBR.

3.7.3 Spherical tokamaks and high temperature superconductors

There are detailed design concepts for variously named neutron sources, fusion neutron science facilities, component test facilities etc. based on small or medium-size spherical tokamaks. The recent industrial maturity of HTS magnets offers a new opportunity for a more efficient, compact and modular device. One of the critical issues with regards to a spherical tokamak is the proximity of the central magnets to the fusion plasma with little room for shielding. Research conducted on a spherical tokamak power plant using ‘conventional’ superconducting magnets considers a 10 cm thick water-cooled steel shield [117]. The paper concludes that the shield serves to reduce the nuclear heating and damage to the conducting magnets within the centre rod to “acceptable levels”.

MCNP has recently been used to assess, amongst other things, the heating within the centre column magnets for spherical tokamak concepts based on the use of HTS magnets [118]. For a given fusion power, the heat deposition in the centre column HTS magnets has been considered as a function of plasma major radius, centre column radius, and tungsten carbide shield thickness. The study included computations over the ranges 0.6 m ≤ major radius ≤ 1.6 m, 0.15 m ≤ centre column ≤ 0.25 m, and 0.15 m ≤ shield thickness ≤ 0.4 m. The aspect ratio was fixed at 1.8. A possible pilot plant with 174 MW fusion power, a major radius of 1 m, centre column size of 0.23 m and shielding thickness of 0.32 m is shown to lead to a peak nuclear heat deposition into the centre column HTS magnets of ~14 kW. The aspect of neutron damage to the HTS magnets was not considered, nor the TBR capabilities.

3.7.4 Radioactive waste assessment of fusion power plants

In terms of radioactive waste assessments through neutronics analysis, the study [119] computes the radiation transport and activation response throughout the ITER machine and updates the previous ITER radioactive waste assessment using modern 3-D models. MCNP5 (with FENDL2.1 nuclear data) was used for particle transport and FISPACT-2007 (with EAF-2007 nuclear data) for activation and nuclide inventory estimations. A cell-based method was used (this is described in more detail with relation to DEMO radioactive waste assessments in Section 0) and the latest information on component design, maintenance, replacement schedules and materials was adopted. All plasma-facing materials except tungsten were found to be classified as type-B (of the French classification, see Section 5.4.1). Elemental concentration limits for type-A classification of first wall and divertor materials were obtained and it was concluded that for steels only a reduction in operation life can reduce the waste class. Comparison of total waste amounts with earlier assessments is limited by the fact that analyses of some components are still preliminary. Importantly the trend, however, indicates a potential reduction in the total amount of waste if component segregation is demonstrated.

A DEMO-relevant radioactive waste assessment was carried out by Someya [120] using the THIDA-2 code. THIDA-2 is an advanced version of the 1978 developed THIDA system. This code coupled the transport calculation (either 1-D/ 2-D discrete ordinate radiation transport codes, or 3-D Monte Carlo ‘MORSE-GG’ code) with an

induced activation code ‘ACT4’. The THIDA code was developed to not only calculated transmutation and activity but also decay heat and delayed gamma source. This paper explored the waste management considerations for a DEMO model based on the Japanese ‘SlimCS’ concept. Some of the main conclusions relevant for this research include:

- The induced radioactivity for tungsten coating was dominated by ^{187}W and ^{188}Re originating from ^{186}W in the tungsten coating at short cooling times. For cooling times between 1 day and 1 year the ^{185}W activity was prominent.
- In the case of long-lived radionuclides, the dominant nuclides determining the activity were ^{186m}Re (2.0×10^5 years) and ^{192m}Ir (241 years).
- The dominant nuclides with regards to activity in the first wall were determined to be ^{56}Mn, ^{54}Mn and ^{55}Fe which originate from ^{54}Fe and ^{56}Fe in the F82H steel of the first wall. The ^{55}Fe activity is prominent 100 years after shutdown. After this the dominant nuclides were shown to be ^{63}Ni and ^{14}C originating from ^{62}Ni and ^{14}N, respectively.

3.7.5 Neutronics modelling techniques

In 2008 a study [121] was conducted into the effects of 1-D, 2-D and 3-D geometric representations of a fusion reactor for neutronics analysis. The neutron wall loading distribution, tritium-breeding ratio and power density distribution were calculated to evaluate the nuclear performance using MCNP (version 4C). Comparison of the results suggested that a 1-D approach overestimates the TBR. The total TBR was calculated to be 1.39, 1.33 and 1.29 based on 1-D, 2-D and 3-D models respectively. It was concluded that for obtaining global scalar quantities for general use, simplified models of the fusion reactor are usually sufficient.

In 2015 a comparative assessment of different approaches for the use of CAD geometry in 3-D Monte Carlo transport calculations was published [122]. Three different approaches for the use of CAD geometries with MCNP calculations were investigated and assessed with regard to calculation performance and ease of use. The first method was the conversion of CAD geometry into an MCNP using the conversion software McCad developed by KIT [123]. The second approach utilised the new MCNP6 unstructured mesh geometry feature for the particle tracking and

relies on the conversion of CAD into an unstructured mesh. The third method employed DAG-MC, developed by the University of Wisconsin-Madison. The obtained results show that each method has its advantages depending on the complexity and size of the model, the calculation problem considered, and the expertise of the user.

A comparison of the model run with no materials (void) showed good agreement between all three approaches, with the MCNP6 unstructured mesh results deviating slightly more than DAG-MC from the McCad results. It was concluded that the model preparation was the most difficult and time consuming for a McCad approach.

The MCNP6 unstructured mesh capability has also been considered for shutdown dose rate analysis. Codes, such as MCR2S, have been written in order to carry out shutdown dose rate calculations for fusion devices. MCR2S (explained in more detail in Section 3.2.3) uses a CSG model and a superimposed structured mesh to calculate 3-D shutdown dose rate maps. A recent paper [124] explores a new approach to MCR2S calculations, implementing the use of a single unstructured mesh to replace both the CSG model and the superimposed structured mesh.

This new MCR2S approach was demonstrated on three models of increasing complexity: a sphere, the ITER shutdown dose rate benchmark and the DEMO shutdown dose rate benchmark. In each case the results were compared to MCR2S calculations performed using MCR2S with a superimposed structured mesh. It was concluded [124] that the results from the unstructured mesh implementation of MCR2S compared well to the structured mesh calculations. It was also concluded that the resolution of the unstructured mesh can significantly affect the results of the calculations, and the importance to finely mesh components with streaming paths or areas that significantly contribute to the dose rate was highlighted.

The paper [124] also concluded that MCR2S has been successfully modified to enable shutdown dose rate calculations on tetrahedral, pentrahedral and hexahedral unstructured mesh geometries. A number of advantages regarding the use of an unstructured mesh approach to shutdown dose rate calculations are discussed in the paper, including motivations for continued investigations.

3.8 Motivations for the thesis

Neutronics assessment regarding the blanket performance of a variety of breeder materials is presented in the literature, with a particular focus on the ITER test blanket modules. Within the EU fusion research programme the four main EU DEMO blanket concepts are also being developed. These concepts focus on the use of two breeder materials; the solid Li_4SiO_4 and the LiPb liquid breeder. A comparison of the solid and liquid breeding materials, including some of those proposed for more advanced blanket concepts and the less conventional, is presented in this thesis. The neutronics analysis method using MCNP is explored and the modelling effects investigated. The performance potential of the liquid breeders is particularly important towards the progress of more advanced fusion concepts making use of dual functional breeder and coolant materials.

Shielding requirements for the centre column of spherical tokamak concepts has recently become a growing area of research, mostly due to the developments of HTS magnets and the potential they possess for producing a compact reactor design. The reduction of heating to the centre column magnets has been considered in some spherical tokamak concepts through the use of a steel or tungsten carbide (and water) inboard shield. Further consideration, however, is required regarding the neutron fast flux, especially if spherical tokamak concepts are to be considered for fusion power plants. A parameterised spherical tokamak neutronics model is used in this thesis to perform a scoping study over a wider range of geometrical configurations than previously published. Importantly, these studies also include fast neutron flux estimations and TBR considerations.

The radioactive waste assessment of ITER and DEMO concepts through material activation calculations is typically conducted using a cell-based approach. The MCR2S code has been used extensively, and benchmarked with other codes and experiments, in fusion neutronics for shutdown dose rate assessment. A development of the MCR2S code has recently been used to perform a structured mesh based preliminary radioactive waste assessment on the UK JET facility. The potential of this method is explored further in this thesis with reference to a DEMO concept using IAEA safety guidelines on radioactive waste. The MCR2S structured mesh approach is compared to a typical cell-base method.

This radioactive waste assessment method comparison is further enhanced with the development of the new MCNP6 unstructured mesh geometry feature. The use of unstructured mesh has been demonstrated for use in shutdown dose rate analysis with MCR2S. The research presented in this thesis explores the use for a more accurate approach to radioactive waste assessments.

4 BLANKET PERFORMANCE; TRITIUM BREEDING, ENERGY MULTIPLICATION AND SHIELDING

4.1 Introduction

The blanket of a fusion reactor, the layer of material surrounding the plasma, will have three main functions: (1) breed tritium fuel to provide a self-sufficient supply, (2) produce energy, and (3) shield surrounding magnets. These three functions have been explored in more detail. In the case of spherical tokamak designs, there is no room for an inboard blanket, therefore consideration needs to be made as to whether the outboard breeder alone can provide sufficient tritium and the requirements for a dedicated inboard shield.

This work has been broken down in to four main areas:

i. assessing the effect of material composition on the blanket performance and the use of homogeneous material mixing for neutronics calculations,
ii. a comparison of the blanket capabilities of some solid and liquid breeding materials,
iii. the shielding requirements for a dedicated inboard shield in spherical tokamaks, and

iv. the neutronics performance, regarding the blanket capabilities, shielding and activation considerations, of a high temperature superconducting spherical tokamak based on the Princeton Plasma Physics Laboratory spherical tokamak fusion nuclear science facility concept.

4.2 Blanket material composition

Tritium is bred mainly through the neutron interactions with ^{7}Li and ^{6}Li isotopes. Both isotopes are found in naturally occurring lithium; ~92.5% ^{7}Li and ~7.5 % ^{6}Li. To utilise the larger cross-section with ^{6}Li at thermal neutron energies (Figure 2.11), neutron multiplying materials are considered (Figure 2.10). Neutron multiplying materials, such as beryllium, create 2 or more neutrons per neutron interaction, with the resulting neutrons having lower energy. The addition of multiplying material can have a significant effect on both the TBR and the energy multiplication.

Tritium breeding blankets will not only consist of a lithium-based material and multiplier, but will also require some cooling medium and structures. Structural material will be required for example to contain the blanket, for cooling pipes, isolation etc. In order to perform neutronics calculations on simple models to assess a range of material options, a homogeneous material mixture was proposed. Studies on the effect of modelling the blanket for a pebble-bed blanket design as a homogeneous mix, as opposed to a more intricate pebble model, has shown overestimation of the TBR by ~2% [125].

Investigations regarding the optimising of material mixtures and the effect of modelling as a homogeneous mix, as opposed to heterogeneous layers, in a simple spherical model are presented in this section.

4.2.1 Blanket materials

In this research, the blanket materials were assumed to be pure lithium (with natural ^{6}Li concentration) for the breeder, beryllium multiplier, helium cooling and EUROFER steel structures. The assumed mass density of each material is given in Table 4.1 and the isotropic material composition, as used in the MCNP definition is given in Table 7.1of Appendix 1.

The percentage volume of each material was varied from 10 - 40 %, assuming a reference mixture of 20 % breeder, 10 % structure, 20 % coolant and 50 % multiplier.

Although this method can create material mixtures without a significant engineering basis, the main aim was to assess purely the TBR, energy multiplication and shielding capabilities from changing material composition. The limit of 10 and 70 % of each material provides a reasonable range without creating extremely unrealistic material compositions.

Table 4.1 - Assumed mass density of materials used.

Material	Mass Density (g/cm^3)
Lithium breeder	0.5400
EUROFER[5] steel structure	7.7980
Helium coolant	0.0002
Beryllium multiplier	1.8500

4.2.2 Neutronics model and calculations

A simple spherical model (Figure 4.1) was used, and in the case of the heterogeneous simulations, this was divided into 50 layers of equal volume. A script was written in order to produce the cell definitions for the heterogeneous model MCNP input files; defining the material for each layer. The layers were defined in a sequence: breeder, structure, coolant and then multiplier, which is then repeated. The script first determines how many times this sequence can be repeated for the given material volume mix. Then, depending on the mixture, layers are assigned one of the four materials.

For example in the case of changing the breeding volume to 40 %: the coolant volume is calculated to be 15 %, multiplier 37.5 %, and the structure 7.5 %. The sequence of breeder, structure, coolant, multiplier, is repeated 4 times. For each sequence, the breeder will be assigned 20 layers, the coolant 8 layers, multiplier 19 layers and the structure assigned 4. The resulting model from this example is shown in Figure 4.2.

[5] EUROFER steel (such as EUROFER-97 variant [185]) is a Reduced Activation Ferritic/Martensitic (RAFM) steel considered for structural applications in fusion devices [186]. The reduced activation composition adopted for fusion structural materials has involved the substitution of some alloying elements such as Mo, Nb and Ni present in the commercial martensitic steels with other elements which exhibit faster decay of induced radioactivity, such as Ta, W and V [187].

For the homogeneous mix simulations, the model remained constant (Figure 4.1) with the material definition and density varied. For each change in percentage volume a new material definition is created along with the effective mass density. The effective volume of each material in the homogeneous material mix should be similar to the volume of the model occupied with that material in the heterogeneous model. The effective mass density of the homogeneous mixtures should be similar to the sum of the material mass within the heterogeneous model, divided by the total volume. A comparison of these values is given in Table 4.2.

The D-T fusion plasma has been modelled as a 14.1 MeV neutron point source in the centre of the spherical model.

Table 4.2 - Comparison of effective mass density as calculated from the two blanket model types; heterogeneous and homogeneous.

Volume of breeder (%)	Mass density of heterogeneous model			Mass density of homogeneous material mix
	Volume of model (cm^3)	Sum of mass (g)	Effective mass density (g/cm^3)	Effective mass density (g/cm^3)
10	1.13E+07	2.19E+07	1.95	1.97
20	1.13E+07	2.04E+07	1.81	1.81
30	1.13E+07	1.77E+07	1.57	1.65
40	1.13E+07	1.69E+07	1.50	1.49
50	1.13E+07	1.47E+07	1.31	1.34
60	1.13E+07	1.20E+07	1.06	1.18
70	1.13E+07	1.16E+07	1.03	1.02

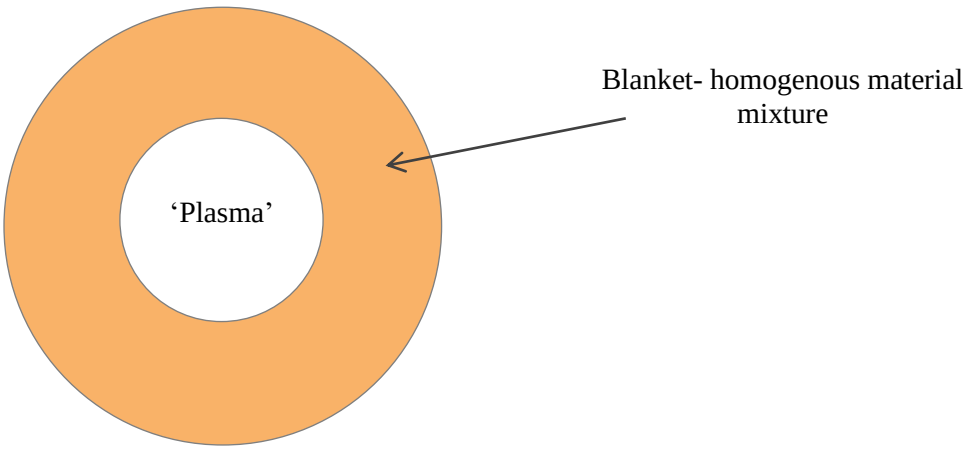

Figure 4.1 - MCNP spherical model created using two concentric spheres. This model was used with homogeneous blanket material mixtures.

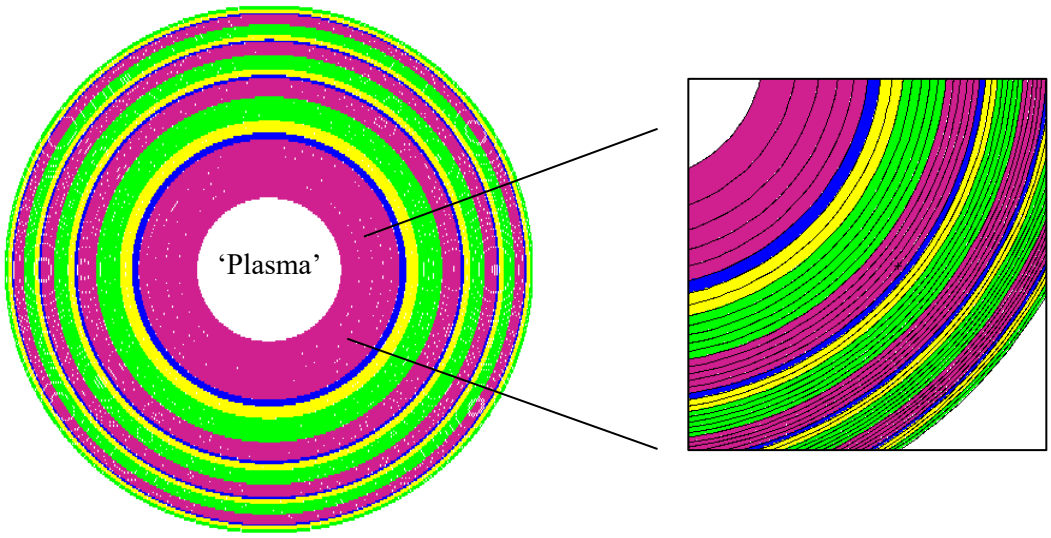

Figure 4.2 - MCNP spherical model created using many concentric spheres as determined by the automated MCNP input generating script (purple = breeder, blue = structure, yellow = coolant and green = multiplier). This model was used with the heterogeneous material simulations; the example shown here is with 40% breeder volume.

4.2.3 Results and discussion

The effect of varying the volume of each material comprising the blanket (the breeder, multiplier, structure and coolant), is presented in the following results, using both a heterogeneous material approach and a homogeneous material mixture.

4.2.3.1 Heterogeneous Blanket

The variation of TBR with changing material composition is shown in Figure 4.3. Increasing the volume of breeder material, increases the TBR as there is more lithium available for the (n,t) reactions. As the percentage of the breeder is increased, however, the percentage of beryllium multiplier decreases, the effect of which can be seen by the steady TBR above approximately 50 % breeder volume. This is due to the reduction of the $(n,2n)$ reaction from the beryllium and the moderated neutrons as required for the high cross-section thermal (n,t) reaction in the ^{6}Li isotope. The optimum percentage of beryllium multiplier (for TBR) is approximately 30-40 %.

The presence of structural material has a negative effect on the TBR. When the structural content is increased above 20-30 % of the total blanket material the TBR falls to below unity, i.e. less than one tritium atoms is being produced per neutron.

Some structural material will obviously be required to ensure the integrity of the blanket.

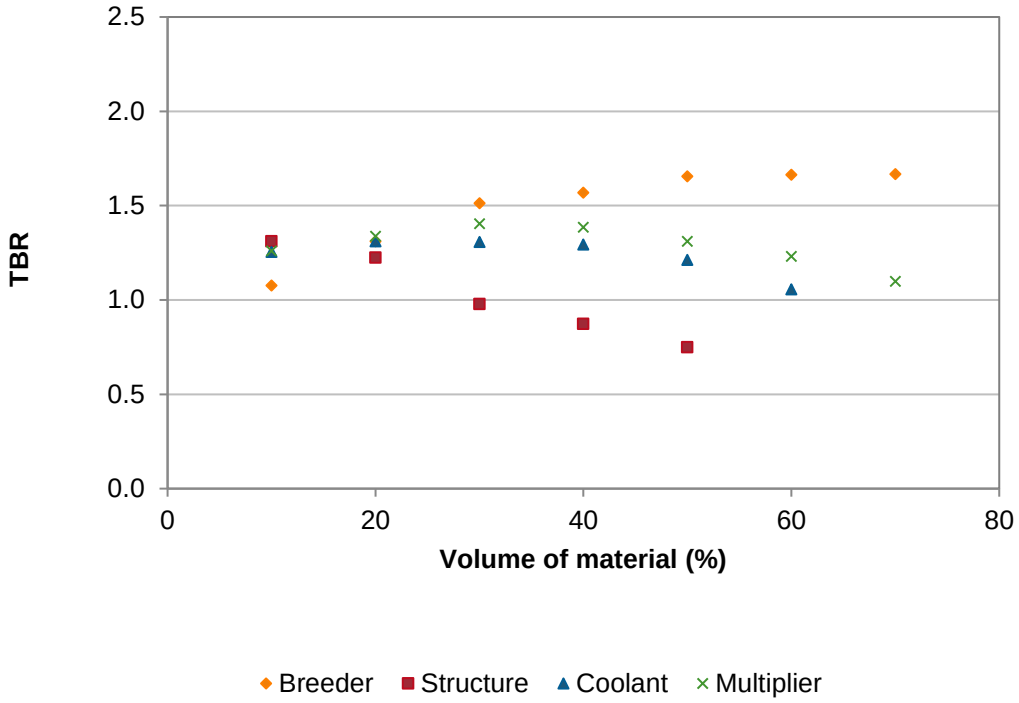

Figure 4.3 - Total TBR for varying percentage volume of material [6].

The effect of material position within the blanket can be seen in Figure 4.4. The presence of the first beryllium neutron multiplying layer (green) increases the TBR at the front of the second breeding layer due to the increased neutrons. The effect of neutron reflection from the structural material can be seen at the back of each breeding layer. The TBR in each layer decreases with distance from the plasma due to neutron absorption through the layers.

The effect of material composition on the energy multiplication is shown in Figure 4.5 and a similar pattern to that shown in the TBR is evident. The ^{6}Li (n, t) reaction is exothermic and so similar to the TBR, the presence of the beryllium multiplier which increases the ^{6}Li reaction due to the increase in thermal neutrons, also serves to increase the energy multiplication.

[6] There are two values missing for the variation in the structural material series, these were not recalculated as the general trend and main conclusions can be drawn from the data collected.

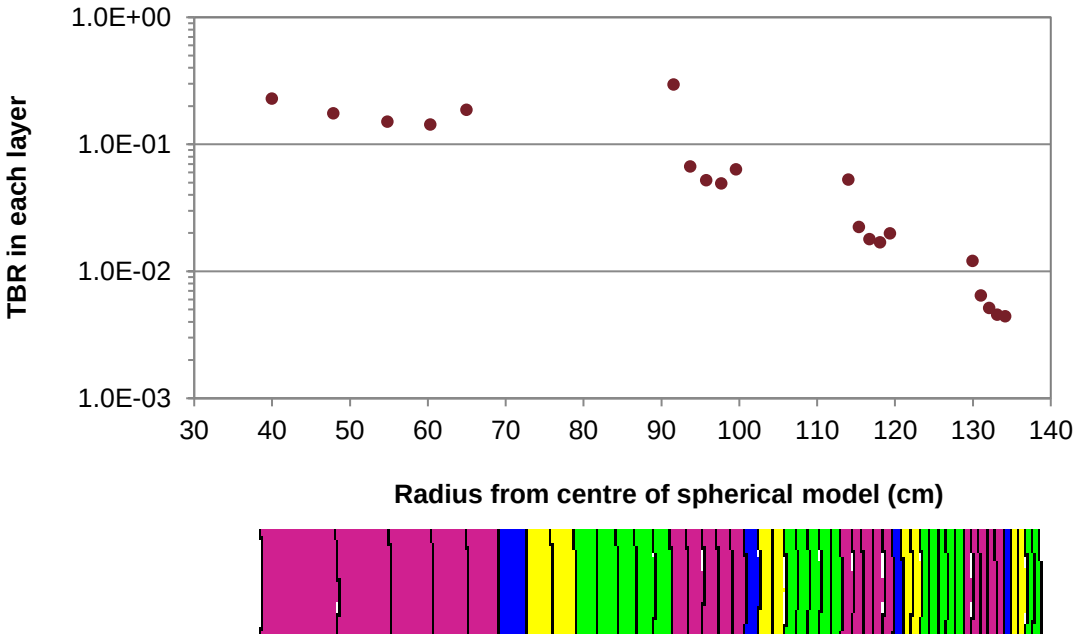

Figure 4.4 - TBR variation with radial distance from the centre of the plasma region. The position of the material layers are shown beneath the graph (purple = breeder, blue = structure, yellow = coolant and green = multiplier). This data is for the 40 % breeder composition.

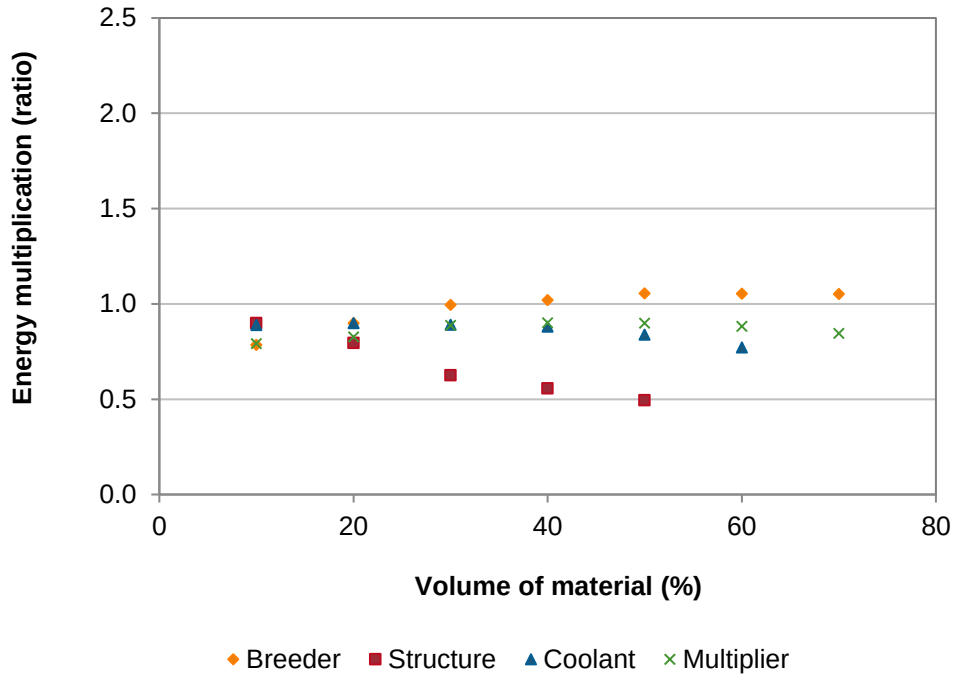

Figure 4.5 - Total energy multiplication (a ratio of the nuclear energy deposited within the material to the energy of D-T neutrons, assumed to be 14.1 MeV) for varying percentage volume of material.

The shielding capabilities were assessed in terms of the flux attenuation through the blanket. The percentage of the incident fast neutron flux that reached the rear of the blanket is shown in Figure 4.6. Increasing the percentage of beryllium present decreases the neutron flux at the rear of the blanket. With only 10 % beryllium, approximately 0.7 % of the incident flux reaches the back of the blanket. This is due to a reduction in the moderation provided by the beryllium.

The concentration of coolant material has the greatest effect. As expected increasing the presence of helium and therefore reducing the quantity of other material causes more flux to pass through the blanket, thus significantly reducing the shielding capabilities. The flux reduction through the blanket layers is show in Figure 4.7 for a 40 % breeder case. The change in the spectrum with the increase in thermal neutrons is evident.

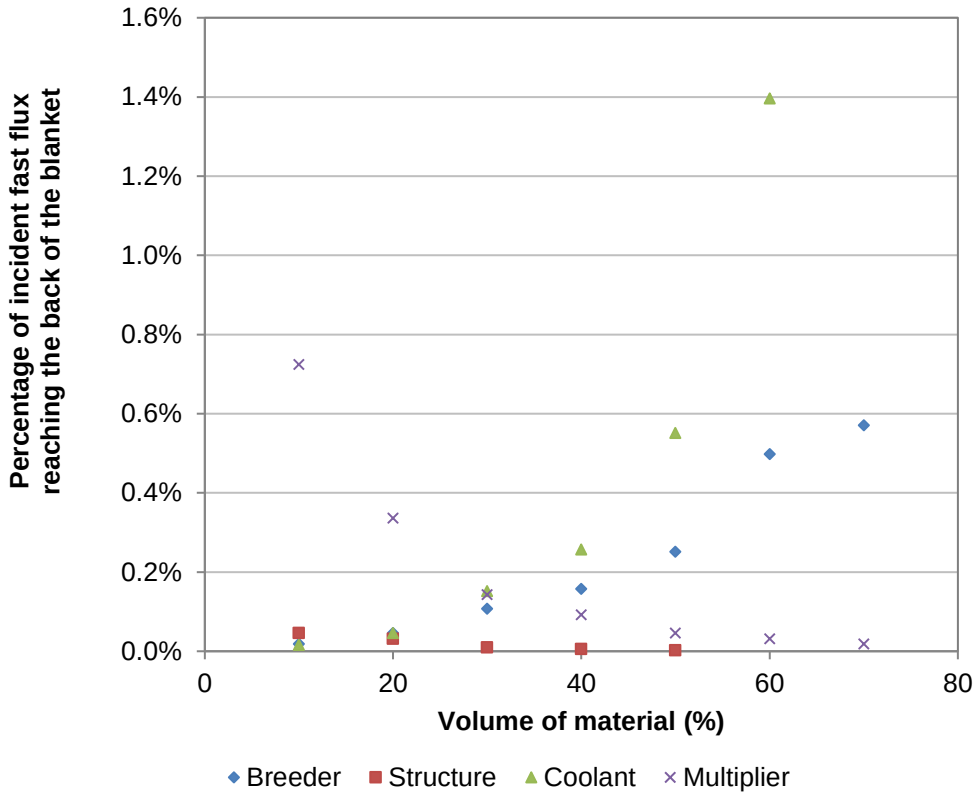

Figure 4.6 - Shielding capabilities, as a measure of the fast flux reaching the back of the blanket, for varying material composition.

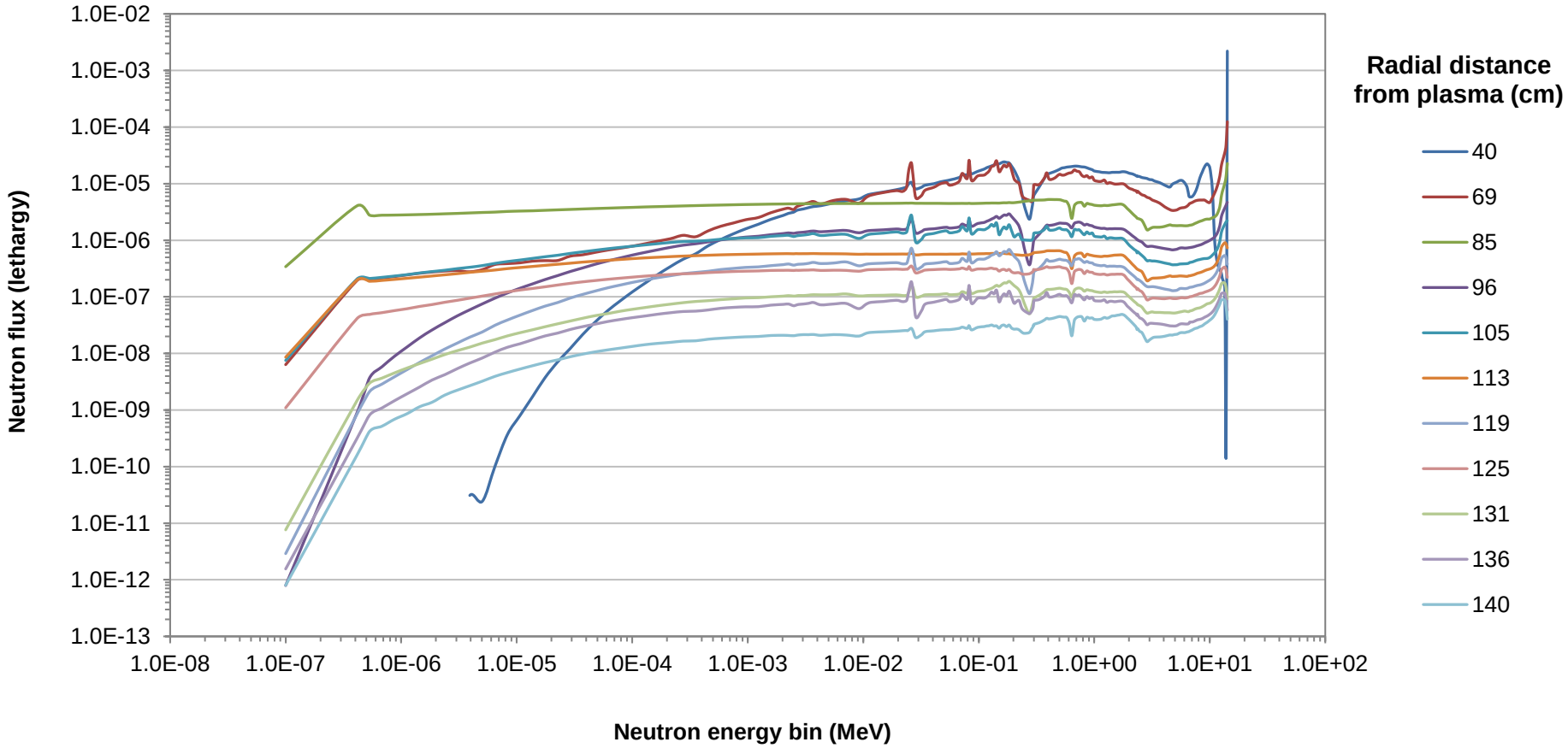

Figure 4.7 - Flux spectrum in each layer (given by radial distance from plasma centre) for a 40 % breeder composition.

4.2.3.2 Homogeneous Blanket

Instead of modelling layers of material, a homogeneous material mix has been used to investigate the effects of approximating the blanket as a uniformly mixed material.

A similar pattern in the effect of material composition in the TBR (Figure 4.8), energy multiplication (Figure 4.10) and shielding (Figure 4.11) is observed in the homogeneous results, when compare to the heterogeneous model results. Increasing the structure or coolant material content reduces the TBR.

Increasing the percentage of multiplier has a larger effect on the TBR than in the case of the heterogeneous model. This is because by approximating the blanket material as a homogeneous mix the beryllium and lithium are assumed to be uniformly 'mixed', resulting in efficient use of the $(n, 2n)$ reactions for interaction with the lithium. In the case of the heterogeneous blanket, neutrons produced in the beryllium multiplying layer need to leave the beryllium and reach the lithium breeding layer for tritium production.

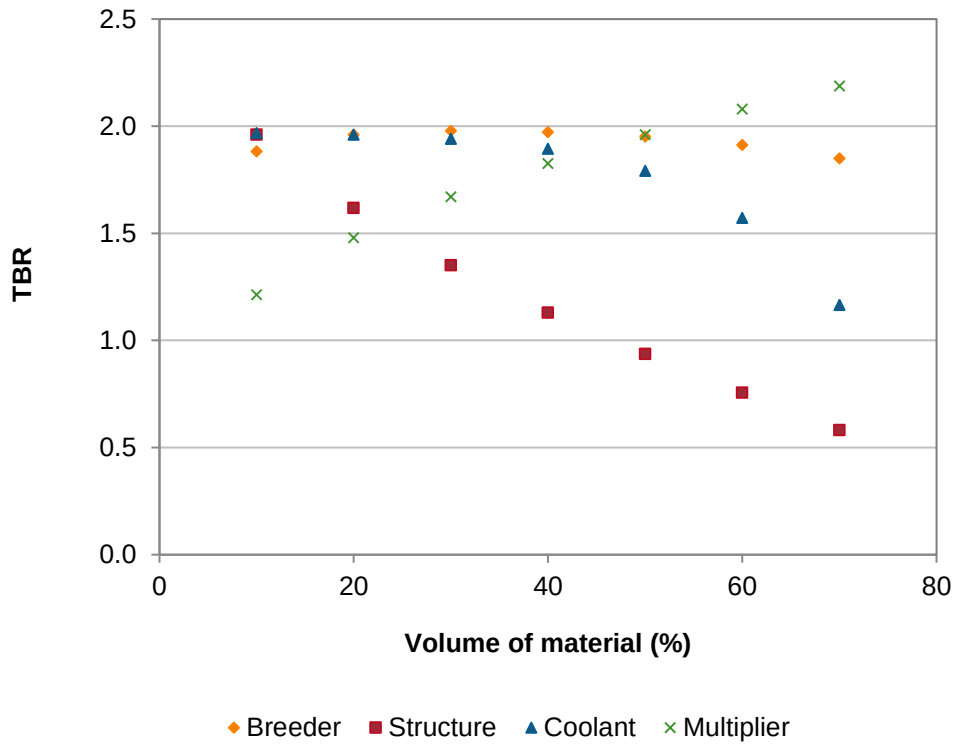

Figure 4.8 - Total TBR for varying percentage volume of material.

The TBR reduces through the blanket (see Figure 4.9 using a 40 % breeder volume mix), reducing to 2 % after ~75 cm compared with 23 % in the heterogeneous model. This is due to tritium breeding throughout the entire blanket thickness in the case of the homogenisation model. The variation of energy multiplication with material composition (Figure 4.10) follows a similar trend to the TBR, as in the case of the heterogeneous model also.

The variation in shielding capabilities with the changing material composition shows a similar pattern to that in the heterogeneous model, despite the different modelling methods. Although the flux spectrum is different through the blanket (comparing Figure 4.12 with Figure 4.7), the overall effect on fast flux reduction is similar.

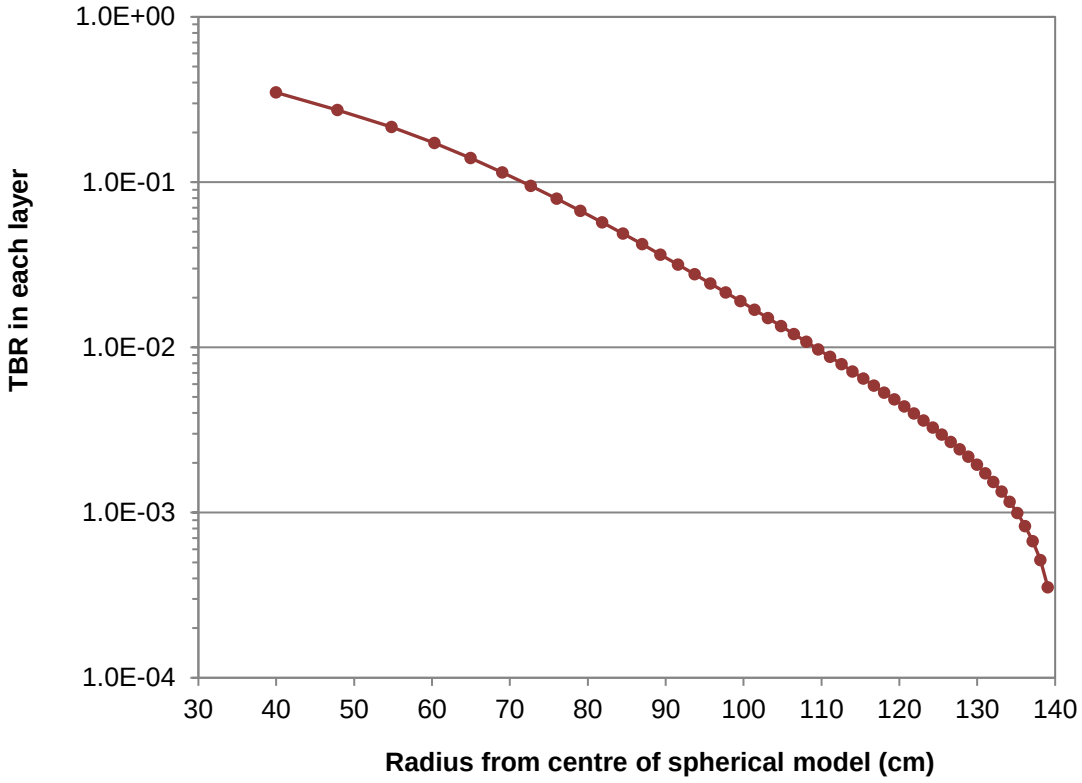

Figure 4.9 - TBR variation with radial distance from the centre of the plasma region. For the case of a 40 % breeder composition.

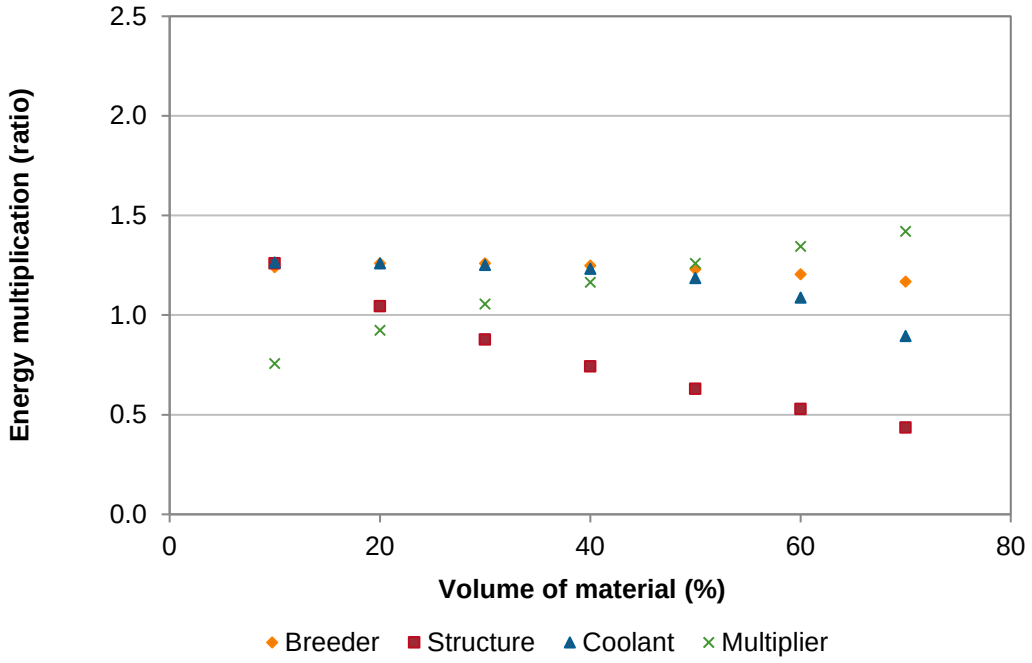

Figure 4.10 - Total energy multiplication (a ratio of the nuclear energy deposited within the material to the energy of D-T neutrons, assumed to be 14.1 MeV) for varying percentage volume of material.

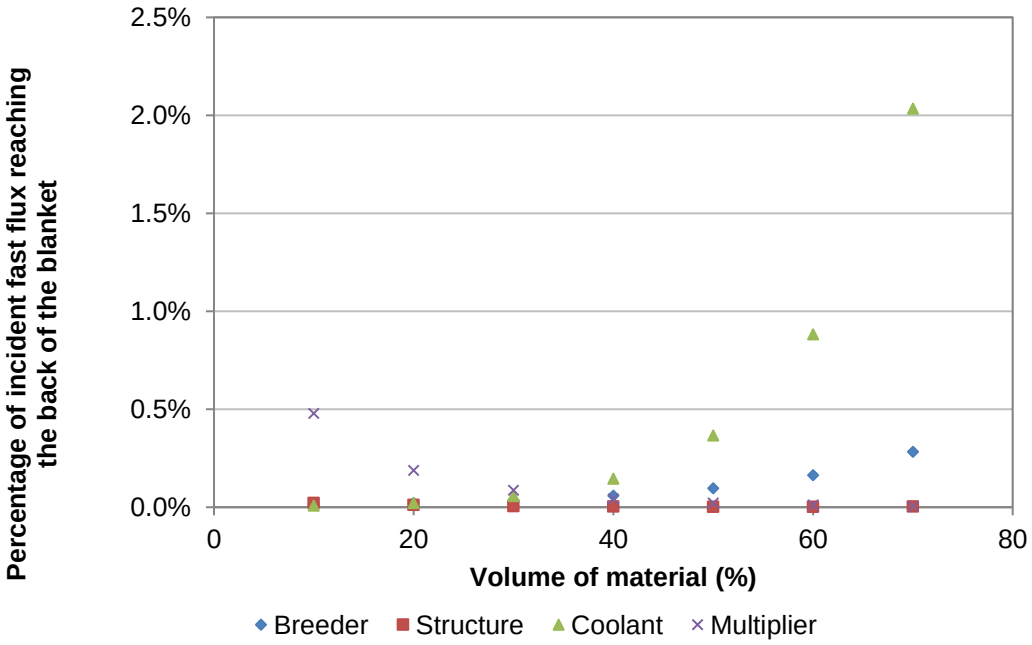

Figure 4.11 - Shielding capabilities, as a measure of the fast flux reaching the back of the blanket, for varying material composition.

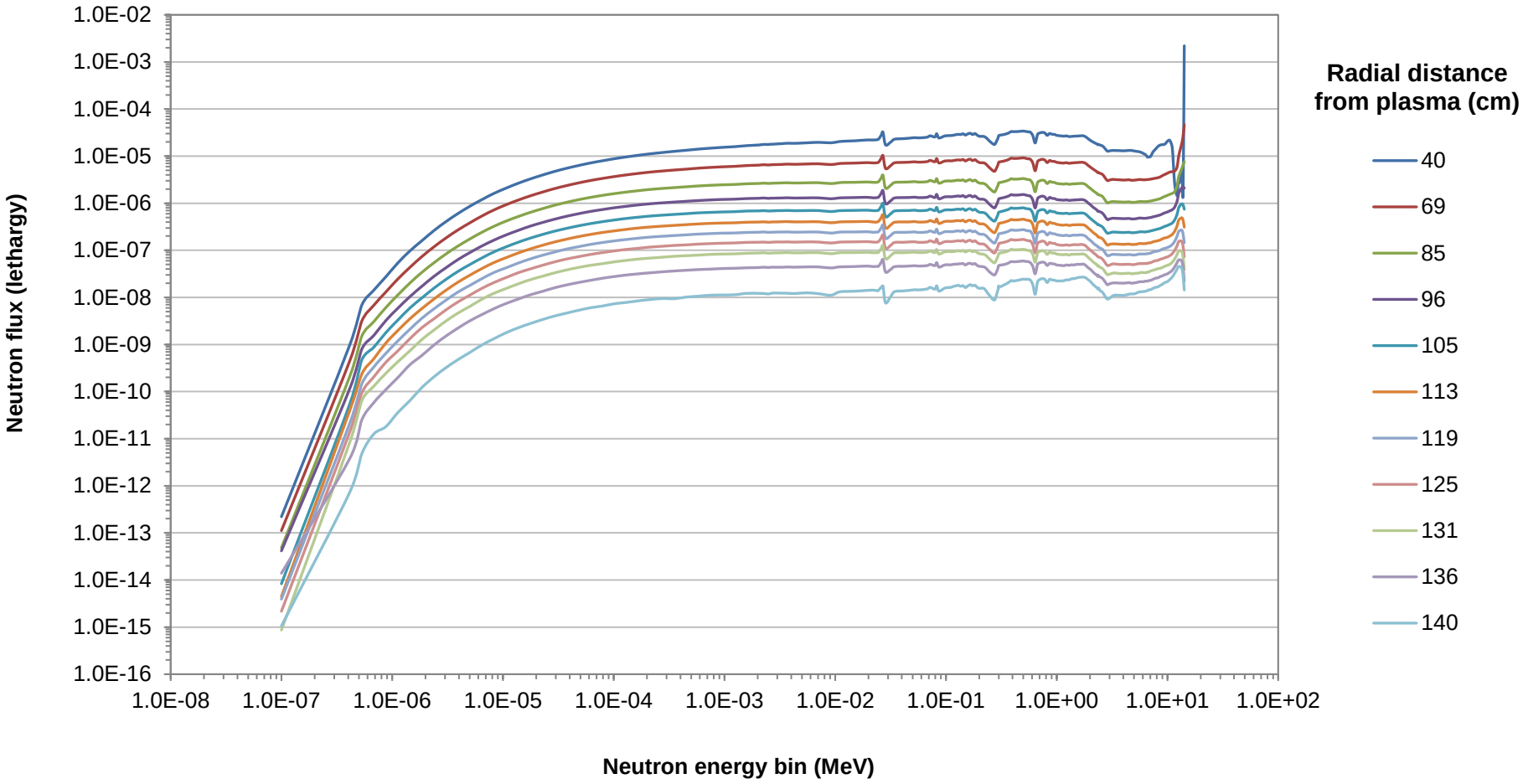

Figure 4.12 - Flux spectrum in each layer (given by radial distance from plasma centre) for a homogeneous 40% breeder composition.

4.2.4 Conclusions

The main conclusions of this material composition investigation:

- Increasing the amount of breeder within the blanket above approximately 40 % has little positive effect on TBR and energy multiplication due to the consequential reduction in beryllium multiplier in the model.
- Increasing the concentration of beryllium within the blanket model increases the number of neutrons and the ^{6}Li (n, t) reactions due to the moderation of neutron energies.
- The presence of structural material within the blanket has a negative effect on the TBR and energy multiplication capabilities.
- From this volumetric material composition comparison, a blanket comprising of 30 % beryllium multiplier, 40 % lithium breeder, 20 % structure and 10 % coolant, assuming all materials need to be present, provides the optimum TBR, energy multiplication and shielding capabilities. This is a reasonably realistic mixture as it is expected that ~20-30 % of the blanket will need to be structural material for cooling channels, supports, containment etc. (see Appendix 1 for materials data for the models used, including the DEMO relevant breeder blanket mixture).
- The approximation of breeder blanket material composition with a homogeneous mix is shown to increase the TBR due to the more efficient use of the $(n, 2n)$ reactions. Breeder blanket concepts with a mixed pebble bed are therefore an attractive option.
- Neutron flux varies through the blanket and is affected by the material within the layers. This is important when considering flux or material averaging in neutronics analysis.

4.3 Solid and liquid breeder materials

In the breeder material optimisation study presented in Section 4.2, the elemental (or pure) form of lithium, with natural isotopic abundance, was used as the breeding material. Due to the high reactivity of lithium it is expected that either compounds of lithium or liquid mixtures will be used as the breeding material. Here a number of

materials are compared for their TBR, energy multiplication and shielding capabilities along with further optimisation through ^{6}Li enrichment. The research draws on and develops the peer-review paper published in the journal of Applied Radiation and Isotopes [126].

4.3.1 Tritium breeding materials

Twelve breeding materials were compared in this study, based on candidate materials proposed for an EU DEMO and some other less conventional options (see Table 2.3 for key material references). The materials can be categorised into two main groups, the solid breeder blanket materials (i.e. the lithium ceramics), and the liquid breeding materials (i.e. the liquid lithium metals and molten salts). A summary of the lithium breeding material, blanket composition and mass density is given in Table 4.3. The ^{6}Li enrichment was varied from 10 - 90 %. Natural lithium contains approximately 7.5 % ^{6}Li, therefore although natural lithium has not been modelled explicitly, the results from the 10 % ^{6}Li are comparable.

Table 4.3 - Summary of materials used in breeder blanket comparison study. Structural material was not included in the homogenous mix and instead modelled as solid layers within the geometry.

Breeding material	Blanket composition (by volume)	Packing fraction	Mass density (g/cm^3)
	Molten lithium		
Li	40% breeder, 40% beryllium, 20% helium coolant	-	0.952
	Liquid lithium metals		
LiPb	80% breeder, 20% lead	-	8.980
LiSn	80% breeder, 20% tin	-	6.200
	Molten lithium salts		
LiBeF	100% breeder	-	2.000
LiFNaK	100% breeder	-	2.020
LiBeFNa	100% breeder	-	2.000
	Ceramic lithium		
Li_2O	40% breeder, 40% beryllium, 20% helium coolant	0.7	1.079
Li_4SiO_4	40% breeder, 40% beryllium, 20% helium coolant	0.7	1.187
Li_2TiO_3	40% breeder, 40% beryllium, 20% helium coolant	0.7	1.476
Li_2ZrO_3	40% breeder, 40% beryllium, 20% helium coolant	0.7	1.100
$LiAlO_2$	40% breeder, 40% beryllium, 20% helium coolant	0.7	1.563
Li_8PbO_6	80% breeder, 20% helium coolant	0.7	3.424

4.3.2 Model and neutronics analysis

For the comparison of solid and liquid breeding materials, a rectangular cross-section model has been used; a modified version of a model provided by CCFE [127]. The model focuses on the breeder blankets only, with the divertor represented by a block of structural material. As discussed in Section 4.2, the position of materials, and homogeneous assumptions, can affect the breeder blanket performance calculations. As the solid and liquid breeder blanket designs are likely to be considerably different, for example, the solid breeders may be in blankets using mixed pebble bed concepts, or separate pebble bed layers, and the liquids will need some form of channel/containment to run through, it was decided to model layers of solid structural material to represent some form of containment. A plan and elevation view of the model can be seen in Figure 4.13.

The D-T plasma source region has been modelled as a volumetric 14.1 MeV neutron source filling the 'plasma' cell shown in Figure 4.13.

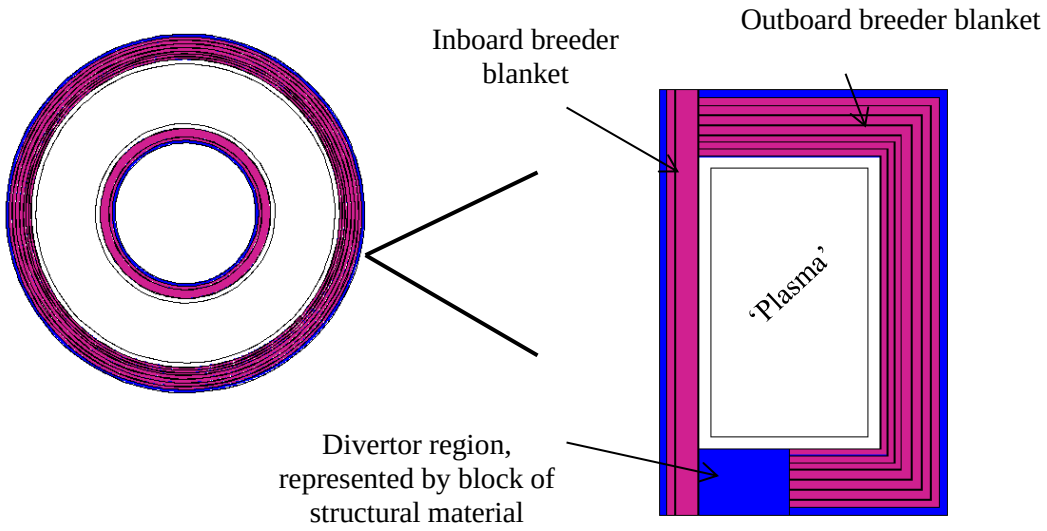

Figure 4.13 - Neutronics MCNP model (based on [127]) used for comparison of solid and liquid breeder materials; a plan and elevation cross-section is shown.

4.3.3 Results and discussion

4.3.3.1 Lithium-6 enrichment

The TBR results for varying ^{6}Li enrichment are shown in Figure 4.14 - Figure 4.15, with the base material (pure lithium) included in both plots of solid and liquid breeders for comparison. The materials containing beryllium vary less in TBR with varying ^{6}Li enrichment. A TBR ≥ 1.1[7] can be achieved in the majority of the solid blankets with natural lithium content. The breeder materials Li_2O and Li_4SiO_4 produce a peak TBR at 30 - 40 % lithium enrichment; above this the effect of reduced moderation from the ^{7}Li dominates the effect. This is not seen in materials such as LiPb and LiSn due to the presence of the moderation from Pb and Sn of which the material is mostly comprised. The liquid materials require higher ^{6}Li enrichment, up to 80 - 90 % for LiPb and LiSn. The potassium-containing materials do not achieve a the required TBR (≥ 1.1), however this could be further optimised through multiplying materials.

A comparison of the peak TBR, enrichment of ^{6}Li required to achieve peak TBR performance, and the minimum enrichment required is given in Table 4.4.

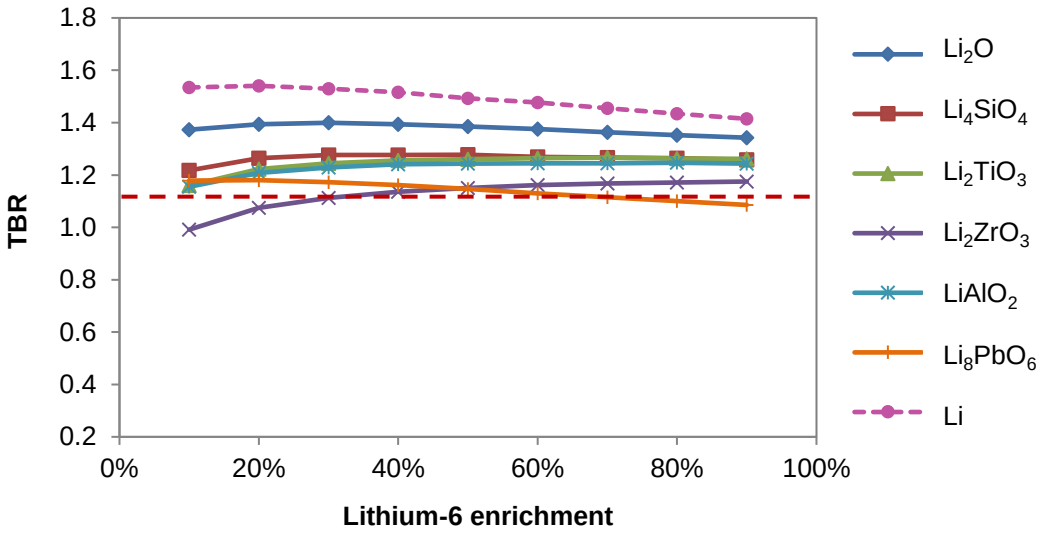

Figure 4.14 - Altering the ^{6}Li enrichment in solid breeder materials, compared with the base material (pure lithium).

[7] This ratio (1.1) includes the extra 0.1 to account for losses within the tritium system, as described in Section 2.5.2.

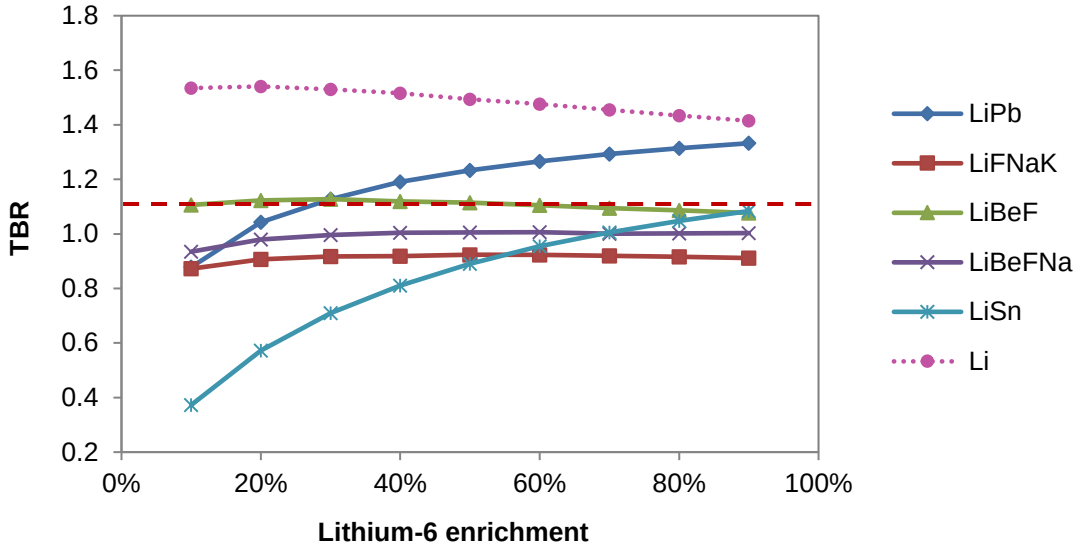

Figure 4.15 - Altering the ^{6}Li enrichment in liquid breeder materials compared with the base material (pure lithium).

Table 4.4 - Comparison of the optimum ^{6}Li enrichment and the minimum required to achieve TBR ≥ 1.1.

Solid breeders				Liquid breeders			
	Peak TBR	Peak enrichment (%)	Minimum enrichment (%)		Peak TBR	Peak enrichment (%)	Minimum enrichment (%)
Li_2O	1.40	30	10	Li	1.54	20	10
Li_4SiO_4	1.28	40	10	LiPb	1.33	90	40
Li_2TiO_3	1.27	70	10	LiFNaK	0.92	50	-
Li_2ZrO_3	1.18	90	20	LiBeF	1.13	30	10
$LiAlO_2$	1.25	70	10	LiBeFNa	1.01	50	-
Li_8PbO_6	1.18	10	10	LiSn	1.08	90	80

4.3.3.2 Comparing blanket performance

The TBR, energy multiplication and neutron fast flux have been compared for the different breeding materials using the optimum ^{6}Li enrichment for peak TBR performance. The TBR is compared in Figure 4.16 and the distribution of TBR through the layers in the outboard blanket can be seen in Figure 4.17 and Figure 4.18 for solid and liquid breeders respectively. A comparison of the percentage contribution to total TBR from the inboard and outboard blankets is given in Table 4.5.

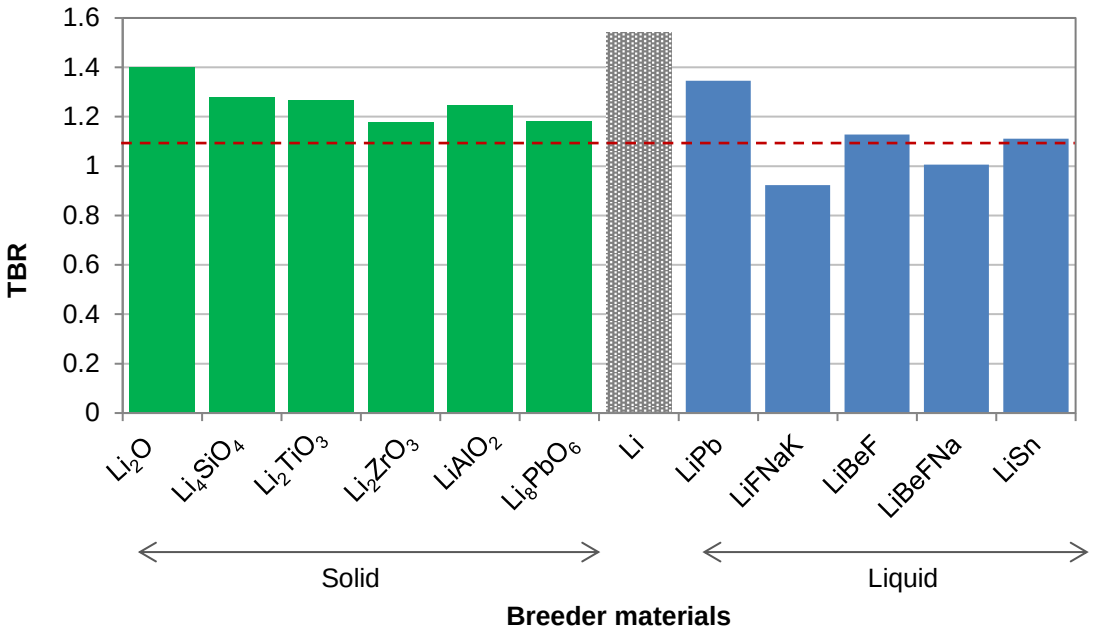

Figure 4.16 - A comparison of TBR for solid and liquid breeding material at 'optimum' enrichment (as determined in Section 4.3.3.1).

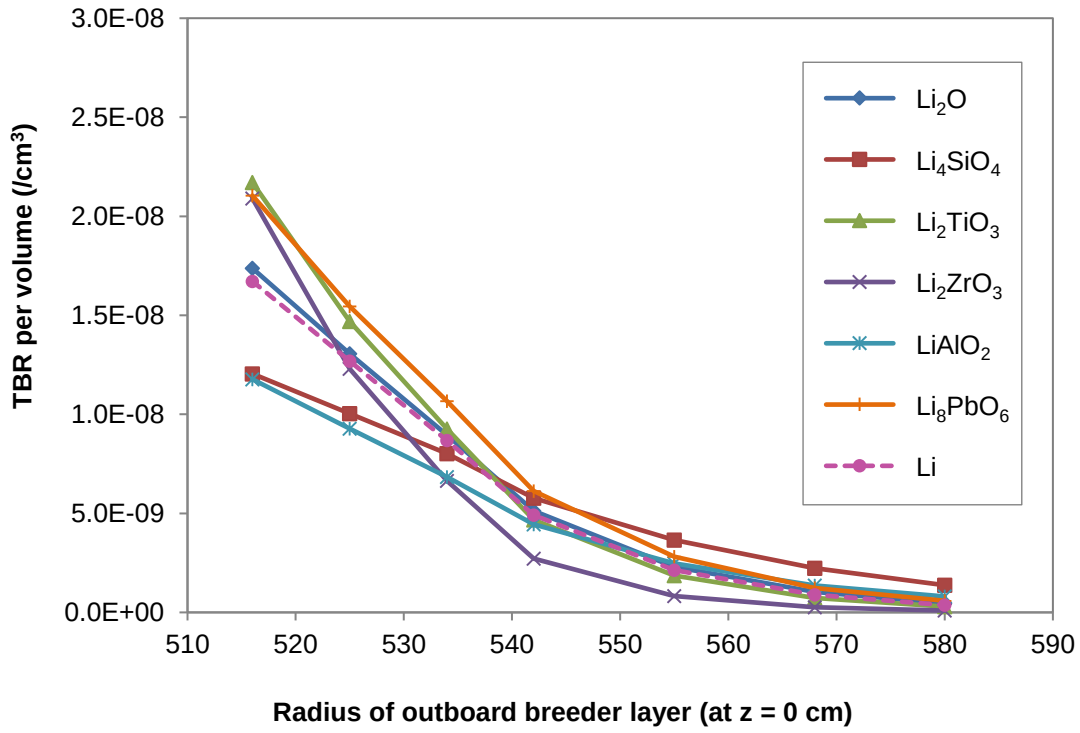

Figure 4.17 - TBR as a function of depth through the outboard blanket (shown as the radius/ distance from the centre of the tokamak). The base material (pure lithium) is also included for comparison.

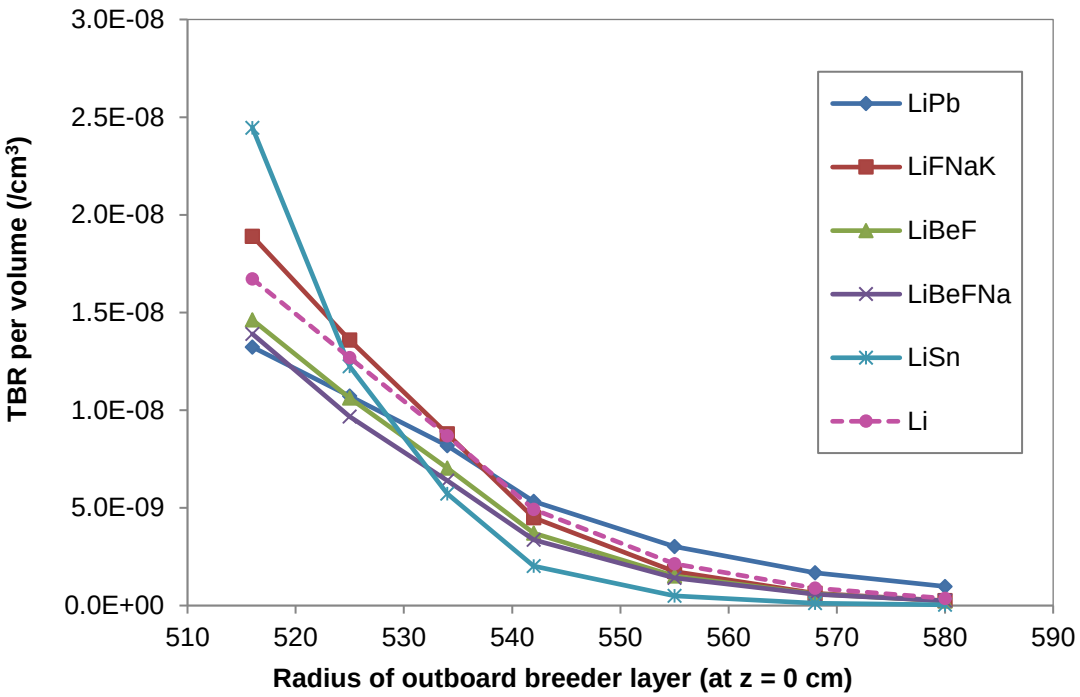

Figure 4.18 - TBR as a function of depth through the inboard blanket (shown as the radius/ distance from the centre of the tokamak). The base material (pure lithium) is also included for comparison.

Table 4.5 - Percentage of tritium breeding in the outboard and inboard blankets.

Solid breeders			Liquid breeders		
	Outboard	Inboard		Outboard	Inboard
Li_2O	77%	23%	Li	77%	23%
Li_4SiO_4	78%	22%	LiPb	80%	20%
Li_2TiO_3	78%	22%	LiFNaK	78%	22%
Li_2ZrO_3	79%	21%	LiBeF	77%	23%
$LiAlO_2$	77%	23%	LiBeFNa	78%	22%
Li_8PbO_6	77%	23%	LiSn	79%	21%

A comparison of the energy multiplication for each of the breeders is given in Figure 4.19 with the variation of energy deposition through the outboard blanket given in Figure 4.20 and Figure 4.21 for the solid and liquid breeding materials, respectively. A comparison of the percentage contribution to total energy multiplication from the inboard and outboard blankets is given in Table 4.6.

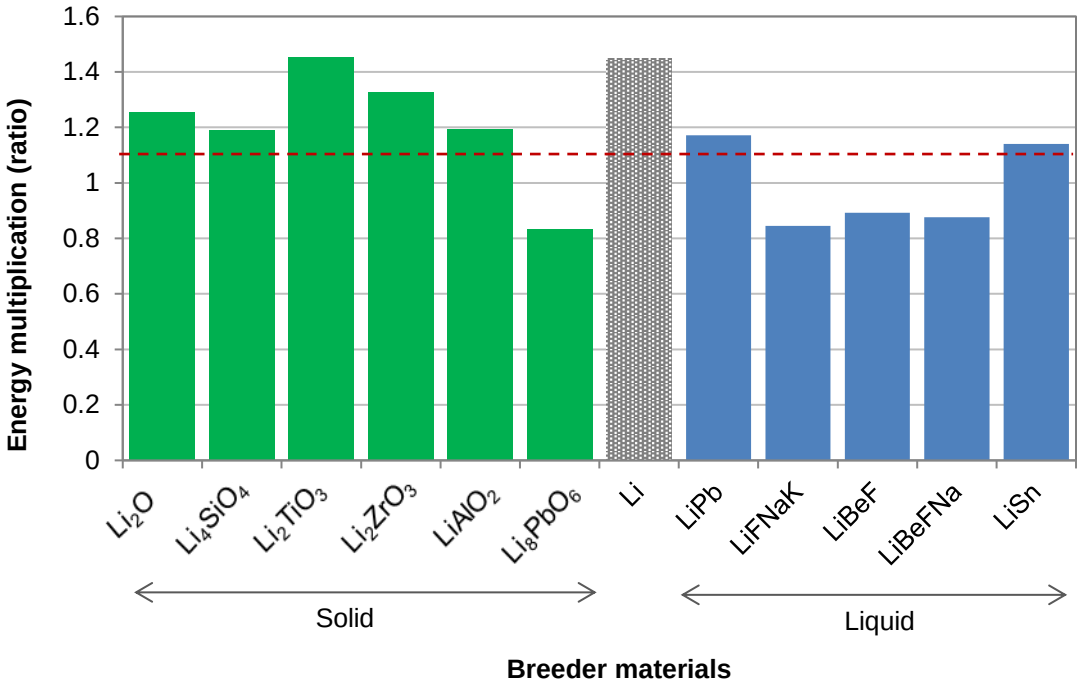

Figure 4.19 - A comparison of energy multiplication for solid and liquid breeding material at 'optimum' enrichment (as determined in Section 4.3.3.1).

Table 4.6 - Percentage of energy multiplication in outboard and inboard blankets.

Solid breeders			Liquid breeders		
	Outboard	Inboard		Outboard	Inboard
Li_2O	79%	21%	Li	79%	21%
Li_4SiO_4	79%	21%	LiPb	80%	20%
Li_2TiO_3	79%	21%	LiFNaK	79%	21%
Li_2ZrO_3	77%	23%	LiBeF	80%	20%
$LiAlO_2$	79%	21%	LiBeFNa	79%	21%
Li_8PbO_6	81%	19%	LiSn	80%	20%

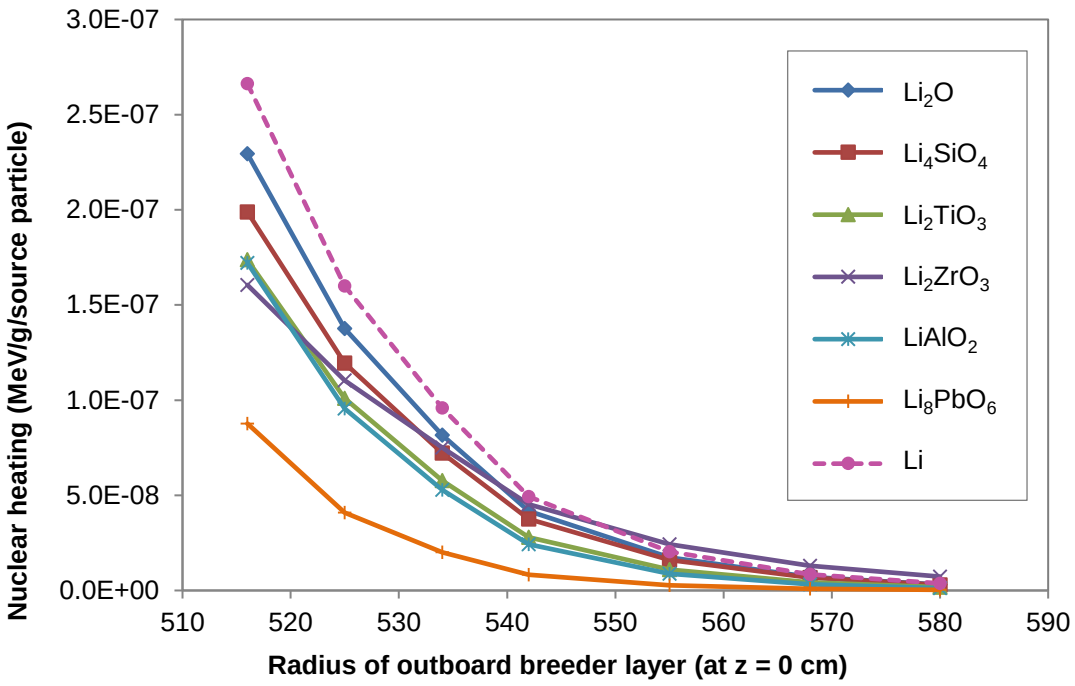

Figure 4.20 - Nuclear heating (MeV/g/neutron source particle) as a function of depth through the outboard blanket (shown as the radius/ distance from the centre of the tokamak). The base material (pure lithium) is also included for comparison.

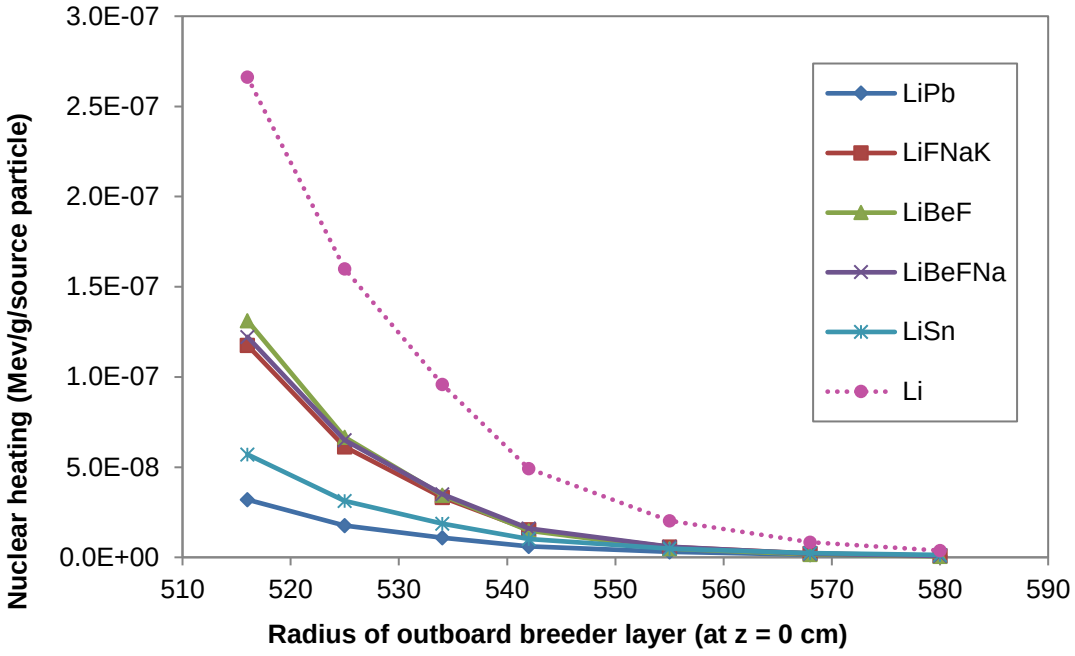

Figure 4.21 - Nuclear heating (MeV/g/neutron source particle) as a function of depth through the inboard blanket (shown as the radius/ distance from the centre of the tokamak). The base material (pure lithium) is also included for comparison.

A measure of the shielding performance, through the percentage of fast flux reaching the back of the blanket, is presented in Table 4.7. The neutron flux spectrum on the inner wall of the inboard and outboard blanket is compared to the spectra on the back of the respective blankets in Figure 4.22 for the lithium base material composition. The flux reaching the back of the outboard blanket is compared for each breeding material in Figure 4.23 and Figure 4.24, for the solid and liquid breeders respectively.

Table 4.7 - Shielding capabilities, as a measure of the fast flux reaching the back of the outboard and inboard blankets.

Solid breeders			Liquid breeders		
	Outboard	Inboard		Outboard	Inboard
Li_2O	0.15%	2.42%	Li	0.16%	2.48%
Li_4SiO_4	0.15%	2.52%	LiPb	0.33%	3.86%
Li_2TiO_3	0.12%	2.11%	LiFNaK	0.09%	3.03%
Li_2ZrO_3	0.54%	5.49%	LiBeF	0.07%	1.14%
$LiAlO_2$	0.08%	1.56%	LiBeFNa	0.09%	1.52%
Li_8PbO_6	0.06%	0.70%	LiSn	0.26%	3.65%

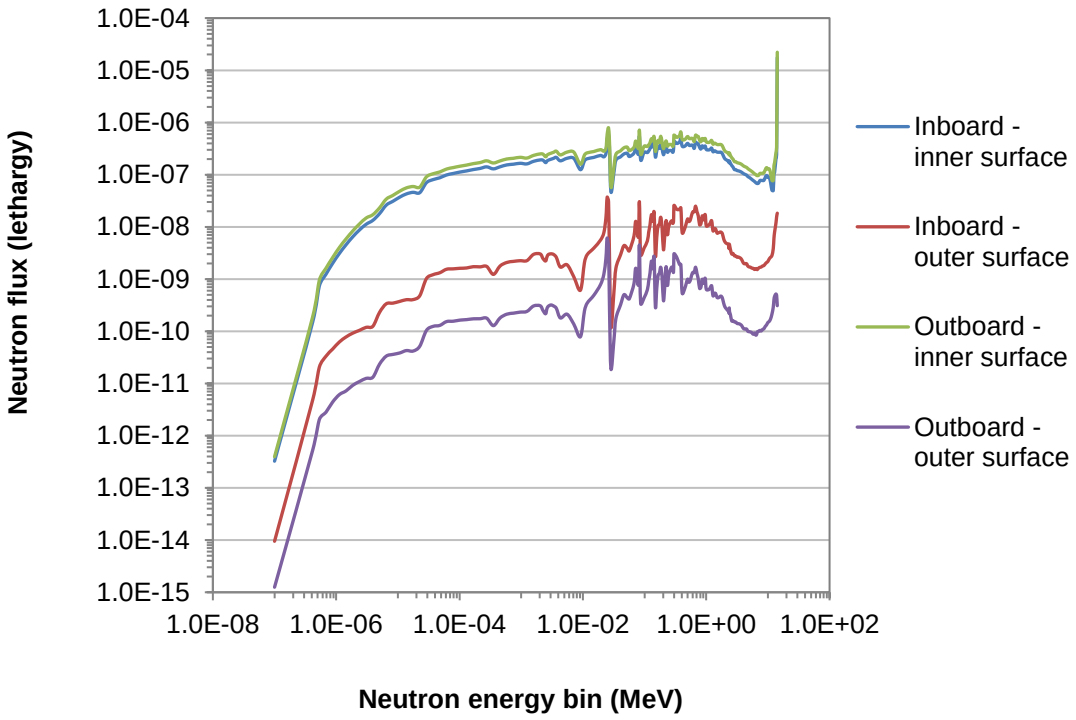

Figure 4.22 - Flux spectrum on the inner and outer surfaces/walls of the inboard and outboard lithium breeder blankets.

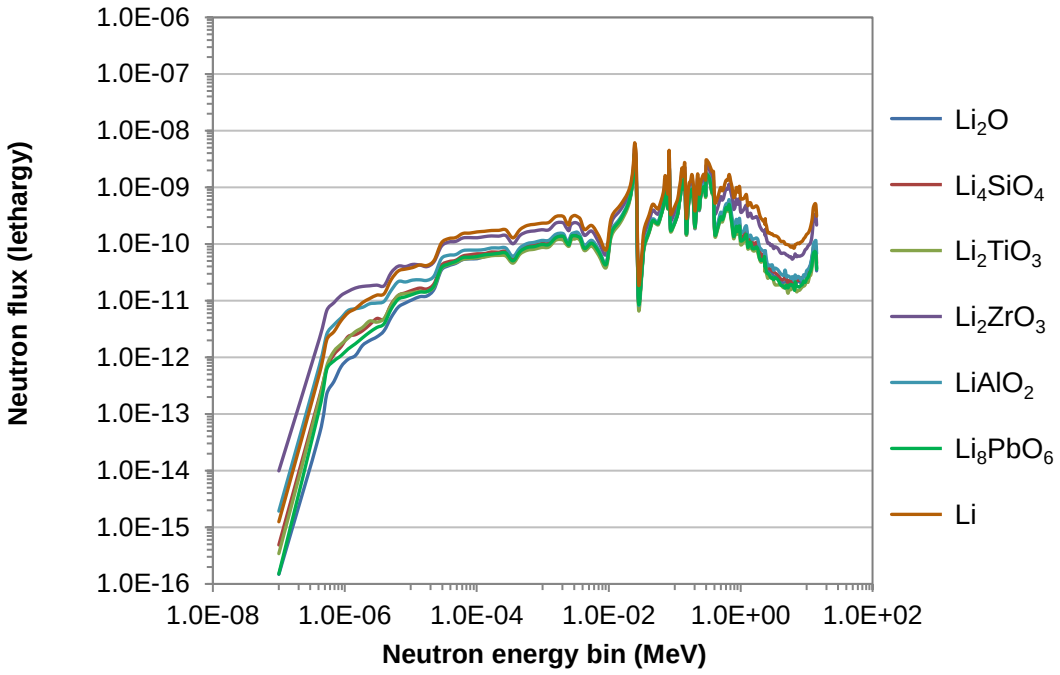

Figure 4.23 - Comparing the flux spectrum on the outer wall of the outboard blanket for each solid breeder. The base material (pure lithium) is also included for comparison.

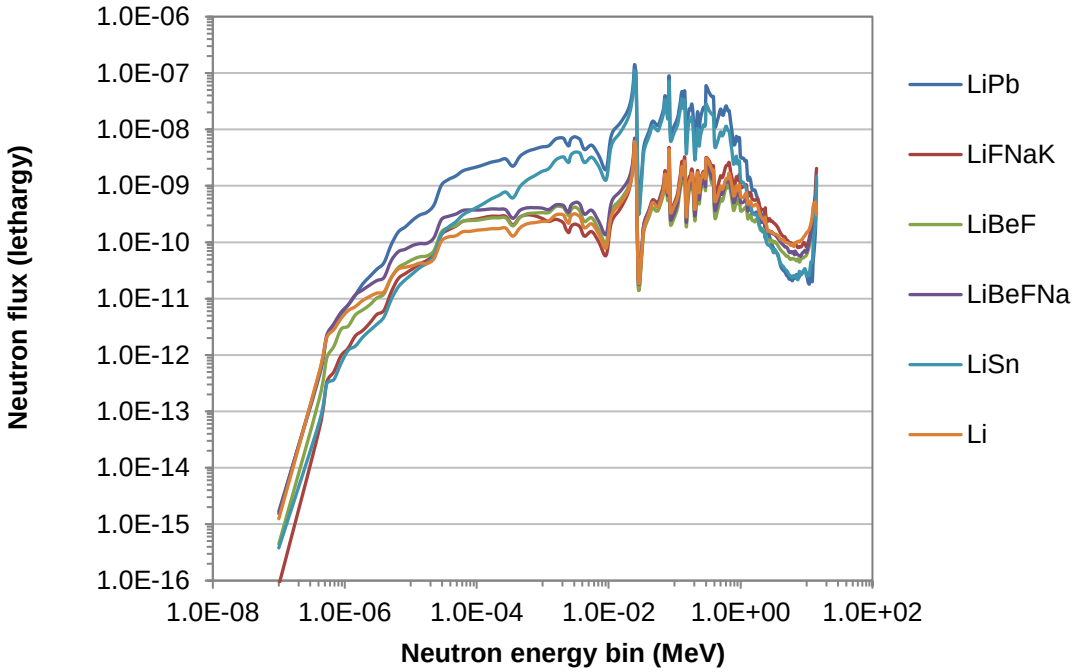

Figure 4.24 - Comparing the flux spectrum on the outer wall of the outboard blanket for each liquid breeder. The base material (pure lithium) is also included for comparison.

4.3.4 Conclusions

The main conclusions from the comparison of some solid and liquid breeding materials:

- Pure molten lithium, enriched with ^{6}Li to 30 - 4 0%, with beryllium multiplier provides a TBR ≥ 1.1, however lithium is highly reactive and unlikely to be used in its pure form.
- One method for stabilising lithium is the formation of salts; these could also be considered for use as the coolant medium. The LiFBe salt performs well with regards to the TBR, energy multiplication and fast flux shielding, however LiFBeNa and LiFNaK only achieve a TBR of 1, and 0.9 respectively. These materials are particularly attractive for use in blankets due to the low melting temperatures and low vapour pressures; the TBR could be improved through further optimisation of multiplying material.
- The molten lithium mixtures of LiPb and LiSn perform well with regard to the TBR, energy multiplication and fast flux shielding, though require ^{6}Li enrichments of 80 - 90 %. These molten lithium mixtures could also be considered as dual coolants and have the added advantage of not requiring the use of beryllium for neutron multiplying.
- The solid breeder blankets require, on average, a lower ^{6}Li enrichment to achieve TBR ≥ 1.1, however all require the use of beryllium to some degree.

Further comparisons regarding the activation considerations of some of the solid and liquid breeding blanket concepts are performed and presented in Section 4.4.5.

4.4 Spherical tokamak shielding requirements

As discussed in Section 2.4.4, the tight aspect ratio of a spherical tokamak results in no space for a breeder blanket on the inboard. This has two main implications, (1) the tritium breeding is limited to just the outboard and (2) a dedicated shield is required on the inboard to limit heating of the magnets within the centre column and the fast neutron flux.

The maximum neutron fluence the HTS magnets can sustain before significant degradation is a particularly important criterion. There is some, but yet limited, data regarding these limits on fast neutron exposure. The literature agrees that a maximum

limit will be in the range of 10^{22} and 10^{23} neutron/m^2 [128]. Initial figures based on Nb_3Sn superconducting magnets suggest ~ 1 x 10^{22} neutrons/m^2 [129]. With production techniques advancing in recent years this figure has been increased to ~3 x 10^{22} neutrons/m^2 [130], [131]. And, if 20 - 30 % degradations in critical temperature and current density could be tolerated then operation to 1 x 10^{23} could be possible [132]. For the use of the HTS material REBCO a fast neutron fluence tolerance limit of 3 x 10^{22} neutrons/m^2 has been used in this work.

In order to reduce the nuclear heat load to the centre column, mitigating thermal stress problems, an allowable peak nuclear heating of 2-5 kW/m^3 [131], [133] is assumed. The lower limit of 2 kw/m^3 [131] is used in the parameterised spherical tokamak shielding studies. To assess the shielding requirements for a range of spherical tokamak sizes a simple parameterised model was created.

4.4.1 Parameterised model and neutronics calculations

A number of approaches for parameterisation were considered and the following option chosen for the ability to scan a wide range of centre column sizes, aspect ratios and shielding thicknesses. If the model and plasma dimensions were kept constant as the shielding thickness was increased, the range in shielding would be limited by the available space between the shield and plasma. Increasing the shielding beyond this would 'eat' into the plasma volume.

The selected approach specifies that the gap between the first wall and the plasma, is a constant. In order to keep this so-called 'scrape-off layer'[8] constant with a simple geometric construction of a spherical tokamak device consisting of a centre column surrounded by a shield which faces the plasma, Equation 12 must be satisfied

$$R - a = CC_r + S_t + SOL \qquad (12)$$

where R is the major radius, a is the minor radius, CC_r the radius of the centre column, S_t the inboard shielding thickness and SOL the scrape-off layer (as previously defined).

[8] It should be noted that the term 'scrape-off layer' is used in plasma physics with a different and more detailed meaning than the use in this thesis.

As the shielding is increased, the major radius, and therefore the minor radius, must increase also, thus preventing a reduction of the plasma volume. The values for the major and minor radii were calculated using Equation (2) and (3) respectively; where AR is the aspect ratio and the SOL fixed at 15 cm.

The effect of changing the shielding thickness can be seen in Figure 4.25; as the shielding increases, the plasma volume is moved out and the overall size of the reactor increased.

$$R = \left(\frac{AR\ \ (CC_r + S_t + 15)}{AR - 1}\right) \qquad (13)$$

$$a = \frac{R}{AR} \qquad (14)$$

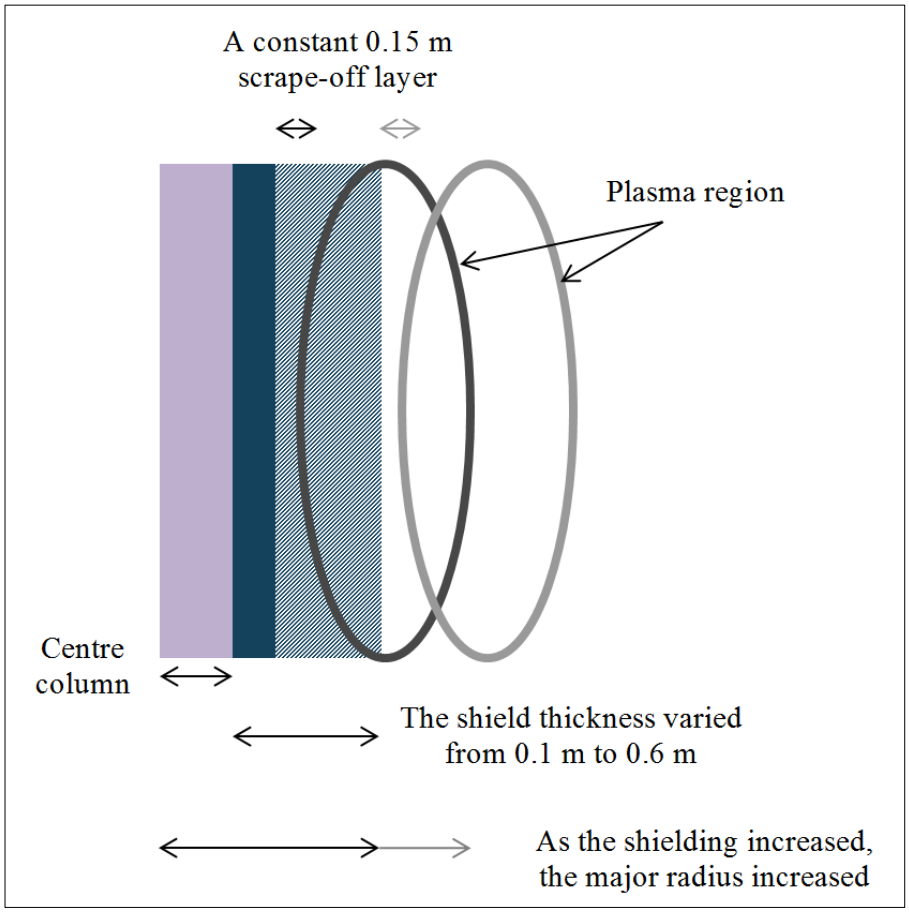

Figure 4.25- Illustrating the change in major radius and overall size of reactor due to changing shielding thickness.

4.4.2 Neutronics model and materials

A 90° sector neutronics model has been used and a CAD image is given in Figure 4.26. Reflecting boundary planes were used to simulate a full 360° tokamak reactor. The centre column is modelled as a homogeneous mixture of copper, steel and helium to represent the centre column magnets. A tungsten carbide inboard shield is used with 13 % water cooling. (Validation of this material selection is given in Appendix 4.) A mix of Li_4SiO_4 with beryllium multiplier, steel and helium coolant is used in the blanket to represent a blanket based on the EU HCPB concept. The materials are summarised in Table 4.8.

The D-T plasma source was modelled with a user defined parametric plasma source subroutine with MCNP. This source was developed by KIT [123] and implemented in MCNP6 by CCFE [134].

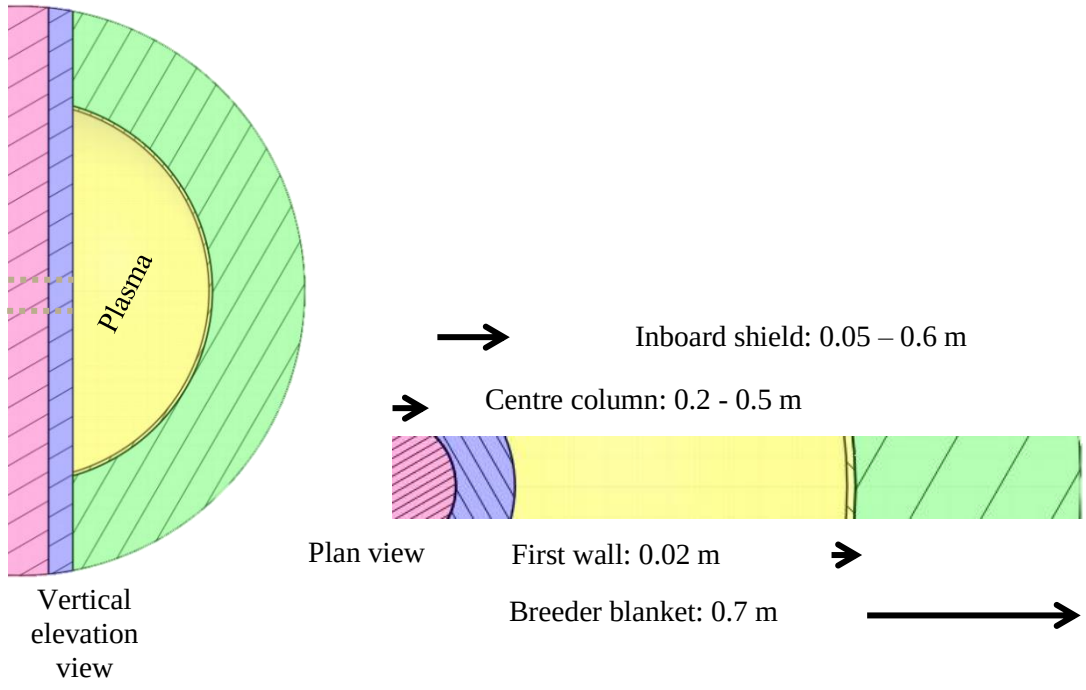

Figure 4.26 - The parameterised spherical model, consisting of spherical and cylindrical surfaces. An elevation view is given on the left, with plan view section on the right with the basic radial build information.

Table 4.8 - A summary of the materials used in the spherical tokamak model. (The isotopic composition of the constituent parts is given in Table 7.2 to Table 7.4 of Appendix 4.)

Component	Material
Centre column (pink)	Copper 57%, steel 38% and helium 5%
Inboard shield (blue/purple)	Tungsten carbide 87% and water cooling 13%
First wall (yellow)	Steel 90%, chromium zirconium copper 5% and helium 5%
Breeder (green)	Li_4SiO_4 (lithium othosilicate) 15%, beryllium multiplier 55%, helium 20% and steel 10%

4.4.3 Neutronic calculations

Calculations were performed with the Monte Carlo N-Particle radiation transport code, MCNP (version 6.1) using the FENDL2.1 and ENDFB7.1 nuclear library data.

Nuclear heating

- The nuclear heating in the centre column is assessed using an F6 tally in MCNP, estimating the heating due to energy deposition from neutron and photon interactions. The heating has been assessed for a number of centre column radii with varying thicknesses of shielding. The peak nuclear heating is taken in a volume of the centre column +-5 cm from the mid-plane.

Fast flux on the centre column

- The neutron flux spectrum has been estimated through the material using an F2 surface tally and the fast flux defined as the neutrons with energy above 0.1 MeV. The peak fast flux is determined +-5cm from the mid-plane on the outer surface of the centre column.

Tritium breeding

- This was calculated using the same method as in the previous sections, using the 205 MT number with a volume average flux F4 tally.

4.4.4 Results and discussion

As described in Section 4.4.1, the approach selected for varying the shielding thickness facilitated a wide range in centre column sizes, aspect ratios and shielding.

4.4.4.1 Varying shielding thickness

Considering, for example, the model with a 0.2 m centre column and aspect ratio 1.4, the major radius is increased from approximately 2 to 3 m as the shielding varies from 0.05 to 0.6 m (see Figure 4.31). The peak nuclear heating within the centre column (Figure 4.27) is approximately 2000 kW/m^3 with 0.2 m of shielding. This is 3 orders of magnitude greater than the anticipated limit on HTS of 2 kW/m^3.To achieve such a limit, more than 0.5 m of tungsten carbide shielding is required.

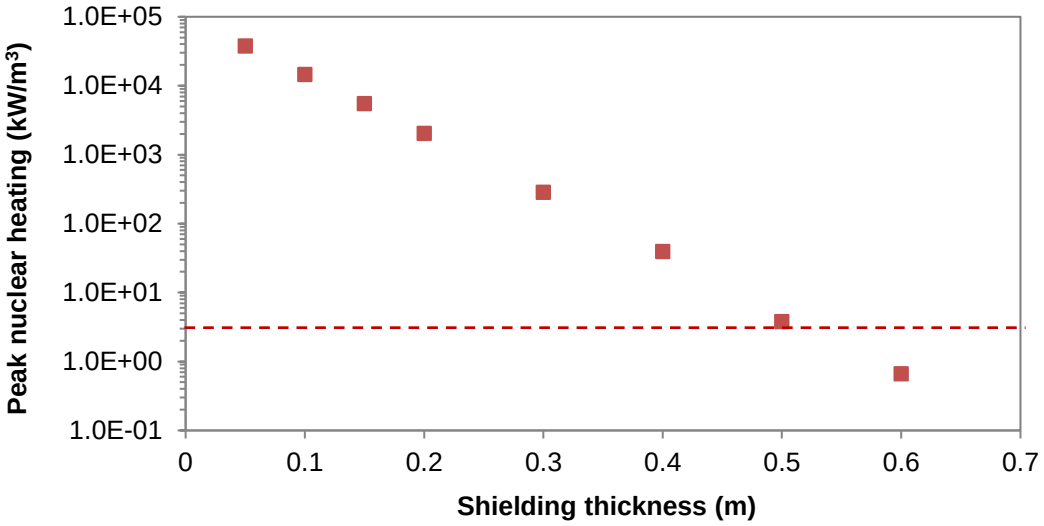

Figure 4.27 - Nuclear heating in the centre column (peak) with varying shielding thickness; for a case with a 0.2 m centre column and 1.4 aspect ratio.

As the overall size of the tokamak is increased with increasing shielding, this also increases the volume of the blanket (as the radial thickness is kept the same, in a sphere, the volume will increase). As a result, the TBR is not significantly affected by this change. When considering the TBR to 1 decimal place it remains constant at 1.3. It should however be noted that in using a spherical tokamak concept to create a compact design, any reduction in the outboard breeder blanket volume will reduce the TBR (see Figure 4.29).

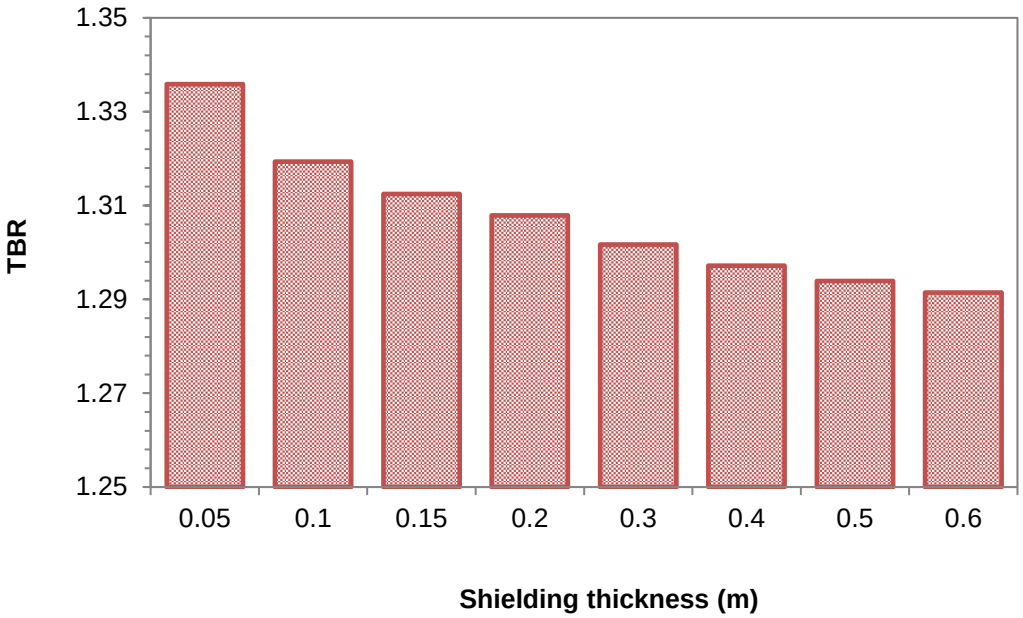

Figure 4.28 - Variation in TBR for changing shielding thickness; for a case with a 0.2 m centre column and 1.4 aspect ratio.

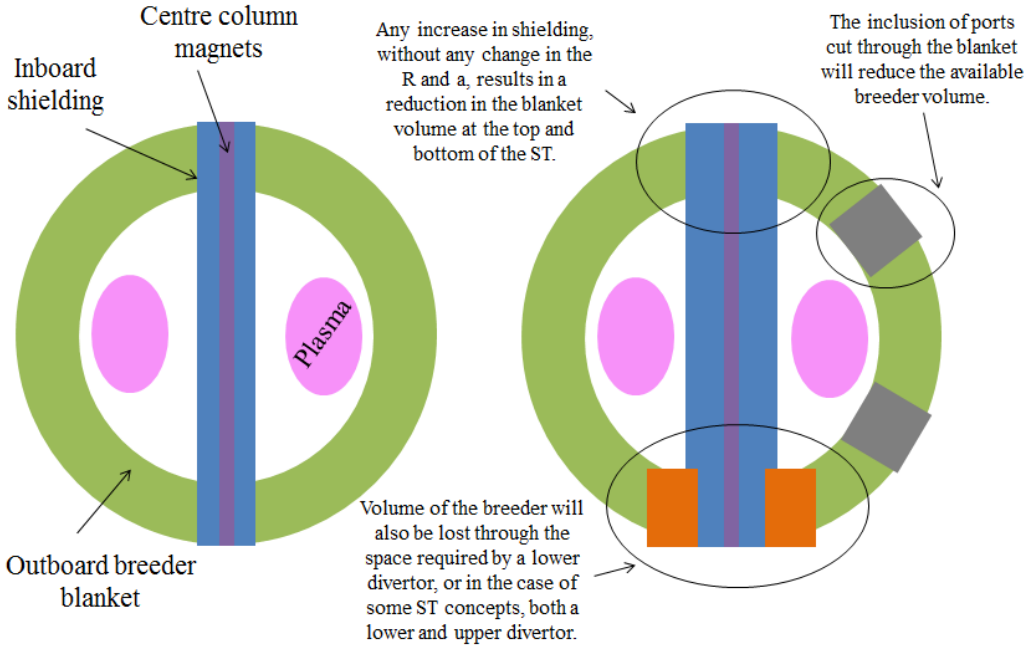

Figure 4.29 - An illustration of a vertical plan through a spherical tokamak. The right image highlights some considerations for potential TBR reduction.

The shielding capability was also assessed through the fast neutron flux on the centre column, i.e. that which has passed through the inboard shield. It can be seen in Figure 4.30 that a 0.05 m shield has little effect on the fast neutron flux. A shield of 0.3 m reduces the fast flux on the shield to approximately 2 orders of magnitude less at the back of the shield, where the centre column magnets are housed.

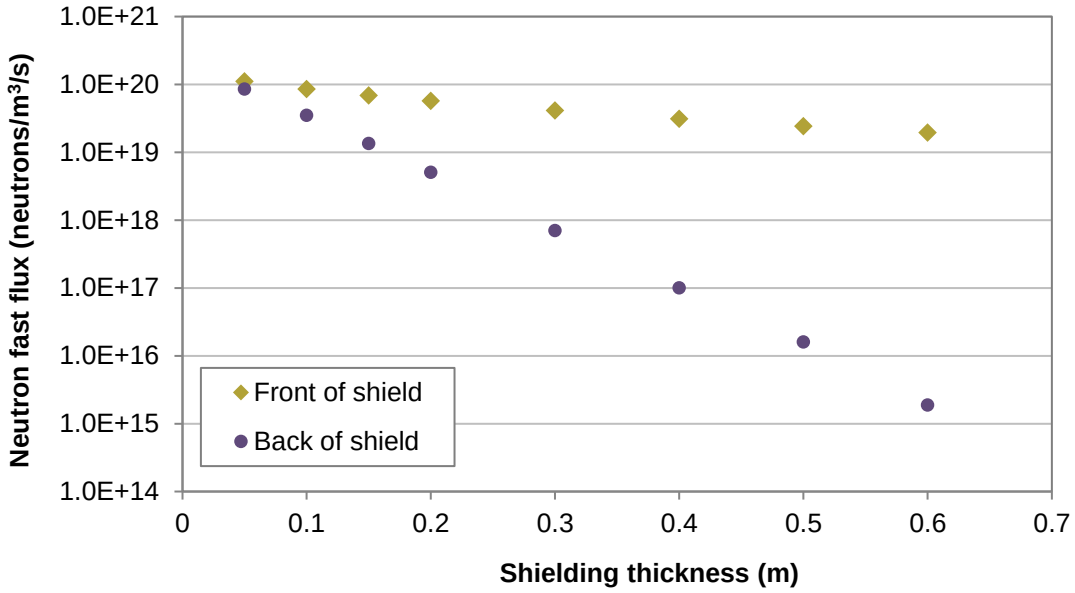

Figure 4.30 - Variation in neutron fast flux (peak) with shielding thickness; for a case with a 0.2 m centre column and 1.4 aspect ratio.

4.4.4.2 Varying centre column and aspect ratio

By considering a range of different geometries, the effect of shielding thickness requirements on the overall size of the reactor was assessed. The centre column was varied from 0.1 - 0.5 metres and aspect ratios of 1.2, 1.4, 1.6, 1.8, 2, 2.5 and 3 were considered. The variation of the major radius for changing shielding thickness in the case of a 0.2 m centre column is shown in Figure 4.31. Peak centre column heating, TBR and fast flux results are presented for a 0.2 m centre column model in Figure 4.32 - Figure 4.33. Data for the other cases is given in Appendix 5.

The geometry arrangements and shielding requirements that fulfil the peak heating limit of 2 kW/m^3 are highlighted in Figure 4.35 where it is shown that at least 0.4 m of dedicated neutron shielding is required on the inboard of a spherical tokamak where no inboard breeder is present.

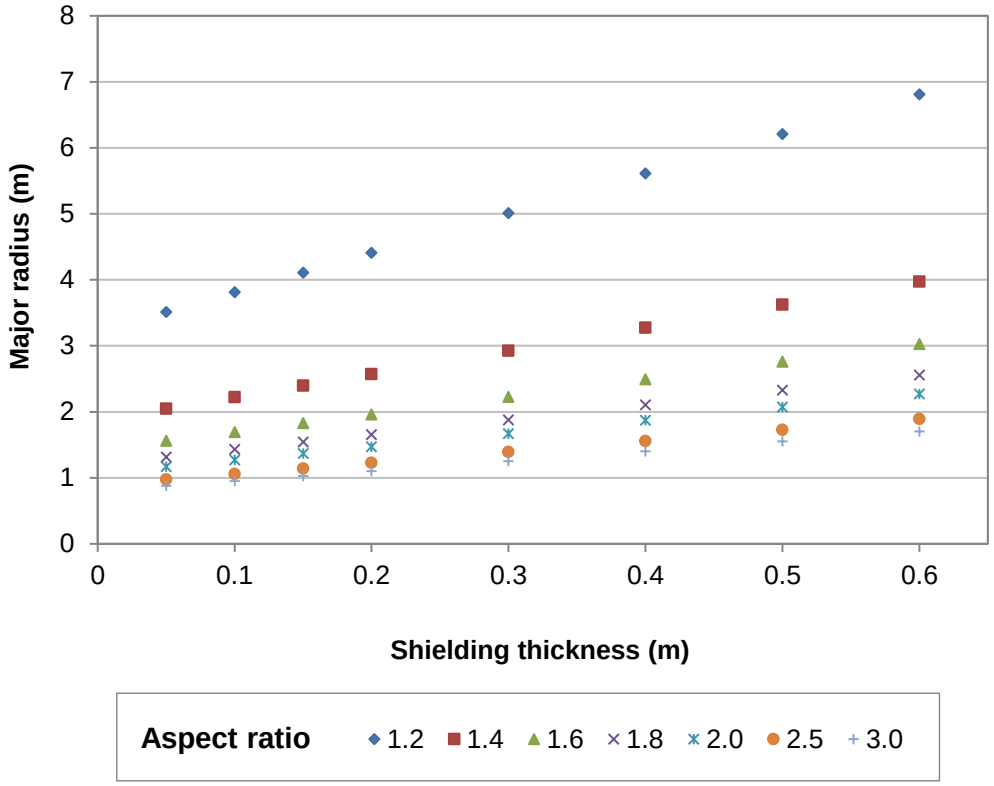

Figure 4.31 - Variation in major radius with increasing shielding thickness for a 0.2 m centre column.

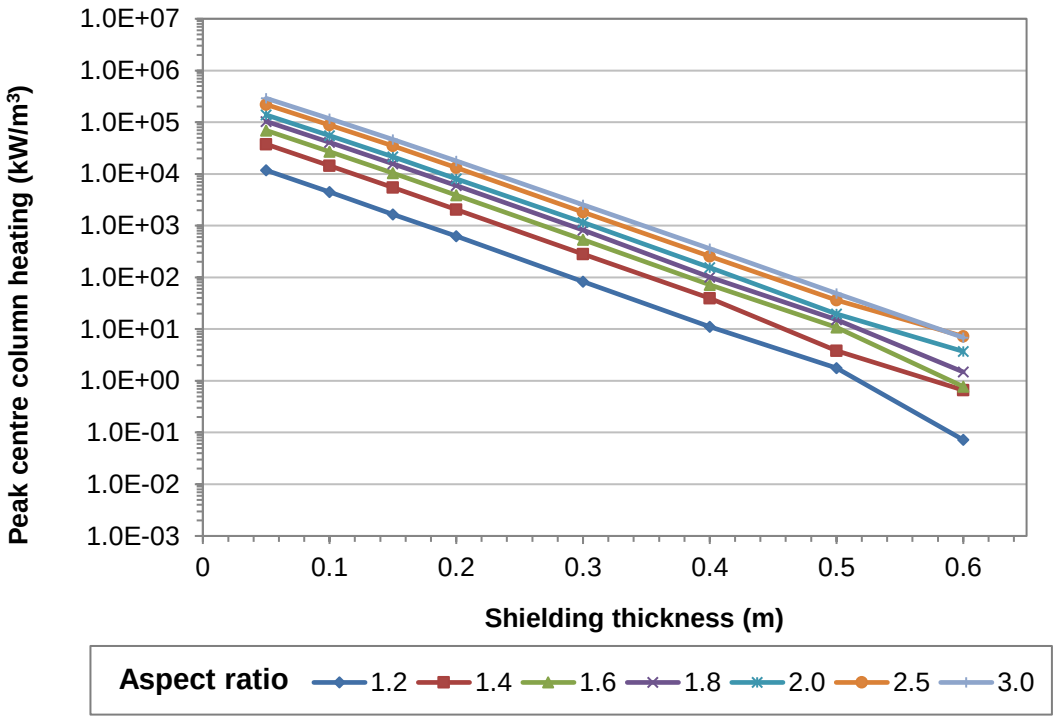

Figure 4.32 - Nuclear heating in the centre column (peak) with varying shielding thickness and aspect ratio; for a 0.2 m centre column.

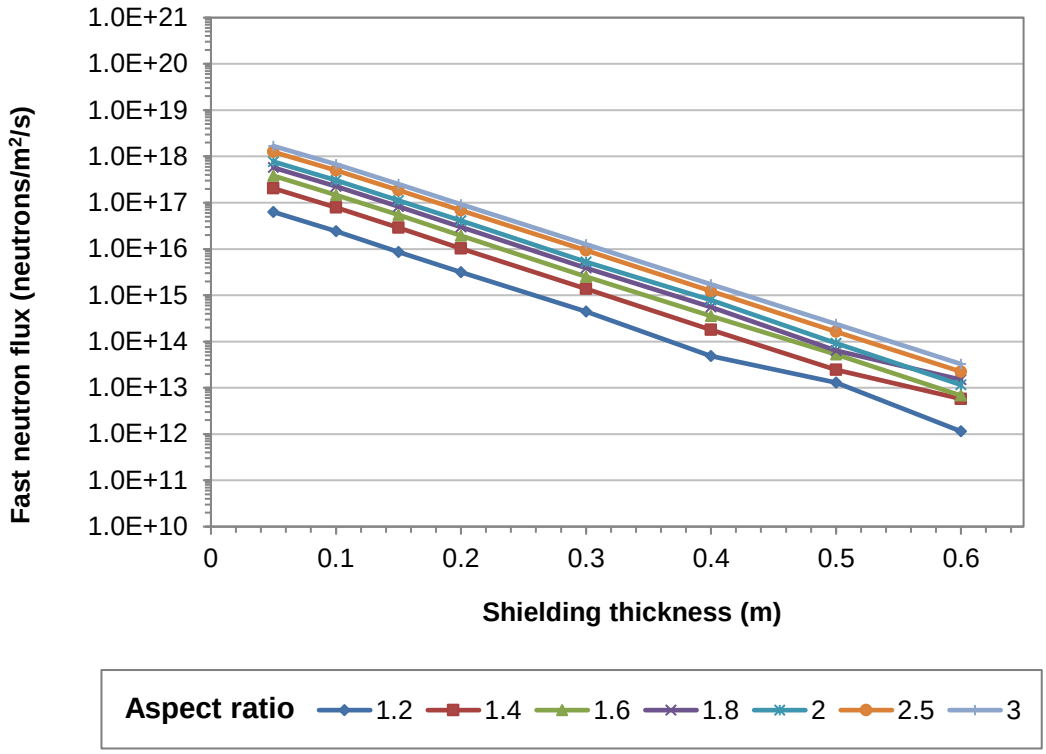

Figure 4.33 - Fast neutron flux in the centre column (peak) with varying shielding thickness and aspect ratio; for a 0.2 m centre column.

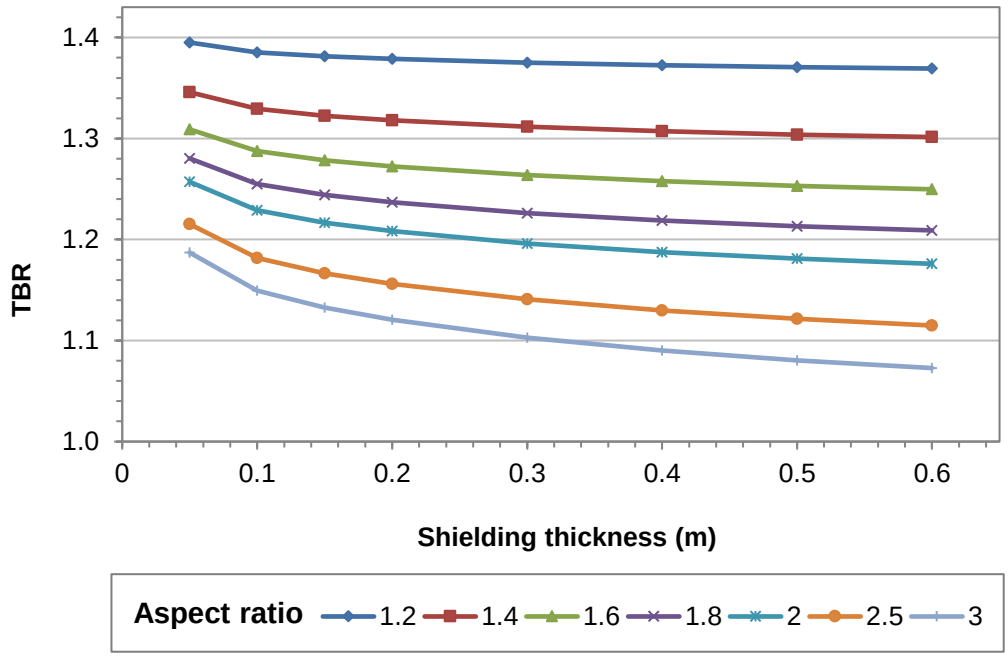

Figure 4.34 - TBR in outboard blanket with varying shielding thickness and aspect ratio; for a 0.2 m centre column.

	Aspect ratio	1.2						1.4						1.6						1.8					
	Centre column radius (m)	0.10	0.15	0.20	0.30	0.40	0.50	0.10	0.15	0.20	0.30	0.40	0.50	0.10	0.15	0.20	0.30	0.40	0.50	0.10	0.15	0.20	0.30	0.40	0.50
Shielding thickness (m)	0.05	4.1E+04	2.1E+04	1.2E+04	4.8E+03	2.4E+03	1.4E+03	1.3E+05	6.5E+04	3.8E+04	1.6E+04	7.9E+03	4.5E+03	2.3E+05	1.2E+05	6.9E+04	2.9E+04	1.5E+04	8.5E+03	3.4E+05	1.8E+05	1.0E+05	4.4E+04	2.3E+04	1.3E+04
	0.10	1.4E+04	7.5E+03	4.5E+03	1.9E+03	1.0E+03	5.8E+02	4.5E+04	2.4E+04	1.4E+04	6.4E+03	3.3E+03	1.9E+03	8.4E+04	4.5E+04	2.7E+04	1.2E+04	6.3E+03	3.6E+03	1.2E+05	6.7E+04	4.1E+04	1.8E+04	9.6E+03	5.6E+03
	0.15	5.1E+03	2.8E+03	1.7E+03	7.6E+02	4.0E+02	2.4E+02	1.6E+04	8.9E+03	5.5E+03	2.5E+03	1.3E+03	7.8E+02	3.0E+04	1.7E+04	1.0E+04	4.8E+03	2.6E+03	1.5E+03	4.5E+04	2.5E+04	1.6E+04	7.3E+03	3.9E+03	2.3E+03
	0.20	1.8E+03	1.0E+03	6.3E+02	2.8E+02	1.5E+02	9.6E+01	5.8E+03	3.3E+03	2.0E+03	9.6E+02	5.2E+02	3.1E+02	1.1E+04	6.2E+03	3.9E+03	1.8E+03	1.0E+03	6.0E+02	1.6E+04	9.5E+03	6.0E+03	2.8E+03	1.5E+03	9.3E+02
	0.30	2.2E+02	1.3E+02	8.3E+01	4.1E+01	2.3E+01	1.4E+01	7.5E+02	4.6E+02	2.8E+02	1.4E+02	8.2E+01	4.7E+01	1.4E+03	8.5E+02	5.4E+02	2.6E+02	1.5E+02	9.3E+01	2.1E+03	1.3E+03	8.2E+02	4.0E+02	2.3E+02	1.4E+02
	0.40	3.3E+01	2.0E+01	1.1E+01	6.3E+00	3.3E+00	2.0E+00	9.7E+01	5.8E+01	4.0E+01	2.0E+01	1.1E+01	6.7E+00	1.8E+02	1.1E+02	7.2E+01	3.5E+01	2.1E+01	1.3E+01	2.8E+02	1.8E+02	1.0E+02	5.4E+01	3.1E+01	2.1E+01
	0.50	7.1E+00	4.2E+00	1.8E+00	9.0E-01	4.0E-01	3.0E-01	1.3E+01	7.6E+00	3.8E+00	2.2E+00	1.3E+00	9.6E-01	3.0E+01	1.4E+01	1.1E+01	4.7E+00	3.2E+00	2.2E+00	3.3E+01	2.7E+01	1.5E+01	7.7E+00	4.6E+00	2.9E+00
	0.60	1.6E+00	1.1E-01	7.2E-02	3.2E-01	1.3E-01	9.4E-03	6.0E-01	6.1E-01	6.6E-01	5.5E-01	2.2E-01	2.2E-01	6.5E+00	1.0E+00	7.7E-01	4.1E-01	3.5E-01	3.7E-01	4.5E+00	2.7E+00	1.5E+00	6.9E-01	5.5E-01	5.0E-01

	Aspect ratio	2						2.5						3					
	Centre column radius (m)	0.10	0.15	0.20	0.30	0.40	0.50	0.10	0.15	0.20	0.30	0.40	0.50	0.10	0.15	0.20	0.30	0.40	0.50
Shielding thickness (m)	0.05	4.5E+05	2.3E+05	1.4E+05	6.0E+04	3.1E+04	1.8E+04	6.9E+05	3.7E+05	2.2E+05	9.7E+04	5.1E+04	3.0E+04	8.8E+05	4.8E+05	2.9E+05	1.3E+05	7.0E+04	4.1E+04
	0.10	1.6E+05	9.0E+04	5.5E+04	2.5E+04	1.3E+04	7.7E+03	2.6E+05	1.4E+05	8.8E+04	4.1E+04	2.2E+04	1.3E+04	3.3E+05	1.9E+05	1.2E+05	5.5E+04	3.0E+04	1.8E+04
	0.15	6.0E+04	3.4E+04	2.1E+04	9.9E+03	5.4E+03	3.2E+03	9.6E+04	5.5E+04	3.5E+04	1.6E+04	9.0E+03	5.4E+03	1.3E+05	7.3E+04	4.6E+04	2.2E+04	1.2E+04	7.5E+03
	0.20	2.2E+04	1.3E+04	8.1E+03	3.9E+03	2.1E+03	1.3E+03	3.5E+04	0.0E+00	1.3E+04	6.4E+03	3.6E+03	2.2E+03	4.7E+04	2.8E+04	1.8E+04	8.8E+03	5.0E+03	3.0E+03
	0.30	2.9E+03	1.7E+03	1.2E+03	5.6E+02	3.1E+02	2.0E+02	4.7E+03	2.9E+03	1.8E+03	9.4E+02	5.4E+02	3.4E+02	6.3E+03	3.8E+03	2.5E+03	1.3E+03	7.5E+02	4.7E+02
	0.40	3.8E+02	2.3E+02	1.6E+02	8.0E+01	4.6E+01	2.8E+01	6.2E+02	3.8E+02	2.6E+02	1.4E+02	7.9E+01	5.1E+01	8.4E+02	5.1E+02	3.6E+02	1.8E+02	1.1E+02	7.0E+01
	0.50	5.5E+01	3.3E+01	2.0E+01	1.1E+01	6.1E+00	4.1E+00	9.6E+01	5.4E+01	3.6E+01	1.9E+01	1.1E+01	7.3E+00	1.1E+02	7.3E+01	4.9E+01	2.5E+01	1.5E+01	1.0E+01
	0.60	3.8E+00	4.0E+00	3.7E+00	1.8E+00	1.1E+00	6.3E-01	1.5E+01	8.0E+00	7.2E+00	1.8E+00	1.5E+00	9.9E-01	1.4E+01	1.1E+01	6.9E+00	3.8E+00	2.6E+00	1.4E+00

Figure 4.35 - Scan of peak centre column heating, across centre column size, aspect ratio and inboard shielding thickness. Models that give a peak centre column nuclear heating $\leq$ ~2 kW/m^3 are highlighted in green.

4.4.5 Conclusions

In this section the aspect ratio, centre column size and shielding thickness has been varied without constraint on the major radius and overall size (outer radius) of the tokamak. This approach was selected because if the major radius is fixed then the range in shielding thicknesses is reduced.

In conclusion:

- At least 0.4 m of dedicated inboard shielding is required to limit the heating with the centre column magnets to a feasibly operating level of 2 kW/m^3 without damage to the magnets and/or associated reduction in efficiency.
- Assuming a maximum fast neutron fluence of 3×10^{22} neutrons/m^2 to the HTS magnets (to prevent damage) the shielding needs to reduce the fast flux to a maximum of 1×10^{15} neutrons/m^2/s in order to achieve a component lifetime of 1 full power year (fpy). At least 0.3 - 0.4 m of shielding is required to reduce the fast flux to these levels.
- A spherical tokamak with 0.4 m of tungsten carbide shielding requires geometries with a major radius of > 3 m, when the boundary conditions are set as shown in Section 4.4.1.

4.5 Neutronics assessment of a spherical tokamak and activity considerations for breeder blanket selection

4.5.1 Introduction

High temperature superconducting spherical tokamaks (HTS-ST) could potentially be a more cost-effective approach to fusion power, mainly due to the compact design. A HTS-ST is also considered as a leading candidate for a fusion nuclear science facility or component test facility. These potential test devices are another option on the pathway towards the successful use of fusion for commercial power plants. They would provide facilities for developing fusion materials and components without requiring the production of net electricity and self-sustaining tritium fuel. Neutronics analysis has been performed on a HTS-ST model and the activation of breeder materials considered.

4.5.2 The HTS-ST model

A neutronics model was created of a HTS-ST using the preliminary CAD [135], radial build and plasma parameters of the Princeton Plasma Physics Laboratory spherical tokamak concept for a fusion nuclear science facility design [133], [136]. The main plasma parameters, dimensions and components are given in Figure 4.36; an image of the generated HTS-ST CAD model. The model was produced using the SpaceClaim module of the ANSYS® package. The original Princeton Plasma Physics Laboratory spherical tokamak CAD model required simplification and rebuild to comprise of only analytical surfaces so that conversion to a CSG definition was possible using the MCAM software [86]. Further details regarding the requirements of a neutronics model for use with MCNP is given in Section 3.3.

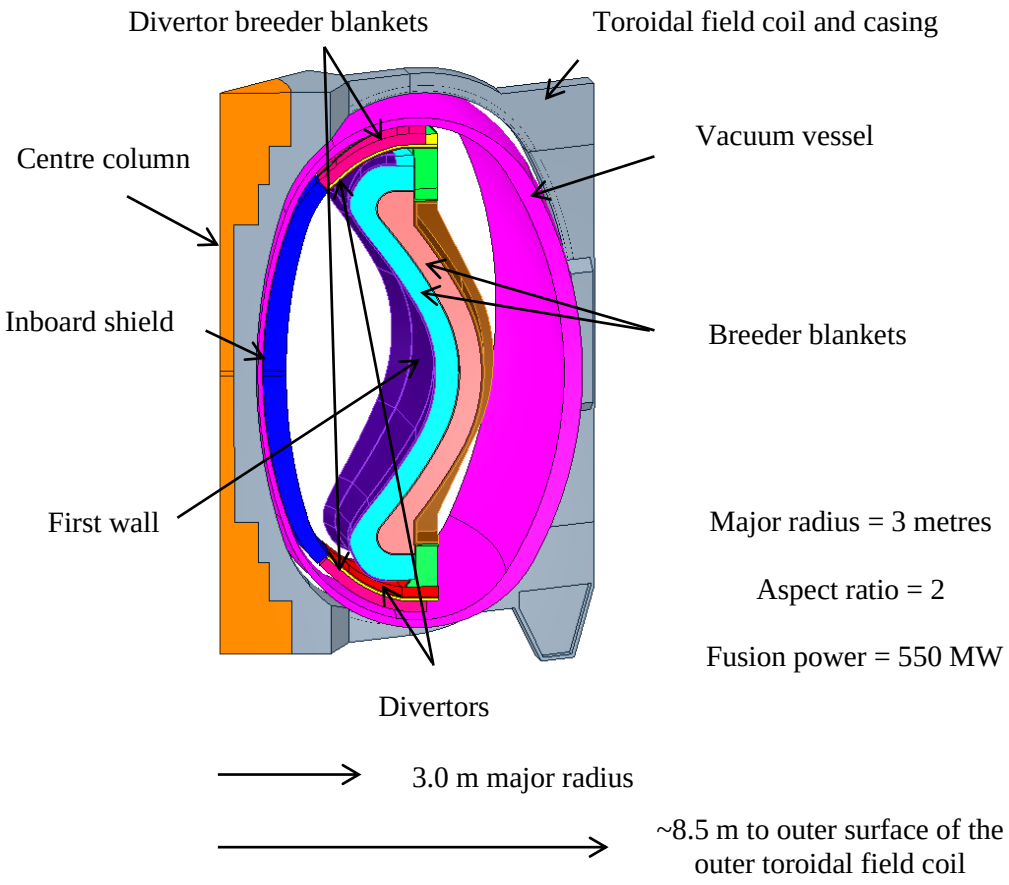

Figure 4.36 - Generated 36º CAD model of the HTS-ST, based on the CAD and radial build information for the Princeton Plasma Physics Laboratory spherical tokamak concept for a fusion nuclear science facility [135], [136].

The centre column of the HTS-ST is modelled as shown in Figure 4.37, comprising of the central solenoid, the toroidal field magnet and the toroidal field casing. The centre column is separated from the plasma by the inboard shield and vacuum vessel structure. The thickness of the inboard shield is 0.5 metres, in-line with the outcomes of the previous shielding analysis detailed in Section 4.4 which contributed to the Princeton Plasma Physics Laboratory spherical tokamak research and fusion nuclear science facility design.

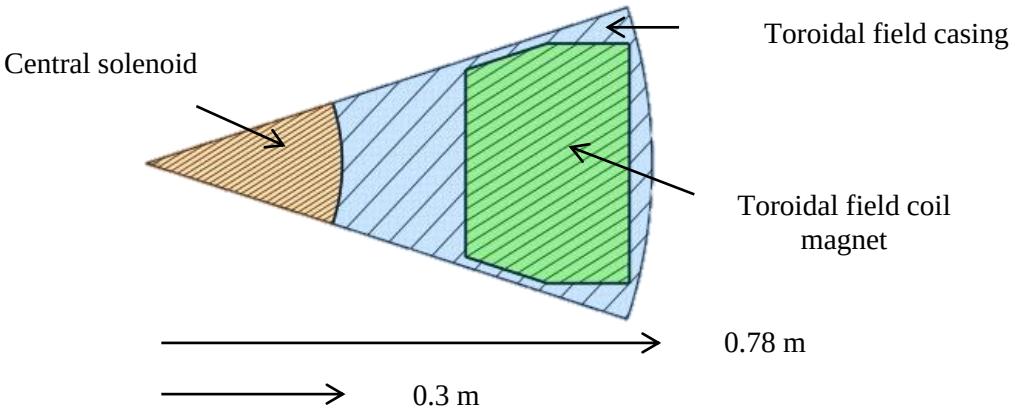

Figure 4.37 - Plan view of the centre column at the mid-plane (i.e. Z = 0 cm).

4.5.3 Materials

In order to create a simple neutronics model for preliminary neutronics assessment and on-going parameter studies, some homogenisation of materials was performed.

In particular:

- Blankets- a homogeneous mix of Li_4SiO_4 breeder and beryllium neutron multiplier pebbles with a packing fraction of 0.7, reduced activation ferritic martensitic (RAFM) steel, and helium coolant represent the blanket material.
- Shield- consisting of a homogeneous mix of tungsten carbide, RAFM steel and water coolant.
- HTS magnets- comprised of a homogeneous mix of 57% REBCO, 38% hastelloy steel and 5% helium.

The material selection was made using information gained from previous parameter studies on a simple spherical model and from materials used in the CCFE 2008 component test facility model [137], [138]. The materials used in the model for neutron transport are summarised in Table 4.9. (The isotopic compositions are given in Table 7.5, Table 7.6 and Table 7.9 of Appendix 4.)

Table 4.9 - Summary of materials used in HTS-ST model.

Component	Material
Blankets	Li_4SiO_4 breeder, beryllium neutron multiplier, steel (RAFM - F82H) & helium coolant
HTS magnets	REBCO, hastelloy steel & helium coolant
Inboard shield	Tungsten carbide, steel (RAFM - F82H) & water coolant
First wall tiles	Steel (RAFM - F82H) & helium coolant
First wall outer structure	Steel (RAFM - F82H)
Divertor tiles	Boronated steel (SS304B7 & boron) & water coolant
Divertor structure/backing	Steel (RAFM - F82H)
Vacuum vessel	Steel (RAFM - F82H) + tungsten + borated water
Toroidal field magnet structure	Steel (RAFM - F82H)

In activation calculations, the candidate breeding materials for an EU DEMO were considered along with Li_8PbO_6, LiFBe and LiSn. In reality the selection of the breeder material will change the blanket design and the required structures, cooling channels etc. In this work a homogeneous mix of materials is used to represent the different breeder blanket concepts. It should be noted that the EU DEMO blanket concepts are optimised for a conventional tokamak, as proposed in the EU power plant conceptual study. In the cases of Li_8PbO_6, LiFBe and LiSn, a homogeneous mixture of breeder, multiplier, coolant and structure was devised based on the analysis conducted in Sections 4.2 and 4.3.

A summary of the materials is given in Table 4.10, the isotopic composition is given in Table 7.7, Table 7.8 and Table 7.9 of Appendix 4. No impurities were considered for the LiFBe, Li_8PbO_6 and LiSn breeding materials.

Table 4.10- The breeder blanket materials used in activation analysis.

Ref	Tritium breeder	Material composition	Mass density (g/cm3)
B1	Li_4SiO_4 (40% ^6Li)	Based on the EU- HCPB (12% EUROFER, 38% beryllium, 13% Li_4SiO_4, 37% helium coolant)	2.4272
B2	LiPb (60% ^6Li)	Based on the EU- HCLL (13% EUROFER, 78% LiPb, 8% helium coolant)	8.4242
B3	LiPb (60% ^6Li)	Based on the EU- DCLL (12% EUROFER, 73% LiPb, 15% helium coolant)	7.8716
B4	LiPb (60% ^6Li)	Based on the EU- HCPB (18% EUROFER, 80% LiPb, 2% water coolant)	9.0311
B5	LiFBe (30% ^6Li)	80% LiFBe, 20% EUROFER	3.1578
B6	Li_8PbO_6 (10% ^6Li)	60% Li_8PbO_6, 20% EUROFER, 20% helium coolant	2.8881
B7	LiSn (90% ^6Li)	80% LiSn, 20% EUROFER	6.5178

4.5.4 Calculations and simulation codes

Neutron transport calculations have been performed using the radiation transport code MCNP [2] with the FENDL-2.1 nuclear data library. The neutron flux was recorded in two superimposed structured mesh tallies with a voxel resolution of 10 cm. The neutron flux was tallied into 175 energy bins for subsequent use with MCR2S for activation calculations. Two mesh tally files are required to limit the amount of mesh voxels which are outside the mesh geometry, as these still take up valuable space in memory though do not hold any useful data (see Figure 4.38).

In addition to the neutron flux, the tritium breeding, peak nuclear heating to the magnets, peak inboard fast flux, and the neutron wall loading were also assessed. The position of the ‘peak’ values can be seen in Figure 4.39.

Activation calculations have been performed using FISPACT-II with the EAF-2010 [109] activation data. In order to assess the activation of various blanket designs without having to perform repeat neutron transport calculations for each material, the same neutron flux has been used in the activation of different blanket materials. The change in material will have some effect on the neutron flux within the breeding

blanket. However, for an initial investigation into the activation of various breeding materials and the dominant nuclides this will be sufficient as neutron transport calculations with MCNP are computationally expensive.

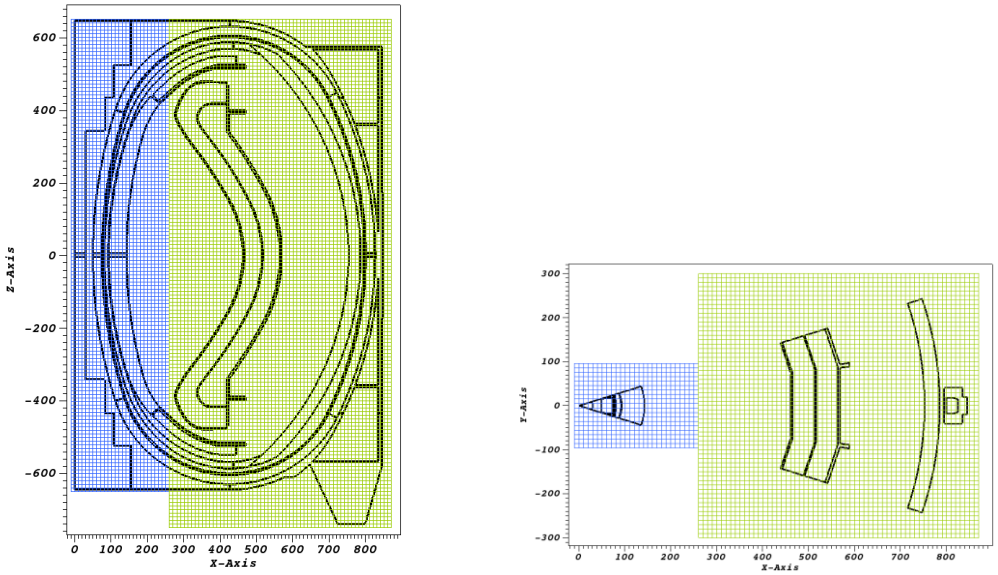

Figure 4.38 - Location of the two superimposed mesh tallies, in a vertical elevation (left) and plan view through the mid-plane, z = 0 cm, (right). (Scale in cm)

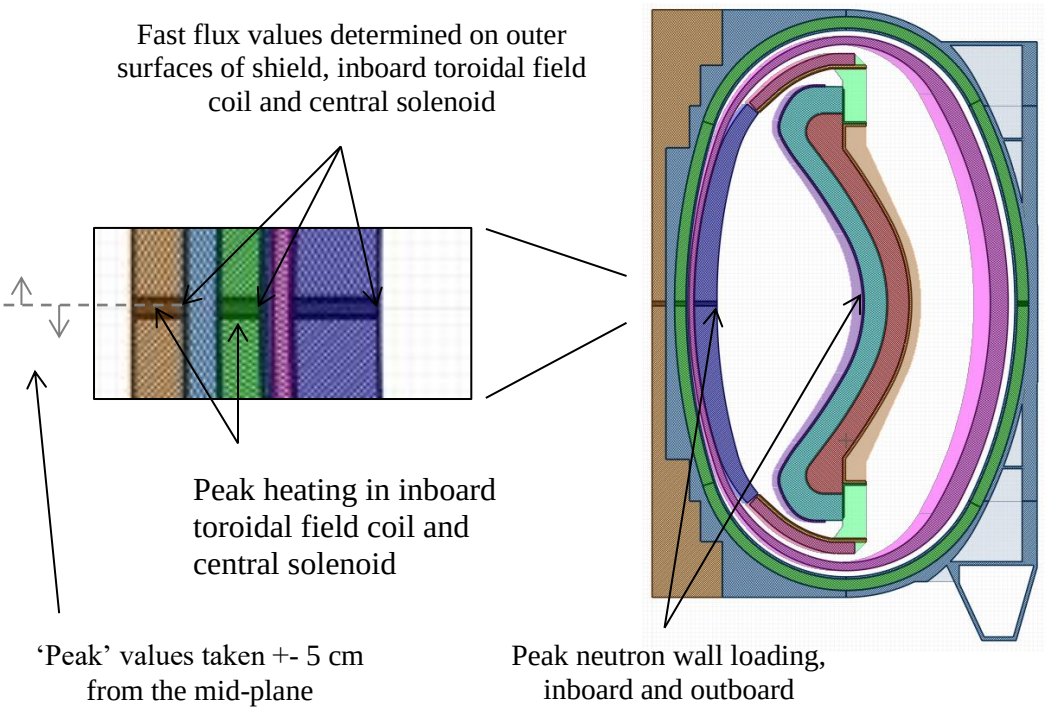

Figure 4.39 - Position of 'peak' values of heating, fast flux and neutron wall loading in the HTS-ST model.

4.5.5 Results

The neutron flux results, recorded in a neutron mesh tally are shown in the 'flux maps' of Figure 4.40. The results have been renormalized to a 550 MW fusion power device, i.e. a source strength of 1.95 x 10^{20} neutrons/second.

The nuclear heating over the reactor sector model, recorded in a mesh using heating reaction multipliers, is shown in the nuclear heating maps (Figure 4.41). To investigate the heating as a function of depth through the centre column, values in each voxel of the mesh were extracted in a line along the mid-plane (Z = 0 cm). These are given in Figure 4.42 alongside a CAD image of the centre column. The change in energy deposition (i.e. nuclear heating) can be observed in the different materials that comprise the centre column. Peak heating, fast flux and neutron wall loading is given in the summary table of the neutronics performance (Table 4.11).

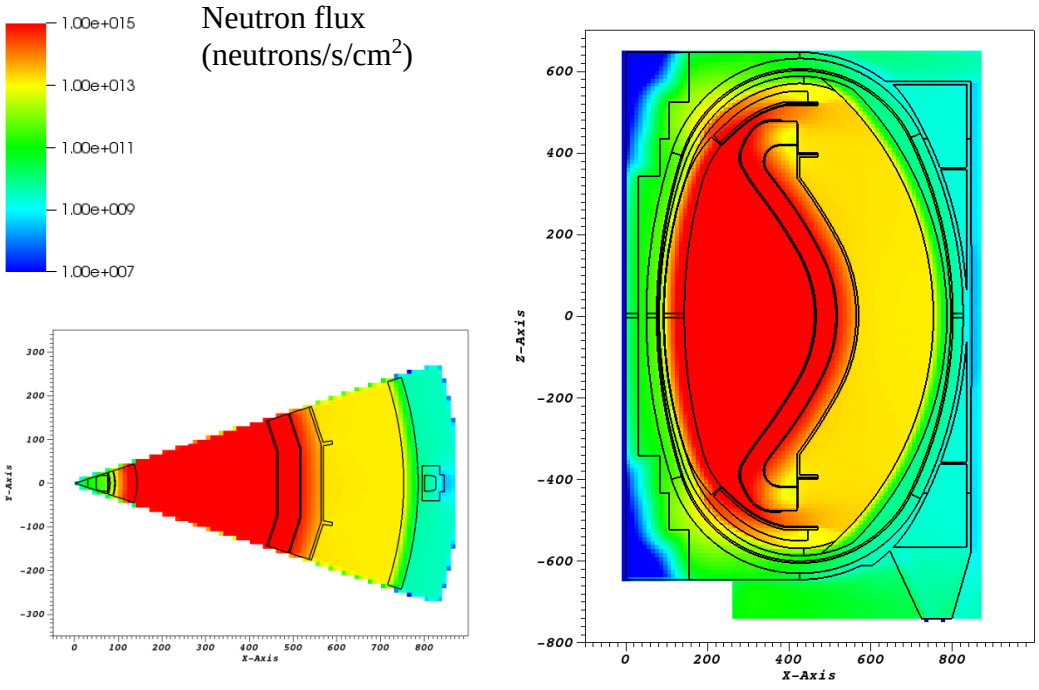

Figure 4.40 - Neutron flux (neutrons/s/cm^2) maps; plan view through mid-plane (left) and vertical elevation (right). (Scale in cm)

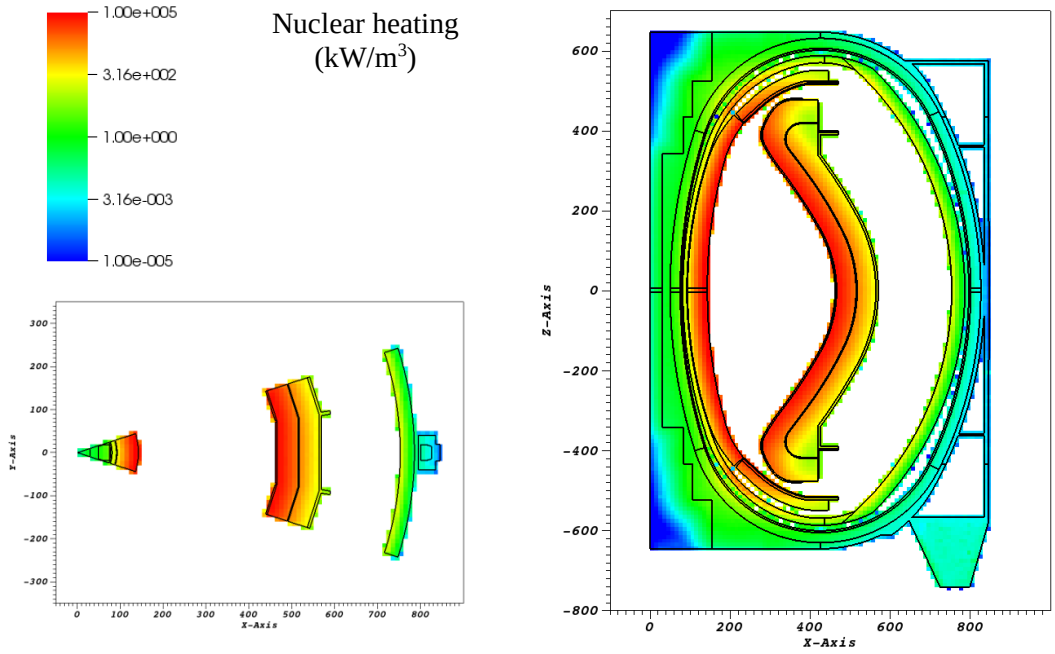

Figure 4.41 - Nuclear heating (kW/m^3) maps; plan view through mid-plane (left) and vertical elevation (right). (Scale in cm)

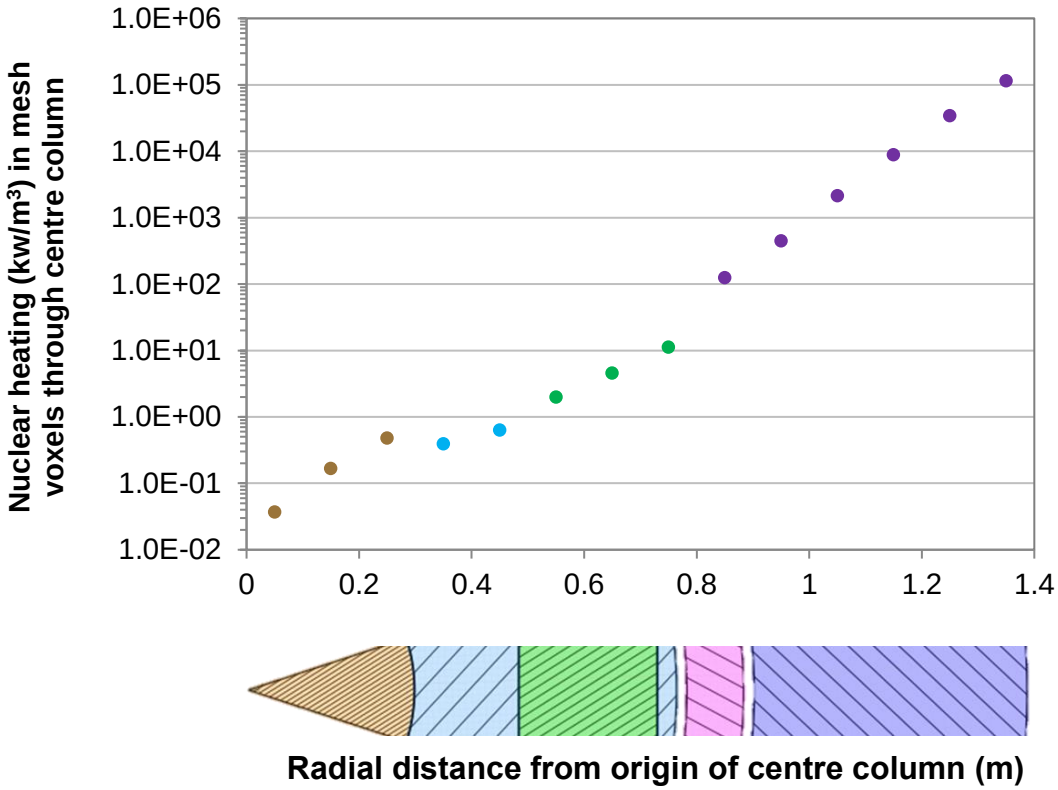

Figure 4.42 - Nuclear heating (kw/m^3) as a function of depth through the centre column and inboard shield. (Brown - central solenoid, light blue -toroidal field coil casing, green - toroidal field coil, pink - vacuum vessel, purple/blue - inboard shield.)

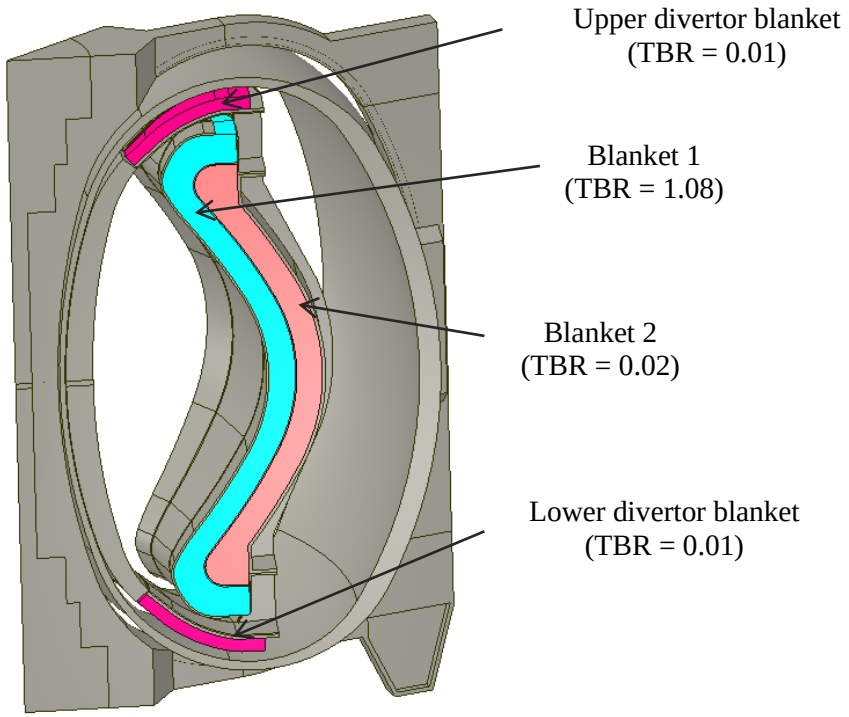

Figure 4.43 - CAD image of the tritium breeding blankets with TBR values determined using the Li_4SiO_4 breeder blanket.

Table 4.11 - Summary of HTS-ST neutronics performance. Peak refers to the volume or area +- 5 cm from the mid-plane.

Neutronics parameter	Position	Value (units)
Peak neutron wall loading	Inboard	1.45 MW/m^2
Peak neutron wall loading	Outboard	1.77 MW/m^2
Neutron wall loading	Machine average	~1.29 MW/m^2
Peak fast flux	Inboard toroidal field	3.8 x 10^{14} neutrons/s/m^2
Peak fast flux	Central solenoid	3.6 x 10^{13} neutrons/s/m^2
Peak nuclear heating	Inboard toroidal field	5.6 kW/m^3
Peak nuclear heating	Central solenoid	0.4 kW/m^3
Total TBR	Outboard & divertor blankets	1.12

Using the neutron flux determined over the two meshes, different breeding materials have been irradiated to compare activation levels and decay products (Table 4.13). Activation concentrations of dominant nuclides, as determined at 50-100 years cooling time, have been investigated. The activity concentration variation with time is given for blanket mix ‘B1’ (with a Li_4SiO_4 breeder material) in Figure 4.44. Graphs

for the other six blanket mixtures activated are given in Figure 7.15 to Figure 7.20 of Appendix 5.2. The total activity of each blanket mix is compared in Figure 4.45 and Table 4.12. For clarity of presentation the discussions are provided in Section 4.5.5.

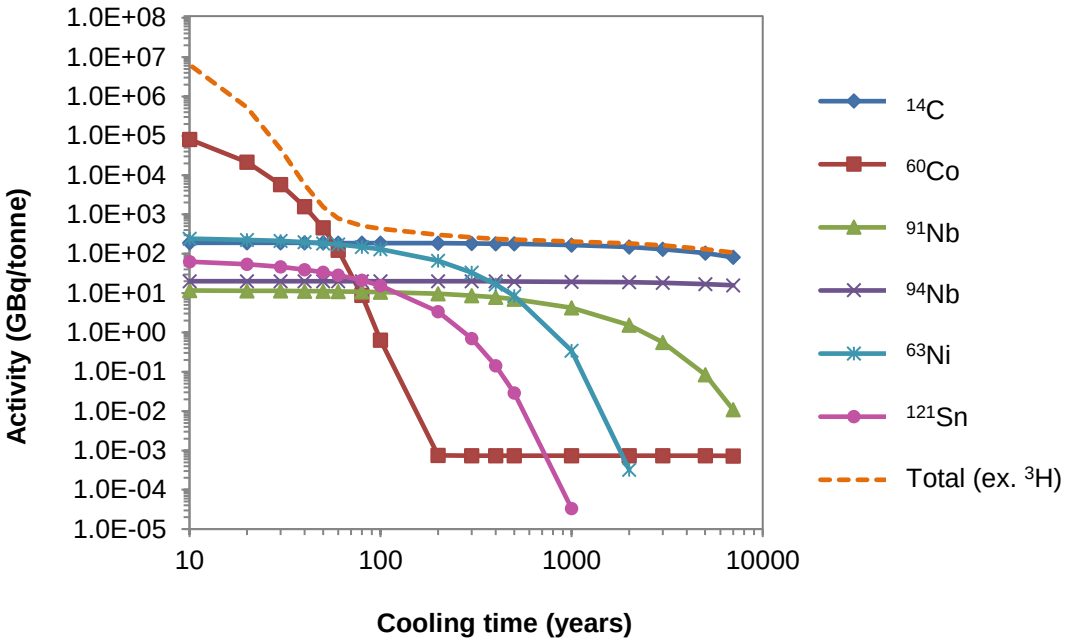

Figure 4.44 - Activity concentration of dominant nuclides for blanket mix B1 using a Li_4SiO_4 breeder material.

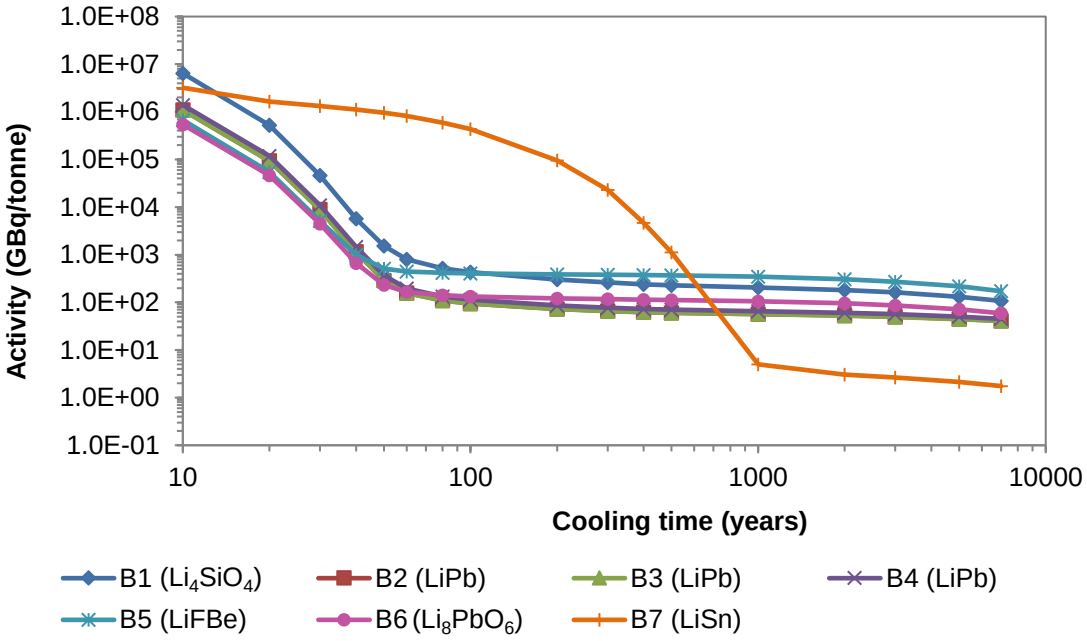

Figure 4.45 - Comparing total activity concentration (excluding tritium) of each blanket mixture (B1-B7).

Table 4.12 - Comparison of total activity concentration (GBq/tonne) (excluding tritium) for each blanket (1-7) at eight cooling times.

	B1	B2	B3	B4	B5	B6	B7
6 months	8.21E+07	1.37E+07	1.35E+07	1.76E+07	8.56E+06	6.66E+06	7.26E+07
1 year	6.89E+07	1.15E+07	1.14E+07	1.48E+07	7.18E+06	5.60E+06	4.65E+07
10 years	6.39E+06	1.09E+06	1.08E+06	1.39E+06	6.65E+05	5.36E+05	3.20E+06
50 years	1.54E+03	2.90E+02	2.88E+02	3.69E+02	5.13E+02	2.31E+02	9.54E+05
100 years	4.31E+02	9.49E+01	9.42E+01	1.14E+02	4.05E+02	1.33E+02	4.33E+05
500 years	2.28E+02	6.04E+01	6.00E+01	7.03E+01	3.67E+02	1.12E+02	1.12E+03
1000 years	2.06E+02	5.68E+01	5.64E+01	6.55E+01	3.44E+02	1.06E+02	4.97E+00
5000 years	1.32E+02	4.48E+01	4.46E+01	5.00E+01	2.17E+02	7.10E+01	2.14E+00

Table 4.13 - Primary pathways for main dominant nuclides identified.

Nuclide	Half-life	Primary pathways
^{3}H	12.32 y	$^{6}\mathrm{Li}(n,\alpha)^{3}\mathrm{H}$
^{14}C	5730 y	$^{14}\mathrm{N}(n,p)^{14}\mathrm{C}$ $^{19}\mathrm{F}(n,n\alpha)^{15}\mathrm{N}(n,p)^{14}\mathrm{C}$ $^{19}\mathrm{F}(n,n\alpha)^{15}\mathrm{N}(n,d)^{14}\mathrm{C}$ $^{19}\mathrm{F}(n,t)\ ^{17}\mathrm{O}(n,\alpha)^{14}\mathrm{C}$
^{205}Pb	1.73x 10^{7} y	$^{206}\mathrm{Pb}(n,2n)^{205}\mathrm{Pb}$
^{63}Ni	9.90 y	$^{63}\mathrm{Cu}(n,p)^{63}\mathrm{Ni}$ $^{62}\mathrm{Ni}(n,\gamma)^{63}\mathrm{Ni}$
^{121}Sn	27.03 h	$^{120}\mathrm{Sn}(n,\gamma)^{121}\mathrm{Sn}$
^{121m}Sn	43.9 y	$^{122}\mathrm{Sn}(n,2n)^{121\mathrm{m}}\mathrm{Sn}$ $^{120}\mathrm{Sn}(n,\gamma)^{121\mathrm{m}}\mathrm{Sn}$
^{94}Nb h	19986 y	$^{93}\mathrm{Nb}(n,\gamma)^{94\mathrm{m}}\mathrm{Nb}(IT)^{94}\mathrm{Nb}$ $^{93}\mathrm{Nb}(n,\gamma)^{94}\mathrm{Nb}$
^{93m}Nb	16.2 y	$^{93}\mathrm{Nb}(n,n)^{93\mathrm{m}}\mathrm{Nb}$
^{53}Mn	3.74 x 10^{6} y	$^{54}\mathrm{Fe}(n,np)^{53}\mathrm{Mn}$
^{60}Co	5.27 y	$^{59}\mathrm{Co}(n,\gamma)^{60\mathrm{m}}\mathrm{Co}(IT)^{60}\mathrm{Co}$ $^{59}\mathrm{Co}(n,\gamma)^{60}\mathrm{Co}$
^{113m}Cd	14.1 y	$^{116}\mathrm{Sn}(n,\alpha)^{113\mathrm{m}}\mathrm{Cd}$
^{108m}Ag	438 y	$^{112}\mathrm{Sn}(n,\alpha)^{109}\mathrm{Cd}(\beta+)^{109\mathrm{m}}\mathrm{Ag}(IT)^{109}\mathrm{Ag}(n,2n)^{108\mathrm{m}}\mathrm{Ag}$

4.5.6 Discussion and conclusions

4.5.6.1 Shielding performance

The HTS-ST shows promising results in terms of the nuclear heating in HTS magnets within the centre column, with a peak nuclear heating 0.4 kW/m^3 in the central solenoid and 5.6 kW/m^3 in the inboard toroidal field coil. A shield of tungsten carbide with 13% water, 58 cm thick was used as the dedicated inboard neutron shield. The HTS-ST geometry provides effective shielding in terms of the centre column heating whilst providing a reasonable neutron wall loading, 1.45 MW/m^2 peak inboard, as required for fusion environment testing. If the HTS magnets are limited to a neutron fast fluence ($E_n > 0.1$ MeV) of 3 x 10^{22} neutrons/m^2 then the toroidal field magnets (based on centre column-toroidal field values) have a lifetime of approximately 2.5 FPY (full power year).

4.5.6.2 Blanket performance

Due to the geometry of spherical tokamaks the breeder blanket is limited to the outboard. In this model the outboard breeder blankets are shown in Figure 4.43 as the light blue and salmon pink regions. In the Princeton Plasma Physics Laboratory spherical tokamak fusion nuclear science facility design, divertor blankets have also been considered (dark pink region). A TBR of 1.12 is achieved using the solid ceramic breeder Li_4SiO_4, enriched with 40% ^{6}Li, based on the EU-HCPB blanket concept. As already mentioned, depending on the purpose and operation of the spherical tokamak fusion device, tritium self-sufficiency may not be a requirement. For any commercial fusion power plant or DEMO, however, tritium self-sufficiency is required (TBR >1.1). Although a TBR of 1.12 is achieved in the blankets of this HTS-ST, no gaps or holes for ports, access, removal, etc., are considered which could reduce the TBR significantly.

The majority (~97 %) of the TBR contribution is from blanket 1, with blanket 2 contributing ~1.5 % and ~1 % from each of the divertor blankets. Of the total TBR, ~96 % is from the ^{6}Li reaction. Further optimisation of the enrichment and quantity of neutron multiplying material (in this case beryllium) could be used to increase the TBR as the blanket material composition used in this study is optimised for an EU DEMO HCPB concept.

4.5.6.3 Activation considerations

Activation calculations have been performed on a number of blanket materials, assuming the neutron flux to be the same for each (as calculated in the neutron transport calculation with the EU HCPB blanket material). The operational scenario is not a particularly close representation of that which may be derived for a fusion neutron science facility and simply assumes a 10 year life at 30% fusion power (equivalent to approximately 3 FPY, as proposed for the Princeton Plasma Physics Laboratory fusion neutron science facility using HTS magnets). An example of the dominant nuclides and time dependency is given in Figure 4.44 for a blanket material based on the EU HCPB concept. Similar plots are available in Appendix 5.2 for the other 6 blanket mixtures.

Comparison of the total activation concentration (Figure 4.45 and Table 4.12) from four different breeder materials (seven blanket mixtures compared in total) shows that the dominant nuclides at 50-100 years are similar in all cases apart from LiSn. The activation of the structural material component is shown to contribute significantly to the total activation.

Of the three EU DEMO concept materials that make use of the molten lithium mixture, LiPb, similar activation products and time variation is shown. The fourth EU DEMO blanket concept makes use of the ceramic solid breeder Li_4SiO_4 which shows slightly higher activity concentration levels.

With regards to the lithium mix, salt or compound materials, the following radionuclides are shown to dominate after a cooling period of 50-100 years (see Table 4.13 for the primary pathways for the main dominant nuclides):

- All LiPb blankets - the very long-lived ^{205}Pb radionuclide
- LiFBe - the long-lived ^{14}C radionuclide resulting from interaction with the fluorine
- LiSn - the radionuclides of ^{121m}Sn, ^{121}Sn, ^{113m}Cd and ^{108m}Ag

The activation of the solid ceramic breeder Li_4SiO_4 blanket is dominated by the steel contribution.

In terms of the radiotoxicity of the nuclides presented in Table 4.13, the majority are considered have low to moderate radiotoxicity levels. In the case of ^{14}C, for example,

the radiotoxicity is only related to radioactive emissions of the pure low-energy (156 keV) β. This toxicity is mainly the result of internalisation through ingestion. Nuclides such as ^{60}Co and ^{94}Nb have a higher radiotoxicity level, mostly due to the very high-energy gamma emission.

4.6 Discussion and conclusion of breeder blanket performance and shielding analysis

4.6.1 Blanket materials

Using a neutron multiplying and moderating material, such as beryllium or lead, is required to ensure a TBR ≥ 1.1 is achievable. If an ideal situation of one tritium is produced for every neutron, if losses surrounding the entire tritium system are considered, this wouldn't be enough to provide a self-sufficient supply. Neutron multipliers increase the number of neutrons and therefore the (n, t) reactions within the lithium. Increasing the volume percentage of beryllium to 40 % gives a TBR of ~1.8 and energy multiplication of ~1.2 in a simple homogeneous spherical model with a pure lithium breeder.

Approximating the blanket material as a homogeneous mix means that the beryllium and lithium are assumed to be uniformly 'mixed', this increases the TBR and energy multiplication as the neutron multiplication effects of beryllium are put to best use i.e. in the case of a heterogeneous model, the neutrons produced through $(n, 2n)$ reactions within the beryllium layer are likely to interact again with the beryllium as opposed to the lithium as they need to get out of the beryllium layer first. If the beryllium layer is increased too much, it no longer has a positive effect on the TBR. Breeder blanket concepts with a mixed pebble bed are therefore more attractive in this context than separate channels or layers of each material.

The homogeneous mix also assumes that the neutron flux is not affected by the different materials although it is shown in comparing Figure 4.7 and Figure 4.12, that the flux is different. This is important when considering the use of neutronics models for activation analysis where the neutron flux is assumed to be the same over the entire cell.

4.6.2 Breeder blanket material selection; solid or liquid?

A number of solid and liquid breeding materials have been considered for their capabilities as a tritium breeding material within the breeding blankets of a fusion magnetic confinement tokamak. The capabilities have been assessed through the tritium breeding potential, energy multiplication and shielding of fast neutron flux. These three aspects cover the main requirements of a fusion blanket.

The breeding materials are compared against the base material of pure lithium. As lithium is highly reactive it is unlikely to be used in its pure form, though there are blanket designs using molten lithium such as the Korean concept. These designs will require considerably greater safety assessment, however, due to the high reactivity of molten lithium with water and air. Lithium is shown to provide a TBR $\geq$ 1.1 regardless of ^{6}Li enrichment, when modelled as a homogeneous mix with 30 – 40 % beryllium multiplier. Without the beryllium the number of neutrons is significantly reduced affecting the tritium breeding potential. Some form of neutron multiplying material is required to ensure TBR $\geq$ 1.1, as producing one tritium atom for every neutron would not be enough when losses are considered. Beryllium is considered as the prime candidate for a neutron multiplying material in the majority of fusion blanket designs, though this has compatibility issues with water leading many designs to move to a helium coolant. The other multiplier considered in this work is lead which features in a number of liquid breeder designs as LiPb and has been considered as a ceramic breeder Li_8PbO_6.

4.6.2.1 Liquid breeding materials

One of the methods to stabilise lithium for use in breeder blankets is via conversation to a salt, LiF. The melting point of LiF is high and can be reduced through the addition of BeF_2, which also acts as a multiplier. The molten salts considered in this work were LiFBe (commonly referred to in literature as Flibe), LiFBeNa and LiFNaK.

The molten salts have a lower TBR than pure lithium (with beryllium neutron multiplier) due to the reduced concentration of lithium resulting from the inclusion of additives, and do not produce an energy multiplication factor of > 1. The LiBeF molten salt is the only one to achieve a TBR greater than the required 1.1, achieving a peak TBR of 1.13 at a 30% enrichment, but an energy multiplication factor of 0.9. The LiFBeNa and LiFNaK achieve some tritium production, 1.0 and 0.9 respectively, with

values of 0.9 and 0.8 for energy multiplication. The breeding potential and energy multiplication could be increased through optimisation of multiplying material and the addition of beryllium to the LiFNaK. The LiFBeNa and LiFNaK are attractive options for coolant in fusion blanket designs due to the low melting temperatures and low vapour pressures. However the breeding potential has been shown to be lower than that of the LiBeF molten salt and the addition of sodium introduces further activation issues. Although the molten salts have lower tritium breeding potential the high electrical resistivity of the molten salts reduces problems regarding the magnetohydrodynamics (MHD) effect making them still an attractive option for use as the coolant and/or as part of a dual-coolant or dual-functional design, whilst also creating tritium.

Other liquid materials considered, the LiPb and LiSn liquid metals, have higher TBR and energy multiplication potential than the molten salts, a peak TBR of 1.3 and 1.1 respectively, but introduce MHD drag effects when considered as a coolant, due to the lower electrical resistance and may necessitate ceramic coatings for electrical insulation on steel structures to reduce the drag. Using these liquid metal mixtures in a slow circulating flow would allow for the continuous control of tritium and purification; however the addition of Pb or Sn requires enrichments of 40 – 90 % for a TBR $\geq$ 1.1. The TBR potential of LiSn can be increased through the addition of beryllium, though this removes the advantage of having a blanket design that does not use beryllium. The liquid metal mixtures do not reduce the fast neutron flux as effectively as the molten salts, though all the liquid breeders reduce the fast neutron flux at the back of the blanket to less than 0.4 % of the first wall fast flux. The molten salts provide similar fast flux shielding to the solid breeder materials.

Additional cooling is likely required, whether or not the liquid metal mixtures are used as coolants or not; the use of an alternative primary coolant also reduces the problems regarding MHD effects. The main primary coolants considered in both liquid and solid blanket designs are water and helium. Tritium recovery from water is more costly than from helium and coatings, such as Al_2O_3, are likely to be required when using water with a LiPb blanket design to act as a tritium permeation barrier. Water is also best avoided when using beryllium in the blanket due to the safety implications of water and beryllium incompatibility, however beryllium features in many designs due to its excellent neutron multiplying capabilities. Designs are moving to use helium as

the primary coolant; however the use of helium in fusion environments is less well researched.

4.6.2.2 Solid breeders

The ceramic or so-called 'solid' breeders all achieve a TBR ≥ 1.1 and on average require a lower enrichment of ^{6}Li to achieve this than the liquid breeders. All but the Li_8PbO_6 achieve an energy multiplication > 1 and reduce the neutron fast flux at the back of the blanket to less than 0.6% of the first wall fast flux. The solid breeders show less of a variation in TBR with increasing ^{6}Li enrichment and a similar trend to the pure lithium. These breeding materials tend to have a peak enrichment of 30 – 40 %. Li_4SiO_4 provides a TBR ≥ 1.1 and energy multiplication > 1.1, and is used as the breeder in the most near-term EU DEMO solid breeder blanket concept, the HCPB blanket. This breeder, along with Li_2TiO_3, are the most advanced of the ceramic breeders in terms of the manufacturing and production processes. Li_2TiO_3 produces a similar TBR to the Li_4SiO_4 but has further advantages regarding the lower thermal expansion that reduces the build-up of stresses caused by heating.

4.6.3 How small can a magnetic confinement fusion tokamak be?

In a conventional tokamak the physical dimensions of the coil rings mean that the 'hole' in the torus can only be reduced so far before the windings of the coil are touching. This limits the aspect ratio of tokamaks to about 2.5. In a spherical tokamak design, the toroidal field coils often either placed closer to the plasma and/or a single central conduct is used. The reduction in overall size of the central column means that the fusion plasma can be held in a tighter magnetic field with a reduced aspect ratio, as low as 1.2. Recent developments in HTS have made the small aspect ratio spherical tokamak a more attractive option as they have the potential to be a more economical and efficient method for fusion power. They are particularly attractive for component test facility or fusion nuclear science facility due to the possible modular design and use of HTS in remountable magnets.

Neutronics analysis on a simple spherical tokamak model, varying the centre column size, aspect ratio and shielding thickness has shown that to reduce the peak heating in the centre column to an appropriate level for HTS, a shield of at least 0.4 m is required. It is expected that HTSs could withstand heating of 2-5 kW/m^3, though the lower limit of 2 kW/m^3 was used in these parameterised spherical tokamak studies. This required

shielding thickness has an impact on the overall size of the reactor. Using the geometry constraints set in this study, a tokamak with a major radius of at least 3 m is required to provide a the space requirements for such a thick shield to reduce peak centre column heating to ≤ 2 kW/m^3.

4.6.4 Neutronics performance of HTS-ST

Neutronics performance analysis of the HTS-ST (based on the Princeton Plasma Physics Laboratory spherical tokamak fusion nuclear science facility concept) has shown promising results. The model provides a reasonable neutron wall loading of ~1.29 MW/m^2 machine average, with 1.45MW/m^2 peak inboard and 1.77MW/m^2 peak outboard, whilst ensuring reasonable shielding to reduce heating in the HTS magnets. The 0.5 m tungsten carbide (and 13% water) inboard shield reduces the peak nuclear heating in the centre column to 0.4 kW/m^3 in the central solenoid and 5.6 kW/m^3 in the inboard toroidal field coil. These values compare well with similar studies using the DAG-MC approach [133], reporting a peak nuclear heating of 4.8 kw/m^3 in a similar region.

If the superconducting magnets are limited to a neutron fast fluence (E_n > 0.1MeV) of 3 x 10^{22} neutrons/m^2 then the toroidal field magnets (based on the inboard toroidal field coil values) have a lifetime of approximately 2.5 FPY. In the case of the fusion nuclear science facility proposed by Princeton Plasma Physics Laboratory, the intended blanket lifetime is 3.1 FPY. Using a fast neutron fluence limit of 4.3 x 10^{22} neutrons/m^2 as proposed in [133], the magnet lifetime can meet this requirement.

The tritium breeding material for the Princeton Plasma Physics Laboratory spherical tokamak fusion nuclear science facility design is the liquid breeder LiPb [133]. In the research presented in this thesis the solid ceramic breeder Li_4SiO_4 has been used. The tritium breeding of the Li_4SiO_4 blankets within the HTS-ST model provides a TBR > 1.1. The geometry of a spherical tokamak does not allow for an inboard breeder blanket, and as such the tritium fuel production is limited to the outboard. This model includes the divertor blankets, as proposed in the Princeton Plasma Physics Laboratory spherical tokamak fusion nuclear science facility design. These divertor blankets contribute ~3% of the total TBR. However in the model used, there was no

provision made for gaps or port holes, therefore the contribution from the divertor blankets may prove to be more significant.

The HTS-ST neutronics model was also used to determine a reasonable fusion blanket neutron flux spectrum for activation analysis of potential tritium breeding materials. The flux, determined in a neutron transport calculation with the Li_4SiO_4 breeder blanket, based on the EU HCPB composition, was used to irradiate blankets of seven different material compositions; the four main EU blankets plus the less common Li_8PbO_6, LiSn and LiFBe. As no detailed irradiation scenario is known for HTS-ST as a component test facility, fusion nuclear science facility or fusion power plant, an operational life of 10 years at 30 % fusion power was assumed [133]. The activation in a voxel within the mesh covering the breeder blanket was compared. The three LiPb EU blanket concepts all have similar activity concentrations. The activation of Sn dominates the activity in the LiSn breeder blanket and does not begin to significantly decrease until after ~200 years cooling time.

5 RADIOACTIVE WASTE ASSESSMENT OF DEMO

5.1 Introduction

A fusion reactor device will become radioactive during operation as a result of irradiation by neutrons generated in the D-T reaction. A fusion power plant will typically receive approximately 1 x 10^{21} neutrons per second during full power pulses. Consequently radioactive waste will be produced, however, only a limited amount of long-lived radioactive waste is generated. Fusion power reactors will not produce any radioactive waste requiring significant active cooling, such as that arising from fission plants where the thermal output can be 2 - 20 kW/m^3 [66]–[68].

Radioactive waste needs to be disposed of using methods that ensure safe isolation from biological systems. There is also a need to reduce the amounts of permanent radioactive waste; an important issue with regards to public acceptance of fusion power. Several paths are available depending on how the waste is classified, national regulations, and existing facilities, such as direct disposal into deep geological disposal facilities, near surface disposal, recycling and clearance of materials that are not active waste.

5.2 Radioactive waste

Radioactive waste in a fusion power facility will be produced during operation of the plant (through maintenance on supporting systems, the replacement of components,

etc.) and in decommissioning. Rosanvallon [139] provides a first estimate, based on 1-D activation calculations, for a total ITER radioactive waste mass of 34 kilotonnes (kt), with 11 % from the operation of the facility and 89 % arising during the decommissioning. Radioactive waste is produced as a result of neutron induced activation of materials. In addition, further radioactive waste will be produced through tritiation. Components may be contaminated with tritium through absorption and permeation.

The research presented in this thesis focused on the radioactive wastes produced through neutron induced activation, though the problem of tritium contamination is discussed. The radioactive waste management issues applicable to a fusion power plant and lessons that can already be learnt from ITER are discussed. A waste classification, based on IAEA and EURATOM safety of radioactive waste guidance, was applied to an EU helium-cooled pebble bed DEMO reactor model. Neutronics methods for performing the radioactive waste calculations are compared.

5.3 Waste management

Within European countries the legal requirement and regulations regarding radioactive waste management are well established but nationally specific. It is the responsibility of the national authorities or regulatory bodies to establish the appropriate criteria for storage and or disposal. Within the scope of this work, the French criteria regarding the ITER facility, along with the UK radioactive waste criteria (as used for radioactive waste assessments of the JET facility), and the IAEA based EU DEMO criteria will be discussed. Detailed conditions, regulations and technological standards for clearance and disposal acceptance criteria established in a number of other European countries are discussed in detail in the Marginer report [140]. In all cases the waste management within the EU is based upon the EURATOM treaty and EURATOM Basic Safety Standards Directive [141] (BSSD-1996).

The end-point for radioactive waste management is disposal providing passive and robust safety features. The waste acceptance criteria are facility/site specific and may also differ on a package type basis. Due to the limited availability of waste burial facilities in the EU and the associated social perceptions regarding radioactive waste, an optimum waste management plan for fusion power plants needs to be developed [68]. Although this is not the main purpose of this thesis, the waste produced by an

EU DEMO model has been explored with an aim to provide recommendations regarding the neutronics analysis methods used and considerations for the waste classification.

5.4 Radioactive waste classification and clearance

Waste characterisation is an important aspect of waste management, providing information required for conditioning needs and disposal decisions. Radioactive waste can be classified into a number of groups, based on the activity, contact dose rate and/or residual heat. The classes of waste vary depending on the regulations of the country and allowable levels associated with the disposal facility.

Table 5.1 - Comparison of UK [142] and IAEA [143], [144] waste classes and disposal.

	JET- UK		**Demo- IAEA**
Out of Scope	Cleared from regulatory control Clearance level < 1	**Non-Active (NAW)**	Cleared from regulatory control Clearance level < 1
Low Level (LLW)	**NEAR SURFACE** Disposal in near-surface facilities Classed by activity: 4GBq/t > alpha > 4 MBq/t 12GBq/t > beta > 12MBq/t	**Low Level (LLW)** **Fraction of LLW possibly available for recycling (LLW-RM)**	Disposal in near-surface facilities Classed by activity: < 12GBq/t Potential for recycling Classed by contact dose: < 2mSv/hr
Intermediate Level (ILW)	Disposal in near-surface facilities for short lived nuclides and/or interim storage Classed by activity: alpha > 4 GBq/t OR beta + gamma > 12 GBq/t	**Intermediate Level (ILW)** **Fraction of ILW possibly available for recycling (ILW-RM)**	Disposal in near-surface facilities for short lived nuclides and/or interim storage Classed by activity: > 12GBq/t Potential for recycling Classed by contact dose: < 2mSv/hr (contact dose)
High Level (HLW)	Deep geological disposal (significant residual heat output requiring active cooling)	**High Level (HLW)**	Deep geological disposal (significant residual heat output requiring active cooling)

A summary of the classes, and associated disposal implications, used in this EU DEMO study is presented in Table 5.1 along with a comparison of criteria used for a recent radioactive waste assessment of JET [145]. A summary of classes and waste management proposed for ITER is given in Table 5.2.

High level waste (HLW) is not relevant for a fusion device as HLW is a category specifically associated with radioactive materials that generate thermal heat.

Table 5.2 - Waste classes and disposal/management using French Regulatory system [146], [147].

<table>
<tr><td></td><td colspan="3">Half-life</td></tr>
<tr><td></td><td>Very short lived (<100days)</td><td>Short lived (<30 years)</td><td>Long lived</td></tr>
<tr><td>Very Low Level (VLLW)</td><td rowspan="4">Management based on interim storage and radioactive decay</td><td colspan="2">Disposal at dedicated Morvilliers interim storage facility or recycling
(based on IRAS index acceptance criteria)</td></tr>
<tr><td>Low Level (LLW)</td><td rowspan="2">Disposal at dedicated Centre de stockage de l'Aube (CSA), expect for tritiated waste
(based on nuclide by nuclide acceptance criteria)</td><td>Sub-surface disposal
(ongoing studies)</td></tr>
<tr><td>Intermediate Level (ILW)</td><td rowspan="2">Pathways under investigation</td></tr>
<tr><td>High Level (HLW)</td><td colspan="2"></td></tr>
</table>

5.4.1 ITER radioactive waste

Radioactive waste management for ITER follows the French framework, a Programme Act on the Sustainable Management of Radioactive Materials and Waste, established in June 2006 [147]. In France, the national agency for radioactive waste management (ANDRA) [148] is in charge of overall radioactive waste management including the inventory, collection, and management of disposal sites and the R&D programme if necessary when no appropriate disposal site is identified.

The classification of radioactive waste is based on nuclide life and activity, as defined by a French decree April 2008 [146] (see Table 5.2). Within the French regulations, there is no exemption or clearance of radioactive material, all the waste arising from a

zone producing radioactive waste will be managed as radioactive waste. The indice radiologique d'acceptabilite de stockage (IRAS) index is used to determine if the material can be classed as very low level waste (VLLW) [119], [149]. For short-lived low level and intermediate level waste a nuclide by nuclide Centre de Stockage de l'Aube (CSA) acceptance criteria is applied [149].

The VLLW arising from ITER will be disposed of via surface disposal at 'CSTFA', the dedicated Morvilliers interim storage facility, unless recycling is feasible. Short-lived low level and intermediate level waste will undergo interim storage until tritium activity and out-gassing is sufficiently reduced for acceptance at the 'CSFM' Aube facility. Any components comprising of long-lived wastes and/or purely tritiated wastes will be kept in interim storage for up to 50 years before being sent on to a final disposal repository.

In terms of radioactive waste disposal or storage, the main objective is to prevent the unacceptable contamination of the environment and protect the health of the public and workers. A secondary objective is to reduce disposal costs.

A preliminary safety report submitted to the French regulator in 2011, using results from 1-D calculations, showed that of an expected 32 kt of waste produced through operation and decommissioning, 58 % was VLLW, 32 % low level waste (LLW) and intermediate level waste (ILW) with a short half-life, and 10 % long-lived ILW [150] at the end of ITER operational lifetime. Further calculations using 3-D analysis considered the waste from different components within the ITER facility (see Table 5.3).

Table 5.3 - Waste classification of main ITER components [151].

ITER component	Mass (kt)	Waste Class
Blanket modules	1530	ILW long-lived
Divertor modules	650	ILW long-lived
Vacuum vessel	5100	LLW and ILW short-lived
Toroidal field coils	6010	VLLW (50 years after shutdown)
Poloidal field coils	1870	VLLW (50 years after shutdown)
Central solenoid	950	VLLW
Cryostat	3500	VLLW (50 years after shutdown)

5.4.2 A ‘non-active waste’ class based on clearance levels

The UK [152] and IAEA guidance [143], [144] includes classes of ‘out of scope’ or ‘non-active waste’ (NAW). These are included in Table 5.1 for completeness, however once the material has been classed as out of scope or NAW it is no longer radioactive waste. The material is no longer under nuclear regulatory control for radiation protection purposes irrespective of where the material is disposed.

Material can be considered cleared of regulatory control if it meets certain criteria regarding clearance levels (Figure 5.1). The EURATOM Basic Safety Standards Directive [141] (BSSD-1996) established uniform safety standards to protect the health of workers and the general public against danger arising from ionizing radiation. The standards are contained within the Council Directive 96/29/EURATOM.

Guidance for practical use of the clearance levels was published in the Radiation Protection publication 122 (RP-122) in 2000 [153] which assigned numerical values to the concept of clearance levels in the form of radionuclide specific levels of activity concentration. Where the material contains a mix of radioactive nuclides, the sum of the nuclide-specific activity divided by the corresponding clearance level should be less than 1.

$$\sum_{i=1}^{n} \frac{C_i}{CL_i} \leq 1.0 \qquad (15)$$

The expression for the clearance index [29] is given in Equation 15 where, C_i is the activity per unit mass (Bq/g) of the radioactive nuclide i, CL_i is the clearance level of the nuclide i, and n is the number of nuclides in the mixture.

Since the publication of RP-122, the IAEA has also published guidance regarding the use of clearance levels in Safety guide RS-G-1.7 in 2004 [154]. As part of on-going revisions of the EURATOM BSSD, the Commission proposed to align the guidance with that from the IAEA to achieve greater international harmonisation and simplification of regulatory control.

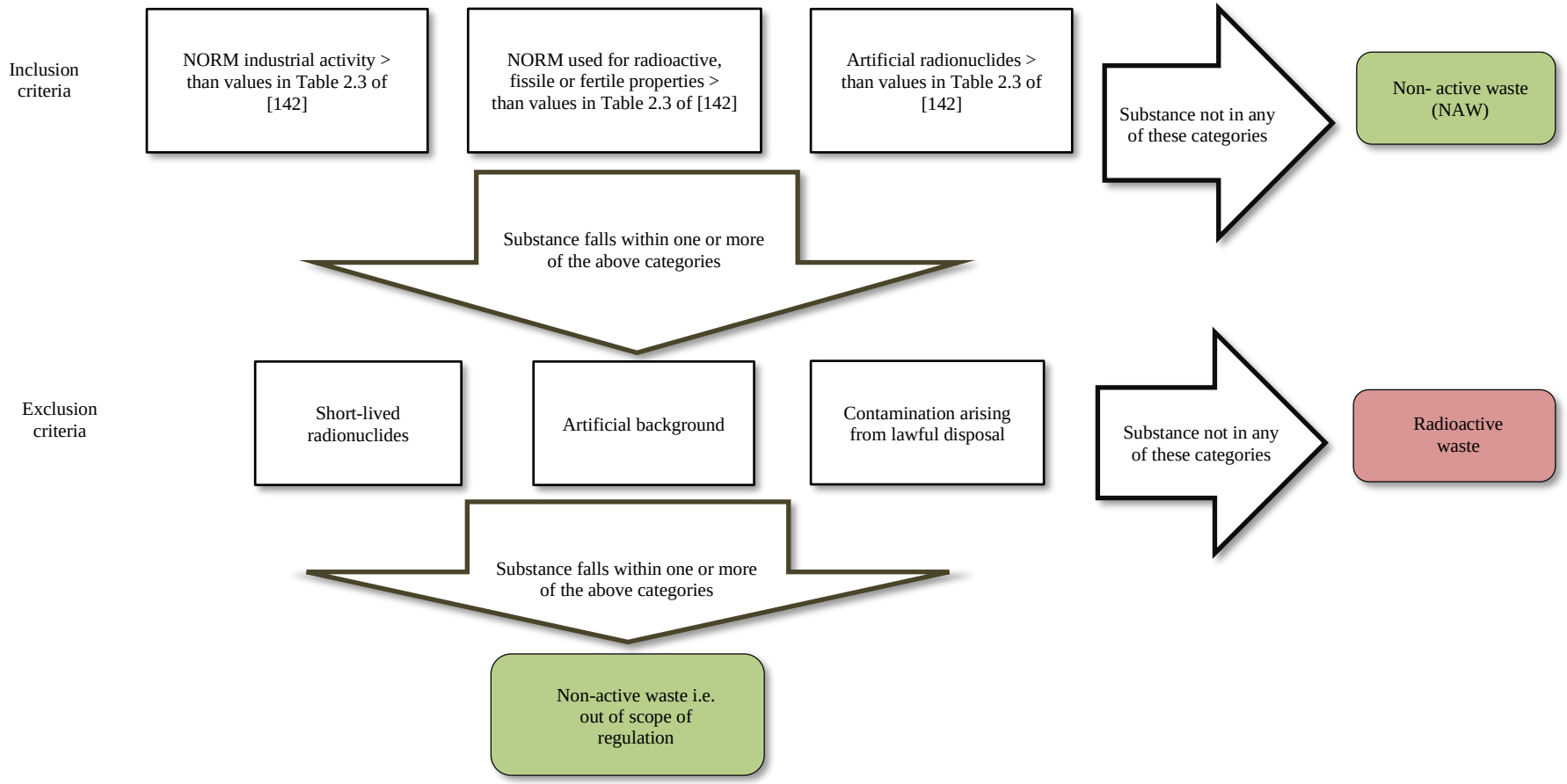

Figure 5.1 - Schematic presentation of the scope of the UK legislation regarding cleared materials. Reproduced with permission (Figure 2.1 [142]) licensed under the Open Government Licence v3.0. Note: Naturally Occurring Radioactive Materials (NORM).

In 2007 a study was launched to assess and evaluate differences in the clearance and exempt values[9], and the underlying scenarios, in RP-122 and RS-G-1.7 along with the consequence of using one set of values for exemption and clearance. This work was awarded under contract to BRENK Systemplanung and the assessment published in (RP-157) [155]. Following from the 2007 study, an updated BSSD was published (2013/59/EURATOM) [156].

5.4.3 Tritium contamination

Most waste within the fusion reactor will be tritiated to some degree, requiring a specific management strategy. For ITER, the strategy includes an interim storage phase allowing for tritium, with a half-life of ~12.5 years, to decay. Alternative and complementary options for reducing tritium content within the waste are also being considered for ITER and beyond to DEMO and fusion power plants.

If the tritium content can be reduced then the waste could potentially be downgraded to a lower waste class with wider options for disposal. Reducing tritium content will also decrease the interim storage period required for the decay of tritium and potentially deplete the amount of tritium out-gassing from waste. Detritiation processes, however, produce secondary tritiated waste (most commonly tritiated water) that will also require management. Detritiation methods need to be adapted to the type and size of the waste.

Several detritiation process have been studied under the European fusion development agreement, for example [157], [158], with a focus on thermal treatment and melting for metallic parts and thermal treatment and full combustion for ‘soft’ housekeeping wastes (such as gloves, paper, clothes etc.). Methods only offering superficial detritiation, such as leaching, abrasion, electrochemical polishing and laser treatment, are shown to be unsuitable as the majority of tritiated waste will be ‘bulk material’ and the these methods can potentially create large amounts of tritiated water.

[9] Exemption applies to sources and practices at the stage when they are being considered for regulatory control, whereas clearance is applied to materials that are already under regulatory control but, because of decay or processing, they now present a negligible risk and can be released from regulatory control.

5.5 Considerations for DEMO

ITER is expected to have 14 MeV neutron fluence on the first wall of about 0.3 MWyr/m^2 over a 12 year operation [149]. In comparison, DEMO reactors are expected to accumulate 1 to 2 orders of magnitude more fluence in only a few years before in-vessel components will require removal.

Studies in 2007 on the DEMO power plant concept model 'AB'[10] show that after 100 years the total fraction of cleared material is ~13 % of the 124 kt of radioactive waste. The 2007 study used the IAEA clearance levels as published in RS-G-1.7 [143] which showed a decrease in the amount of cleared material in comparison to earlier work using the BSSD-1996 levels [141]. Studies [159] on a dual-coolant lithium-lead DEMO model (based on the power plant conceptual study model C) with regards to Spanish regulations, using MCNPx and the ACAB code, showed that radioactive waste from all components, after a 40 year operational life, could be classed as LLW and ILW before 100 years after shutdown. Consideration is given to the storage and disposal options in the context of Spain.

It is shown in 2011 studies [68] on a EU helium-cooled lithium-lead (HCLL) DEMO concept that even after a significant cooling period there is no cleared materials from the inner components of the fusion reactor (i.e. the blanket/divertor), based on German regulations which are similar to IAEA guidance. According to a radioactive waste assessment [160] on the Russian DEMO-S model, assuming a 10 MWyr/m^2 first wall neutron fluence, after 30 years cooling time, approximately 60 % of the total mass of reactor materials could be hands-on recycled, 25 % could be hands-on recycled after 100 years, and the remaining 15 % of reactor materials require disposal.

The radioactive waste issues discussed, and the experience gained from ITER, will play an important role for DEMO and future fusion power plants. In order to meet ambitious goals set within the European fusion framework for a DEMO fusion power plant, further research and development is required into the use of low/reduced activation materials, the design of fusion power plants and the operational actions, with an aim to reduce tritiated wastes and longer lived radioactive nuclides so that the

[10] The power plant conceptual study models are developed by the EU under the European fusion development agreement. As part of the study 5 models are considered: A, B, AB, C, and D. [32], [188]

majority of radioactive waste resulting from the operation of a fusion power reactor will be either recyclable or comprise of low and very low level wastes 100 years after shutdown.

The discussed studies also show that considering the waste inventory for components separately and assessing the material effects on resulting activation is an important factor in the development of a fusion DEMO that meets European goals.

5.6 Radioactive waste assessment of EU DEMO

The IAEA safety standards [143] were used to formulate a set of 'general classes' for fusion, as the allowable limits of a specific disposal facility are not defined here. Radionuclide specific activation concentration levels in becquerels per gram (Bq/g) presented in the UK Government guidance on the scope of and exemptions from the radioactive substances legislation [142], which originate from RP-122, were used in this work.

Within the IAEA guidelines, any material that does not meet the clearance level requirements is classed as either LLW or ILW. LLW is radioactive material that is above the clearance levels but with limited amounts of long-lived radionuclides. For this EU DEMO studies this waste class is defined by the total activity concentration which must be less than 12 GBq/tonne. All other radioactive material is classed as ILW i.e. all material with activity levels above 12 GBq/tonne. Although this type of waste requires a greater degree of containment and isolation than that provided by the near surface disposal routes available to LLW, it requires no or little provision for long-term heat removal.

Material recycling after the reactor is dismantled and reuse of components is preferred due to a more economic use of materials and reduced quantities of radioactive waste for disposal. The criteria for recycling vary by country [161] and in some studies arbitrary recycling limits are used; realistic criteria for recycling need to be established based on viable processes. In this study recyclable materials (RM) were identified separately to the activated waste class. Both materials classed as LLW and ILW were assessed for possible recycling based on a contact dose rate limit of 2 mSv/hr as adopted in similar studies for 'simple recycling' materials [161], [162], as opposed to 'complex recycling' materials which works to a 20 mSv/hr contact dose rate limit. These were identified as either LLW-RM or ILW-RM.

In this work, 3-D neutron transport was performed on the EU 2015 Generic DEMO model [40], [163] and used in inventory calculations to determine the radioactive waste quantities resulting from the neutron irradiation and variations with time. Methods for calculating the activation inventory were compared with a focus on the possible advantages of considering the radioactive waste of a reactor not only by component but also through further dismantling.

5.7 DEMO model and materials

The EU generic DEMO 2015 model was used to compare the neutronic response and radioactive waste inventory calculated using an unstructured mesh method against the conventional CSG definition with cell based and superimposed mesh methods. This DEMO model has been supplied as the CAD model [40] and as an MCNP input deck [163].

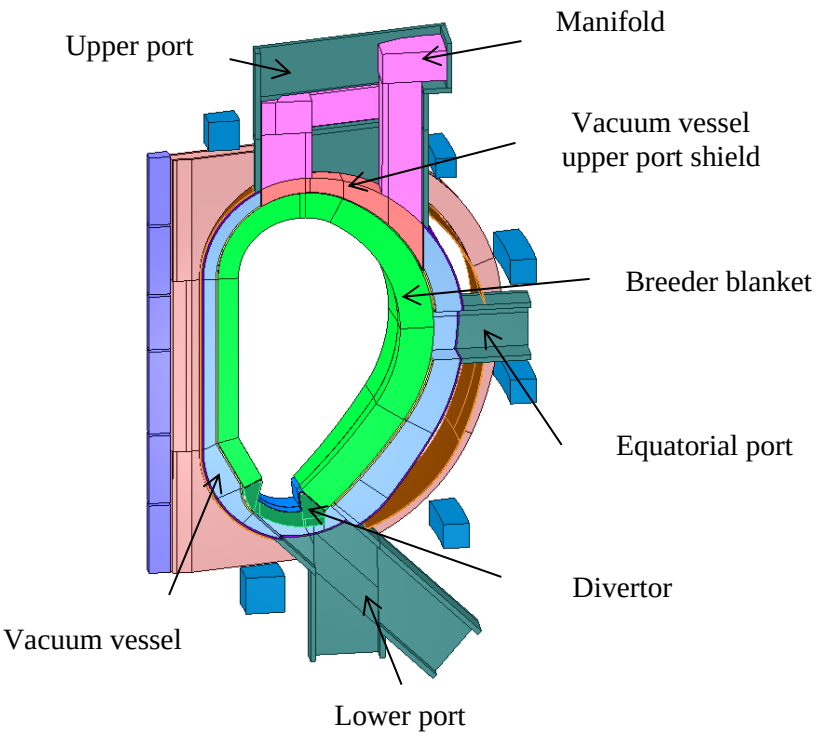

Figure 5.2 - A 3-D CAD image of the 10° sector EU Generic DEMO model [40].

The DEMO 2015 CAD model is a 10° sector, shown in Figure 5.2, consisting primarily of a breeding blanket, vacuum vessel, ports, toroidal and poloidal field coils, and divertor (see Table 5.4 for material composition). The main components are labelled in Figure 5.2, a 3-D image of the CAD model. The magnets, and related casing and shielding, are labelled in Figure 5.3, a 2-D slice through the model along the toroidal field coil. The DEMO model can be used to simulate a full 360º tokamak in MCNP with reflecting boundary planes in the input deck which assumes symmetry around the full tokamak.

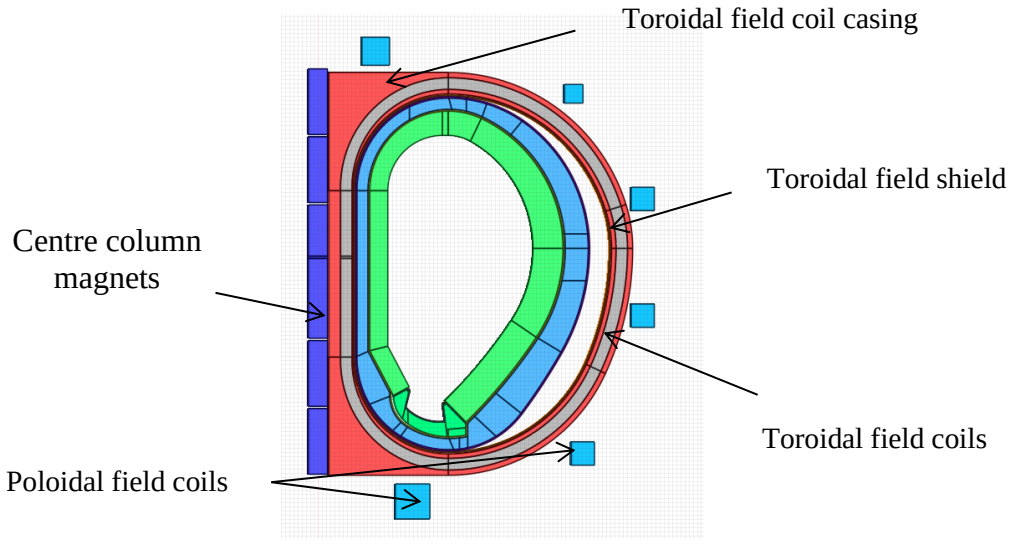

Figure 5.3 - A vertical elevation view through the toroidal field coils.

The breeder blanket in the DEMO 2015 was provided empty and therefore filled with a homogenised helium cooled pebble bed blanket concept comprising steel structure, beryllium multiplier and Li_4SiO_4 breeder. See Section 4 for further information on breeder blanket materials. The steel structures of the ports are modelled as ITER grade stainless steel (SS316L(N)-IG), with a mix of steel and water used in the upper port shield and manifold.

The vacuum vessel is also modelled as a mix of steel and water in a steel casing. The divertor, shown in closer detail in Figure 5.4, consists of a tungsten first wall followed by a layer of homogenised steel & water and a second layer of tungsten. The largest volume of the divertor (shown in green) is modelled as EUROFER steel. The toroidal field coils, poloidal field coils and centre column magnets are modelled as a

homogeneous mix of niobium-tin (Nb_3Sn) conductor with steel. A steel casing surrounds the toroidal field coils.

Table 5.4 - Summary of materials used with the EU DEMO 2015 model (see Table 7.9 - Table 7.11 of Appendix 4 for isotopic composition).

Part/component	Main material composition
Blanket	23% steel (EUROFER) + 21.02% beryllium + 10.2% Li_4SiO_4 (Li_4SiO_4) + 45.78% void
Ports	100% steel (SS316L(N)-IG)
Upper port shield	77% steel (SS316L(N)-IG) + 23% water
Manifold	77% steel (SS316L(N)-IG) + 23% water
Vacuum vessel	
Layer 1	100% steel (SS316L(N)-IG)
Layer 2	77% steel (SS316L(N)-IG) + 23% water
Layer 3	100% steel (SS316L(N)-IG)
Divertor	
Layer 1	100% tungsten
Layer 2	77% steel (SS316L(N)-IG) + 23% water + void
Layer 3	100% tungsten
Layer 4	100% EUROFER
Magnets (centre column, toroidal and poloidal field coils)	% niobium-tin (Nb_3Sn) + % steel (SS316L(N)-IG)
Toroidal field coil casing	100% steel (SS316L(N)-IG)
Toroidal field coil shield	100% steel (SS316L(N)-IG)

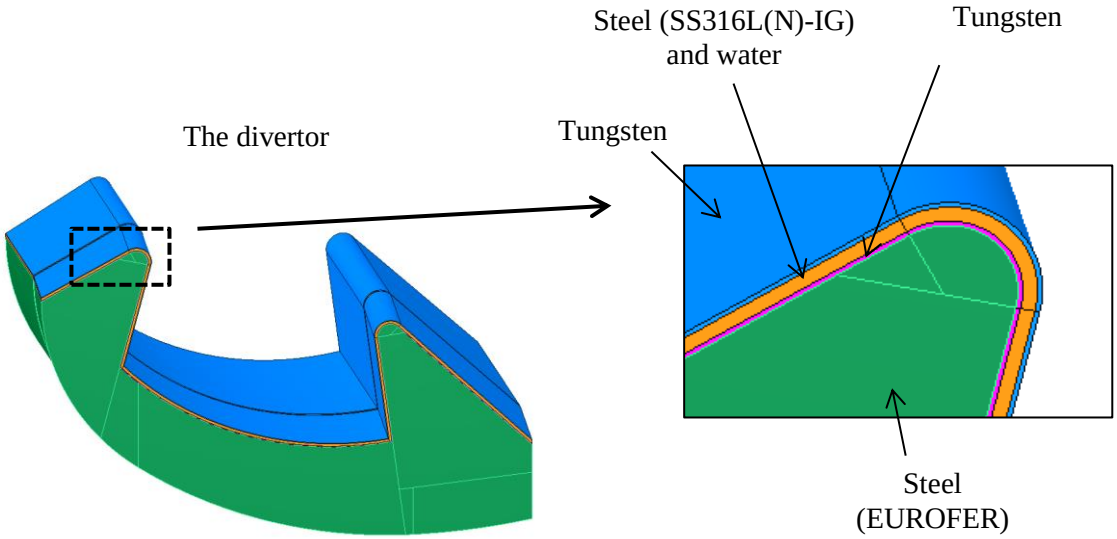

Figure 5.4 - The divertor model and close-up of the material layers.

The use of MCNP for particle transport calculations has historically required the CAD model to be converted into CSG form, a timely and often troublesome process. The MCNP input deck was provided which had been created via the conversion of the CAD for the generic DEMO model to MCNP with McCad [164].

The latest version of MCNP (version 6 [96]) now includes a capability for which the geometry of a model can be represented using an unstructured mesh in Abaqus® [165] form. As well as removing the CSG conversion process, the unstructured mesh representation has other potential benefits. As the mesh is not confined to a structured shape, either rectangular or cylindrical, the mesh conforms to the geometry shape i.e. the mesh voxels contain only one material, removing the effects of material mixing of different components and void mixing. This allows for streaming gaps to be modelled more effectively, and this is particularly important for shutdown dose rate analysis [166].

To create the Abaqus® mesh file for the volumetric unstructured mesh input the ANSYS® [167] workbench package was used. The CAD model was prepared for meshing in the SpaceClaim module [168] of ANSYS® and then imported into the mechanical modeller of ANSYS® for meshing. Curvature and size refinement was used when creating the mesh (see Table 5.5), creating a mesh with 112305 elements. Dummy materials were assigned to each component so that not only could the correct materials be assigned to the associated pseudo cells but also for identification of components for tallying.

Table 5.5 - Refinement parameters used for unstructured mesh.

Refinement	Value
Curvature	5 degrees
Max face size	15 cm
Max size	15 cm

The unstructured mesh is shown in Figure 5.5 with a closer view of the divertor. This shows the use of the curvature refinement for efficient mesh element production. In regions where refinement is not needed, larger elements can be seen. This helps to reduce the overall size of the mesh whilst ensuring adequate resolution in areas of particular significance or curvature or small detail.

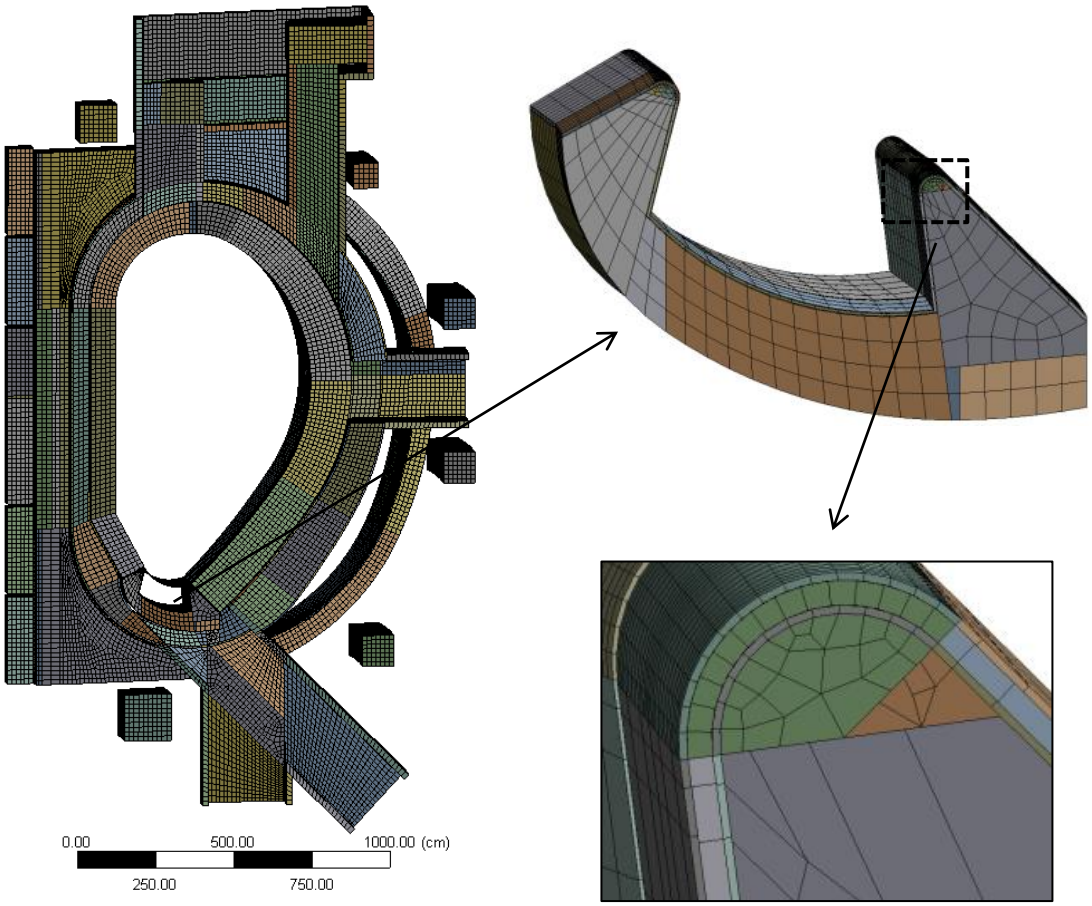

Figure 5.5 - A 3-D image of the unstructured mesh with a closer view on the divertor region as an example of the curvature refinement. (Image produced in the mechanical modeller of ANSYS®.)

5.8 Neutronics analysis

In order to compute the radioactive waste inventory, neutron flux is determined through a transport calculation with MCNP6 and subsequently used for irradiation in an activation calculation with FISPACT. (See Section 3.2 for a more detailed explanation of MCNP and FISPACT.) A number of methods for computing the waste inventory were considered; methods 1, 2 and 3. These methods differ mainly in the geometry and MCNP tallying, and are described in further detail later in this section.

5.8.1 Simulation codes, nuclear data and irradiation/decay scenario

Neutron transport calculations were carried out using MCNP6v1 with FENDL2.1 [103] neutron cross-section data and where this was unavailable, ENDF-B-VII [169]. This neutron flux, tallied in the 175 VITAMIN-J energy group structure, was then used to irradiate the materials comprising the various components of the EU DEMO

2015 model using FISPACT-II (release 2.20 and release 3.00) [76] with the EAF-2010 activation data [109]. The simulation codes, nuclear data and irradiation/decay scenario were common in all methods.

A number of variance reduction techniques are available to use with MCNP in an attempt to achieve neutron flux results with sufficiently low variance within an acceptable time frame. In this work, global variance reduction (GVR) was implemented through use of the recently released Automated Variance Reduction Generator (ADVANTG) code developed by Oak Ridge National Laboratory [111]. Using ADVANTG a neutron weight window was generated along with additional source biasing [112]. Further detail regarding the variance reduction and uncertainties is given in Appendix 7.

An irradiation scenario based on the operational scheme previously specified for DEMO [39] was used. This scheme includes operation for 20 calendar years at an average availability of 30 %. This results in a total DEMO plant lifetime of 6 FPY. Two operation phases (see Table 5.6) are assumed; the first phase covers 5.2 calendar years reaching 1.57 FPY and the second phase will last 14.8 calendar years (4.43 FPY). A 1-year shutdown time is included between the phases. It is assumed that the first phase will include a so-called starter blanket with a maximum displacement damage accumulation of 20 dpa in the steel of the first wall, replaced with another blanket for phase 2 which can withstand at least 50 dpa. The divertor is also assumed to be replaced 3 times, with 1 divertor for the first phase and 3 in the second. The replacement in the second phase is assumed to be at every 4.92 calendar years with 8 month down time for each replacement.

Table 5.6 - Summary of the irradiation scenario used with FISPACT.

Irradiation phase	Summary of operation
Phase 1	Continuous operation over 5.2 calendar years minus 10 days, at 30 % of the nominal fusion power. Followed by 10 days pulsed operation with 48 full power 4 hour pulses with 1 hour dwell time between each.
Phase 2	Operation over 4.92 calendar years minus 10 days, at 30 % of the nominal fusion power, followed by 10 days pulsed operation with 48 full power 4 hour pulses with 1 hour dwell time between each. Repeated 3 times.

To include the waste from all components, including the removed blanket and divertors, different irradiation scenarios were used for each of those components i.e. a different irradiation file for blanket 1 (B1), blanket 2 (B2), divertor 1 (D1), divertor 2 (D2), divertor 3 (D3) and divertor 4 (D4). The irradiation scenarios for each of the replaced components B 1-2, and D 1-4, include the remaining operation but with flux set to zero when the component is removed from the reactor. This ensures that all components can be totalled at time 't' after shutdown, whilst still taking into account any decay of the components once removed from the reactor.

To investigate the variation of waste inventory with time, 26 cooling times/decay intervals were used, with the inventory determined at each time step shown in Table 5.7, ranging from a few hours to 1000 years.

Table 5.7 - The cooling times (decay intervals) used with FISPACT to record inventory/activation/contact dose etc.

Decay intervals in FISPACT input	Cumulative time
TIME 1 SECS ATOMS	1 second
TIME 299 SECS ATOMS	5 mins
TIME 1500 SECS ATOMS	30 mins
TIME 1800 SECS ATOMS	1 hour
TIME 7200 SECS ATOMS	3 hours
TIME 7200 SECS ATOMS	5 hours
TIME 18000 SECS ATOMS	10 hours
TIME 50400 SECS ATOMS	1 day
TIME 172800 SECS ATOMS	3 days
TIME 345600 SECS ATOMS	1 weeks
TIME 604800 SECS ATOMS	2 weeks
TIME 1209600 SECS ATOMS	4 weeks
TIME 2419200 SECS ATOMS	8 weeks
TIME 10940054 SECS ATOMS	6 months
TIME 15778454 SECS ATOMS	1 year
TIME 284012179 SECS ATOMS	10 years
TIME 2840121792 SECS ATOMS	100 years
TIME 28401217920 SECS ATOMS	1000 years

5.8.2 Method 1- Cell based

Using the CSG model of DEMO, the neutron flux was tallied in each cell using the F4 volume average tally. As can be seen in Figure 5.2 many of the components in the CSG model are made up of more than 1 cell. This geometry splitting was already present in the model and no further splitting has been implemented. Splitting the geometry can be used to reduce flux averaging over large volumes.

Table 5.8 - Waste classes used with automated cell-based script [170] and FISPACT-II.

DEMO- IAEA [143], [170]	
NAW	Clearance level < 1
LLW	beta + gamma < 12GBq/t alpha < 4GBq/t
Fraction of LLW possibly available for recycling (LLW-RM)	< 2mSv/hr (contact dose)
ILW	beta + gamma > 12GBq/t alpha > 4GBq/t
Fraction of ILW possibly available for recycling(ILW-RM)	< 2mSv/hr (contact dose)

A script [170] was used to perform an activation calculation using FISPACT-II for each of the 150+ cells and determine the radioactive waste levels based on the criteria shown in Table 5.8. Only material with a clearance level greater than one is considered for radioactive waste classification. The clearance index is provided in the output file from FISPACT-II.

5.8.3 Method 2- Structured rectangular mesh

The neutron flux was recorded/tallied in each voxel of a 3-D structured rectangular mesh, superimposed over the CSG model. The nature of the structured rectangular mesh results in many mesh voxels that do not cover the sector model. For each voxel the flux in 175 energy groups was tallied, requiring approximately 80 bytes of memory per voxel. Voxels that do not cover the geometry are an inefficient use of memory. Due to memory limitations, and to reduce the inefficiencies of the mesh coverage, 3 separate mesh tallies were used (see Figure 5.6) in order to achieve a 9 cm resolution. A second calculation with a 15 cm resolution mesh tally was also performed (Figure 5.7).

To compute the mass of material designated as radioactive waste and the corresponding waste class for each voxel, a development of the CCFE MCR2S code [79] was used. MCR2S was originally designed for shutdown dose rate calculations, implementing the rigorous-2-step method [80]. The code takes the neutron spectra for each voxel of a 3-D mesh and performs an activation calculation for each using FISPACT-II with the EAF-2010 nuclear data. In the case of a structured mesh, a materials mixing step takes place within MCR2S, when the mesh voxel covers more than one material and or a void region. The information regarding the materials within each voxel is provided to MCR2S through a POSMAT file, this lists each voxel and the fraction of each material in the voxel. In order to irradiate components separately, as is required for the blankets and divertors due to the difference irradiation schedules, the materials file provided is altered setting any materials that are not part of the component to void.

Within MCR2S, a FISPACT calculation is performed for each voxel for each of the meshes, using each of the component specific materials files and irradiation scenarios. With large meshes this can require many calculations. In the case of the 15cm mesh which was contained in a single mesh file, the process of inventory calculations was much quicker.

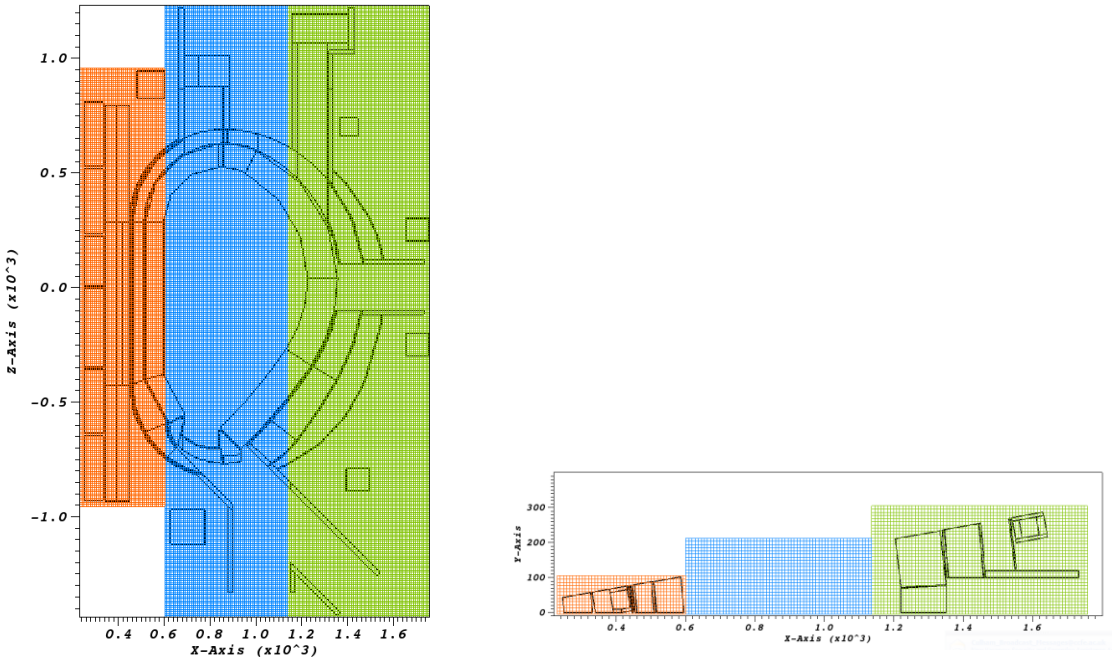

Figure 5.6 - Three 9 cm resolution superimposed structured meshes; vertical elevation at Y = 5 cm (left) and plan view at Z = 0 cm (right). (Scale in cm)

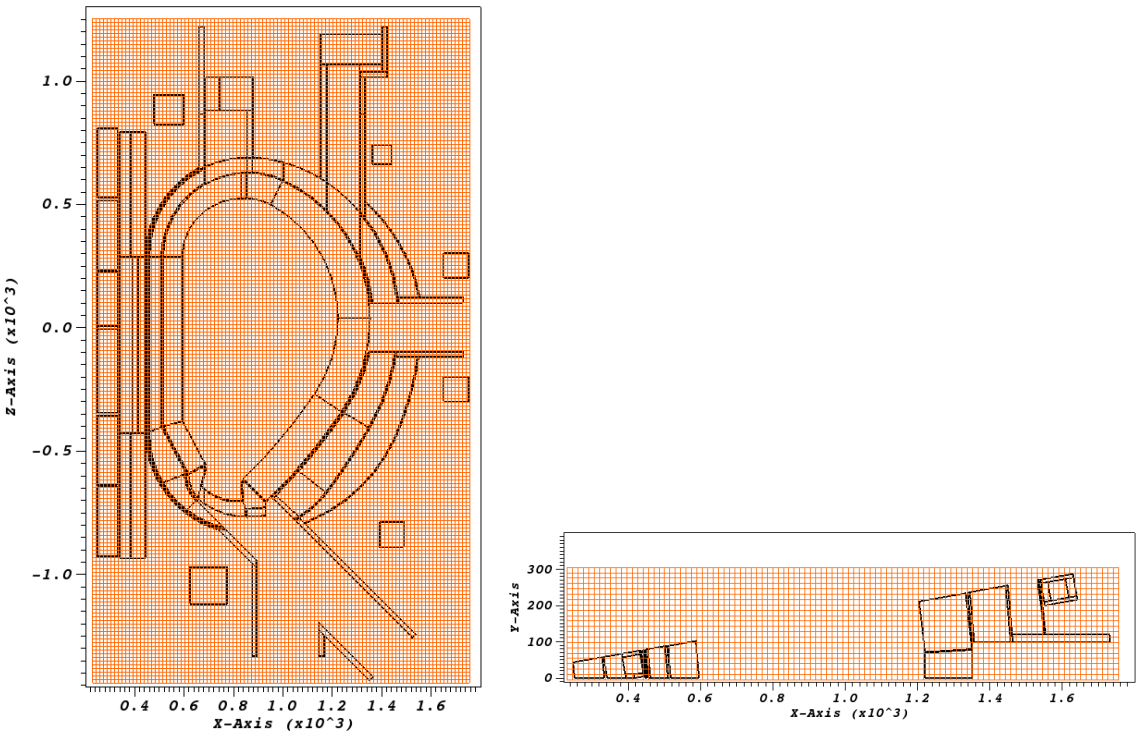

Figure 5.7 - A 15 cm resolution superimposed structured mesh; vertical elevation at Y = 5 cm (left) and plan view at Z = 0 cm (right). (Scale in cm)

5.8.3.1 Using the MCR2S Nuclear Radioactive Waste module

A module within the MCR2S code was developed for calculating the mass of radioactive waste materials specific to the JET facility in the UK. The classes as defined in the Office of Nuclear Regulations (ONR) guide 'Disposal of Radioactive Waste' [145] have been used (see Table 5.9). This has been implemented by considering the classes from ILW to out of scope, i.e. the activity levels of each voxel of material within the mesh has been compared against the ILW level first, then if the activity is not greater than the lower bound of the ILW, it is compared against the LLW level. If the activity is within the LLW criteria then the concentrations of radioactive nuclides are compared against the clearance limits to determine whether the LLW can actually be cleared from regulatory control. Where the activation of the material within the voxel is less than the lower bound of the LLW, the radionuclides are compared against the clearance limits; if these are not met the material is classified as LLW.

This method should be reversed, with the radionuclide concentrations assessed first to determine whether the material can be cleared from regulatory control. If the material

is not cleared, i.e. the radionuclide specific limits are not met, the material is classed as radioactive waste. The activity of the radioactive waste material is compared against the LLW criteria, and if this is not met, it is classed as ILW. There is no explicit recyclable material assessment made in the current MCR2S waste assessment calculations; the fractions of ILW and LLW which are deemed recyclable material are not considered.

5.8.3.2 Modification to MCR2S

In order to implement an alternative IAEA waste classification (see Table 5.9) for DEMO studies, a modification to MCR2S was required. A copy of the nuclear waste module was made, called 'Nuclear_Waste_IAEA.mod', which can be called using '-a' in the command arguments. This new module was restructured to consider the clearance level first. Once the material is determined to be classed as radioactive waste, the activation is then compared to the limits for LLW and ILW. The mass of material categorised as LLW and ILW is further considered for its recyclable potential, comparing the total contact dose, as calculated in FISPACT, against a 2 mSv/hr limit. The modification to MCR2S was tested using simple cases and the vacuum vessel of the DEMO 2013 model [171], [172].

Table 5.9 - Comparison of UK and IAEA waste classes as implemented in MCR2S.

JET- UK		**DEMO- IAEA**	
Out of scope	Clearance level <1	NAW	Clearance level <1
LLW	4GBq/t > alpha > 4 MBq/t 12GBq/t > beta > 12MBq/t	LLW	< 12GBq/t
		Fraction of LLW possibly available for recycling (LLW-RM)	< 2mSv/hr (contact dose)
ILW	alpha > 4 GBq/t OR beta + gamma > 12 GBq/t	ILW	> 12GBq/t
		Fraction of ILW possibly available for recycling (ILW-RM)	< 2mSv/hr (contact dose)

5.8.4 Method 3- Unstructured mesh

The use of an unstructured mesh geometry with MCNP has not only advantages associated with model creation (as discussed in Section 5.7) but also enables the neutron flux to be tallied directly on to the same mesh. The neutron flux is recorded in all elements comprising the mesh used to describe the geometry, therefore conforming to the geometry exactly as used in the simulation.

The modified MCR2S module was used with the neutron flux tallied on the unstructured mesh, which MCNP outputs in an 'eeout' file. As the neutron flux was contained within 1 file, as opposed to the 3 mesh files required for the 9 cm structured mesh, fewer MCR2S calculations were required. As with method 2, used for the structured mesh, different material files provided to MCR2S allow for calculations to be performed for each component. This enables only specific components to be irradiated and provides the resulting activation and inventory information for the individual component, which in turn is used to determine the component-specific waste class.

Unlike the cell based method, the results for waste inventory can also be considered on an element-by-element basis. For example a component-specific analysis will lead to the whole component being classed as the same waste type; in some larger components it may be possibly that some of the component is in fact recyclable. Unlike in the structured mesh where the waste is considered in structured voxels, requiring materials mixing where there are 2 or more materials, and or where the voxel covers more than 1 component, unstructured mesh elements conform to the geometry of the components and so only ever contain 1 material and form part of 1 component.

Difficulties in using a weight window with the unstructured mesh model meant that GVR was not used for the neutron transport calculation. The lack of GVR resulted in a higher number of particle histories necessary to adequately sample the problem and to obtain reasonable statistical uncertainty. Some variance reduction through the use of the biased source, as produced using the ADVANTG code, was used.

5.8.5 Points for comparison

To aid comparison, some points have been identified and can be seen in Figure 5.8, with point coordinates in Table 5.10. These points have been used for neutron flux

comparisons and as locations for investigating dominant nuclides within the activation and inventory calculations with MCR2S. As MCR2S computes the inventory for every irradiation and decay step for every voxel in the mesh(s), for each irradiation schedule and component combination, there are a large number of output files; these were continually deleted automatically as MCR2S completed each voxel. The use of a keyword 'points_file' specified in the MCR2S input saves the input and output files for the voxel covering the points provided in the list.

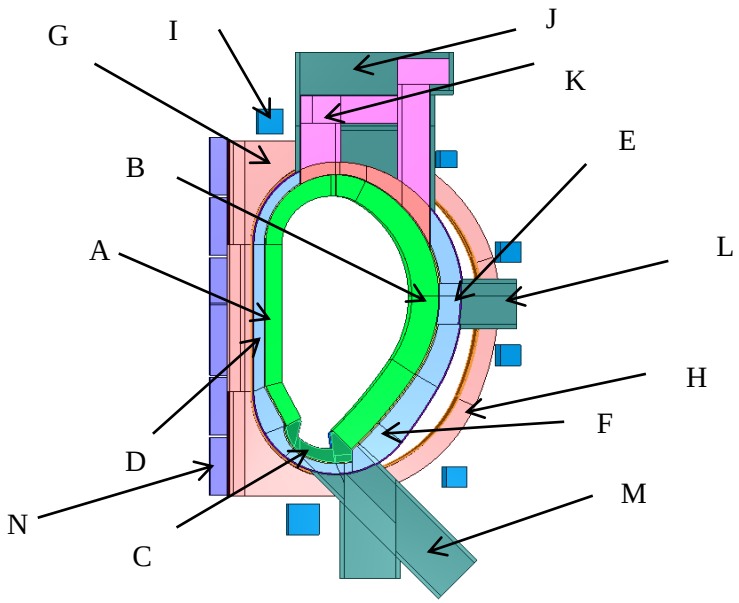

Figure 5.8 - Location of some reference points used for comparison of neutron flux and extracting full activation data from FISPACT including input/output files. Point coordinates given in Table 5.10.

Table 5.10 - Coordinates (cm) of points shown in Figure 5.8.

Point				Point			
	x	y	z		x	y	z
A	550	55	0	H	1440	220	-550
B	1280	55	-30	I	535	40	880
C	755	55	-715	J	1030	125	1130
D	470	40	0	K	818	30	940
E	1400	180	0	L	1600	110	0
F	1060	40	-670	M	1300	75	-1200
G	535	55	600	N	285	21	-815

5.9 Neutron flux results and observations

The neutron flux results are presented in neutron flux maps plotted at Y = 5 cm, for method 2 using the superimposed rectangular structured meshes, 9 cm resolution (Figure 5.9) and 15 cm resolution (Figure 5.10) and for method 3 using the unstructured mesh, (Figure 5.11). A comparison of the neutron flux at a number of specified points is presented in Table 5.11 along with a comparison of the relative statistical uncertainties in Table 5.12.

It can be seen in Figure 5.9 and Figure 5.10 that the statistical uncertainty for the results produced using method 2 is below 5% in the majority of the mesh voxels. In deep shield areas, such as along the manifold in the upper port and the outer vacuum vessel, the uncertainty increases slightly. In some of the poloidal field coils and centre column magnets uncertainties increase to 25 - 50 %, though these areas are less likely to have a significant impact on the radioactive waste inventory calculations due to shielding provided by the blanket.

The shielding effect of the blanket can be seen in the left-hand image of Figure 5.9 and Figure 5.10, with the flux decreasing by approximately an order of magnitude through the inboard blanket and by over 2 orders of magnitude in the outboard blanket. The lack of shielding in the equatorial port leads to higher fluxes in the vacuum vessel round this region. There is also significant neutron flux in the lower port behind the divertor.

For method 3, as already mentioned, a weight window was not use; this is evident in the lack of neutron flux in areas behind the blanket, in particular the poloidal field coils, centre column magnets, manifold and some areas of the vacuum vessel. Due to memory limitations the statistical uncertainty information for the unstructured mesh neutron transport calculation was not stored. In order to give some visualisation of the statistical uncertainty, a superimposed structured mesh of 15 cm resolution was also used (presented alongside the unstructured neutron flux results in Figure 5.11). It should be noted that the uncertainties shown have been determined on 15 x 15 x15 cm voxels, averaging over the voxel and materials. This is not the uncertainty as determined in each element of the unstructured mesh.

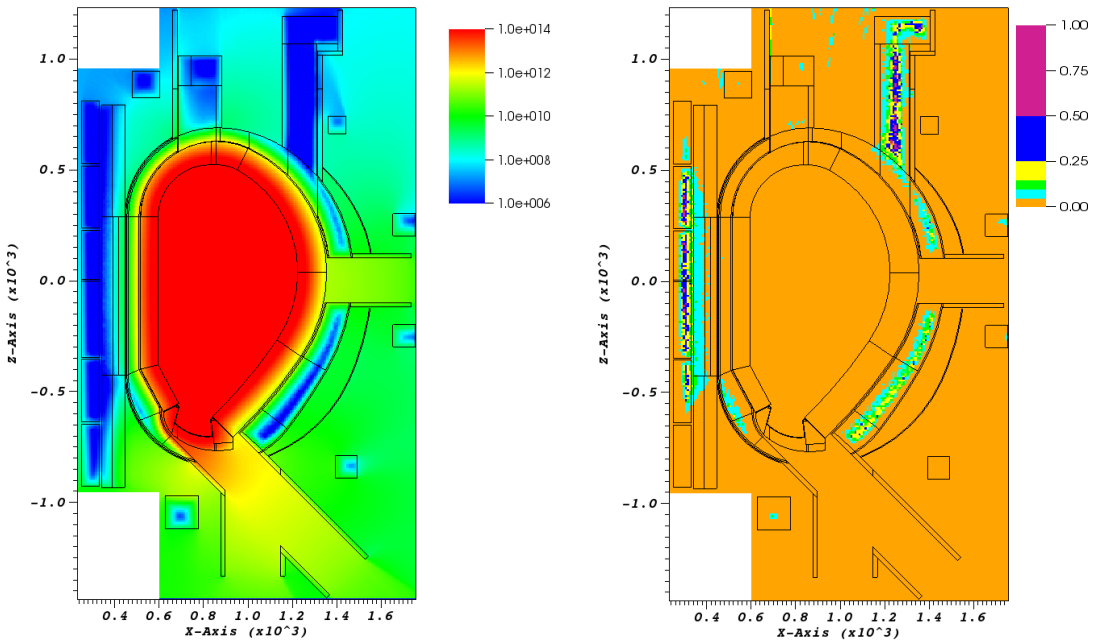

Figure 5.9 - Neutron flux map (neutron flux neutrons/s/cm^2) using method 2 with a 9 cm resolution (left) and relative statistical uncertainty map (right). (Scale in cm)

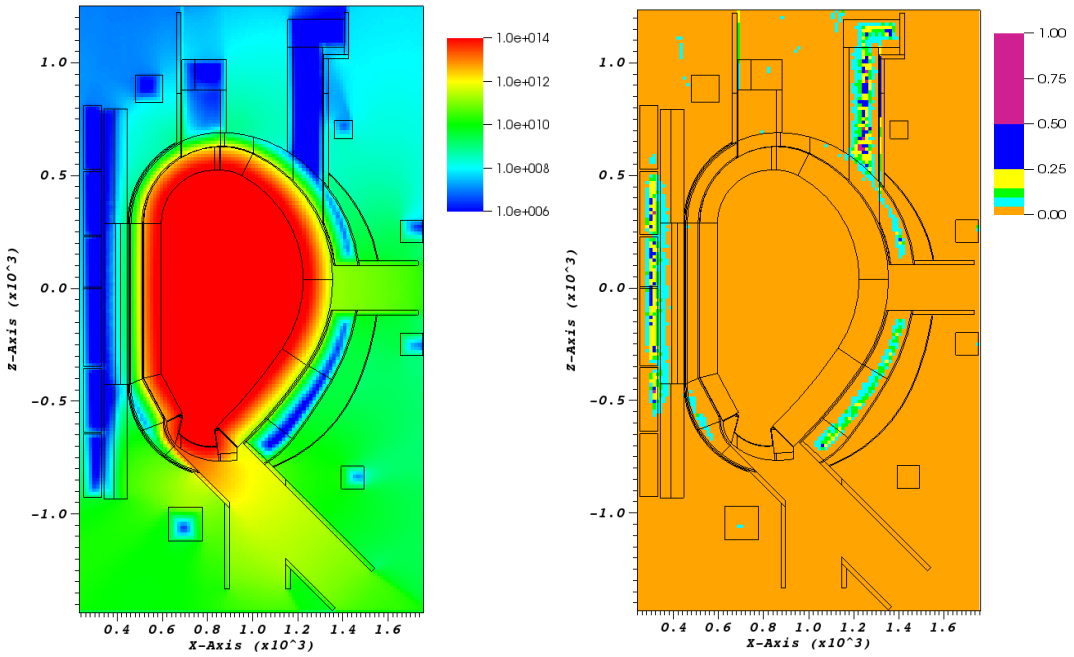

Figure 5.10 - Neutron flux map (neutron flux neutrons/s/cm^2) using method 2 with a 15 cm resolution (left) and relative statistical uncertainty map (right). (Scale in cm)

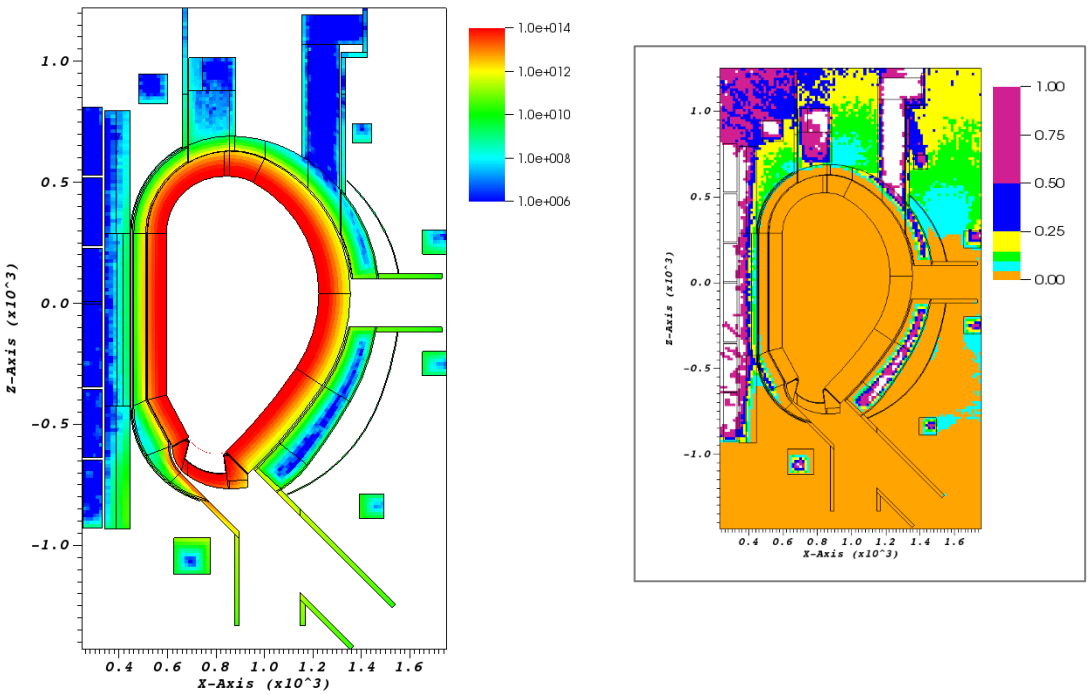

Figure 5.11 - Neutron flux map (neutron flux neutrons/s/cm^2) using method 3 the unstructured mesh (left). A relative statistical uncertainty map on a superimposed 15 cm structured mesh is shown on the right. (Scale in cm)

Table 5.11 - Comparison of the neutron flux at points A-N (as shown in Figure 5.8).

Point location				Neutron flux (n/cm^2/s)			
				Flux in cell	Flux in voxel		
	x	y	z	Method 1	Method 2 9 cm	Method 2 15 cm	Method 3
A	550	55	0	1.10E+14	8.24E+13	9.12E+13	8.45E+13
B	1280	55	-30	7.18E+13	2.45E+13	2.42E+13	2.33E+13
C	755	55	-715	1.04E+14	1.42E+14	1.55E+14	1.37E+14
D	470	40	0	8.14E+11	3.43E+10	1.43E+11	2.15E+10
E	1400	180	0	2.46E+10	9.93E+07	7.36E+07	1.21E+08
F	1060	40	-670	1.08E+10	5.30E+07	7.41E+07	7.46E+07
G	535	55	600	1.81E+08	1.06E+08	1.30E+08	1.35E+08
H	1440	220	-550	6.44E+09	7.47E+07	7.27E+07	6.39E+07
I	535	40	880	1.97E+07	3.31E+05	2.20E+05	2.47E+07
J	1030	125	1130	3.48E+07	4.01E+07	6.93E+07	2.90E+07
K	818	30	940	1.02E+08	7.74E+05	6.39E+05	
L	1600	110	0	3.48E+10	3.47E+10	5.15E+10	3.47E+10
M	1300	75	-1200	8.13E+10	7.62E+10	6.43E+10	7.24E+10
N	285	21	-815	2.10E+08	5.36E+06	1.79E+07	

Table 5.12 - Comparison of statistical uncertainty at points A-N (as shown in Figure 5.8).

Point location				Relative Statistical Uncertainty			
				In cell	In voxel		
	x	y	z	Method 1	Method 2 9 cm	Method 2 15 cm	Method 3
A	550	55	0	0.010%	0.139%	0.086%	0.028%
B	1280	55	-30	0.010%	0.097%	0.060%	0.055%
C	755	55	-715	0.020%	0.037%	0.030%	0.024%
D	470	40	0	0.060%	3.167%	1.005%	0.647%
E	1400	180	0	0.160%	8.860%	9.308%	26.455%
F	1060	40	-670	0.200%	5.162%	4.185%	30.275%
G	535	55	600	0.420%	4.213%	2.257%	35.527%
H	1440	220	-550	0.060%	1.051%	0.722%	39.026%
I	535	40	880	0.610%	3.991%	2.257%	100.000%
J	1030	125	1130	0.680%	0.259%	0.616%	40.193%
K	818	30	940	4.450%	1.517%	1.582%	
L	1600	110	0	0.160%	0.127%	0.252%	1.445%
M	1300	75	-1200	0.040%	0.043%	0.032%	1.325%
N	285	21	-815	0.090%	1.028%	0.536%	

5.10 Radioactive waste results and observations

The radioactive waste inventory was calculated using each of the three methods mentioned previously. The results have been presented for some separate components and an estimation of the total waste. As shown in the neutron flux results for method 4, Figure 5.11 with the unstructured mesh, there are some areas of zero neutron flux. Elements with zero neutron flux are not irradiated in the activation calculation and this is observed in the total waste results as an apparent overall loss of mass (Table 5.13). The difficulty in adequate sampling of the full phase-space of the model with an unstructured mesh approach is evident in the mass difference.

Table 5.13 - Mass of each component (kilotonne, kt).

	Actual mass	Mass irradiated			
		Cell	Structured 9 cm	Structured 15 cm	Unstructured
Blankets	8.8	8.8	8.8	8.8	8.8
Vacuum Vessel	13.3	13.3	13.3	13.3	13.0
Divertor	3.9	3.9	3.9	3.9	3.9
Toroidal field	2.4	2.4	2.3	2.4	2.3
Remainder	23.2	23.2	23.2	23.2	18.8
Total	51.5	51.5	51.4	51.5	46.8

It can be seen from the neutron flux map (Figure 5.11) that there is little or no sampling in the centre column magnets and upper port manifold using method 3. These voxels are not included in the activation analysis and are therefore not included in the 'mass irradiated' quantity.

5.10.1 Whole model radioactive waste estimation

An estimate of the total waste inventory is presented in Figure 5.12 using method 2 (a structured mesh with a 15 cm voxel resolution). The variation in the material classification, not active waste (NAW), low level waste (LLW) and intermediate level waste (ILW) is shown with different cooling times. The dashed lines show the mass of material that could be considered for recycling (i.e. contact dose < 2 mSv/hr).

Of the total mass of the DEMO model (~51 kt), the largest component is the vacuum vessel, accounting for 25 % of the total mass. As such, the variation observed in the total waste is dominated by the vacuum vessel waste classification. Approximately 60 % of the total mass of the DEMO reactor is classed as ILW 6 months after shutdown, reducing to 10 % after 500 years. The majority of the ILW is recyclable after approximately 60 years of decay time. For the LLW, between 80 and 100 % is recyclable 1 year after shutdown.

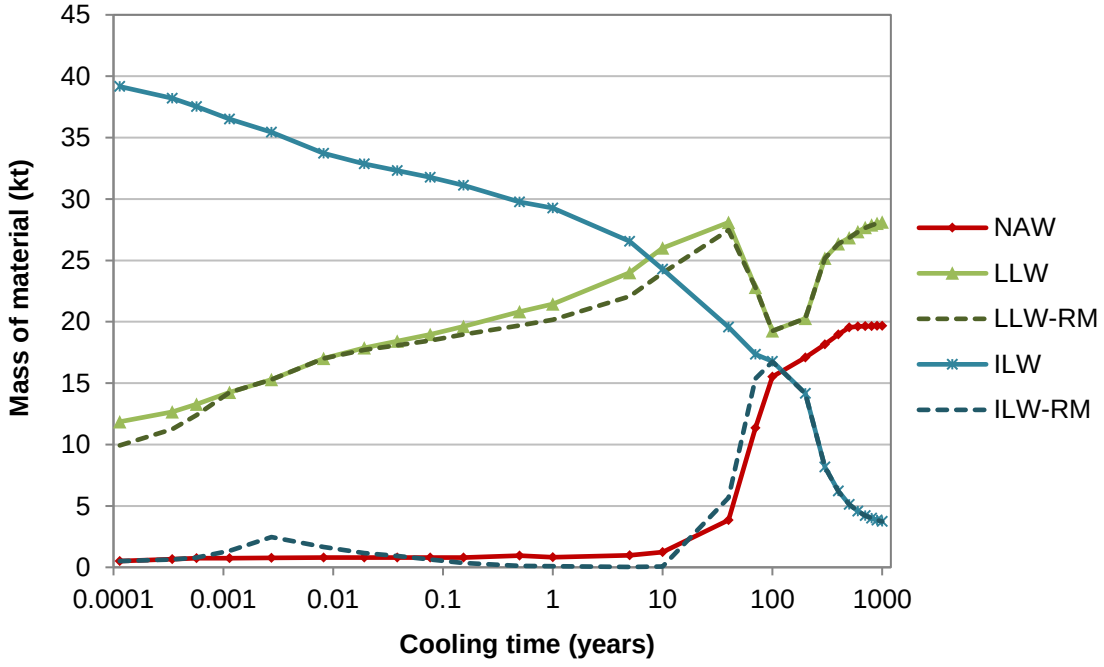

Figure 5.12 - Waste class of total material mass (kilotonne), using method 2 (15 cm resolution structured mesh).

The anticipated minimum interim cooling period for a DEMO reactor is 40 - 50 years, therefore the variations in waste classification for short decay periods (< 1 year) are not shown in the remainder of the figures presented in Section 5.10. The full data is, however, available in Appendix 5.3.

The variation in waste classification for the 3 methods used (cell-based, structured mesh and an unstructured mesh) is shown in Figure 5.13 to Figure 5.17. It should be reminded that these figures show the quantity of mass (kt) and that the total irradiated mass for the 3 methods differs. Due to the difference in irradiated mass it is useful to also consider the percentage of mass (%) that falls in each waste category; this is provided in Table 5.14 to Table 7.14.

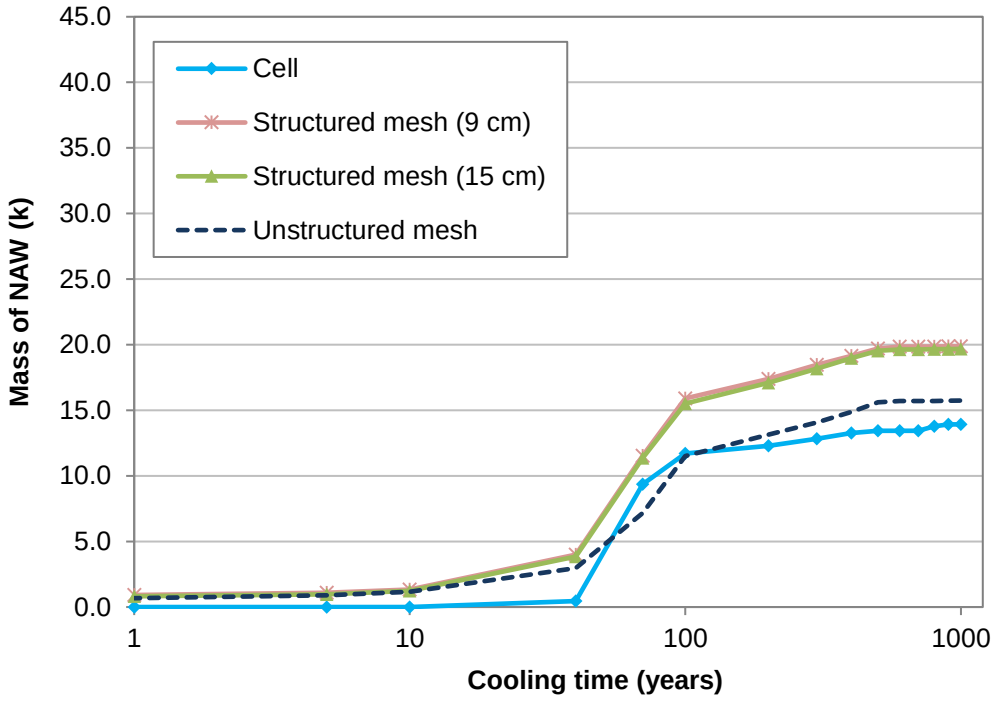

Figure 5.13 - Mass (kilotonne) of total material classed as NAW.

Using a cell-base method, after 1 year cooling time, none of the material can be cleared from regulatory control (i.e. NAW). By cooling times of 40 - 50 years, the level of NAW material has increased to ~1 % (Figure 5.13). Using a mesh approach to the calculations, both structured and unstructured, the amount of material classed as NAW increases to 6 - 8 %. This equates to around 4 kt of material.

At cooling times below 100 years, the cell-based method shows approximately 8 % lower quantities of LLW than mesh analysis (Figure 5.14). Above 100 years the cell-based method has approximately 10 % higher levels of LLW than the other methods. This cross over is due to the increasing NAW material within the mesh-based results.

As shown in Figure 5.12 the majority of material comprising the reactor is ILW. This decreases over time and more rapidly after approximately 100 years. The results for the mesh-based analysis, i.e. both the 9 cm and 15 cm structured mesh and the unstructured mesh, are very similar (varying by a few percent only). The steep reduction of ILW at around 100 years is seen more significantly in the mesh-based approaches then the cell-based method (Figure 5.15).

The majority of LLW (Figure 5.16) could be considered for recycling and the results do not significantly differ between the calculation methods. Some ILW (Figure 5.17) could be considered for recycling after 10 years. Again the results for recycling are very similar between the different methods. It is encouraging to see that after 100 years the majority of radioactive waste produced by a fusion power plant could potentially be recycled.

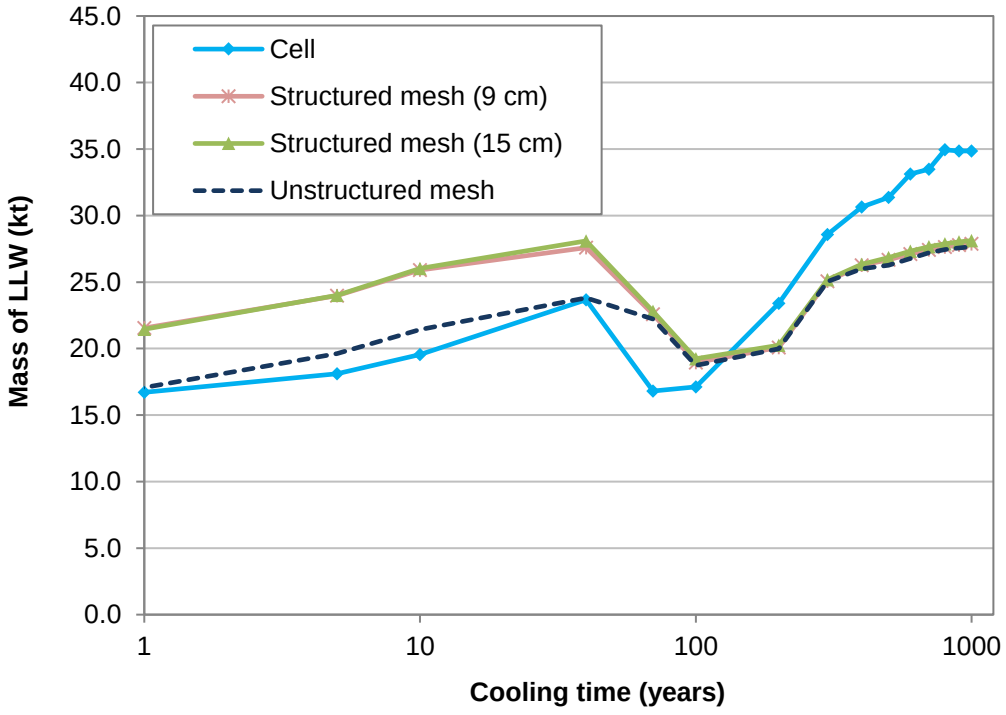

Figure 5.14 - Mass (kilotonne) of total material classed as LLW.

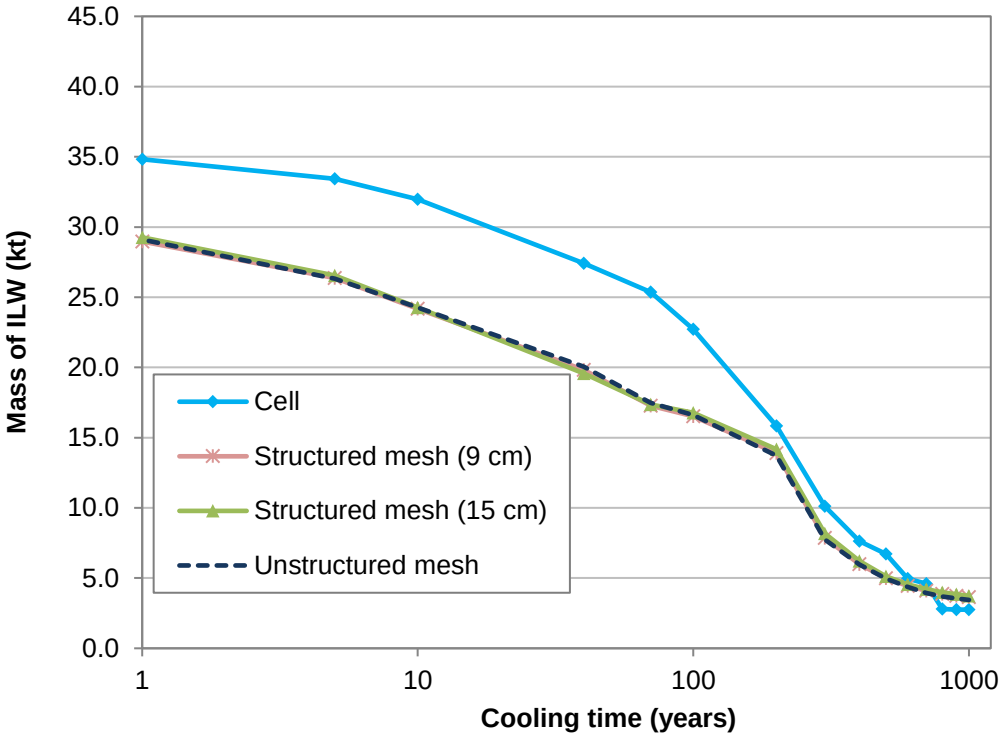

Figure 5.15 - Mass (kilotonne) of total material classed as ILW.

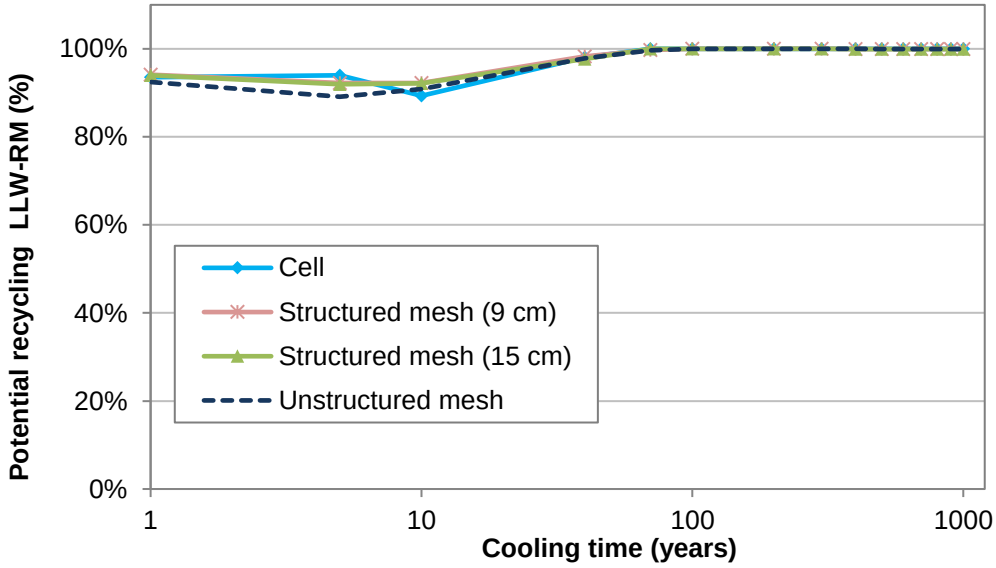

Figure 5.16 - Percentage of total LLW with recycling potential (LLW-RM).

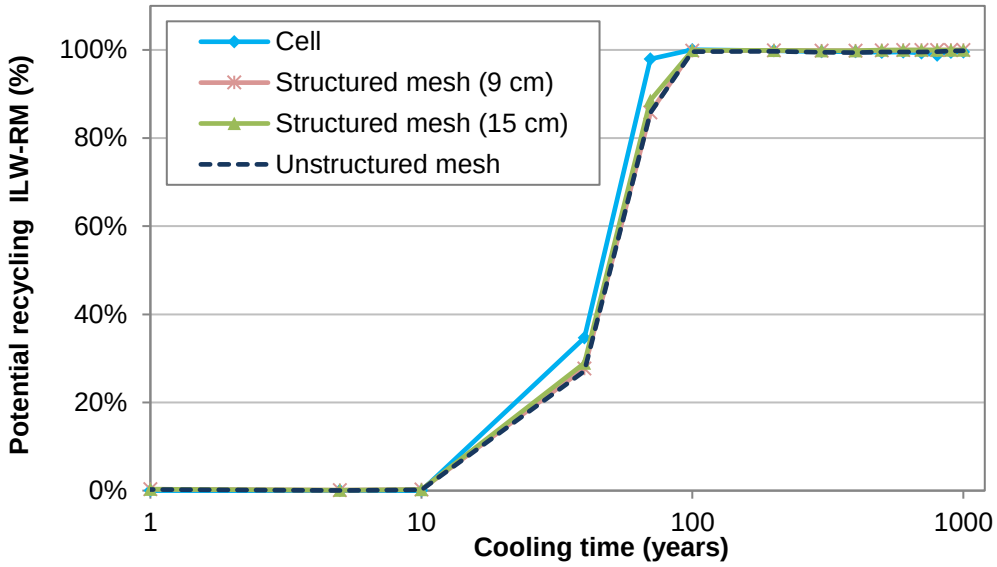

Figure 5.17 - Percentage of total ILW with recycling potential (ILW-RM).

Some of the components comprising the reactor have been investigated individually to assess the contributions from each and the effects of different calculation approaches. The components considered are the blankets, divertors, vacuum vessel and toroidal field coils. A summary of component contribution is given in Table 5.14 - Table 7.14 for the cell-based and structured mesh methods used, and are considered in further detail in the following subsections.

Table 5.14 - Material classification for each component after 100 years cooling (using method 1 - cell based).

	Mass (kt) (Percentage of component)			Potential recycling (%)	
	NAW	LLW	ILW	LLW-RM	ILW-RM
Divertor	0.0 (0%)	3.7 (95%)	0.2 (5%)	100%	84%
Blanket	0.0 (0%)	0.0 (0%)	8.8 (100%)		100%
Vacuum vessel	0.0 (0%)	1.7 (13%)	11.6 (87%)	100%	100%
Toroidal field coils	0.5 (21%)	1.9 (79%)	0.0 (0%)	100%	
Remaining materials	11.2 (48%)	9.8 (42%)	2.2 (9%)	100%	100%
Total	11.7 (23%)	17.1 (33%)	22.7 (44%)	100%	100%

Table 5.15 - Material classification for each component after 100 years cooling (using method 2 – structured mesh 15 cm resolution).

	Mass (kt) (Percentage of component)			Potential recycling (%)	
	NAW	LLW	ILW	LLW-RM	ILW-RM
Divertor	0.0 (0%)	2.8 (71%)	1.1 (29%)	100%	100%
Blanket	0.0 (0%)	0.0 (0%)	8.8 (100%)		100%
Vacuum vessel	2.5 (19%)	5.7 (43%)	5.1 (38%)	100%	100%
TF coils	0.0 (1%)	2.3 (96%)	0.1 (3%)	100%	88%
Remaining materials	13.0 (57%)	8.5 (36%)	1.7 (7%)	100%	100%
Total	15.5 (30%)	19.2 (37%)	16.8 (33%)	100%	100%

5.10.2 The breeder blankets

The breeder blanket is replaced once during the operational scenario assumed in this research; after the first phase of irradiation. The results for both the first and second blanket are added together to give the total mass of waste as shown in Figure 5.18, using a structured mesh approach (method 2) with a 15 cm voxel resolution. The full data for all methods is presented in Appendix 5.3, for clarity of presentation a summary of results at 5 cooling times are compared in Table 5.16 and Table 5.17.

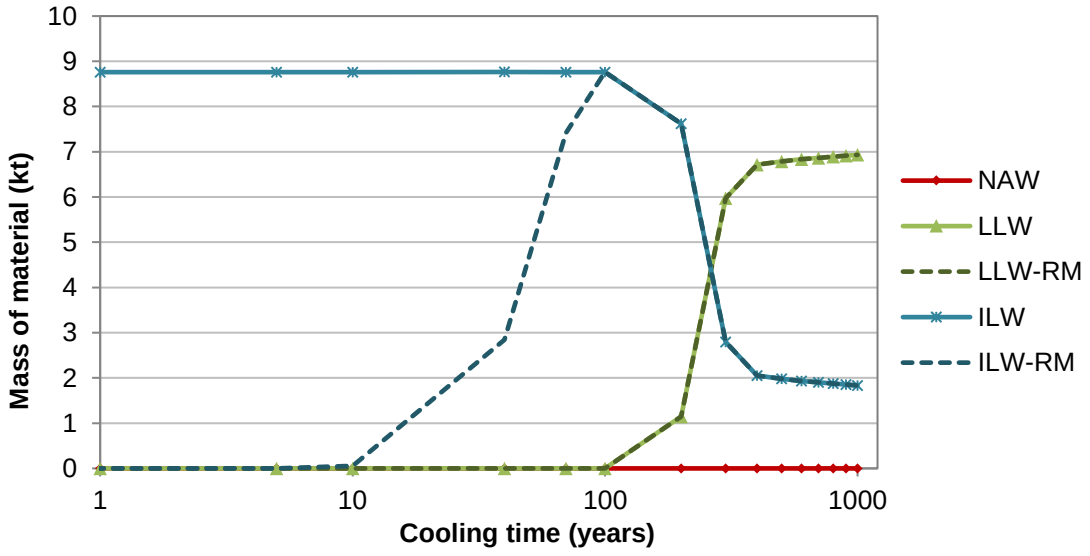

Figure 5.18 - Blanket material waste classes, using method 2 (15 cm resolution structured mesh).

Whilst the blankets remain ILW beyond 100 years, the results show that some material may be suitable for recycling after 10 - 40 years. As the blanket is the closest component to the plasma it receives high neutron irradiation, as does the divertor, leading to highly activated components. Even 1000 years after shutdown there is no fraction that can be considered as NAW based on activation concentration limits.

Table 5.16 - Mass of blanket materials classed as LLW (kt) with the percentage for potential recycling given in parenthesis (RM = recyclable material).

Cooling time (years)	LLW (kt)			
	Cell	Structured mesh (9 cm)	Structured mesh (15 cm)	Unstructured mesh
10	0.0	0.0	0.0	0.0
40	0.0	0.0	0.0	0.0
100	0.0	0.0	0.0	0.0
500	5.3 (RM- 100%)	6.8 (RM- 100%)	6.8 (RM- 100%)	6.7 (RM- 100%)
1000	7.8 (RM- 100%)	6.9 (RM- 100%)	6.9 (RM- 100%)	6.9 (RM- 100%)

Table 5.17 - Mass of blanket materials classed as ILW (kt) with the percentage for potential recycling given in parenthesis.

Cooling time (years)	ILW (kt)			
	Cell	Structured mesh (9 cm)	Structured mesh (15 cm)	Unstructured mesh
10	8.8 (RM- 0%)	8.8 (RM- 1%)	8.8 (RM- 1%)	8.8 (RM- 0%)
40	8.8 (RM- 0%)	8.8 (RM- 32%)	8.8 (RM- 32%)	8.8 (RM- 32%)
100	8.8 (RM- 100%)	8.8 (RM- 100%)	8.8 (RM- 100%)	8.8 (RM- 100%)
500	3.4 (RM- 100%)	2.0 (RM- 100%)	2.0 (RM- 100%)	2.1 (RM- 100%)
1000	1.0 (RM- 100%)	1.8 (RM- 100%)	1.8 (RM- 100%)	1.8 (RM- 100%)

During operation the blanket is intended, amongst other things, to create tritium as fuel for a self-sustaining fusion reactor. In the main results presented it has been assumed that the tritium remains in the blanket, in reality the tritium should be extracted for use as fuel in the plasma. Also, as the tritium is gaseous it cannot be assumed to be fixed to a location and will disperse. Considering the blankets with the

assumption that all the tritium is removed continuously results in the ILW reducing after approximately 6 years (Figure 5.19). It should be noted that although the intention is to remove all tritium from the blanket, some will be retained within the structure of the blanket.

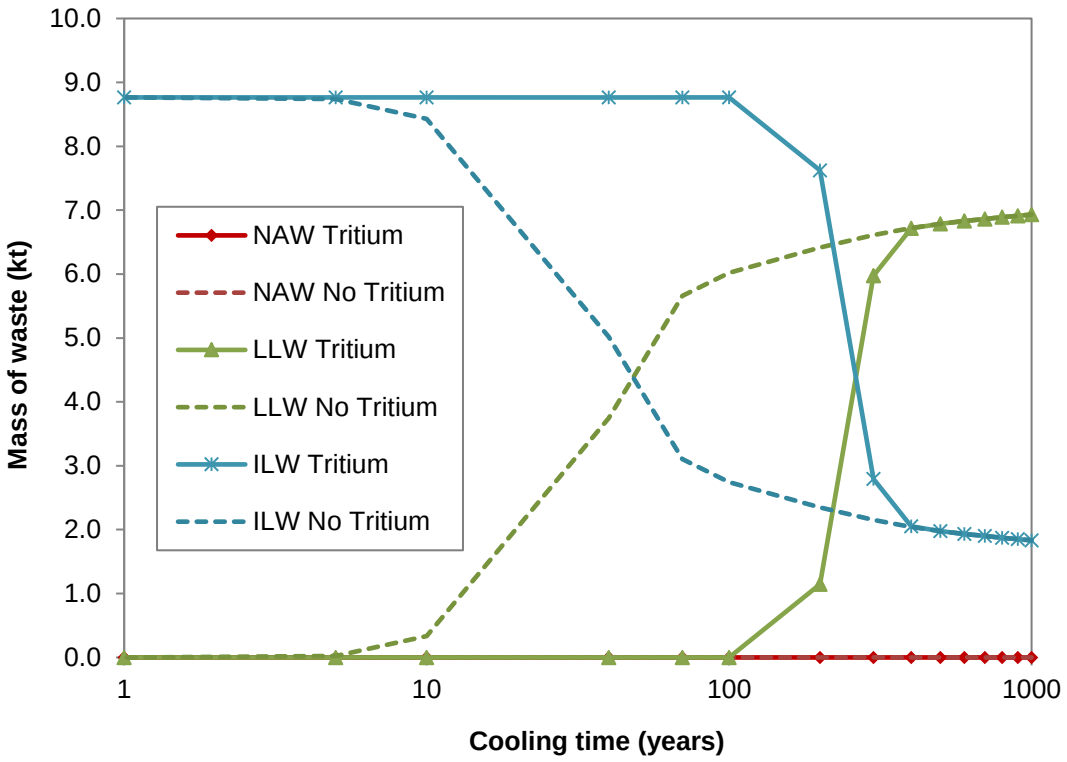

Figure 5.19 - Blanket material waste classes, using method 2 (15 cm resolution structured mesh), with and without tritium.

5.10.3 The reactor vacuum vessel

The waste classes for the mass comprising the vacuum vessel are given in Figure 5.20 to Figure 5.22. The time response of the recyclable material fraction is similar to that shown in previous plots and is therefore not reproduced here (see Appendix 5.3 for the complete data).

A comparison of the mass of material within each waste category is given in Table 5.18 to Table 5.20 for 5 cooling times; 10, 40, 100, 500 and 1000 years. The corresponding percentage of material that has recycling potential is shown in parenthesis.

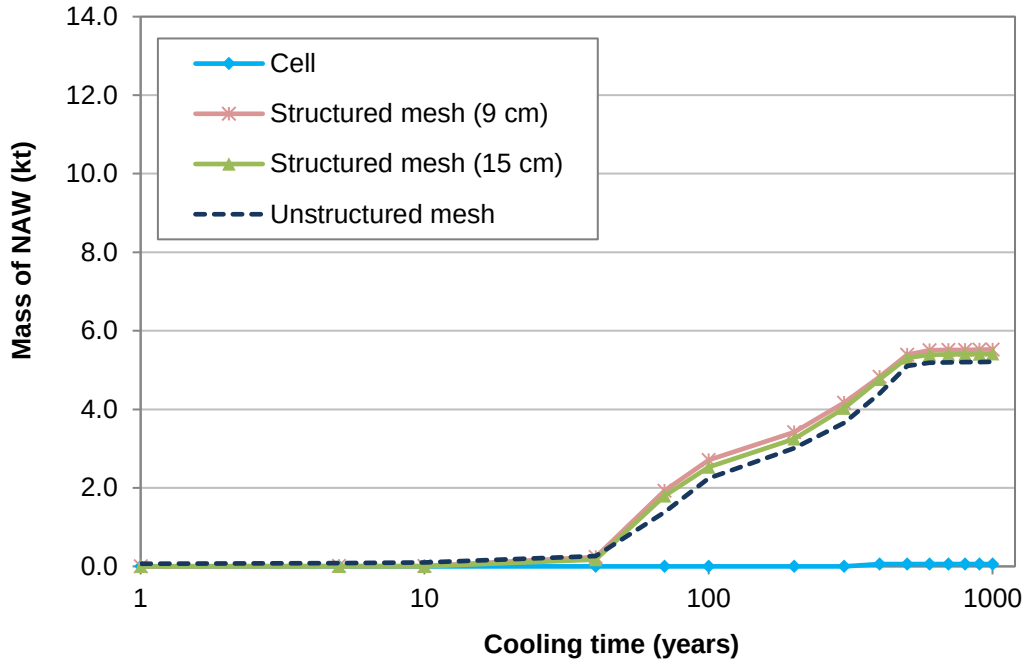

Figure 5.20 - Mass (kilotonne) of vacuum vessel material classed as NAW.

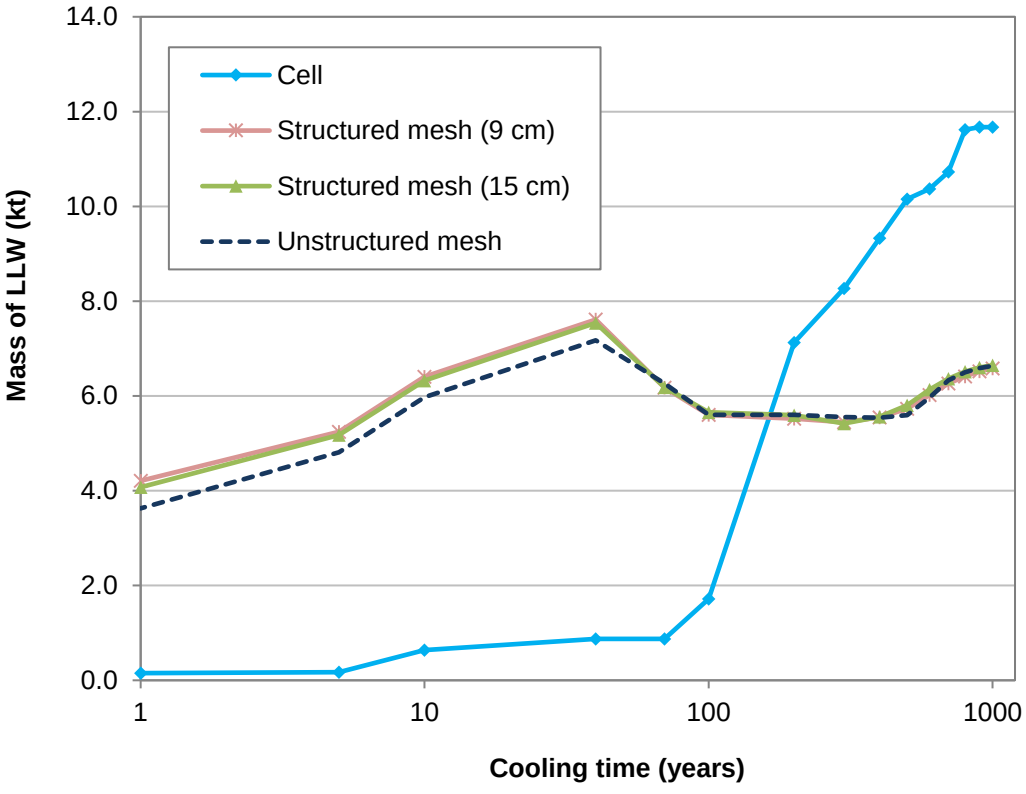

Figure 5.21 - Mass (kilotonne) of vacuum vessel material classed as LLW.

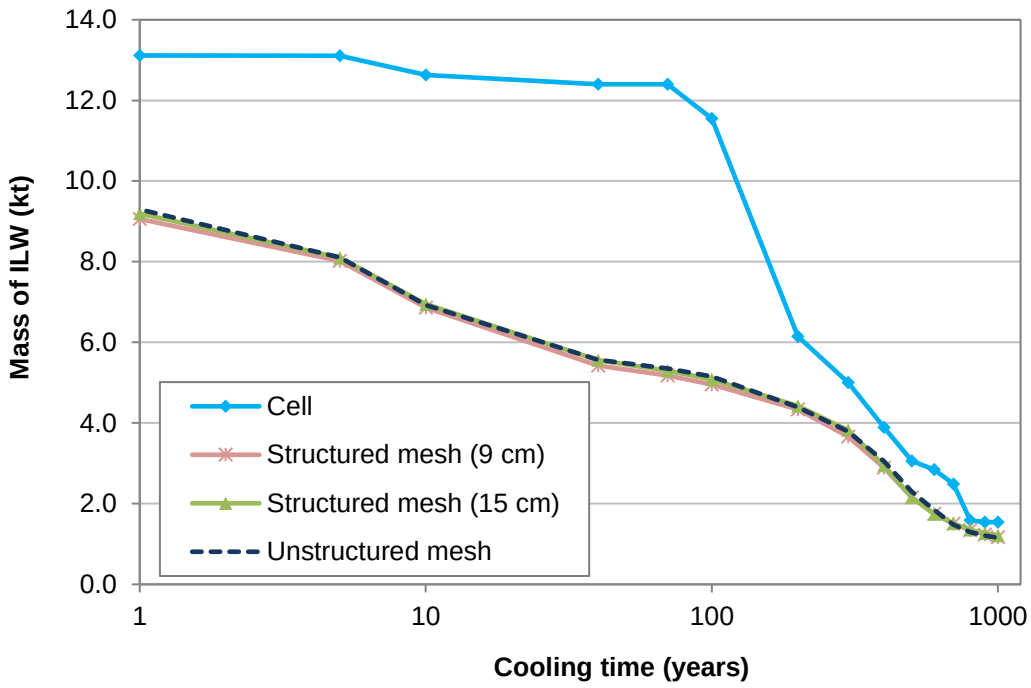

Figure 5.22 - Mass (kilotonne) of vacuum vessel material classed as ILW.

The mass of the vacuum vessel is predominantly ILW until approximately 10 years after shutdown. By 100 years there is approximately 40 % ILW, 40 % LLW and 20 % NAW. Through considering the waste class of the vacuum vessel by voxel or element, some of the material can be classed as LLW just after shutdown. Flux averaging over large cells, method 1, causes the whole component to be classed as ILW for approximately 100 years. For mesh-based methods the ILW decreases steadily to approximately 17 % ILW by 1000 years after shutdown.

The mass of LLW within the vacuum vessel peaks at approximately 60 years, when the activation decreases due to the decay of ^{55}Fe (see Section 5.10.6). After 60 years the quantity LLW declines as it becomes classed as NAW. After 100 years, the majority of the ILW and LLW is considered to be potentially recyclable. The percentage of ILW that could be recycled increases most significantly after 10 years.

Table 5.18 - Mass of blanket materials classed as NAW (kt) with the percentage for potential recycling given in parenthesis (RM = recyclable material).

Cooling time (years)	NAW (kt)			
	Cell	Structured mesh (9 cm)	Structured mesh (15 cm)	Unstructured mesh
10	0.0	0.0	0.0	0.1
40	0.0	0.2	0.2	0.3
100	0.0	2.7	2.5	2.2
500	0.1	5.4	5.3	5.1
1000	0.1	5.5	5.4	5.2

Table 5.19 - Mass of blanket materials classed as LLW (kt) with the percentage for potential recycling given in parenthesis (RM = recyclable material).

Cooling time (years)	LLW (kt)			
	Cell	Structured mesh (9 cm)	Structured mesh (15 cm)	Unstructured mesh
10	0.6 (RM- 26%)	6.4 (RM- 88%)	6.3 (RM- 88%)	6.0 (RM- 87%)
40	0.9 (RM- 100%)	7.6 (RM- 100%)	7.5 (RM- 100%)	7.2 (RM- 100%)
100	1.7 (RM- 100%)	5.6 (RM- 100%)	5.7 (RM- 100%)	5.6 (RM- 100%)
500	10.2 (RM- 100%)	5.7 (RM- 100%)	5.8 (RM- 100%)	5.6 (RM- 100%)
1000	11.7 (RM- 100%)	6.6 (RM- 100%)	6.7 (RM- 100%)	6.6 (RM- 100%)

Table 5.20 - Mass of blanket materials classed as ILW (kt) with the percentage for potential recycling given in parenthesis (RM = recyclable material).

Cooling time (years)	ILW (kt)			
	Cell	Structured mesh (9 cm)	Structured mesh (15 cm)	Unstructured mesh
10	12.6 (RM- 0%)	6.9 (RM- 0%)	6.9 (RM- 0%)	6.9 (RM- 0%)
40	12.4 (RM- 66%)	5.4 (RM- 36%)	5.6 (RM- 36%)	5.6 (RM- 35%)
100	11.6 (RM- 100%)	5.0 (RM- 100%)	5.1 (RM- 100%)	5.2 (RM- 100%)
500	3.1 (RM- 100%)	2.2 (RM- 100%)	2.2 (RM- 100%)	2.3 (RM- 100%)
1000	1.5 (RM- 100%)	1.2 (RM- 100%)	1.2 (RM- 100%)	1.2 (RM- 100%)

The vacuum vessel comprises of three layers, a layer of 77 % steel and 23 % water cooling, with an inner and outer layer of 100 % steel. After shutdown the cooling water will be removed and not form part of the solid radioactive waste assessment.

With this in mind a further calculation has been performed, using method 2 considering the waste in the vacuum vessel without water in the inventory i.e. the water was removed after the neutron transport calculation.

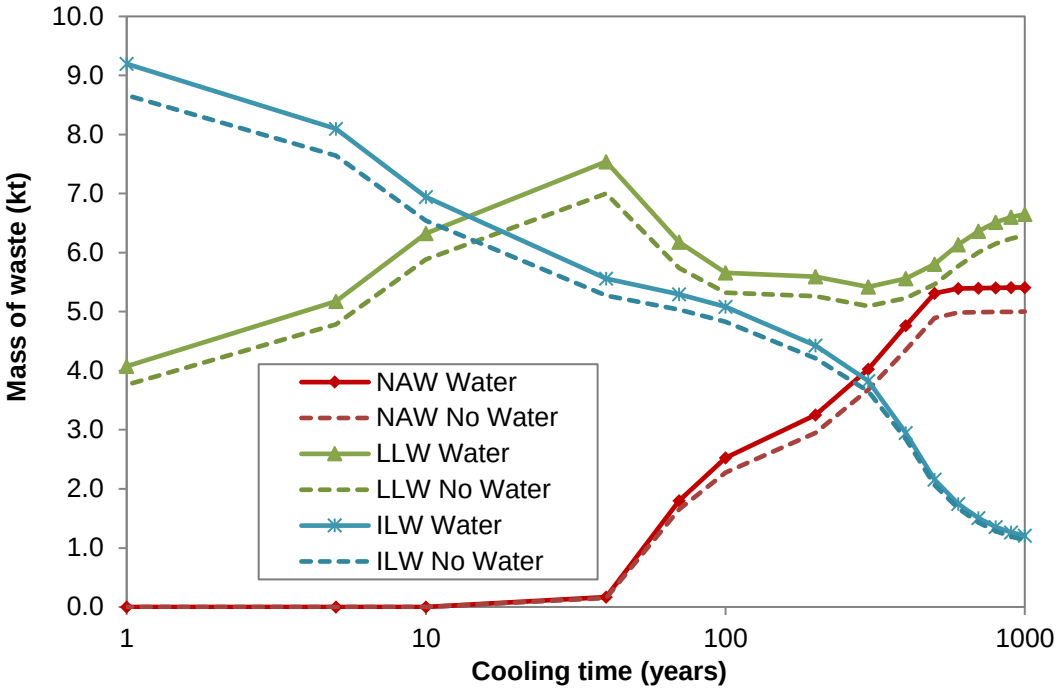

Figure 5.23 - Vacuum vessel material waste classes, using method 2 (15 cm resolution structured mesh), with and without water.

Table 5.21 - Comparison of waste classes with and without water in vacuum vessel.

Cooling time (years)	Water			No Water		
	NAW	LLW	ILW	NAW	LLW	ILW
1	0%	31%	69%	0%	30%	70%
5	0%	39%	61%	0%	39%	61%
10	0%	48%	52%	0%	47%	53%
100	19%	43%	38%	18%	43%	39%
500	40%	44%	16%	39%	44%	17%
1000	41%	50%	9%	40%	51%	9%

Removing the water reduced the overall mass of the vacuum vessel and reduced the waste in all classes (Figure 5.23). At approximately 1 day after shutdown the amount of ILW is reduced from 11 kt to 10 kt. As a percentage of the total vacuum vessel mass (Table 5.21) there is minimal difference observed in the waste classes, approximately 1 % decrease in the radioactivity level of waste is observed after 10 years.

5.10.4 The divertors

There are four divertors used throughout the operational scenario of the DEMO reactor simulated in this work. One divertor is replaced after the first phase and this is replaced twice more during the second phase. The results presented are a summation of all four divertors.

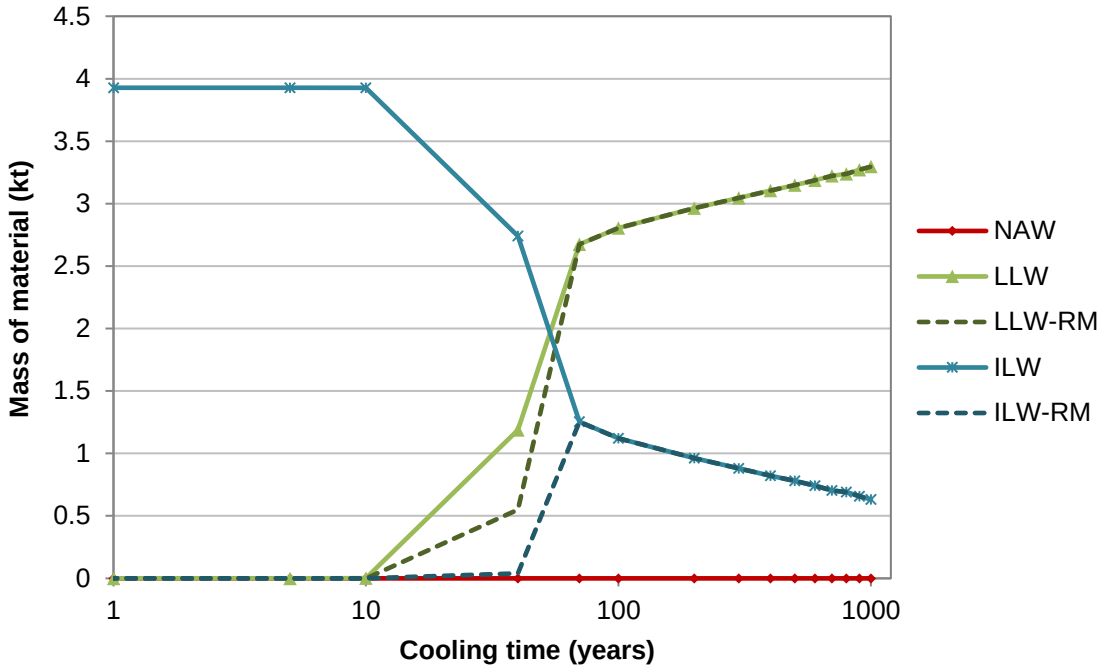

Figure 5.24 - Divertor material waste classes, using method 2 (a 15 cm resolution structured mesh).

Figure 5.24 shows the variation in waste material with time when using method 2, the structured mesh with a 15 cm voxel resolution. Whilst full data for all methods is given in Appendix 5.3., a comparison for 5 cooling times is presented in Table 5.22 and Table 5.23.

As with the blanket, the divertors are plasma facing components and as a result receive high neutron flux. Consequently even after 1000 years there is no NAW. The divertor is mainly ILW until approximately 10 years where it decreases from approximately 4 kt to 1 kt by 100 years. This then slowly decreases further to approximately 0.5 kt ILW by 1000 years. As the ILW decreases, the mass becomes classed as LLW. Of the LLW, the majority is classed as recyclable after around 60 years.

Table 5.22 - Mass of divertor materials classed as LLW (kt) with the percentage for potential recycling given in parenthesis (RM = recyclable material).

Cooling time (years)	LLW (kt)			
	Cell	Structured mesh (9 cm)	Structured mesh (15 cm)	Unstructured mesh
10	0.0	0.0	0.0	0.0
40	0.4 (RM- 38%)	0.7 (RM- 33%)	1.2 (RM- 46%)	0.8 (RM- 34%)
100	3.7 (RM- 100%)	2.9 (RM- 100%)	2.8 (RM- 100%)	3.2 (RM- 100%)
500	3.8 (RM- 100%)	3.3 (RM- 100%)	3.1 (RM- 100%)	3.5 (RM- 100%)
1000	3.8 (RM- 100%)	3.3 (RM- 100%)	3.3 (RM- 100%)	3.5 (RM- 100%)

Table 5.23 - Mass of divertor materials classed as ILW (kt) with the percentage for potential recycling given in parenthesis (RM = recyclable material).

Cooling time (years)	ILW (kt)			
	Cell	Structured mesh (9 cm)	Structured mesh (15 cm)	Unstructured mesh
10	3.9 (RM- 0%)	3.9 (RM- 0%)	3.9 (RM- 0%)	3.9 (RM- 50%)
40	3.5 (RM- 0%)	3.2 (RM- 1%)	2.7 (RM- 33%)	3.2 (RM- 46%)
100	0.2 (RM- 84%)	1.0 (RM- 100%)	1.1 (RM- 100%)	0.8 (RM- 100%)
500	0.1 (RM- 70%)	0.7 (RM- 100%)	0.8 (RM- 100%)	0.5 (RM- 100%)
1000	0.1 (RM- 91%)	0.6 (RM- 100%)	0.6 (RM- 100%)	0.4 (RM- 100%)

5.10.5 The toroidal field coils

The waste inventory for the toroidal field coils is presented in Figure 5.25. The mass of the toroidal field coils only accounts for a small fraction of the total mass of the DEMO reactor model used here. As the ILW decreases, the LLW increases steadily with only a small fraction of the toroidal field coils classed as NAW; approximately 3 % of the waste is classed as NAW 500 years after shutdown.

The variation in the different methods is provided in Appendix 5.3 along with data corresponding to the recyclable material. The majority of LLW could be recycled, with 40 - 90 % of the ILW recyclable after 50 years. The significant differences

observed in the absolute mass of waste values using method 4 are due to the zero neutron flux values in some voxels of the toroidal field coils from poor sampling.

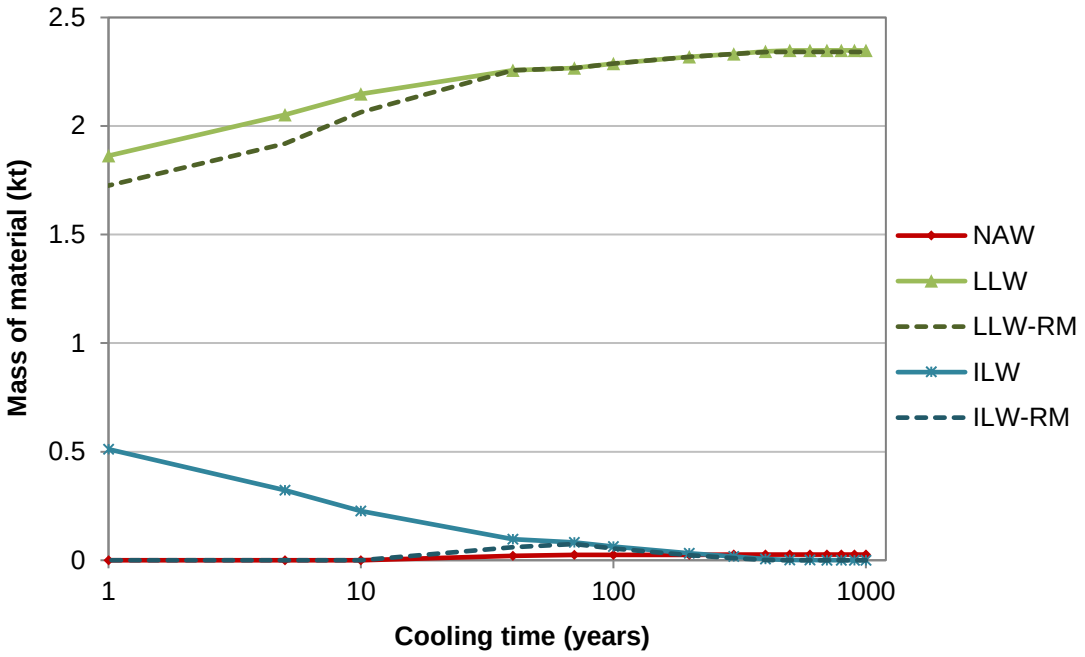

Figure 5.25 - Toroidal field coil material waste classes, using method 2 (15 cm resolution structured mesh).

5.10.6 Dominant nuclides

The FISPACT i/o files were saved for 4 points within the model. This enabled the nuclide inventory and activation to be investigated in further detail. Re-running the activation calculation for these points using the 'UNCERT' keyword with FISPACT enabled the pathway information to be obtained. The nuclides that dominate the activation at 100 years are presented in the following figures:

Figure 5.26 - point B within the outboard breeder blanket.

Figure 5.28 - point C in the middle of the divertor.

Figure 5.27 - point D in the vacuum vessel (inboard side).

Figure 5.29 - point G in the upper inboard side of the toroidal field coil.

The activation in the breeder blanket (Figure 5.26) is dominated by the tritium, however as already discussed; this should not be assumed to stay in its birth location. The activation in the breeder material is therefore dominated by the ^{60}Co, ^{93m}Nb and ^{14}C nuclides. Between cooling times of 1 and 70 years the nuclides of ^{60}Co and ^{93m}Nb

dominant, with half-lives of approximately 5 and 16 years respectively. Beyond 70 years, the long-lived ^{14}C nuclide dominates; with a half-life of greater than 5700 years.

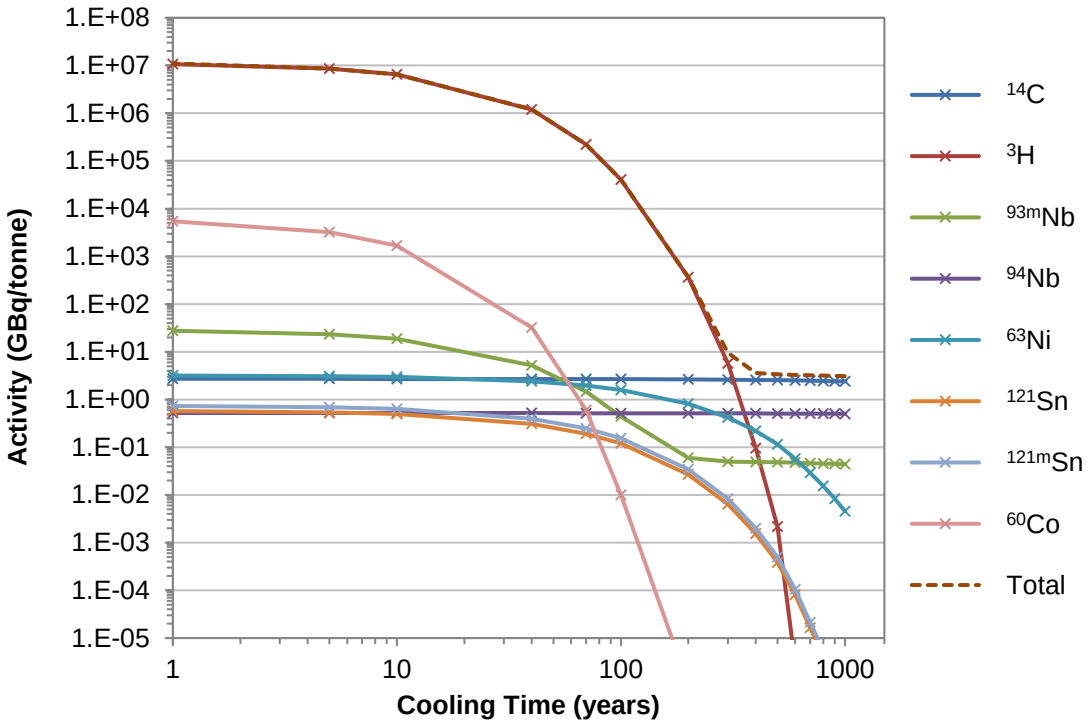

Figure 5.26 - Activity concentration of dominant nuclides at point B in the outer blanket.

The nuclides of ^{55}Fe, ^{60}Co and ^{14}C dominate the activity within the vacuum vessel (Figure 5.27). Iron-55 originates from the ^{56}Fe and ^{54}Fe isotopes, through the $(n, 2n)$ and (n, a) reactions respectively. The vacuum vessel is a structural component comprising of mainly steel, therefore iron is a fundamental element within the material. The presence of ^{60}Co, however, can be reduced through impurity reduction in steels (where technology allows). The EUROFER specification provides a target of 'as low as possible' and less than 0.005 w% for Co. Carbon-14 is formed through the (n, p) reactions with ^{14}N. Steels in some ITER components will use a reduced Ni variation. In DEMO a Ni content of between 0.015 - 0.045 w% is anticipated.

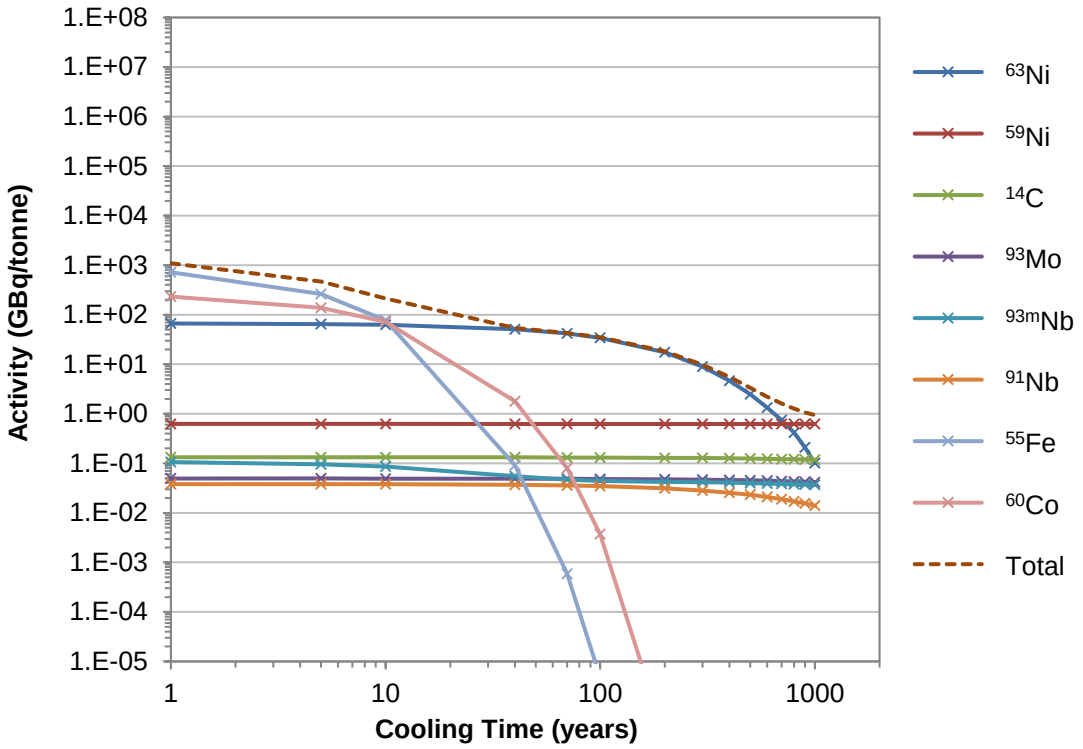

Figure 5.27 - Activity concentration of dominant nuclides at point D in the inboard vacuum vessel.

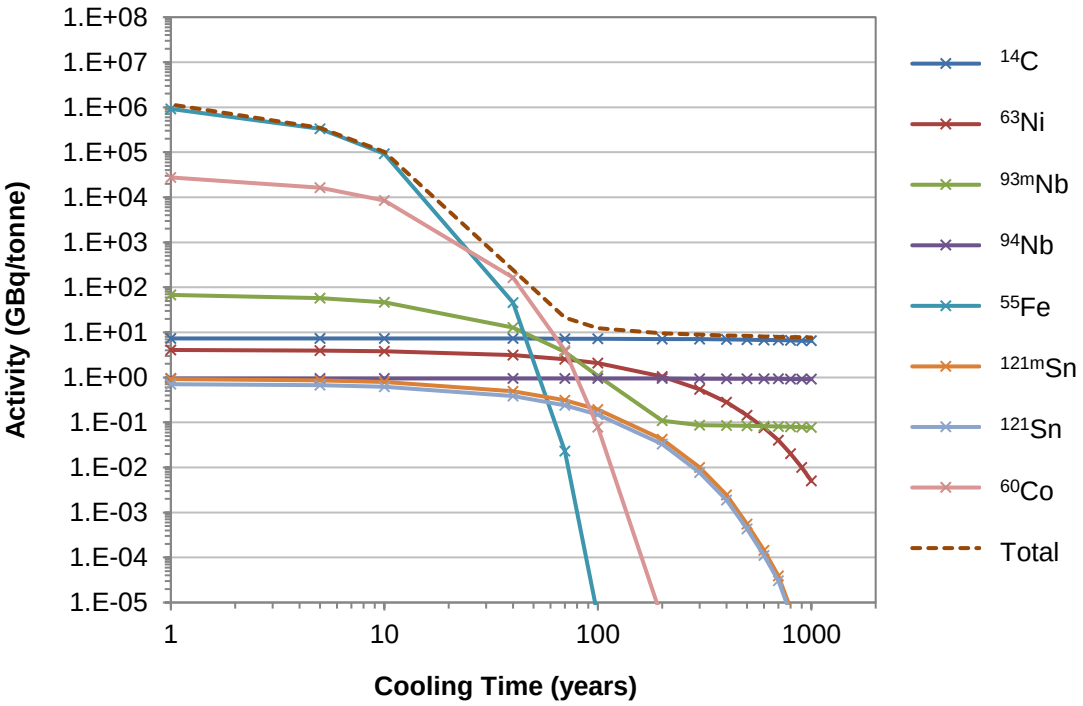

Figure 5.28 - Activity concentration of dominant nuclides at point C in the divertor.

The divertor structure is a particularly difficult component for materials due to the high flux loads. In this research, steels of EUROFER and ITER grade stainless steels were used in the divertor. Significant research within published literature has been performed on these materials, however, the conditions within DEMO will require other types of structural material due to the higher operating temperatures and to avoid excessive volume changes under neutron irradiation. The structural materials for DEMO are based on assumed technological advances; some materials are discussed in Section 2.5.6.

In this research the activation in the divertor (Figure 5.28) is comprised of similar dominant nuclides to the vacuum vessel. The nuclides of ^{55}Fe, ^{60}Co and ^{93m}Nb dominate activation up to approximately 100 years. Above this the long-lived ^{14}C nuclide dominates.

The toroidal field coil is significantly less activated than the blankets, vacuum vessel and divertor as they are shielded by the in-vessel components (Figure 5.29). At cooling times between 1 and ~ 10 years the ^{60}Co nuclide dominates the activation. Above this, the ^{63}Ni nuclide dominates up to ~ 500 years. The activation is then dominated by the long lived ^{94}Nb nuclide with a half-life of 19986 y.

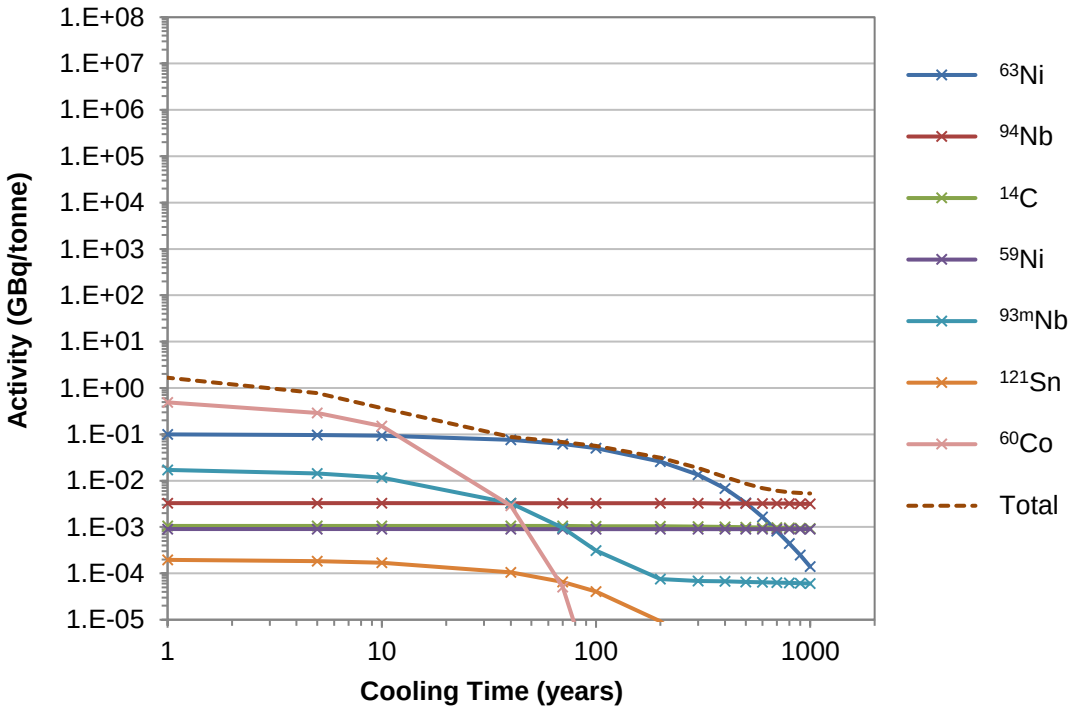

Figure 5.29 - Activity concentration of dominant nuclides at point G in the inboard toroidal field coil.

5.11 Discussion

5.11.1 The radioactive waste inventory

Fusion power plants have a significant environmental and social acceptability advantage over fission due to the differences in the radioactive waste produced. Fusion plants will not produce radioactive products as a result of the fusion reaction, unlike fission by-products. The high level wastes from the fission spent fuel and waste arising from reprocessing require active cooling due to the thermal power. Within the UK approximately 0.1 % (1000 m^3) of the total radioactive waste is classed as high-level waste; although the volume is relatively small, it contains about 95 % of the total inventory of radioactivity [173]. According to a report by the World Nuclear Association [174], a typical 1000 MW(e) light water reactor will generate (directly and indirectly) 200 - 350 m^3 ILW and LLW per year. It will also produce around 20 m^3 (27 tonnes) of used fuel per year, which corresponds to a 75 m^3 disposal volume following encapsulation procedures.

Although a fusion power plant will not produce HLW, the tokamak is likely to create a higher percentage of ILW and LLW than fission. Whilst this waste is more socially acceptable than high level wastes it still is not well received. There are also still significant costs associated with dealing with such wastes with limited disposal repositories available and difficulties in constructing new facilities. In terms of cost it is anticipated to be roughly tens of thousands of pounds per cubic metre of ILW and hundreds of thousands per tonne of uranium for high level waste [174]. (This is assuming such facilities are available). Fusion research has focused on creating a ‘clean’ energy supply and this has driven the requirement for the materials of a fusion power plant to be recycled or cleared after 100 years. Using lower activation materials and dismantling components can help to reduced quantities of material that will need to be considered for storage and/or disposal.

By considering the waste in each voxel or element of a mesh, the effect of dismantling/segregation can be considered for a HCPB DEMO. (This mesh-based approach also reduces neutron flux averaging assumptions, as discussed later in this section.) If the components could be assumed to be dismantled into 15 cm cubes, then results show that ~ 7 % of the waste could be cleared from regulatory control after 40 years and 30 % after 100 years. For example, the vacuum vessel is classed as ILW

after 100 years cooling time. By dismantling into 15 cm cubes, approximately 10 % of the material could be cleared, and 43 % classed as LLW, providing more options for disposal and lowering difficulties faced with storage and eventual disposal of ILW.

Splitting a reactor into 9 or 15 cm cubes is obviously not a practical option. However the results demonstrate some of the advantages from the dismantling of components if suitable dismantling and separation techniques are developed. Dismantling in itself can produce more radioactive waste depending on the methods employed. The process of dismantling requires cutting and severing tools with the likely potential of causing dust, fumes and secondary liquid waste. Where suitable it would be advantageous to make use of demountable components with a process which could be undertaken remotely.

The effect of flux averaging is evident when comparing the cell-based results to those using a mesh-based approach. As discussed in Section 5.7, some of the components have been split into smaller cells, mainly for the CAD to MCNP conversion process, though there are still a number of 'large cells' with deep shielding effects. Table 5.11 shows the flux approximation for a number of points in the model. In areas where the cells are respectively small, and for components close to the plasma, the effect of flux averaging is low, whereas outside the shielding of the blanket, the effect becomes more significant.

The flux averaging in turn effects the radioactive waste assessment, as the entire cell is assumed to have the same neutron flux irradiation. By making this assumption, less than 1 % of the waste can be cleared after 40 years, and ~22 % after 100 years, with ~27 kt and 23 kt of ILW at 40 and 100 years respectively.

Recycling is the preferred method for dealing with waste arising from a power plant that cannot be cleared from regulatory control; either due to activation products or for example in the case of France, where no clearance procedures are in place. In this research the contact dose rate has been used to assess the potential for recycling material. This research shows that after an interim cooling period of 60 years the majority of the ILW is recyclable. The majority of the LLW is shown to be recyclable shortly after shutdown and well within a 40 - 50 year interim cooling period. The limit of 2 mSv/hr has been used, as adopted in similar studies on the recycling of radioactive waste materials (see Section 5.5). Recycling could also be considered for materials with a contact dose rate < 10 mSv/hr (and even up to 20 mSv/hr is possible),

but this would require specific remote handling equipment often at a high economic expense.

Due to the different waste classes and approaches considered throughout the literature, it is difficult to draw comparisons with the data generated in this research for a DEMO model. Similar trends in the results are observed however. Analysis conducted on the Russian Federation DEMO-S model [160] shows that the steel within the vacuum vessel contributes significantly to the activity and as such does not reduce to a lower level waste class until 100 years after shutdown. It also shows that some recycling of material (mostly the coils) is achievable after approximately 30 years.

A DEMO HCLL radioactive waste study using an approach similar to that of a cell-based method is presented in [68]. The study uses reasonably similar waste classification to that in this thesis, it is shown that the ILW reduced more rapidly with the majority gone 50 - 100 years after shutdown. This however does not include the LiPb breeder material used in the blanket. Comparing the quantity of cleared material for the different materials/components and the variation with time shows some agreement, particularly for the toroidal field coils and plasma facing components (blanket first wall and divertor first wall).

Comparing the cleared material after 100 years cooling time with [175] also shows similar agreement with the results using the BSSD-1996 clearance index (as used in this work). It reports that after 100 years, 21 % of the materials could be cleared (~13 % using the IAEA clearance levels). Results from the cell-based method in this thesis show that ~23 % of the material comprising the DEMO model can be cleared. Further discussion and comment on the use of clearance index values is given in Section 5.11.3.

5.11.2 Use of unstructured mesh

Radioactive waste assessments for fusion power plants using neutron flux data from MCNP have in the past been carried out using a cell-based approach. In this work, recent developments regarding the coupled use of MCNP and FISPACT with mesh-based neutron spectra results, has been considered, along with the state-of the art unstructured mesh capabilities within the latest release of MCNP.

In theory the unstructured mesh approach is the most appropriate; there are no introduced errors through material mixing of different components and materials, and

reduced flux averaging by effective use of mesh elements. The method of using unstructured mesh in calculations is also advantageous as the mesh only covers the solid bodies of the model, increasing the efficiency of the mesh and removing unnecessary elements that take up valuable computing resource but are not need, as in the case of a structured rectangular mesh over say a 10° fusion tokamak sector model. Coupled 3-D neutronics and activation analysis is 'expensive' both in terms of computational requirements and human time. The majority of human time is spent in creating neutronics compatible models.

The use of unstructured mesh within neutronics could facilitate the use of 'shared' models between departments, and shared time in creating the suitable models. Currently the geometry requirements for a model to be converted into CSG, result in neutronics specific, and even analysis specific, models being created. This is a large amount of human time which could be reduced with the development of unstructured mesh methods.

Although the model could be shared the resulting unstructured mesh may not be so compatible between analysis departments due to refinement requirements. Using a 'fine' mesh for unstructured mesh based neutronics analysis would be computationally expensive, and quite possibly, impractical or infeasible due to the memory requirements. For use in activation analysis, where neutron flux in the transport calculation is recorded in 175 energy groups for each element, a mesh resolution of 15 cm required approximately 2 Gb of memory. Using a more refined mesh, such as 5 cm, this increases to 36 Gb - impractical for this type of analysis. In the case of full tokamak models, i.e. the full 360º, a mesh resolution of 30 cm would require 10 - 15 Gb (based on the reasonably uncomplicated EU DEMO model used in the work presented here). More complex geometry could increase the mesh size (i.e. the number of elements) significantly. The increased opportunities regarding the efficiency and refinement of the unstructured mesh, however, are still advantageous compared to the superimposed structured rectangular mesh. Additional consideration and thought should be given to the size of the unstructured mesh being created.

In this work it was found that although the unstructured mesh has many potential benefits, as of yet it is still widely untested with many of the analysis techniques and methods used within neutronics. This needs further development to ensure a robust methodology for using an unstructured mesh approach in fusion neutronics.

5.11.3 Using clearance levels

Clearance levels are used to determine the clearance index of a material and in turn whether it can be cleared from regulatory control. Within French regulations, as used for ITER, no waste can be classed as cleared; all waste produced on a nuclear licensed site must be classes as radioactive waste and disposed of with an appropriate method. As discussed in Section 5.4.2, there are a number of clearance levels available for different material types and scenarios. The levels used in this work are directly derived from the BSSD-1996, as reproduced in the UK radioactive safety guidance [142]. After inspection and comparison of the activation concentration levels between those used in this work, those presented in Table 3.2 of RP-122 [153] and those in Table 2.3 of RS-G-1.7 [154], it was shown that there are some difference. Studies into the effect of using the clearance levels in RS-G-1.7, which are now included as the standard clearance levels in the BSSD-2007, replacing those from BSSD-1996, on the ITER waste inventory showed that the clearance potential of material and the time scales were effected [175]. In general, the IAEA levels (RS-G-1.7), presented as activity concentrations, are the same as, or lower than, the BSSD-1996 levels, and result in less ITER material achieving clearance within the same time scale and with longer interim decay periods.

A test case on the radioactive waste inventory of a component of the EU HCPB DEMO model showed that on the time scales investigated, there was little impact on the amount of cleared waste.

During comparison tests it also became apparent that were some discrepancies in the list of activity concentrations used for clearance in this work; this is likely due to human error (prior to this research) in transferring the data from [142] into the tabulated form used in the calculations. This was shown in a test case not to have any significant effect on the radioactive waste inventory calculations performed on this DEMO model.

5.11.4 Tritiated waste

The main focus of a large portion of the research presented in Section 4 is on the production of tritium. Tritium production in the blanket is a requirement of the currently pursued magnetically confined fusion power plants. In the blankets where tritium production is designed to take place, a tritium recovery system will be used. In

the case of solid blankets this is likely to be a purge gas, for liquid breeders it is proposed that the tritium recovery could take place continuously from the flowing breeder. Tritium management should be addressed through the plant's full lifetime, conception to decommissioning. The fusion fuel cycle has a poor tritium burning efficiency, for DEMO this anticipated to be around 10 %. The majority of the tritium is recovered for recycling, via purification steps. Some of the tritium is effectively 'lost' in the surrounding in-vessel components and will be difficult to recover. Further tritium contamination arises as a result of activation products from the materials comprising the tokamak.

Tritium activity has not been considered explicitly within the radioactive waste assessment carried out as part of this research however some of the considerations are explored. As discussed in Section 5.4.3, it is expected that a large amount of waste will be contaminated with tritium. Regardless of the IAEA waste level (as calculated in this work), the disposal options for the waste is likely to be further restricted by the tritium activity [151]. Many repositories impose limits on the activity due to tritium contamination. Tritium is a low energy beta emitter with a range of up to 0.6 cm in air (6 μm in tissue). Material contaminated with tritium does not, therefore, pose a particular external threat to human life. However tritium can permeate materials and once airborne can be more easily inhaled.

The most radiotoxic issue arises from tritiated water vapour as the tritium readily exchanges with water vapour in the air. Once inhaled or absorbed the tritium disperses rapidly through the body giving rise to a whole body dose. Tritiated water vapour is up to 25000 times more radiotoxic than tritium as a gas. Reducing the tritium retention in materials is therefore particularly important [176]. Techniques for detritiation are also being pursued [149]; some are discussed in Section 5.4.3.

In radioactive waste assessments like that carried out in this research, it is difficult to quantify the tritium content and associated activity as it should not be assumed that all the tritium created in the blanket will stay there. Primarily this should be assumed to be removed through the tritium recovery system, however some will remain. Due to the gaseous nature of the tritium it will permeate out of the blanket and into other surrounding structures/ components and specifying the exact location would be challenging. Comments regarding recommendations for further work in this area are included in final remarks and suggestions for further work in Section 6.

5.12 Conclusions

A neutronics model of the EU generic DEMO 2015 model (using HCPB blanket material) was used to conduct a radioactive waste assessment with a focus on the effect of using cell-based, structured or unstructured mesh based approaches. The model includes in-vessel components, toroidal field coil, centre column magnets and some of the poloidal field coils closest to the plasma. These components will contribute the most to the higher levels of radioactive waste. Beyond this the neutron fluxes will be significantly reduced due to the shielding effect the components provide.

The research regarding radioactive waste assessments for fusion using neutronics analysis techniques can be summarised in the following conclusions:

- Dismantling components and or the design of demountable sections should be considered in an effort to reduce the levels of radioactive waste requiring long storage and or disposal.
- Of the total mass of the DEMO reactor as modelled, approximately 25 % comprises the vacuum vessel. If the vessel is considered as one component, or in large sections, then the calculations show that this would be considered as ILW for at least 100 years. Dismantling sections of the outboard vacuum vessel could reduce the ILW waste at 100 years cooling time from ~12 kt to 5 kt.
- An unstructured mesh approach to performing radioactive waste assessments is in theory the most appropriate, potentially providing a quicker route to MCNP model creation, removing uncertainties introduced through material mixing within voxels of a structured mesh, and providing options for using a more efficient mesh that can also be shared with other analysis uses.
- Further testing and development of the unstructured mesh method is required to make it more robust and compatible with current global variance reduction techniques.
- The ADVANTG variance reduction technique has been shown to produce a more efficient weight window. The production of the weight window also required less computing time than the iterative approach implemented in the WWiter code.

6 FINAL REMARKS

The main purpose of the research presented in this thesis was to use neutronics analysis to assess blanket performance, shielding requirements and radioactive waste inventory. The use of a novel approach to radioactive waste inventory through the unstructured mesh geometry capability with MCNP was also investigated for the potential of a more accurate analysis method.

6.1 Breeder blanket performance

A selection of solid and liquid tritium breeding materials have been compared with regards to blanket performance, i.e. TBR, energy multiplication and shielding, using neutronics analysis through MCNP particle transport. The overall conclusions drawn from this research are:

- The solid breeder type materials require less ^{6}Li enrichment, than the majority of the liquid breeder types, to achieve a similar tritium production and energy multiplication ratio.
- Although some of the solid breeder concepts are more developed, the liquid breeder blankets have some compelling advantages, such as the potential for continual purification and improved tritium control. Also, the majority of the liquid breeder materials do not require the use of beryllium for reasonable tritium production levels. (Whilst beryllium does feature in many blanket concepts there is also on-going research in an effort to reduce usage. Beryllium

is not particularly abundant and causes a number of safety issues, not least due to the high reactivity with water.)

- The molten salt materials are perhaps more suited to use in a component test facility (or similar fusion testing device) where tritium self-sufficiency is not a set requirement. The advantages surrounding the use of molten salts can be utilised with a small loss of performance regarding TBR and energy multiplication.
- The thick breeder blanket in conventional tokamaks provides adequate shielding of the magnets, both on the outboard and inboard.

Some recommendations for further blanket performance studies, developing on work presented in this thesis:

- The liquid metal breeders of LiPb and LiSn, and the molten salt LiBeF, have the most potential for use in liquid blanket concepts for fusion power plants. Further optimisation of these should be considered and the performance in a more mature DEMO neutronics model assessed. Considering the effects of liquid breeder flow rate on the tritium control and activation would also be advantageous.
- In terms of the shutdown activation, the dominant long-lived nuclides (in particular the ^{14}C and ^{205}Pb and Sn radionuclides) could potentially impact on the radioactive waste disposal options. This should be studied in further detail and with respect to a DEMO model using a more detailed irradiation scenario than that used with the HTS spherical tokamak.

6.2 Shielding requirements of HTS spherical tokamaks

Scoping studies have been performed to investigate the effect on shielding requirements due to varying geometric parameters, and how this limits the reduction in overall size of spherical tokamaks. The neutronics performance of a more detailed high temperature spherical tokamaks model (HTS-ST) was also assessed. The research can be summarised in the following:

- At least 0.4 m of tungsten carbide shielding is required to reduce the centre column heating and neutron fast flux to acceptable levels. This thickness of

shielding required a tokamak major radius of 3 m based on the geometry conditions set in the parameterisation.

- In scoping studies, the TBR was relatively unaffected by the changing shielding thickness. No ports, divertor regions or blanket gaps were considered.
- The TBR performance of a solid breeder (Li_4SiO_4) in the HTS-ST model compared well against the liquid breeder proposed by Princeton Plasma Physics Laboratory. Further optimisation of the TBR could be performed through ^6Li enrichment and multiplier ratios. The use of different optimisation in each blanket could also be considered to increase TBR and make more efficient use of the lithium and multiplying materials.
- The fast neutron flux will limit the lifetime of the magnets. In the HTS-ST model the centre column magnets were shown to have an estimated lifetime of ~2.5 FPY. If the magnets can be assumed to withstand higher neutron fluence (as is anticipated due to advances in manufacturing techniques) then the 3.1 FPY operational life for the Princeton Plasma Physics Laboratory proposed fusion nuclear science facility can reasonably be achieved.
- It is increasingly accepted within the fusion community that another fusion device, whether called a fusion nuclear science facility, fusion neutron source, component test facility, materials testing device, etc., will be required before a DEMO power plant. A HTS spherical tokamak looks to be a favourable option, with reduced size and associated lower costs. The neutronics assessment provides encouraging results.

6.3 Radioactive waste assessment for DEMO

The radioactive waste assessment using the EU generic 2015 DEMO model demonstrates some of the important aspects for a fusion relevant waste management plan. The conclusions are summarised as:

- Fusion plants will not produce radioactive products as a result of the fusion reaction, such as those associated with nuclear fission.
- Although a fusion power plant will not produce high level wastes, the tokamak could create substantial quantities of ILW and LLW. Even after 1000 years

there will still be some radioactive waste, ~ 4 kt ILW and 27 kt of LLW. However the results also suggest that after 100 years nearly all of the material could be considered for recycling, satisfying the intended waste strategy of a fusion power plant.

- The use of dismantling techniques will be imperative in reducing the amount of ILW and LLW by segregating wastes. In this research dismantling sections of the outboard vacuum vessel has shown to reduce the ILW waste from the vacuum vessel at 100 years cooling time from ~12 kt to 5 kt.

The radioactive waste assessment was also used to compare neutronics methods and the effect of neutronic modelling approximations, such as neutron flux averaging. The following recommendations are made regarding the neutronics methods:

- The conventional cell-based approach relies of flux averaging over cells comprising the geometry. This can be reduced through cell-splitting, however this is time consuming and an inefficient method.
- A mesh-based approach allows the dismantling and separation of waste to be investigated. A significant increase in the potential output data can be acquired, when using a mesh-based method, from what is essential the same calculation. There is an increase in computational time as a FISPACT irradiation calculation is performed on every voxel instead of every cell, however these calculations are relatively quick compared to the neutron transport - which must be performed for either approach.
- In the case of a structured mesh, a material mixing step is introduced which is not ideal.
- The use of unstructured mesh geometry alleviates the materials mixing problem. The neutron flux is tallied directly on the mesh elements comprising the geometry with a FISPACT calculation performed on each of the elements.
- The unstructured mesh approach has the potential to be a more accurate method for calculating radioactive waste whilst also reducing neutronics model building efforts.

Important areas for further development and future studies include:

- The effect of different waste classes could be considered in further work, particularly around the use of the French system that does not allow for clearing of waste material created on a nuclear site.
- A comparison should be made on the neutronics assessment of an unstructured mesh created using the original CAD (with only minimum simplifications) and a CSG model created using a suitably simplified CAD model. This would investigate the effects of the simplification and be useful in cost benefit analysis with respect to model production time.
- Further testing of the unstructured mesh geometry with GVR techniques is a particularly important development requirement for producing a robust neutronic relevant analysis method.
- On-going investigations into uncertainty propagation for shutdown dose rate analysis should be investigated further with relation to radioactive waste inventory, and comparison made to uncertainty assumptions similar to those made in this research.
- The effect on radioactive waste inventory due to the retention of tritium should be investigated. An initial approach could be to add a quantity of tritium into the materials file during the irradiation step of the neutronics method.

6.4 Closing comment

Although there are a number of significant challenges surrounding fusion power, these are not insurmountable. The advantages regarding waste arising is of particular importance when considering options for future energy sources. With the recent advances in HTS magnets there is further optimism with regards to a reduced cost, near-term, compact device using a spherical tokamak concept.

REFERENCES

[1] W. M. Stacey, *Fusion Plasma Physics*. Weinheim, Germany: WILEY-VCH, 2012.

[2] J. P. Freidberg, *Plasma Physics and Fusion Energy*. Cambridge University Press, 2007.

[3] C. Llewellyn Smith, "The path to fusion power," *Eur. Phys. J. Spec. Top.*, vol. 176, no. 1, pp. 167–178, Sep. 2009.

[4] Kaye & Laby, *Tables of Physical & Chemical Constants (16th edition 1995). 2.1.4 Hygrometry.* 2005.

[5] Culham Centre for Fusion Energy, "Introduction to fusion," *United Kingdom Atomic Energy Authority*, 2012. .

[6] EUROfusion Consortium., "EUROfusion." [Online]. Available: www.euro-fusion.org. [Accessed: 01-Jan-2016].

[7] "ITER Organization." [Online]. Available: http://www.iter.org/. [Accessed: 01-Jan-2016].

[8] MIT Department of Physics, "Superconductivity : The Meissner Effect , Persistent Currents and the Josephson Effects," pp. 1–16, 2011.

[9] C. B. Eom, M. K. Lee, J. H. Choi, et al., "High critical current density and enhanced irreversibility field in superconducting MgB2 thin films," *Nature*, vol. 411, no. 6837, pp. 558–560, May 2001.

[10] Z. S. Hartwig, C. B. Haakonsen, R. T. Mumgaard, et al., "An initial study of demountable high-temperature superconducting toroidal field magnets for the Vulcan tokamak conceptual design," *Fusion Eng. Des.*, vol. 87, no. 3, pp. 201–214, Mar. 2012.

[11] W. H. Fietz, C. Barth, S. Drotziger, et al., "Prospects of High Temperature Superconductors for fusion magnets and power applications," *Fusion Eng. Des.*, vol. 88, no. 6–8, pp. 440–445, Oct. 2013.

[12] A. P. Malozemoff, *Superconductors in the Power Grid*. Elsevier, 2015.

[13] N. Fujiwara, H. Hayashi, S. Nagaya, et al., "Development of YBCO power devices in Japan," *Phys. C Supercond.*, vol. 470, no. 20, pp. 980–985, Nov. 2010.

[14] P. N. Barnes, M. D. Sumption, & G. L. Rhoads, "Review of high power density superconducting generators: Present state and prospects for incorporating YBCO windings," *Cryogenics (Guildf).*, vol. 45, no. 10–11, pp. 670–686, Oct. 2005.

[15] A. Sykes, M. P. Gryaznevich, D. Kingham, et al., "Recent Advances on the Spherical Tokamak Route to Fusion Power," *IEEE Trans. Plasma Sci.*, vol. 42, no. 3, pp. 482–488, 2014.

[16] H. Hashizume & S. Ito, "Design prospect of remountable high-temperature superconducting magnet," *Fusion Eng. Des.*, vol. 89, no. 9–10, pp. 2241–2245, Oct. 2014.

[17] V. Selvamanickam, Y. Chen, X. Xiong, et al., "Progress in second-generation

HTS wire development and manufacturing," *Phys. C Supercond.*, vol. 468, no. 15–20, pp. 1504–1509, Sep. 2008.

[18] F. Dahlgren & T. Brown, "ARIES-AT magnet systems," *Fusion Eng. Des.*, vol. 80, pp. 139–160, Mar. 2006.

[19] M. Carrera, X. Granados, J. Amorós, et al., "Current distribution in wide YBCO tapes," *Phys. Procedia*, vol. 36, pp. 1625–1630, 2012.

[20] D. Maisonnier & EFDA, "Final Report of the European Fusion Power Plant Conceptual Study," 2005.

[21] D. Maisonnier, D. Campbell, I. Cook, et al., "Power plant conceptual studies in Europe," *Nucl. Fusion*, vol. 47, no. 11, pp. 1524–1532, Nov. 2007.

[22] D. a. Gates, C. Jun, I. Zatz, et al., "All-metal transformer core for a low aspect ratio tokamak," *Fusion Eng. Des.*, vol. 86, no. 1, pp. 41–44, 2011.

[23] Y.-K. M. Peng & J. B. Hicks, "Engineering feasibility of tight aspect ratio Tokamak (spherical torus) reactors," 1990.

[24] D. Fasel & M. Q. Tran, "Availability of lithium in the context of future D–T fusion reactors," *Fusion Eng. Des.*, vol. 75–79, pp. 1163–1168, Nov. 2005.

[25] L. W. Packer, R. Pampin, & S. Zheng, "Tritium self-sufficiency time and inventory evolution for solid-type breeding blanket materials for DEMO," *J. Nucl. Mater.*, vol. 417, no. 1–3, pp. 718–722, Oct. 2011.

[26] M. A. Abdou, E. L. Vold, C. Y. Gung, et al., "Deuterium-Tritium fuel self-sufficiency in fusion reactors," *Fusion Technol.*, vol. 9, pp. 250–285, 1985.

[27] L. . Boccaccini, L. Giancarli, G. Janeschitz, et al., "Materials and design of the European DEMO blankets," *J. Nucl. Mater.*, vol. 329–333, no. 2004, pp. 148–155, Aug. 2004.

[28] R. A. Causey, J. N. Brooks, & G. Federici, "Tritium in v entory and reco v ery in next-step fusion de v ices," vol. 62, 2002.

[29] L. M. Giancarli, M. Abdou, D. J. Campbell, et al., "Overview of the ITER TBM Program," *Fusion Eng. Des.*, vol. 87, no. 5–6, pp. 395–402, Aug. 2012.

[30] L. Giancarli, V. Chuyanov, M. Abdou, et al., "Test blanket modules in ITER: An overview on proposed designs and required DEMO-relevant materials," *J. Nucl. Mater.*, vol. 367–370, pp. 1271–1280, Aug. 2007.

[31] F. Romanelli, "EFDA, Fusion Electricity: A roadmap to the realisation of fusion energy," pp. 1–75, 2012.

[32] D. Maisonnier, I. Cook, S. Pierre, et al., "DEMO and fusion power plant conceptual studies in Europe," *Fusion Eng. Des.*, vol. 81, no. 8–14, pp. 1123–1130, Feb. 2006.

[33] D. Maisonnier, "European DEMO design and maintenance strategy," *Fusion Eng. Des.*, vol. 83, no. 7–9, pp. 858–864, Dec. 2008.

[34] A. . Raffray, R. Jones, G. Aiello, et al., "Design and material issues for high performance SiCf/SiC-based fusion power cores," *Fusion Eng. Des.*, vol. 55, no. 1, pp. 55–95, May 2001.

[35] G. Federici, R. Kemp, D. Ward, et al., "Overview of EU DEMO design and

R&D activities," *Fusion Eng. Des.*, vol. 89, no. 7–8, pp. 882–889, Oct. 2014.

[36] D. Stork, P. Agostini, J.-L. Boutard, et al., "Materials R&D for a timely DEMO: Key findings and recommendations of the EU Roadmap Materials Assessment Group," *Fusion Eng. Des.*, vol. 89, no. 7–8, pp. 1586–1594, Oct. 2014.

[37] M. Kovari, R. Kemp, H. Lux, et al., "'PROCESS': A systems code for fusion power plants—Part 1: Physics," *Fusion Eng. Des.*, vol. 89, no. 12, pp. 3054–3069, Dec. 2014.

[38] U. Fischer, C. Bachmann, J.-C. Jaboulay, et al., "Neutronic performance issues of the breeding blanket options for the European DEMO fusion power plant," *Fusion Eng. Des.*, Dec. 2015.

[39] U. Fischer, "Guidelines for Neutronic Analyses," *Priv. Commun.*, 2015.

[40] EUROfusion Consortium., "Generic DEMO 2015 CAD model," *Priv. Commun.*, 2015.

[41] M. E. Sawan & M. a. Abdou, "Physics and technology conditions for attaining tritium self-sufficiency for the DT fuel cycle," *Fusion Eng. Des.*, vol. 81, no. 8–14, pp. 1131–1144, Feb. 2006.

[42] J. P. Catalán, F. Ogando, J. Sanz, et al., "Neutronic analysis of a dual He/LiPb coolant breeding blanket for DEMO," *Fusion Eng. Des.*, vol. 86, no. 9–11, pp. 2293–2296, Oct. 2011.

[43] T. Nishitani, M. Yamauchi, S. Nishio, et al., "Neutronics design of the low aspect ratio tokamak reactor, VECTOR," *Fusion Eng. Des.*, vol. 81, no. 8–14, pp. 1245–1249, Feb. 2006.

[44] Z. Zhu, Q. Huang, S. Gao, et al., "Design analysis of DRAGON-IV LiPb loop," *Fusion Eng. Des.*, vol. 86, no. 9–11, pp. 2666–2669, Oct. 2011.

[45] Y. Chen, U. Fischer, & P. Pereslavtsev, "Neutronic design issues of the WCLL and HCPB power plant models," *Fusion Eng. Des.*, vol. 69, no. 1–4, pp. 655–661, Sep. 2003.

[46] P. Batistoni, M. Angelone, U. Fischer, et al., "Design optimisation and measuring techniques for the neutronics experiment on a HCLL–TBM mock-up," *Fusion Eng. Des.*, vol. 84, no. 2–6, pp. 430–434, Jun. 2009.

[47] W. Pohorecki, T. Kuc, B. Ostachowicz, et al., "Novel methods of tritium production rate measurements in HCLL TBM mock-up experiment with liquid scintillation technique," *Fusion Eng. Des.*, vol. 86, no. 9–11, pp. 2429–2432, Oct. 2011.

[48] I. Kodeli, a. Trkov, P. Batistoni, et al., "Sensitivity and uncertainty analysis of the HCLL breeder blanket experiment in the frame of the EU fusion technology programme," *Nucl. Eng. Des.*, vol. 241, no. 4, pp. 1243–1247, Apr. 2011.

[49] M. Übeyli, "On the Tritium Breeding Capability of Flibe , Flinabe , and Li 20 Sn 80 in a Fusion-Fission (Hybrid) Reactor," vol. 22, no. 1, 2004.

[50] M. Sawan, "Tritium Breeding Potential of Lithium-Tin," no. November, 1998.

[51] Y. Kang, K. Okamura, & T. Terai, "Tritium generation rate in the Li20Sn80 neutron irradiation experiments," *Fusion Eng. Des.*, vol. 75–79, pp. 1009–1013,

Nov. 2005.

[52] Y. Kang & T. Terai, “Moderate tritium properties in lithium–tin alloy as a liquid breeder/coolant,” *Fusion Eng. Des.*, vol. 81, no. 1–7, pp. 519–523, Feb. 2006.

[53] M. Sawan, “Tritium Breeding Potential of Flibe Tritium Breeding in Flibe is Marginal,” no. November, 1998.

[54] M. . Youssef, M. . Sawan, & D.-K. Sze, “The breeding potential of ‘flinabe’ and comparison to ‘flibe’ in ‘CLiFF’ high power density concept,” *Fusion Eng. Des.*, vol. 61–62, pp. 497–503, Nov. 2002.

[55] C. P. C. Wong, S. Malang, M. Sawan, et al., “Molten salt self-cooled solid first wall and blanket design based on advanced ferritic steel,” *Fusion Eng. Des.*, vol. 72, no. 1–3, pp. 245–275, Nov. 2004.

[56] Y. Someya, H. Takase, H. Utoh, et al., “Simplification of blanket system for SlimCS fusion DEMO reactor,” *Fusion Eng. Des.*, vol. 86, no. 9–11, pp. 2269–2272, Oct. 2011.

[57] K. M. Feng, G. S. Zhang, G. Y. Zheng, et al., “Conceptual design study of fusion DEMO plant at SWIP,” *Fusion Eng. Des.*, vol. 84, no. 12, pp. 2109–2113, Dec. 2009.

[58] N. Roux, S. Tanaka, C. Johnson, et al., “Ceramic breeder material development,” *Fusion Eng. Des.*, vol. 41, no. 1–4, pp. 31–38, Sep. 1998.

[59] I. Palermo, J. M. Gómez-Ros, G. Veredas, et al., “Preliminary neutronic assessment of a helium-cooled Li8PbO6 breeding blanket design for DEMO,” *Fusion Eng. Des.*, vol. 87, no. 2, pp. 195–199, Feb. 2012.

[60] S. Colominas, I. Palermo, J. Abellà, et al., “Octalithium plumbate as breeding blanket ceramic: Neutronic performances, synthesis and partial characterization,” *Fusion Eng. Des.*, vol. 87, no. 5–6, pp. 482–485, Aug. 2012.

[61] R. Lässer, N. Baluc, J.-L. Boutard, et al., “Structural materials for DEMO: The EU development, strategy, testing and modelling,” *Fusion Eng. Des.*, vol. 82, no. 5–14, pp. 511–520, Oct. 2007.

[62] R. Lindau, a. Möslang, M. Rieth, et al., “Present development status of EUROFER and ODS-EUROFER for application in blanket concepts,” *Fusion Eng. Des.*, vol. 75–79, pp. 989–996, Nov. 2005.

[63] M. Gasparotto, L. V Boccaccini, L. Giancarli, et al., “Demo blanket technology R & D results in EU,” vol. 62, pp. 263–271, 2002.

[64] D. Aquaro, N. Cerullo, I. Ciucci, et al., “Adaptation of the HCPB DEMO TBM as breeding blanket for ITER: Neutronic and thermal analyses,” *Fusion Eng. Des.*, vol. 82, no. 15–24, pp. 2226–2232, Oct. 2007.

[65] a K. Suri, N. Krishnamurthy, & I. S. Batra, “Materials issues in fusion reactors,” *J. Phys. Conf. Ser.*, vol. 208, p. 012001, Feb. 2010.

[66] D. Cutoiu, “ASPECTS OF RADIOACTIVE WASTE MANAGEMENT Dan Cutoiu Institute for Physics and Nuclear Engineering,” vol. 55, no. 1, pp. 102–117, 2003.

[67] ONR, “Basic principles of radioactive waste management An introduction to

the management of higher activity radioactive waste on nuclear licensed sites," no. February, pp. 1–22, 2015.

[68] W. Pohorecki, S. Taczanowski, M. Kopec, et al., "Activation, decay heat and waste analysis for a European HCLL DEMO concept," *Fusion Eng. Des.*, vol. 86, no. 9–11, pp. 2705–2708, Oct. 2011.

[69] L. L. Carter & E. D. Cashwell, "Particle-Transport Simulation with the Monte Carlo Method." 1975.

[70] B. L. Kirk, "Overview of Monte Carlo radiation transport codes," *Radiat. Meas.*, vol. 45, no. 10, pp. 1318–1322, Dec. 2010.

[71] R. Kong, M. Ambrose, & J. Spanier, "Efficient, Automated Monte Carlo Methods for Radiation Transport.," *J. Comput. Phys.*, vol. 227, no. 22, pp. 9463–9476, Nov. 2008.

[72] X-5 Monte Carlo Team, "MCNP - A General Monte Carlo N-Particle Transport Code, Version 5 Volume 1: Overview and Theory," *Los Alamos Nucl. Lab.*, 2008.

[73] J. K. Shultis & R. E. Faw, "An mcnp primer," vol. 66506, no. c, 2011.

[74] F. B. Brown, "Fundamentals of Monte Carlo particle transport," *Los Alamos Natl. Lab. LA-UR-05-4983*, vol. 836, 2005.

[75] R.A. Forrest, "FISPACT-2007 user manual," *UKAEA Rep. FUS 534*.

[76] J. Sublet, "The FISPACT-II User Manual," *CCFE-R(11)*, no. 6, 2014.

[77] JC. Sublet, J. W. Eastwood, J. G. Morgan, et al., "The FISPACT-II User Manual," *UKAEA-R(11)11 Issue 7*, 2015.

[78] J. C. Sublet, J. W. Eastwood, & J. G. Morgan, "Reaction rate uncertainty quantification and propagation."

[79] A. Davis & R. Pampin, "Benchmarking the MCR2S system for highresolution activations dose analysis in ITER," *Fusion Eng. Des.*, vol. 85, pp. 87–92, 2010.

[80] Y. Chen & U. Fischer, "Rigorous MCNP based shutdown dose rate calculations: computational scheme, verification calculations and application to ITER," *Fusion Eng. Des.*, no. 63/64, pp. 107–114, 2002.

[81] S. Chiocchio & et al., "ITER Project Requirements," *Priv. Commun.*, 2015.

[82] D. Leichtle, P. Y. Chaffard, J. Izquierdo, et al., "Status of the ITER tokamak nuclear shielding and radiological protection design," *Fusion Eng. Des.*, Feb. 2016.

[83] B. Colling, T. Eade, M. J. Joyce, et al., "Neutronics analysis for integration of ITER diagnostics port EP10," *Fusion Eng. Des.*, Jan. 2016.

[84] R. Villari, U. Fischer, F. Moro, et al., "Shutdown dose rate assessment with the Advanced D1S method: Development, applications and validation," *Fusion Eng. Des.*, vol. 89, no. 9–10, pp. 2083–2087, Oct. 2014.

[85] R. Villari, P. Batistoni, M. Angelone, et al., "Neutronics experiments and analyses in preparation of DT operations at JET," *Fusion Eng. Des.*, Feb. 2016.

[86] Y. Wu & FDS Team, "CAD-based interface programs for fusion neutron transport simulation," *Fusion Eng. Des.*, vol. 84, pp. 1987–1992, 2009.

[87] Sandia Corporation, “Cubit 14.1.” 2014.

[88] “ANSYS Workbench 2.0 Framework.” 2014.

[89] “ANSYS Workbench.” 2015.

[90] The UW CNERG Team, “DAGMC,” 2015. [Online]. Available: http://svalinn.github.io/DAGMC/. [Accessed: 01-Dec-2015].

[91] The UW CNERG Team, “Using DAGMC - The DAGMC Workflow,” 2015. [Online]. Available: http://svalinn.github.io/DAGMC/usersguide/workflow.html. [Accessed: 01-Dec-2015].

[92] The UW CNERG Team, “DAGMC Developers Guide,” 2015. [Online]. Available: http://svalinn.github.io/DAGMC/devguide/index.html. [Accessed: 01-Dec-2015].

[93] Sandia Corporation, “Cubit 12.2.” 2010.

[94] Sandia Corporation, “Sandia National Laboratories,” 2015. [Online]. Available: http://www.sandia.gov/.

[95] D. Pelowitz et al., “MCNP6 Users Manual – Code Version 1.0, LA-CP-13-00634 Rev 0.”

[96] T. Goorley & et al, “Initial MCNP6 Release Overview,” *Nucl. Technol.*, no. 180, pp. 298–315, 2012.

[97] R. L. Martz & D. L. Crane, “The MCNP6 Book On Unstructured Mesh Geometry : Foundations Chapter 1 : Fundamentals,” 2012.

[98] R. L. Martz, “The MCNP6 Book On Unstructured Mesh Geometry : User ’ s Guide,” no. April, 2013.

[99] M. B. Chadwick, M. Herman, P. Obložinský, et al., “ENDF/B-VII.1: Nuclear Data for Science and Technology: Cross Sections, Covariances, Fission Product Yields and Decay Data,” *Nucl. Data Sheets*, vol. 112, no. 12, pp. 2887–2996, 2011.

[100] K. Shibata, O. IWAMOTO, T. NAKAGAWA, et al., “JENDL-4.0: A New Library for Nuclear Science and Engineering,” *J. Nucl. Sci. Technol.*, Jan. 2012.

[101] A. Koning, R. Forrest, & Et al., *The JEFF-3 . 1 Nuclear Data Library*, no. 6190. NUCLEAR ENERGY AGENCY, 2006.

[102] A. Koning, D. Rochman, S. van der Marck, et al., “TENDL-2014: TALYS-based evaluated nuclear data library,” *NRG Petten*, 2014. [Online]. Available: www.talys.eu/tendl-2014.html.

[103] D. L. Aldama & D. Lopez Al-dama and A. Trkov, “FENDL-2.1: update of an evaluated nuclear data library for fusion applications,” *IAEA Rep. INDC(NDS)-46*, no. December 2004, 2004.

[104] R. Forest et al., “FENDL3 Library, Final Report of the Coordinated Research Project on Nuclear Data Libraries for Advance Systems: Fusion Devices,” *INDC(NDS)-0645*.

[105] A. Sood, “Doppler Energy Broadening for Incoherent Scattering in MCNP5, Part I,” *LA-UR-04-0487*, vol. 836, pp. 0–19, 2004.

[106] A. Sood, “Doppler Energy Broadening for Incoherent Scattering in MCNP5, Part II,” *LA-UR-04-0488*, vol. 836, pp. 0–19, 2004.

[107] B. C. Kiedrowski, F. B. Brown, M. C. White, et al., “Testing for the Photon Doppler Broadening Data Sampling,” vol. 836.

[108] M. C. White, “Further Notes on MCPLIB03/04 and New MCPLIB63/84 Compton Broadening Data For All Versions of MCNP5,” *LA-UR-12-00018*, 2012.

[109] JC. Sublet, “EAF 2010 neutron-induced cross section library,” *CCFE-R(10)05*.

[110] M. A. Cooper & E. W. Larsen, “Automated weight windows for global Monte Carlo particle transport calculations,” *Nucl. Sci. Eng.*, vol. 137, no. 1, pp. 1–13, 2001.

[111] S. W. Mosher & et al., “ADVANTG—AN AUTOMATED VARIANCE REDUCTION PARAMETER GENERATOR,” *OAK RIDGE Natl. Lab.*, 2015.

[112] A. M. Bevill & S. W. Mosher, “A New Source Biasing Approach in ADVANTG.”,” *Trans. Am. Nucl. Soc.*, no. 106, pp. 350–353, 2012.

[113] M. E. Sawan, B. Smith, E. P. Marriott, et al., “Three-dimensional nuclear analysis for the US dual coolant lead lithium ITER test blanket module,” *Fusion Eng. Des.*, vol. 85, no. 7–9, pp. 1027–1032, Dec. 2010.

[114] J. Cheng, Y. Wu, W. Tian, et al., “Neutronics and thermo-hydraulic design of supercritical-water cooled solid breeder TBM,” *Fusion Eng. Des.*, vol. 92, pp. 52–58, Mar. 2015.

[115] P. Pereslavtsev, C. Bachmann, & U. Fischer, “Neutronic analyses of design issues affecting the tritium breeding performance in different DEMO blanket concepts,” *Fusion Eng. Des.*, Jan. 2016.

[116] J. Shimwell, S. Lilley, L. Morgan, et al., “Reducing beryllium content in mixed bed solid-type breeder blankets,” *Fusion Eng. Des.*, Nov. 2015.

[117] G. . Voss, A. Bond, J. E. . Edwards, et al., “Toroidal field coil design for the spherical tokamak power plant,” *Fusion Eng. Des.*, vol. 48, no. 3–4, pp. 407–418, Sep. 2000.

[118] C. G. Windsor, J. G. Morgan, & P. F. Buxton, “Heat deposition into the superconducting central column of a spherical tokamak fusion plant,” *Nucl. Fusion*, vol. 55, no. 2, p. 023014, Feb. 2015.

[119] R. Pampin, S. Zheng, S. Lilley, et al., “Activation analyses updating the ITER radioactive waste assessment,” *Fusion Eng. Des.*, vol. 87, no. 7–8, pp. 1230–1234, Aug. 2012.

[120] Y. Someya, K. Tobita, S. Yanagihara, et al., “Waste management scenario in the hot cell and waste storage for DEMO,” *Fusion Eng. Des.*, vol. 89, no. 9–10, pp. 2033–2037, Oct. 2014.

[121] J. Li, Q. Zeng, M. Chen, et al., “Comparison analysis of 1D/2D/3D neutronics modeling for a fusion reactor,” *Fusion Eng. Des.*, vol. 83, no. 10–12, pp. 1678–1682, Dec. 2008.

[122] B. Weinhorst, U. Fischer, L. Lu, et al., “Comparative assessment of different approaches for the use of CAD geometry in Monte Carlo transport calculations,”

Fusion Eng. Des., vol. 98–99, pp. 2094–2097, Oct. 2015.

[123] "Karlsruhe Institute of Technology." Karlsruhe, Germany.

[124] T. Eade, D. Stonell, & A. Turner, "MCR2S unstructured mesh capabilities for use in shutdown dose rate analysis," *Fusion Eng. Des.*, vol. 100, pp. 321–333, Nov. 2015.

[125] C. W. Lee, Y.-O. Lee, M.-Y. Ahn, et al., "Sensitivity of the homogenized model in the neutronics analysis for the Korea Helium Cooled Solid Breeder Test Blanket Module," *Fusion Eng. Des.*, vol. 87, no. 5–6, pp. 575–579, Aug. 2012.

[126] B. R. Colling & S. D. Monk, "Development of fusion blanket technology for the DEMO reactor.," *Appl. Radiat. Isot.*, vol. 70, no. 7, pp. 1370–2, Jul. 2012.

[127] S. Zheng & CCFE, "Rectangular cross-section MCNP tokamak model." 2010.

[128] L. Bromberg, M. Tekula, L. . El-Guebaly, et al., "Options for the use of high temperature superconductor in tokamak fusion reactor designs," *Fusion Eng. Des.*, vol. 54, no. 2, pp. 167–180, Feb. 2001.

[129] A. Nishimura, T. Takeuchi, S. Nishijima, et al., "Neutron irradiation effects on superconducting wires and insulating materials," *Fusion Eng. Des.*, vol. 84, no. 7–11, pp. 1425–1428, Jun. 2009.

[130] R. Prokopec, D. X. Fischer, H. W. Weber, et al., "Suitability of coated conductors for fusion magnets in view of their radiation response," *Supercond. Sci. Technol.*, vol. 28, no. 1, p. 014005, Jan. 2015.

[131] L. A. El-Guebaly, "ARIES-ST nuclear analysis and shield design," *Fusion Eng. Des.*, vol. 65, no. 2, pp. 263–284, Feb. 2003.

[132] A. Nishimura, T. Takeuchi, S. Nishijima, et al., "Fast neutron irradiation effect on superconducting properties of Nb3Sn and Nb3Al strands," 2012, pp. 217–224.

[133] L. El-Guebaly, M. Harb, A. Davis, et al., "Shielding and Breeding Considerations for ST-Based HTS-FNSF Design," *18th Internaonal Spherical Torus Work. Princet. Univ.*, 2015.

[134] Neutronics Group, "Culham Centre for Fusion Energy (CCFE)." Oxfordshire.

[135] T. Brown, "ST-FNSF Preliminary CAD model (FNSF-3M)." PPPL, 2015.

[136] J. Menard, T. Brown, & L. El-Guebaly, "PPPL LDRD status and CCFE collaboration possibilities for 'High temperature superconductors for increased efficiency Spherical Tokamaks.'" 2015.

[137] S. Zheng, "CTF2008-neutronics-model." CCFE, 2009.

[138] S. Zheng, G. M. Voss, & R. Pampin, "Neutronics analysis of the conceptual design of a component test facility based on the spherical tokamak," *Fusion Eng. Des.*, vol. 85, no. 10–12, pp. 2300–2304, 2010.

[139] S. Rosanvallon, B. C. Na, M. Benchikhoune, et al., "ITER waste management-2010," *Fusion Eng. Des.*, vol. 85, no. 10–12, pp. 1788–1791, Dec. 2010.

[140] F. J. Maringer, G. Mirescu, P. Ková, et al., "MetroRWM - Metrology for radioactive waste management Review of clearance levels and acceptance

criteria legislation ," 2011.

[141] Council of the European Union, "Council Directive 96/29/Euratom," *Off. J. Eur. Union*, no. L, pp. L159/1–159/114, 1996.

[142] DEFRA, "Guidance on the scope of and exemptions from the radioactive substances legislation in the UK ," no. September, p. 112, 2011.

[143] INTERNATIONAL ATOMIC ENERGY AGENCY, "IAEA Safety Standards: Classification of Radioactive Waste - No. GSG-1," *Gen. Saf. Guid. IAEA*, p. 68, 2009.

[144] "IAEA SAFETY STANDARDS SERIES." [Online]. Available: http://www-pub.iaea.org/MTCD/Publications/PDF/Pub1202_web.pdf. [Accessed: 22-Nov-2015].

[145] ONR GUIDE, "LC33: Disposal of radioactive waste; ONR GUIDE," 2013.

[146] "Decree No. 2008-357 of 16 April 2008 made for the implementation of Article L. 542-1-2 the environmental code and determining the requirements for the National Plan of management of radioactive materials and waste."

[147] Office parlementaire, "THE 2006 PROGRAMME ACT ON THE SUSTAINABLE MANAGEMENT OF RADIOACTIVE MATERIALS AND WASTES," vol. 2006, no. April, 2006.

[148] ANDRA, "Activity report and sustainable development #13," 2013.

[149] J. Pamela, J.-M. Bottereau, D. Canas, et al., "ITER tritiated waste management by the Host state and first lessons learned for fusion development," *Fusion Eng. Des.*, vol. 89, no. 9–10, pp. 2001–2007, Oct. 2014.

[150] S. Rosanvallon, "Waste management within the framework of ITER in Cadarache," *Fusion Eng. Des.*, vol. 69, no. 1–4, pp. 531–536, Sep. 2003.

[151] S. Rosanvallon, D. Torcy, J. K. Chon, et al., "Waste management plans for ITER," *Fusion Eng. Des.*, Dec. 2015.

[152] DEFRA, "Environmental Permitting Guidance Radioactive Substances Regulation," *Energy and climate change*, 2011. [Online]. Available: https://www.gov.uk/government/uploads/system/uploads/attachment_data/file/69503/pb13632-ep-guidance-rsr-110909.pdf. [Accessed: 12-Jan-2016].

[153] EUROPEAN COMMISSION, "Practical use of the concepts of clearance and exemption – Part I: Guidance on General Clearance Levels for Practices; Recommendations of Group of Experts established under the terms of Article 31 of the Euratom Treaty; Radiation Protection No. 122," vol. 6, no. 376 2, 2000.

[154] INTERNATIONAL ATOMIC ENERGY AGENCY, *Application of the Concepts of Exclusion, Exemption and Clearance Safety Guide RS-G-1.7*, vol. SAFETY GUI. 2004.

[155] S. Thierfeldt, B. Rainer, & W. Stefan, "RADIATION PROTECTION NO 157; Comparative Study of EC and IAEA Guidance on Exemption and Clearance Levels," no. 157, 2010.

[156] Council of the European Union, "Council Directive 2013/59/Euratom," *Off. J. Eur. Union*, vol. 56, p. 216, 2013.

[157] K. Liger, P. Trabuc, J. Mascarade, et al., “Preliminary results from a detritiation facility dedicated to soft housekeeping waste and tritium valorization,” *Fusion Eng. Des.*, vol. 89, no. 9–10, pp. 2103–2107, Oct. 2014.

[158] A. N. Perevezentsev, A. C. Bell, J. Williams, et al., “Detritiation studies for JET decommissioning,” *Fusion Eng. Des.*, vol. 83, no. 10–12, pp. 1364–1367, Dec. 2008.

[159] R. García, J. P. Catalán, & J. Sanz, “Assessment of radioactive wastes from a DCLL fusion reactor: Disposal in El Cabril facility,” *Fusion Eng. Des.*, vol. 89, no. 9–10, pp. 2038–2042, Oct. 2014.

[160] A. . Serikov & R. . Forrest, “Activation analysis and waste management for RF DEMO-S materials,” *Fusion Eng. Des.*, vol. 51–52, pp. 617–622, Nov. 2000.

[161] M. Zucchetti, L. A. El-Guebaly, R. A. Forrest, et al., “The feasibility of recycling and clearance of active materials from fusion power plants,” *J. Nucl. Mater.*, vol. 367–370, pp. 1355–1360, Aug. 2007.

[162] M. Zucchetti, R. Forrest, C. Forty, et al., “Clearance, recycling and disposal of fusion activated material,” *Fusion Eng. Des.*, vol. 54, no. 3–4, pp. 635–643, Apr. 2001.

[163] EUROfusion Consortium., “Generic DEMO 2015 model- MCNP input,” *Priv. Commun.*, 2015.

[164] D. GROSSE & H. TSIGE-TAMIRAT, “Current Status of the CAD Interface Program for MC Particle Transport Codes McCad.” Int. Conf. on Advances in Mathematics, Computational Methods, and Reactor Physics, Saratoga Springs, 2009.

[165] Dassault Systèmes Simulia, “Abaqus CAE User’s Manual,” *Abaqus 6.12*, p. 1174, 2012.

[166] P. Pereslavtsev, U. Fischer, D. Grosse, et al., “Shutdown dose rate analysis for the European TBM system in ITER,” *Fusion Eng. Des.*, vol. 87, no. 5–6, pp. 493–497, Aug. 2012.

[167] ANSYS Inc., “Meshing User’s Guide.” .

[168] ANSYS Inc., “SpaceClaim.” .

[169] M.B. Chadwick et al., “ENDF/B-VII.1: Nuclear Data for Science and Technology: Cross Sections, Covariances, Fission Product Yields and Decay Data,” *Nucl. Data Sheets 112(2011)2887*.

[170] M. R. Gilbert, “Automated cell-based waste inventory script,” *Priv. Commun.*, 2015.

[171] EUROfusion Consortium., “Generic Demo 2013 CAD model,” *Priv. Commun.*, 2013.

[172] EUROfusion Consortium., “Generic DEMO 2013 model- MCNP input,” *Priv. Commun.*, 2013.

[173] S. Bimpson, “Estimating the disposal costs of spent fuel,” *Nucl. Eng. Int.*, pp. 45–46, 2011.

[174] World Nuclear Association, “Radioactive Waste Management,” 2015. [Online]. Available: http://www.world-nuclear.org/information-library/nuclear-fuel-

cycle/nuclear-wastes/radioactive-waste-management.aspx. [Accessed: 01-Jan-2016].

[175] R. Pampin, V. Massaut, & N. P. Taylor, “Revision of the inventory and recycling scenario of active material in near-term PPCS models,” vol. 469, 2007.

[176] R. . Causey, J. . Brooks, & G. Federici, “Tritium inventory and recovery in next-step fusion devices,” *Fusion Eng. Des.*, vol. 61–62, pp. 525–536, Nov. 2002.

[177] T. Hayashi, K. Tobita, Y. Nakamori, et al., “Advanced neutron shielding material using zirconium borohydride and zirconium hydride,” *J. Nucl. Mater.*, vol. 386–388, pp. 119–121, Apr. 2009.

[178] T. Dhliwayo, “Development of advanced shield systems for fast neutrons,” *International Nuclear Safety Journal*, vol. 3, no. 2. 09-Jun-2014.

[179] J. S. Hendricks, “Mcnp 0 X Form Factor Upgrade for Improved Photon Transport,” vol. 836, 2011.

[180] D. B. Pelowitz, “Mcnpx User’ S Manual,” *LA-CP-11-00438*, no. April, 2005.

[181] H. Hughes, “Quick - Start Guide to Low - Energy Photon / Electron Transport in MCNP6,” 2013.

[182] P. Pereslavtsev, D. Grosse, U. Fischer, et al., “HCLL DEMO 2012 Model - MCNP input.” Developed by Forschungszentrum Karlsruhe (KIT) for EUROfusion, 2012.

[183] M. Coleman, F. Maviglia, C. Bachmann, et al., “On the EU approach for DEMO architecture exploration and dealing with uncertainties,” *Fusion Eng. Des.*, Jan. 2016.

[184] J. C. Wagner, E. D. Blakeman, & D. E. Peplow, “Forward-Weighted CADIS Method for Global Variance Reduction,” *Ans_Winter*, no. 1, pp. 630–633, 2007.

[185] P. M. Kozikowski, A. T. Krawczyńska, M. Kulczyk, et al., “Tailoring mechanical properties of nano-structured Eurofer 97 steel for fusion applications,” *Phys. status solidi*, vol. 7, no. 5, pp. 1388–1390, Apr. 2010.

[186] P. Fernández, A. . Lancha, J. Lapeña, et al., “Metallurgical characterization of the reduced activation ferritic/martensitic steel Eurofer’97 on as-received condition,” *Fusion Eng. Des.*, vol. 58–59, pp. 787–792, Nov. 2001.

[187] A. Kohyama, A. Hishinuma, D. S. Gelles, et al., “Low-activation ferritic and martensitic steels for fusion application,” *J. Nucl. Mater.*, vol. 233–237, pp. 138–147, Oct. 1996.

[188] G. Marbach, I. Cook, & D. Maisonnier, “The EU power plant conceptual study,” *Fusion Eng. Des.*, vol. 63–64, pp. 1–9, Dec. 2002.

7 APPENDICES

APPENDIX 1: MATERIALS DATA

The following tables contain detailed material compositions for the materials (or for material homogenisation) used in the neutronics models of this thesis.

Table 7.1 - Materials used in blanket material composition study (Section 4.2).

Material	Lithium breeder	
Mass Density		0.5400
Element	ZAID	Fraction
Li	3006	7.5000E-02
	3007	9.2500E-01

Material	Helium coolant	
Mass Density		0.0002
Element	ZAID	Fraction
He	2004	1.0000E+00

Material	Beryllium multiplier	
Mass Density		1.8500
Element	ZAID	Fraction
Be	4009	1.0000E+00

Material	EUROFER steel structure	
Mass Density		7.7980
Element	ZAID	Fraction
C	6012	4.6029E-03
N	7014	1.1798E-03
	7015	4.3339E-06
O	8016	3.4542E-04
V	23000	2.1706E-03
Cr	24050	4.1579E-03
	24052	8.0181E-02
	24053	9.0919E-03
	24054	2.2632E-03
Mn	25055	4.0258E-03
Fe	26054	5.2586E-02
	26056	8.1748E-01
	26057	1.8717E-02
	26058	2.4956E-03
Ta	73181	3.6664E-04
W	74182	8.7000E-05
	74183	4.7304E-05
	74184	1.0156E-04
	74186	9.4608E-05

Table 7.2 - Composition of spherical tokamak materials (Section 4.4).

Component	**Homogenised material mix**	**Detailed composition**
Centre column magnet	95% HTSC coils + 5% helium (by volume)	HTSC- 42.55% Cu + 53.19% hastelloy steel + 2.13% Ag + 2.13% REBCO (by volume) Hastelloy steel- 55% Ni + 16% Mo + 15.5% Cr + 9.5% Fe + 4% W REBCO- $YBa_2Cu_3O_7$ (by mass)
Inboard shield	87% tungsten carbide + 13% water (by volume)	
Outboard first wall	90% EUROFER + 5% CuCrZr + 5% helium	EUROFER- 89.04% Fe + 9% Cr + 0.1% C + 0.4% Mn + 0.2% V + 0.03% N + 0.01% O + 0.12% Ta + 1.1% W CuCrZr- 98.9% Cu + 1% Cr + 0.1% Zr
Outboard breeder blanket	55% beryllium + 20% helium + 15% lithium breeder + 10% EUROFER	Lithium breeder- Li_4SiO_4 (natural ^6Li) EUROFER- 89.04% Fe + 9% Cr + 0.1% C + 0.4% Mn + 0.2% V + 0.03% N + 0.01% O + 0.12% Ta + 1.1%W
Outer structure	70% EUROFER + 30% water	EUROFER- 89.04% Fe + 9% Cr + 0.1% C + 0.4% Mn + 0.2% V + 0.03% N + 0.01% O + 0.12% Ta + 1.1%W Water- H_2O

Table 7.3 - Materials spherical tokamak (Section 4.4) continued.

Material	95% HTSC magnets + 5% helium (by volume)		**Material**	87% tungsten carbide + 13% water (by volume)		**Material**	90% EUROFER + 5% CuCrZr + 5% helium	
Mass density (g/cm^3)		8.327	Mass density (g/cm^3)		13.73	Mass density (g/cm^3)		7.466
Element	ZAID	Fraction	Element	ZAID	Fraction	Element	ZAID	Fraction
Cu	29063	3.00e-01	C	6012	4.33e-01	Fe	26056	7.71e-01
Ni	28058	2.17e-01	W	74184	1.33e-01	Cr	24052	7.70e-02
Cu	29065	1.34e-01	W	74186	1.24e-01	Fe	26054	4.96e-02
Cr	24052	8.48e-02	W	74182	1.14e-01	Cu	29063	3.62e-02
Ni	28060	8.34e-02	H	1001	8.94e-02	Fe	26057	1.77e-02
Fe	26056	5.29e-02	W	74183	6.19e-02	Cu	29065	1.61e-02
Mo	42098	1.37e-02	O	8016	4.50e-02	Cr	24053	8.73e-03
Ni	28062	1.16e-02	H	1002	1.34e-05	C	6012	4.39e-03
Cr	24053	9.61e-03				Cr	24050	3.99e-03
Mo	42096	9.44e-03				Mn	25055	3.84e-03
Mo	42095	9.01e-03				Fe	26058	2.35e-03
Mo	42092	8.40e-03				Cr	24054	2.17e-03
Ag	47107	7.70e-03				V	23000	2.07e-03
O	8016	7.37e-03				N	7014	1.12e-03
Ag	47109	7.15e-03				W	74184	9.68e-04
Mo	42100	5.45e-03				W	74186	9.02e-04
Mo	42097	5.40e-03				W	74182	8.30e-04
Mo	42094	5.23e-03				W	74183	4.51e-04
Cr	24050	4.39e-03				Ta	73181	3.50e-04
Ni	28061	3.63e-03				O	8016	3.29e-04
Fe	26054	3.41e-03				Zr	40000	3.68e-05
Ni	28064	2.94e-03				He	2004	1.59e-05
Cr	24054	2.39e-03				N	7015	4.13e-06
W	74184	2.27e-03						
W	74186	2.11e-03						
W	74182	1.94e-03						
Ba	56138	1.51e-03						
Fe	26057	1.21e-03						
W	74183	1.06e-03						
Y	39089	1.05e-03						
Ba	56137	2.37e-04						
Ba	56136	1.66e-04						
Fe	26058	1.62e-04						
Ba	56135	1.39e-04						
Ba	56134	5.10e-05						
He	2004	1.61e-05						
Ba	56130	2.23e-06						
Ba	56132	2.13e-06						

Table 7.4 - Materials spherical tokamak (Section 4.4) continued.

Material	55%Be + 20% helium + 15% lithium breeder + 10% EUROFER		**Material**	70% EUROFER + 30% water	
Mass density (g/cm^3)		7.466	Mass density (g/cm^3)		5.758
Element	ZAID	Fraction	Element	ZAID	Fraction
He	2004	5.46e-05	H	1001	2.24e-01
Li	3006	6.22e-03		1002	3.36e-05
	3007	7.67e-02	C	6012	3.08e-03

Be	4009	7.29e-01	N	7014	7.88e-04
C	6012	4.19e-04		7015	2.90e-06
N	7014	1.08e-04	O	8016	1.13e-01
	7015	3.95e-07	V	23000	1.45e-03
O	8016	7.76e-02	Cr	24050	2.78e-03
Si	14028	1.79e-02		24052	5.36e-02
	14029	9.08e-04		24053	6.07e-03
	14030	6.02e-04		24054	1.51e-03
V	23000	1.98e-04	Mn	25055	2.69e-03
Cr	24050	3.79e-04	Fe	26054	3.47e-02
	24052	7.31e-03		26056	5.40e-01
	24053	8.29e-04		26057	1.24e-02
	24054	2.06e-04		26058	1.65e-03
Mn	25055	3.67e-04	Ta	73181	2.45e-04
Fe	26054	4.74e-03	W	74182	5.81e-04
	26056	7.37e-02		74183	3.16e-04
	26057	1.69e-03		74184	6.78e-04
	26058	2.25e-04		74186	6.32e-04
Ta	73181	3.34e-05			
W	74182	7.93e-05			
	74183	4.31e-05			
	74184	9.26e-05			
	74186	8.62e-05			

Table 7.5 - Materials used within material homogenisation for HTS-ST (Section 4.4.5).

Material	F82H		**Material**	Water SS304B7 + boron	
Mass density (g/cm^3)		7.8000	Mass density (g/cm^3)		4.3275
Atomic density atoms/bn-cm (atoms/10^{-24} cm^3)		0.0809	Atomic density atoms/bn-cm (atoms/10^{-24} cm^3)		0.0934
Element	ZAID	Fraction	Element	ZAID	Fraction
Cr	24050	3.4759e-03	H	1001	3.3860e-01
	24052	6.7030e-02		1002	5.0798e-05
V	24053	7.6006e-03	O	8016	1.6936e-01
	24054	1.8920e-03	C	6012	1.6568e-03
Si	14028	9.2221e-04	Mn	25055	9.0474e-03
	14029	4.6849e-05	P	15031	3.6106e-04
	14030	3.0919e-05	S	16032	2.2088e-04
Ni	28058	3.4038e-04		16033	1.7439e-06
	28060	1.3111e-04		16034	9.8823e-06
	28061	5.6994e-06		16036	2.3252e-08
	28062	1.8172e-05	Si	14028	6.1202e-03
	28064	4.6279e-06		14029	3.1125e-04
Ti	22046	4.1249e-06		14030	2.0507e-04
	22047	3.7199e-06	Cr	24050	3.9459e-03
	22048	3.6859e-05		24052	7.6092e-02
	22049	2.7049e-06		24053	8.6283e-03
	22050	2.5899e-06		24054	2.1478e-03
Mn	25055	9.9998e-04	Ni	28058	3.8914e-02
W	74180	2.4000e-05		28060	1.4990e-02
	74182	5.2999e-03		28061	6.5160e-04
	74183	2.8619e-03		28062	2.0776e-03
	74184	6.1279e-03		28064	5.2910e-04
	74186	5.6859e-03	N	7014	1.7679e-03
Mo	42092	2.9539e-06		7015	6.5297e-06

	42094	1.8460e-06	B	5010	9.1492e-03
	42095	3.1799e-06		5011	3.6827e-02
	42096	3.3359e-06	Co	27059	2.1085e-04
	42097	1.9120e-06	Nb	41093	2.6750e-05
	42098	4.8379e-06	Ta	73181	1.3735e-05
	42100	1.9340e-06	Ti	22046	6.4231e-05
C	6012	9.8928e-04		22047	5.7925e-05
	6013	1.0700e-05		22048	5.7395e-04
O	8016	4.9878e-05		22049	4.2120e-05
	8017	1.9000e-08		22050	4.0329e-05
	8018	1.0250e-07	Cu	29063	2.7052e-04
Al	13027	9.9998e-05		29065	1.2057e-04
Ta	73180	4.7999e-08	Al	13027	4.6054e-04
	73181	3.9994e-04	K	19039	2.9637e-06
V	23050	4.9999e-06		19040	3.7181e-10
	23051	1.9950e-03		19041	2.1388e-07
Fe	26054	5.2247e-02	Bi	83209	9.5138e-07
	26056	8.2017e-01	V	23050	4.8784e-08
	26057	1.8941e-02		23051	1.9465e-05
	26058	2.5207e-03	Zr	40090	2.8030e-06
				40091	6.1128e-07
				40092	9.3435e-07
				40094	9.4688e-07
				40096	1.5255e-07
			Sn	50112	4.0615e-08
				50114	2.7635e-08
				50115	1.4236e-08
				50116	6.0880e-07
				50117	3.2157e-07
				50118	1.0141e-06
				50119	3.5967e-07
				50120	1.3642e-06
				50122	1.9386e-07
				50124	2.4243e-07
			W	74182	3.5863e-07
				74183	1.9373e-07
				74184	4.1471e-07
				74186	3.8472e-07
			Pb	82206	2.3447e-07
				82207	2.1501e-07
				82208	5.0979e-07
			Fe	26054	1.6156e-02
				26056	2.5362e-01
				26057	5.8571e-03
				26058	7.7948e-04

Table 7.6 - Materials used within material homogenisation for HTS-ST (Section 4.4.5) continued.

Material HTSC+5% helium			**Material** Tungsten		
Mass density (g/cm^3)		8.4194	Mass density (g/cm^3)		19.2500
Atomic density atoms/bn-cm (atoms/10^{-24} cm^3)		0.0797	Atomic density atoms/bn-cm (atoms/10^{-24} cm^3)		0.0632
Element	ZAID	Fraction	Element	ZAID	Fraction
Ni	28058	1.3576e-01	Al	13027	1.0205e-04
	28060	5.2296e-02	C	6012	4.5359e-04

	28061	2.2733e-03
	28062	7.2482e-03
	28064	1.8459e-03
Mo	42092	8.5687e-03
	42094	5.3547e-03
	42095	9.2242e-03
	42096	9.6768e-03
	42097	5.5462e-03
	42098	1.4034e-02
	42100	5.6100e-03
Cr	24050	2.4419e-03
	24052	4.7090e-02
	24053	5.3397e-03
	24054	1.3292e-03
Fe	26054	2.0134e-03
	26056	3.1606e-02
	26057	7.2991e-04
	26058	9.7138e-05
C	6012	3.5871e-05
	6013	3.8797e-07
Si	14028	3.3439e-04
	14029	1.6987e-05
	14030	1.1211e-05
Y	39089	1.0734e-03
Ba	56130	2.2758e-06
	56132	2.1684e-06
	56134	5.1892e-05
	56135	1.4153e-04
	56136	1.6862e-04
	56137	2.4115e-04
	56138	1.5393e-03
Cu	29063	1.9500e-01
	29065	8.6996e-02
O	8016	7.4962e-03
	8017	2.8555e-06
	8018	1.5405e-05
Ag	47107	7.2342e-03
	47109	6.7209e-03
Be	4009	3.4483e-01

Ca	20040	4.4402e-05
	20042	2.9635e-07
	20043	6.1834e-08
	20044	9.5545e-07
	20046	1.8321e-09
	20048	8.5652e-08
Co	27059	3.1147e-05
Cr	24050	1.5339e-06
	24052	2.9580e-05
	24053	3.3541e-06
	24054	8.3491e-07
Cu	29063	1.9981e-05
	29065	8.9057e-06
Fe	26054	5.7637e-06
	26056	9.0478e-05
	26057	2.0895e-06
	26058	2.7808e-07
H	1001	9.1047e-04
	1002	1.0472e-07
K	19039	4.3779e-05
	19040	5.4925e-09
	19041	3.1594e-06
Mg	12024	2.9828e-05
	12025	3.7762e-06
	12026	4.1576e-06
Mn	25055	1.6706e-05
Mo	42092	2.8396e-05
	42094	1.7700e-05
	42095	3.0462e-05
	42096	3.1917e-05
	42097	1.8274e-05
	42098	4.6172e-05
	42100	1.8427e-05
N	7014	1.3057e-04
	7015	4.8719e-07
Na	11023	7.9845e-05
Nb	41093	1.9758e-05
Ni	28058	4.2581e-05
	28060	1.6402e-05
	28061	7.1300e-07
	28062	2.2734e-06
	28064	5.7895e-07
O	8016	3.4335e-04
P	15031	2.9631e-04
Pb	82206	2.1349e-06
	82207	1.9577e-06
	82208	4.6418e-06
S	16032	2.7190e-05
	16033	2.1468e-07
	16034	1.2165e-06
	16036	2.8624e-09
Si	14028	1.2056e-04
	14029	6.1216e-06
	14030	4.0354e-06
Ta	73181	1.0144e-05
Ti	22046	3.1637e-06

		22047	2.8531e-06
		22048	2.8259e-05
		22049	2.0747e-06
		22050	1.9864e-06
	Zr	40090	1.0352e-05
		40091	2.2575e-06
		40092	3.4506e-06
		40094	3.4969e-06
		40096	5.6336e-07
	W	74182	2.6447e-01
		74183	1.4282e-01
		74184	3.0580e-01
		74186	2.8374e-01

Table 7.7 - Materials used with HTS-ST model for activation considerations (Section 4.5.6.3).

Material HCLL			**Material** DCLL			**Material** WCLL		
Mass density (g/cm^3)		8.4242	Mass density (g/cm^3)		7.8716	Mass density (g/cm^3)		9.0311
Element	ZAID	Fraction	Element	ZAID	Fraction	Element	ZAID	Fraction
Fe	26054	1.5949e-02	Fe	26054	1.5766e-02	Fe	26054	1.8681e-02
	26056	2.4142e-01		26056	2.3865e-01		26056	2.8277e-01
	26057	5.4777e-03		26057	5.4148e-03		26057	6.4159e-03
	26058	7.1642e-04		26058	7.0819e-04		26058	8.3912e-04
C	6012	1.6751e-03	C	6012	1.6559e-03	C	6012	1.9620e-03
Mn	25055	1.8274e-03	Mn	25055	1.8064e-03	Mn	25055	2.1404e-03
P	15031	2.7018e-05	P	15031	2.6708e-05	P	15031	3.1645e-05
S	16000	2.6125e-05	S	16000	2.5825e-05	S	16000	3.0599e-05
Si	14028	2.7588e-04	Si	14028	2.7271e-04	Si	14028	3.2314e-04
	14029	1.3526e-05		14029	1.3370e-05		14029	1.5842e-05
	14030	8.6190e-06		14030	8.5200e-06		14030	1.0095e-05
Ni	28058	1.9661e-05	Ni	28058	1.9436e-05	Ni	28058	2.3029e-05
	28060	7.3211e-06		28060	7.2370e-06		28060	8.5750e-06
	28061	3.1303e-07		28061	3.0943e-07		28061	3.6664e-07
	28062	9.8196e-07		28062	9.7068e-07		28062	1.1502e-06
	28064	2.4226e-07		28064	2.3948e-07		28064	2.8376e-07
Cr	24050	1.3829e-03	Cr	24050	1.3670e-03	Cr	24050	1.6197e-03
	24052	2.5642e-02		24052	2.5347e-02		24052	3.0034e-02
	24053	2.8527e-03		24053	2.8200e-03		24053	3.3413e-03
	24054	6.9695e-04		24054	6.8895e-04		24054	8.1633e-04
Mo	42092	1.3510e-06	Mo	42092	1.3355e-06	Mo	42092	1.5824e-06
	42094	8.2419e-07		42094	8.1472e-07		42094	9.6535e-07
	42095	1.4036e-06		42095	1.3874e-06		42095	1.6440e-06
	42096	1.4553e-06		42096	1.4385e-06		42096	1.7045e-06
	42097	8.2460e-07		42097	8.1513e-07		42097	9.6584e-07
	42098	2.0623e-06		42098	2.0386e-06		42098	2.4155e-06
	42100	8.0657e-07		42100	7.9730e-07		42100	9.4471e-07
V	23000	8.2207e-04	V	23000	8.1262e-04	V	23000	9.6287e-04
Ta	73181	1.2957e-04	Ta	73181	1.2808e-04	Ta	73181	1.5176e-04
W	74182	2.9268e-04	W	74182	2.8932e-04	W	74182	3.4281e-04
	74183	1.5719e-04		74183	1.5538e-04		74183	1.8411e-04
	74184	3.3473e-04		74184	3.3089e-04		74184	3.9206e-04
	74186	3.0725e-04		74186	3.0372e-04		74186	3.5987e-04
Ti	22046	6.0086e-06	Ti	22046	5.9395e-06	Ti	22046	7.0377e-06
	22047	5.3033e-06		22047	5.2424e-06		22047	6.2117e-06
	22048	5.1454e-05		22048	5.0863e-05		22048	6.0267e-05

	22049	3.6989e-06		22049	3.6564e-06		22049	4.3324e-06
	22050	3.4708e-06		22050	3.4310e-06		22050	4.0653e-06
Cu	29063	1.8392e-05	Cu	29063	1.8180e-05	Cu	29063	2.1542e-05
	29065	7.9452e-06		29065	7.8539e-06		29065	9.3060e-06
Nb	41093	9.0060e-06	Nb	41093	8.9025e-06	Nb	41093	1.0548e-05
Al	13027	6.2041e-05	Al	13027	6.1328e-05	Al	13027	7.2667e-05
N	7014	5.3645e-04	N	7014	5.3028e-04	N	7014	6.2833e-04
	7015	1.8493e-06		7015	1.8281e-06		7015	2.1661e-06
B	5010	6.6669e-06	B	5010	6.5904e-06	B	5010	7.8088e-06
	5011	2.4396e-05		5011	2.4115e-05		5011	2.8574e-05
Co	27059	2.8392e-05	Co	27059	2.8066e-05	Co	27059	3.3255e-05
As	33075	2.2335e-05	As	33075	2.2078e-05	As	33075	2.6160e-05
Sn	50000	1.4111e-05	Sn	50000	1.3949e-05	Sn	50000	1.6528e-05
Sb	51121	7.9201e-06	Sb	51121	7.8291e-06	Sb	51121	9.2766e-06
	51123	5.8275e-06		51123	5.7605e-06		51123	6.8256e-06
Zr	40000	1.8363e-05	Zr	40000	1.8152e-05	Zr	40000	2.1508e-05
O	8016	1.0469e-04	O	8016	1.0349e-04	O	8016	1.4052e-02
Li	3006	9.9128e-02	He	2004	3.7756e-03	H	1001	2.7924e-02
	3007	1.1014e-02	Li	3006	9.9351e-02		1002	3.2116e-06
Pb	82204	8.2175e-03		3007	1.1039e-02	Li	3006	8.6112e-02
	82206	1.4146e-01	Pb	82204	8.2359e-03		3007	9.5680e-03
	82207	1.2972e-01		82206	1.4178e-01	Pb	82204	7.1385e-03
	82208	3.0757e-01		82207	1.3001e-01		82206	1.2288e-01
He	2004	1.8803e-03		82208	3.0826e-01		82207	1.1269e-01
							82208	2.6718e-01

Table 7.8 - Materials used with HTS-ST model for activation considerations (Section 4.5.6.3) continued.

Material LiFBe + EUROFER			**Material** Li_8PbO_6 + EUROFER			**Material** LiSn + EUROFER		
Mass density (g/cm^3)		3.1578	Mass density (g/cm^3)		2.8881	Mass density (g/cm^3)		6.5178
Element	ZAID	Fraction	Element	ZAID	Fraction	Element	ZAID	Fraction
Li	3006	6.8571e-02	Li	3006	3.2000e-02	Li	3006	1.4400e-01
	3007	1.6000e-01		3007	2.8800e-01		3007	1.6000e-02
F	9019	4.5714e-01	Pb	82206	9.6400e-03	Sn	50112	6.2080e-03
Be	4009	1.1429e-01		82207	8.8400e-03		50114	4.2240e-03
Fe	26054	8.9422e-04		82208	2.0960e-02		50115	2.1760e-03
	26056	1.3536e-02		82204	5.6000e-04		50116	9.3056e-02
	26057	3.0712e-04	O	8016	2.3986e-01		50117	4.9152e-02
	26058	4.0168e-05		8017	9.1200e-05		50118	1.5501e-01
C	6012	9.3919e-05	He	2004	2.0000e-01		50119	5.4976e-02
Mn	25055	1.0246e-04	Fe	26054	8.9422e-04		50120	2.0851e-01
P	15031	1.5148e-06		26056	1.3536e-02		50122	2.9632e-02
S	16000	1.4647e-06		26057	3.0712e-04		50124	3.7056e-02
Si	14028	1.5468e-05		26058	4.0168e-05	Fe	26054	8.9422e-04
	14029	7.5835e-07	C	6012	9.3919e-05		26056	1.3536e-02
	14030	4.8325e-07	Mn	25055	1.0246e-04		26057	3.0712e-04
Ni	28058	1.1024e-06	P	15031	1.5148e-06		26058	4.0168e-05
	28060	4.1048e-07	S	16000	1.4647e-06	C	6012	9.3919e-05
	28061	1.7551e-08	Si	14028	1.5468e-05	Mn	25055	1.0246e-04
	28062	5.5056e-08		14029	7.5835e-07	P	15031	1.5148e-06
	28064	1.3583e-08		14030	4.8325e-07	S	16000	1.4647e-06
Cr	24050	7.7535e-05	Ni	28058	1.1024e-06	Si	14028	1.5468e-05
	24052	1.4377e-03		28060	4.1048e-07		14029	7.5835e-07
	24053	1.5995e-04		28061	1.7551e-08		14030	4.8325e-07
	24054	3.9076e-05		28062	5.5056e-08	Ni	28058	1.1024e-06

Mo	42092	7.5748e-08		28064	1.3583e-08		28060	4.1048e-07
	42094	4.6210e-08	Cr	24050	7.7535e-05		28061	1.7551e-08
	42095	7.8694e-08		24052	1.4377e-03		28062	5.5056e-08
	42096	8.1592e-08		24053	1.5995e-04		28064	1.3583e-08
	42097	4.6233e-08		24054	3.9076e-05	Cr	24050	7.7535e-05
	42098	1.1563e-07	Mo	42092	7.5748e-08		24052	1.4377e-03
	42100	4.5222e-08		42094	4.6210e-08		24053	1.5995e-04
V	23000	4.6091e-05		42095	7.8694e-08		24054	3.9076e-05
Ta	73181	7.2645e-06		42096	8.1592e-08	Mo	42092	7.5748e-08
W	74182	1.6410e-05		42097	4.6233e-08		42094	4.6210e-08
	74183	8.8130e-06		42098	1.1563e-07		42095	7.8694e-08
	74184	1.8768e-05		42100	4.5222e-08		42096	8.1592e-08
	74186	1.7227e-05	V	23000	4.6091e-05		42097	4.6233e-08
Ti	22046	3.3688e-07	Ta	73181	7.2645e-06		42098	1.1563e-07
	22047	2.9734e-07	W	74182	1.6410e-05		42100	4.5222e-08
	22048	2.8849e-06		74183	8.8130e-06	V	23000	4.6091e-05
	22049	2.0739e-07		74184	1.8768e-05	Ta	73181	7.2645e-06
	22050	1.9460e-07		74186	1.7227e-05	W	74182	1.6410e-05
Cu	29063	1.0312e-06	Ti	22046	3.3688e-07		74183	8.8130e-06
	29065	4.4547e-07		22047	2.9734e-07		74184	1.8768e-05
Nb	41093	5.0494e-07		22048	2.8849e-06		74186	1.7227e-05
Al	13027	3.4785e-06		22049	2.0739e-07	Ti	22046	3.3688e-07
N	7014	3.0077e-05		22050	1.9460e-07		22047	2.9734e-07
	7015	1.0369e-07	Cu	29063	1.0312e-06		22048	2.8849e-06
B	5010	3.7380e-07		29065	4.4547e-07		22049	2.0739e-07
	5011	1.3678e-06	Nb	41093	5.0494e-07		22050	1.9460e-07
Co	27059	1.5919e-06	Al	13027	3.4785e-06	Cu	29063	1.0312e-06
As	33075	1.2523e-06	N	7014	3.0077e-05	Cu	29065	4.4547e-07
Sn	50000	7.9116E-07		7015	1.0369E-07	NB	41093	5.0494E-07
Sb	51121	4.4406e-07	B	5010	3.7380e-07	Al	13027	3.4785e-06
	51123	3.2673e-07		5011	1.3678e-06	N	7014	3.0077e-05
Zr	40000	1.0295e-06	Co	27059	1.5919e-06		7015	1.0369e-07
O	8016	5.8699e-06	As	33075	1.2523e-06	B	5010	3.7380e-07
			Sn	50000	7.9116E-07		5011	1.3678E-06
			Sb	51121	4.4406E-07	Co	27059	1.5919E-06
				51123	3.2673E-07	As	33075	1.2523E-06
			Zr	40000	1.0295E-06	Sn	50000	7.9116E-07
			O	8016	5.8699E-06	Sb	51121	4.4406E-07
							51123	3.2673E-07
						Zr	40000	1.0295E-06
						O	8016	5.8699E-06

Table 7.9 – Blanket material used in the HTS-ST and EU DEMO 2015 model for neutron transport and activation analysis (sections 4.4.5 and 5).

Material HCPB blanket								
Mass density (g/cm^3)		1.93279						
Element	ZAID	Fraction	Element	ZAID	Fraction	Element	ZAID	Fraction
Fe	26054	0.00739	Mo	42092	6.26e-07	Nb	41093	4.17e-06
	26056	0.11186		42094	3.82e-07	Al	13027	2.87e-05
	26057	0.002538		42095	6.5e-07	N	7014	0.000249
	26058	0.000332		42096	6.74e-07		7015	8.57e-07
C	6012	0.000776		42097	3.82e-07	B	5010	3.09e-06
Mn	25055	0.000847		42098	9.55e-07		5011	1.13e-05
P	15031	1.25e-05		42100	3.74e-07	Co	27059	1.32e-05
S	16000	1.21e-05	V	23000	0.000381	As	33075	1.03e-05

Si	14028	0.021143	Ta	73181	6e-05	Sn	50000	6.54e-06
	14029	0.00107	W	74182	0.000136	Sb	51121	3.67e-06
	14030	0.00071		74183	7.28e-05		51123	2.7e-06
Ni	28058	9.11e-06		74184	0.000155	Zr	40000	8.51e-06
	28060	3.39e-06		74186	0.000142	O	8016	0.089307
	28061	1.45e-07	Ti	22046	2.78e-06	Be	4009	0.65767
	28062	4.55e-07		22047	2.46e-06	Li	3006	0.03495
	28064	1.12e-07		22048	2.38e-05		3007	0.05241
Cr	24050	0.000641		22049	1.71e-06	He	2004	0.003456
	24052	0.01188		22050	1.61e-06			
	24053	0.001322	Cu	29063	8.52e-06			
	24054	0.000323		29065	3.68e-06			

Table 7.10 - Materials used with EU DEMO 2015 model for neutron transport and activation/radioactive waste assessments (Section 5).

Material	Tungsten		**Material**	SS316 LN-IG- 77%, water - 23%		**Material**	EUROFER	
Mass density (g/cm^3)		19.1864	Mass density (g/cm^3)		6.5366	Mass density (g/cm^3)		7.7888
Atomic density atoms/bn-cm ($atoms/10^{-24}$ cm^3)		0.0630	Atomic density atoms/bn-cm ($atoms/10^{-24}$ cm^3)		0.0887	Atomic density atoms/bn-cm ($atoms/10^{-24}$ cm^3)		0.0844
Element	ZAID	Fraction	Element	ZAID	Fraction	Element	ZAID	Fraction
Al	13027	4.4038E-06	Fe	26054	2.6335E-03	Fe	26054	4.4711E-03
C	6012	1.9574E-05		26056	3.9863E-02		26056	6.7680E-02
Ca	20000	1.9766E-06		26057	9.0446E-04		26057	1.5356E-03
Co	27059	1.3442E-06		26058	1.1829E-04		26058	2.0084E-04
Cr	24050	6.6195E-08	C	6012	9.5509E-05	C	6012	4.6960E-04
	24052	1.2765E-06	Mn	25055	1.3892E-03	Mn	25055	5.1229E-04
	24053	1.4475E-07	Si	14028	6.2920E-04	P	15031	7.5741E-06
	24054	3.6030E-08		14029	3.0847E-05	S	16000	7.3237E-06
Cu	29063	8.6226E-07		14030	1.9657E-05	Si	14028	7.7341E-05
	29065	3.8432E-07	P	15031	3.0809E-05		14029	3.7917E-06
Fe	26054	2.4873E-07	S	16000	1.1916E-05		14030	2.4162E-06
	26056	3.9045E-06	Cr	24050	5.9758E-04	Ni	28058	5.5118E-06
	26057	9.0173E-08		24052	1.1081E-02		28060	2.0524E-06
	26058	1.2000E-08		24053	1.2327E-03		28061	8.7753E-08
H	1001	3.9291E-05		24054	3.0117E-04		28062	2.7528E-07
	1002	4.5190E-09	Ni	28058	5.6051E-03		28064	6.7915E-08
K	19000	2.0259E-06		28060	2.0871E-03	Cr	24050	3.8768E-04
Mg	12000	1.6296E-06		28061	8.9238E-05		24052	7.1884E-03
Mn	25055	7.2095E-07		28062	2.7994E-04		24053	7.9973E-04
Mo	42092	1.2254E-06		28064	6.9065E-05		24054	1.9538E-04
	42094	7.6382E-07	Mo	42092	1.6639E-04	Mo	42092	3.7874E-07
	42095	1.3146E-06		42094	1.0150E-04		42094	2.3105E-07
	42096	1.3773E-06		42095	1.7286E-04		42095	3.9347E-07
	42097	7.8859E-07		42096	1.7922E-04		42096	4.0796E-07
	42098	1.9925E-06		42097	1.0156E-04		42097	2.3117E-07
	42100	7.9519E-07		42098	2.5398E-04		42098	5.7813E-07
N	7014	5.6347E-06		42100	9.9333E-05		42100	2.2611E-07
	7015	2.1024E-08	N	7014	2.1750E-04	V	23000	2.3046E-04
Na	11023	3.4457E-06		7015	7.4981E-07	Ta	73181	3.6322E-05
Nb	41093	8.5263E-07	B	5010	7.6025E-07	W	74182	8.2050E-05
Ni	28058	1.8376E-06		5011	2.7819E-06		74183	4.4065E-05
	28060	7.0783E-07	Cu	29063	1.2584E-04		74184	9.3837E-05
	28061	3.0769E-08		29065	5.4361E-05		74186	8.6133E-05

	28062	9.8105E-08	Co	27059	3.2376E-05	Ti	22046	1.6844E-06
	28064	2.4984E-08	Nb	41093	4.1079E-06		22047	1.4867E-06
O	8016	1.4817E-05	Ti	22046	6.8517E-06		22048	1.4424E-05
P	15031	1.2787E-05		22047	6.0475E-06		22049	1.0369E-06
Pb	82206	9.2132E-08		22048	5.8674E-05		22050	9.7300E-07
	82207	8.4483E-08		22049	4.2180E-06	Cu	29063	5.1559E-06
	82208	2.0032E-07		22050	3.9579E-06		29065	2.2273E-06
S	16000	1.2353E-06	Ta	73181	2.1107E-06	Nb	41093	2.5247E-06
Si	14028	5.2026E-06	H	1001	1.3382E-02	Al	13027	1.7392E-05
	14029	2.6417E-07	O	8016	6.6911E-03	N	7014	1.5039E-04
	14030	1.7414E-07					7015	5.1843E-07
Ta	73181	4.3778E-07				B	5010	1.8690E-06
Ti	22046	1.3653E-07					5011	6.8390E-06
	22047	1.2313E-07				Co	27059	7.9593E-06
	22048	1.2195E-06				As	33075	6.2613E-06
	22049	8.9530E-08				Sn	50000	3.9558E-06
	22050	8.5724E-08				Sb	51121	2.2203E-06
Zr	40000	8.6826E-07					51123	1.6337E-06
W	74182	1.1413E-02				Zr	40000	5.1477E-06
	74183	6.1633E-03				O	8016	2.9350E-05
	74184	1.3197E-02						
	74186	1.2245E-02						

Table 7.11 - Materials used with EU DEMO 2015 model for neutron transport and activation/radioactive waste assessments (Section 5) continued.

Material	EUROFER - 23%, Be - 21.02%, Li_4SiO_4 - 10.2%, void - 45.78%		**Material**	SS-316L(N)-IG		**Material**	Magnet-conductor in Nb_3Sn with cryogenic SS 316 LN	
Mass density (g/cm^3)		3.8456	Mass density (g/cm^3)		7.9205	Mass density (g/cm^3)		5.5050
Atomic density atoms/bn-cm (atoms/10^{-24} cm^3)		0.0899	Atomic density atoms/bn-cm (atoms/10^{-24} cm^3)		0.0858	Atomic density atoms/bn-cm (atoms/10^{-24} cm^3)		0.0719
Element	ZAID	Fraction	Element	ZAID	Fraction	Element	ZAID	Fraction
Fe	26054	1.0284E-03	Fe	26054	3.2918E-03	H	1001	3.8934E-03
	26056	1.5566E-02		26056	4.9829E-02	C	6012	3.4056E-03
	26057	3.5319E-04		26057	1.1306E-03	N	7014	3.7080E-04
	26058	4.6193E-05		26058	1.4787E-04	O	8016	4.8708E-03
C	6012	1.0801E-04	C	6012	1.1939E-04	Mg	12000	2.1420E-04
Mn	25055	1.1783E-04	Mn	25055	1.7365E-03	Al	13027	7.0740E-04
P	15031	1.7421E-06	Si	14028	7.8650E-04	Si	14028	1.3280E-03
S	16000	1.6845E-06		14029	3.8559E-05		14029	6.7200E-05
Si	14028	1.7788E-05		14030	2.4571E-05		14030	4.4600E-03
	14029	8.7210E-07	P	15031	3.8512E-05	S	16000	9.1800E-05
	14030	5.5573E-07	S	16000	1.4895E-05	Cu	29063	6.8359E-03
Ni	28058	1.2677E-06	Cr	24050	7.4698E-04		29065	3.0568E-03
	28060	4.7205E-07		24052	1.3851E-02	Nb	41093	1.1844E-03
	28061	2.0183E-08		24053	1.5409E-03	Sn	50000	3.9480E-04
	28062	6.3315E-08		24054	3.7646E-04	He	2004	3.0889E-03
	28064	1.5621E-08	Ni	28058	7.0064E-03	B	5010	4.0629E-07
Cr	24050	8.9165E-05		28060	2.6089E-03		5011	1.4874E-06
	24052	1.6533E-03		28061	1.1155E-04	C	6012	1.7020E-04
	24053	1.8394E-04		28062	3.4993E-04	N	7014	2.7738E-04
	24054	4.4938E-05		28064	8.6331E-05	O	8016	2.5562E-06
Mo	42092	8.7110E-08	Mo	42092	2.0798E-04	Al	13027	2.2730E-04
	42094	5.3142E-08		42094	1.2688E-04	Si	14028	7.2789E-05

	42095	9.0499E-08		42095	2.1607E-04	P	15031	1.6500E-05
	42096	9.3831E-08		42096	2.2403E-04	S	16000	8.9259E-07
	42097	5.3168E-08		42097	1.2694E-04	K	19000	2.6143E-07
	42098	1.3297E-07		42098	3.1748E-04	Ti	22046	1.4090E-06
	42100	5.2005E-08		42100	1.2417E-04		22047	1.2707E-06
V	23000	5.3005E-05	N	7014	2.7188E-04		22048	1.259086-05
Ta	73181	8.3541E-06		7015	9.3726E-07		22049	9.2399E-07
W	74182	1.8872E-05	B	5010	9.5031E-07		22050	8.8471E-07
	74183	1.0135E-05		5011	3.4774E-06	V	23000	1.6052E-06
	74184	2.1583E-05	Cu	29063	1.5729E-04	Cr	24050	3.0343E-04
	74186	1.9811E-05		29065	6.7951E-05		24052	5.6705E-03
Ti	22046	3.8742E-07	Co	27059	4.0470E-05		24053	6.3429E-04
	22047	3.4195E-07	Nb	41093	5.1349E-06		24054	1.5515E-04
	22048	3.3176E-06	Ti	22046	8.5647E-06	Mn	25055	5.5817E-04
	22049	2.3850E-07		22047	7.5594E-06	Fe	26054	1.4658E-03
	22050	2.2379E-07		22048	7.3343E-05		26056	2.2190E-02
Cu	29063	1.1859E-06		22049	5.2725E-06		26057	5.1600E-04
	29065	5.1229E-07		22050	4.9474E-06		26058	7.2442E-05
Nb	41093	5.8068E-07	Ta	73181	2.6384E-06	Co	27059	1.7344E-05
Al	13027	4.0003E-06				Ni	28058	2.8935E-03
N	7014	3.4589E-05					28060	1.0798E-03
	7015	1.1924E-07					28061	5.0746E-05
B	5010	4.2987E-07					28062	1.4619E-04
	5011	1.5730E-06					28064	4.4885E-05
Co	27059	1.8306E-06				Cu	29063	2.2448E-05
As	33075	1.4401E-06					29065	9.7292E-06
Sn	50000	9.0984E-07				Zr	40000	4.4803E-07
Sb	51121	5.1067E-07				Nb	41093	1.2102E-05
	51123	3.7574E-07				Mo	42092	6.3249E-05
Zr	40000	1.1840E-06					42094	3.9424E-05
O	8016	6.7504E-06					42095	6.7852E-05
Be	4009	2.6020E-02					42096	7.1091E-05
Li	3006	3.2091E-03					42097	4.2407E-05
	3007	1.8338E-03					42098	1.0284E-04
Si	14028	1.1562E-03					42100	4.1044E-05
	14029	5.6682E-05				Sn	50000	3.4442E-07
	14030	3.6120E-05				Ta	73181	5.6489E-08
O	8016	5.0142E-03				W	74182	2.9662E-08
							74183	1.6091E-08
							74184	3.4007E-08
							74186	3.1222E-08
						Pb	82206	1.7873E-08
							82207	1.7858E-08
							82208	4.1945E-08
						Bi	83209	7.8259E-08
						Cu	29063	3.3891E-03
							29065	1.5155E-03
						Sn	50000	2.6254E-04

Table 7.12 - Mass composition of main bulk materials used in activation analysis.

F82H		EUROFER		SS304B7		Tungsten		SS-316L(N)-IG	
Fe	89.388%	Fe	87.963%	Fe	62.111%	W	99.957%	Fe	64.753%
Cr	8.000%	Cr	9.500%	Cr	19.000%	Mo	0.010%	Cr	17.500%
W	2.000%	W	1.200%	Ni	13.500%	P	0.005%	Ni	12.250%
V	0.200%	Mn	0.600%	Mn	2.000%	C	0.003%	Mo	2.500%
Si	0.100%	V	0.250%	B	2.000%	Fe	0.003%	Mn	1.800%

Mn	0.100%	Ta	0.140%	Si	0.750%	O	0.003%	Si	0.500%
C	0.100%	C	0.120%	Ti	0.150%	Ni	0.002%	Cu	0.300%
Ni	0.050%	Si	0.050%	N	0.100%	Si	0.002%	Ti	0.100%
Ta	0.040%	N	0.045%	Cu	0.100%	Al	0.002%	Nb	0.100%
Al	0.010%	Ti	0.020%	C	0.080%	Ca	0.001%	N	0.070%
Ti	0.005%	Ni	0.010%	Co	0.050%	Co	0.001%	Co	0.050%
O	0.005%	Cu	0.010%	Al	0.050%	Cr	0.001%	C	0.030%
Mo	0.002%	Al	0.010%	P	0.045%	Cu	0.001%	P	0.025%
		Co	0.010%	S	0.030%	K	0.001%	S	0.010%
		As	0.010%	Nb	0.010%	N	0.001%	Ta	0.010%
		Sn	0.010%	Ta	0.010%	Na	0.001%	B	0.002%
		Sb	0.010%	V	0.004%	Nb	0.001%		
		Zr	0.010%	O	0.002%	Pb	0.001%		
		O	0.010%	Zr	0.002%	Ta	0.001%		
		P	0.005%	Sn	0.002%	Ti	0.001%		
		S	0.005%	W	0.001%	Zr	0.001%		
		Mo	0.005%	Bi	0.001%	H	0.001%		
		Nb	0.005%	Pb	0.001%	Mg	0.001%		
		B	0.002%	K	0.001%	Mn	0.001%		
						S	0.001%		

APPENDIX 2: MCNP INPUT FILE

The MCNP input file contains 3 main blocks containing the cell definitions, surfaces and data/physics/tally options (see Figure 7.1). The geometry of the problem must be provided to MCNP within this input file, described using the surfaces within the tally block. The geometry definition requirement is known as constructive solid geometry (CSG). The cell block uses the surfaces to define all regions of the phase space, including void regions. Void regions are volumes that do not contain any material and may or may not have any significance in the problem, they must however still be fully defined.

One line title card
Cell cards [Block 1]
blank line delimiter
Surface cards [Block 2]
blank line delimiter
Data cards [Block 3]

Figure 7.1 - Basic three block structure of MCNP input file and title card.

An example of what is meant by fully defining the phase space is given in Figure 7.2. The inner lithium sphere is defined as being inside the spherical surface '1'. It is also defined to consist of the material '10' (that is defined later in the input file) and with a mass density of 0.54 g/cm3. The use of the negative sign denotes a mass value as opposed to atom density or atom fraction. A further sphere is described in cell 2, this is defined as the volume within the 100 cm spherical surface, but outside the 20 cm lithium sphere. Cell 2 is a void cell and so does not have an associated material number.

The final cell defined is often called the 'outer universe' or 'graveyard'. As already mentioned, all of the phase space must be defined and therefore cell 3 defines all geometry outside of the 100 cm sphere, to an effective infinity. When importances are set, this outer universe will be set to zero. All particles leaving the important geometry (i.e. escaping cell 2) will be killed and the history no longer followed.

An example of an input file generated using the parameterised script for spherical tokamak scoping studies (Section 4.4) is given in Figure 7.3. For a detailed description of the code and further examples of use, refer to the MCNP user guide [95].

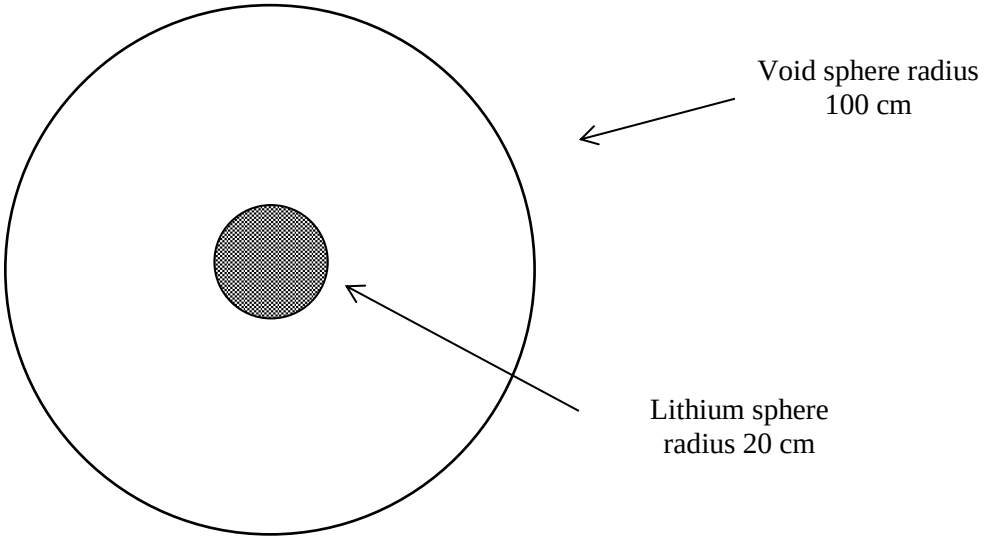


```
C         Cell Card
1     10     - 0.54     -1
2      0                -2    1
3      0                 2

C       Surface Card
1    so 20
2    so 100
```

Figure 7.2 - Example of CSG definition for MCNP.

```
C Parameterised generation of simplified ST model
C B Colling 2015
C 147.0 Major Radius (cm)
C 2 Aspect ratio
C 2 Elongation
C 0.5 Triangularity
C 2 Inboard FW thickness (cm)
C 70 Blanket thickness (cm)
C 30 Centre column radius (cm)
C 40 Centre column n-shield thickness (cm)
C 1.6 Plasma peaking factor
C 1.5 Inboard Scrape off layer (cm)
C
1     1 -8.5       -1 101 -7 200 -201
2     1 -8.5       -1 -101 100 200 -201
3     1 -8.5       -1 -100 -7 200 -201
4     2 -13.7281   -2 1  101 -7 200 -201
5     2 -13.7281   -2 1 -101 100 200 -201
6     2 -13.7281   -2 1 -100 -7 200 -201
```

```
7     3 -7.528     -3 2  101 -7 200 -201
8     3 -7.528     -3 2 -101 100 200 -201
9     3 -7.528     -3 2 -100 -7 200 -201
10    3 -7.528     -5 4 3 101 200 -201
11    3 -7.528     -5 4  -101 100 200 -201
12    3 -7.528     -5 4 3 -100 200 -201
13    4 -2.157     -6 5 3 101 200 -201
14    4 -2.157     -6 5 -101 100 200 -201
15    4 -2.157     -6 5 3 -100 200 -201
16    5 -5.758     -7 6 3 101 200 -201
17    5 -5.758     -7 6 -101 100 200 -201
18    5 -5.758     -7 6 3 -100 200 -201
19    0            -4 3 200 -201
99    0            7:-200:201

1     CZ     30.0
2     CZ      70.0
3     CZ      72.0
4     SO      235.5
5     SO      237.5
6     SO      307.5
7     SO      337.5
100   PZ      -5.0
101   PZ      5.0
*200   PX      0.0
*201   PY     0.0

mode n p
C ************************************
C *  38%Eurofer+57%Cu+5%He
C *  density = 8.5 g/cm3
C ************************************
M1 26054.21c 1.94E-02
     26056.21c 3.06E-01
     26057.21c 7.01E-03
     26058.21c 1.00E-03
     24050.21c 1.66E-03
     24052.21c 3.23E-02
     24053.21c 3.67E-03
     24054.21c 9.26E-04
     6012. 2.11E-03
     25055.21c 2.31E-03
     23000.21c 2.59E-06
     23000.21c 1.03E-03
     7014.21c 6.76E-04
     7015.21c 2.48E-06
     8016.21c 1.32E-04
     8017. 5.03E-08
     73181.21c 1.05E-04
     74182.21c 3.63E-04
     74183.21c 1.97E-04
     74184.21c 4.24E-04
     74186.21c 3.95E-04
     29063.21c 3.94E-01
     29065.21c 1.76E-01
     2003.21c 6.70E-08
     2004.21c 5.00E-02
C ************************************
C *  13%H2O+87%WC
C *  density = 13.7281 g/cm3
C ************************************
```

```
M2 1001.21c    0.0899
     1002.21c    0.00001
     8016.21c    0.0450
     74182.21c   0.1142
     74183.21c   0.0623
     74184.21c   0.1324
     74186.21c   0.1229
     6012.21c    0.4327
C ************************************
C CuCrZr@5.00e-02/Eurofer@9.00e-01/Helium@5.00e-02/Void@0.00e+00/Void@0.00e+00/Void@0.00e+00:
C *  density = 7.528 g/cm3
c ************************************
M3    26054.21c   4.82666e-02
      26056.21c   7.63944e-01
      26057.21c   1.74758e-02
      26058.21c   2.49655e-03
      24050.21c   4.16488e-03
      24052.21c   8.11668e-02
      24053.21c   9.20149e-03
      24054.21c   2.32459e-03
       6012.   5.26520E-03
      25055.21c   5.75567e-03
      23000.21c   6.46586e-06
      23000.21c   2.57988e-03
       7014.21c   1.68695e-03
       7015.21c   6.19691e-06
       8016.21c   3.29352e-04
       8017.   1.25455e-07
      73181.21c   2.62124e-04
      74182.21c   9.04794e-04
      74183.21c   4.92522e-04
      74184.21c   1.05737e-03
      74186.21c   9.85044e-04
      29063.21c   3.56780e-02
      29065.21c   1.58798e-02
      40090.   2.80384e-05
      40091.   6.09768e-06
      40092.   9.30985e-06
      40094.   9.47318e-06
      40096.   1.52442e-06
       2003.21c   2.10019e-11
       2004.21c   1.50014e-05
C ************************************
C Beryllium@5.50e-01/Eurofer@1.00e-01/Helium@2.00e-01/Lithium-Silicate@1.50e-01
C *  density = 2.157 g/cm3
c ************************************
M4     2004.21c 5.4569E-05
     3006.21c 6.2150E-03
     3007.21c 7.6652E-02
     4009.21c 7.2948E-01
     6012.21c 4.1948E-04
     7014.21c 1.0752E-04
     7015.21c 3.9497E-07
     8016.21c 7.7649E-02
     14028.21c 1.7924E-02
     14029.21c 9.0759E-04
     14030.21c 6.0247E-04
     23000.21c 1.9781E-04
     24050.21c 3.7893E-04
     24052.21c 7.3072E-03
     24053.21c 8.2858E-04
```

```
      24054.21c 2.0625E-04
      25055.21c 3.6689E-04
      26054.21c 4.7397E-03
      26056.21c 7.3682E-02
      26057.21c 1.6870E-03
      26058.21c 2.2493E-04
      73181.21c 3.3414E-05
      74182.21c 7.9287E-05
      74183.21c 4.3111E-05
      74184.21c 9.2552E-05
      74186.21c 8.6221E-05
C ************************************
C 70%EUROFER 30%Water
C EUROFER(7.798)- 89.04%Fe 9%Cr 0.1%C 0.4%Mn 0.2%V 0.03%N 0.01%O 0.12%Ta 1.1%W Water(0.995)-
H2O
C *  density = 5.758 g/cm3
c ************************************
M5     1001.21c 2.2373E-01
      1002.21c 3.3565E-05
      6012.21c 3.0751E-03
      7014.21c 7.8819E-04
      7015.21c 2.8954E-06
      8016.21c 1.1290E-01
      23000.21c 1.4501E-03
      24050.21c 2.7778E-03
      24052.21c 5.3567E-02
      24053.21c 6.0741E-03
      24054.21c 1.5120E-03
      25055.21c 2.6896E-03
      26054.21c 3.4745E-02
      26056.21c 5.4014E-01
      26057.21c 1.2367E-02
      26058.21c 1.6489E-03
      73181.21c 2.4494E-04
      74182.21c 5.8123E-04
      74183.21c 3.1603E-04
      74184.21c 6.7847E-04
      74186.21c 6.3206E-04
C SOURCE SPECIFICATION ----------------------------  -------------
C MUIR GAUSSIAN FUSION ENERGY SPECTRUM IN USER DEFINED SUBROUTINE
C NINE PARAMETERS TO DESCRIBE THE PLASMA:
C RDUM(1) = Reaction selector 1=DD otherwise DT
C RDUM(2) = TEMPERATURE OF PLASMA IN KEV
C RDUM(3) = RM  = MAJOR RADIUS
C RDUM(4) = AP  = MINOR RADIUS
C RDUM(5) = E   = ELONGATION
C RDUM(6) = CP  = TRIANGUARITY
C RDUM(7) = ESH = PLASMA SHIFT
C RDUM(8) = EPK = PLASMA PEAKING
C RDUM(9) = DELTAZ = PLASMA VERTICAL SHIFT (+=UP)
C RDUM(10) = Start of angular extent
C RDUM(11) = Range of angular extent
C IDUM(1) = 1
C IDUM(2) = number of valid cell numbers to follow
C IDUM(3) to IDUM(IDUM(2)+1) = valid source cells
RDUM   2 20 147.0 73.5 2.0 0.5 0 1.6   0   0 360  0
IDUM     1 1 19
c -------------
cut:n   j 1e-11  0.2 0.1 j
c    -----------------Importances-----------------
IMP:n 1 18r 0
```

```
IMP:p 1 18r 0
c    ---------------Run Information---------------
NPS 1E8
prdmp 1E8 5E7 j 2 5E7
c    ---------------------Tallies------------------
c
FC16     Neutron Heating
F16:n 1 2 3 4 5 6 7 8 9
SD16  1 1 1 1 1 1 1 1 1
FC26     Photon Heating
F26:p 1 2 3 4 5 6 7 8 9
SD26  1 1 1 1 1 1 1 1 1
FC4      TBR
F4:n 13 14 15
FM4  (-1 4 205)
SD4 1 1 1
FC2   Segment Flux
F2:n 1 2 3 4 5 6 7
FS2 -100 -101
SD2   1 1 1 1 1 1 1
     1 1 1 1 1 1 1
     1 1 1 1 1 1 1
FC22   Segment Flux
F22:n 1 2 3 4 5 6 7
FS22 -100 -101
SD22   1 1 1 1 1 1 1
     1 1 1 1 1 1 1
     1 1 1 1 1 1 1
E22     1.0000E-07  4.1399E-07  5.3158E-07  6.8256E-07  8.7643E-07  1.1254E-06
       1.4450E-06  1.8554E-06  2.3824E-06  3.0590E-06  3.9279E-06  5.0435E-06
       6.4760E-06  8.3153E-06  1.0677E-05  1.3710E-05  1.7604E-05  2.2603E-05
       2.9023E-05  3.7267E-05  4.7851E-05  6.1442E-05  7.8893E-05  1.0130E-04
       1.3007E-04  1.6702E-04  2.1445E-04  2.7536E-04  3.5358E-04  4.5400E-04
       5.8295E-04  7.4852E-04  9.6112E-04  1.2341E-03  1.5846E-03  2.0347E-03
       2.2487E-03  2.4852E-03  2.6126E-03  2.7465E-03  3.0354E-03  3.3546E-03
       3.7074E-03  4.3074E-03  5.5308E-03  7.1017E-03  9.1188E-03  1.0595E-02
       1.1709E-02  1.5034E-02  1.9305E-02  2.1875E-02  2.3579E-02  2.4176E-02
       2.4788E-02  2.6058E-02  2.7000E-02  2.8501E-02  3.1828E-02  3.4307E-02
       4.0868E-02  4.6309E-02  5.2475E-02  5.6562E-02  6.7380E-02  7.2025E-02
       7.9499E-02  8.2503E-02  8.6517E-02  9.8037E-02  1.1109E-01  1.1679E-01
       1.2277E-01  1.2907E-01  1.3569E-01  1.4264E-01  1.4996E-01  1.5764E-01
       1.6573E-01  1.7422E-01  1.8316E-01  1.9255E-01  2.0242E-01  2.1280E-01
       2.2371E-01  2.3518E-01  2.4724E-01  2.7324E-01  2.8725E-01  2.9452E-01
       2.9721E-01  2.9849E-01  3.0197E-01  3.3373E-01  3.6883E-01  3.8774E-01
       4.0762E-01  4.5049E-01  4.9787E-01  5.2340E-01  5.5023E-01  5.7844E-01
       6.0810E-01  6.3928E-01  6.7206E-01  7.0651E-01  7.4274E-01  7.8082E-01
       8.2085E-01  8.6294E-01  9.0718E-01  9.6167E-01  1.0026E+00  1.1080E+00
       1.1648E+00  1.2246E+00  1.2874E+00  1.3534E+00  1.4227E+00  1.4957E+00
       1.5724E+00  1.6530E+00  1.7377E+00  1.8268E+00  1.9205E+00  2.0190E+00
       2.1225E+00  2.2313E+00  2.3069E+00  2.3457E+00  2.3653E+00  2.3851E+00
       2.4660E+00  2.5924E+00  2.7253E+00  2.8651E+00  3.0119E+00  3.1664E+00
       3.3287E+00  3.6788E+00  4.0657E+00  4.4933E+00  4.7237E+00  4.9659E+00
       5.2205E+00  5.4881E+00  5.7695E+00  6.0653E+00  6.3763E+00  6.5924E+00
       6.7032E+00  7.0469E+00  7.4082E+00  7.7880E+00  8.1873E+00  8.6071E+00
       9.0484E+00  9.5123E+00  1.0000E+01  1.0513E+01  1.1052E+01  1.1618E+01
       1.2214E+01  1.2523E+01  1.2840E+01  1.3499E+01  1.3840E+01  1.4191E+01
       1.4550E+01  1.4918E+01  1.5683E+01  1.6487E+01  1.6905E+01  1.7333E+01
       1.9640E+01
```

Figure 7.3 - Example of MCNP input file for spherical tokamak shielding research.

APPENDIX 3: FISPACT INPUT EXAMPLE

The FISPACT-II code has four main stages: (1) process library data (including collapsing of cross-section data and condensing of decay and fission data), (2) set initial conditions, (3) run irradiation phases and finally (4) run cooling phases. All four stages can be carried out within one input file, though intermediate output files are produced after each stage.

An example FISPACT-II input is provided in Figure 7.4 with some explanatory annotations.

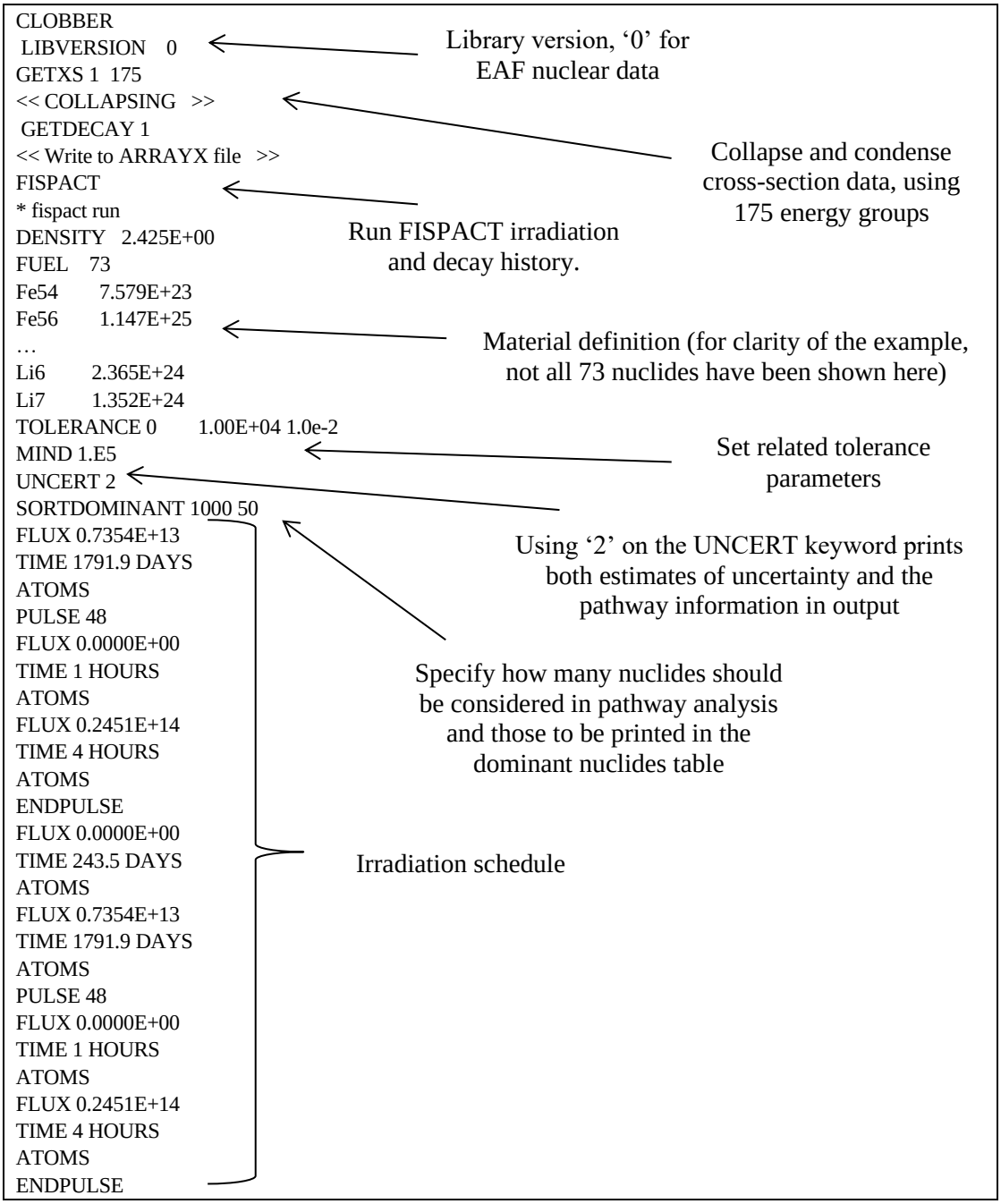

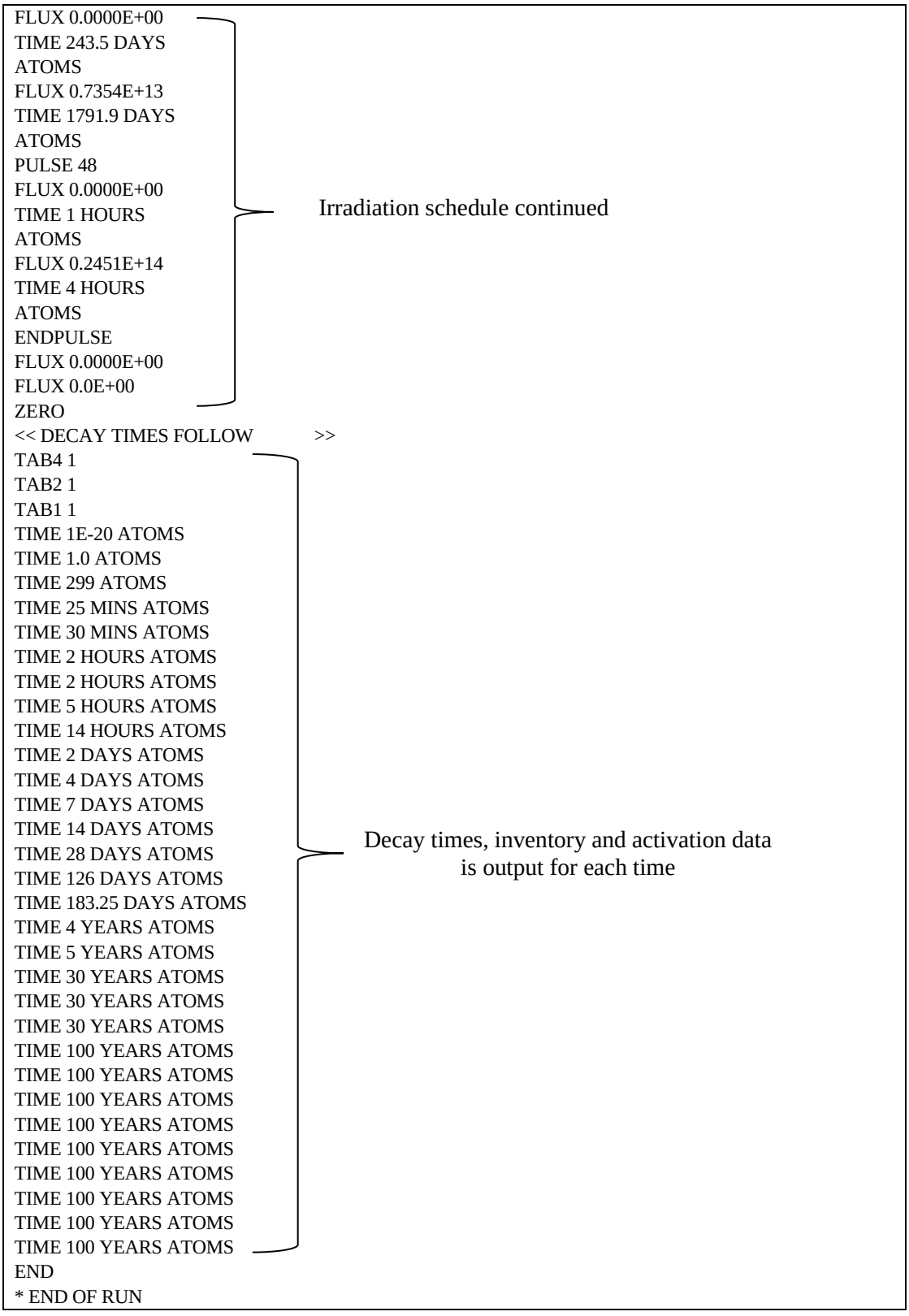

Figure 7.4 - FISPACT-II example input file.

APPENDIX 4: MATERIALS FOR INBOARD SHIELD

To mitigate heating and damage to the HTS magnets, radiation must be prevented from reaching the coils or attenuated to an acceptable level. In a conventional fusion tokamak, the shielding is provided by the neutron absorbing thick breeding blanket. Spherical tokamaks must have an explicit radiation shield on the inboard. Possible materials are assessed for their suitability through the reduction in fast neutron flux ($E_n > 0.1$ MeV) observed through a block of material. A number of identified shield materials are compared for their performance in terms of fast neutron flux and heating of the magnets. The effect of adding coolant to the shielding material is also considered.

Model and calculations

A simple block model 'model A' was used with F2 MCNP surface tallies estimating the neutron flux on the front and back of the block (Figure 7.5). For heating calculations, another block was placed behind the shielding block to represent the copper conductor 'model B', comprising 57 % copper, 38 % EUROFER and 5 % helium (Figure 7.6). Heating calculations used the F6 energy deposition tally for neutrons and photons.

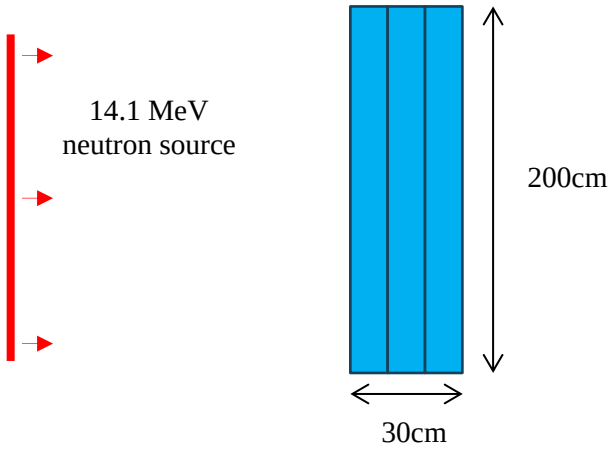

Figure 7.5 - Model A: a block model split into 6 layers for tallying fast flux through material.

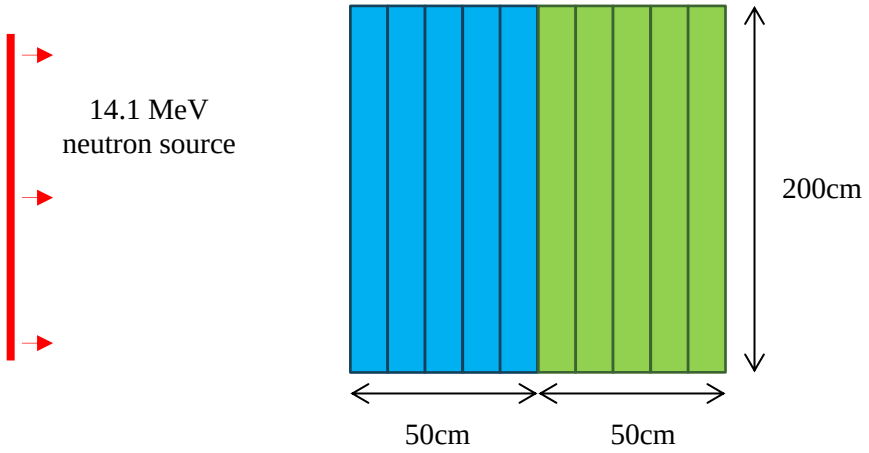

Figure 7.6 - Model B: a block model with two materials, blue- element being tested, green- copper to represent conductor in magnets, the blocks are each split into 10 layers for tallying fast flux through material.

Elemental test

The capability for reducing the fast neutrons ($E_n > 0.1$ MeV) has been investigated, using model A, for all stable isotopes (where cross-section data exists and apart from gaseous elements) with a view to verify the use of tungsten and/or highlight other possible candidate materials. The results are presented as the percentage of incident fast neutron flux to reach the back of the block (Figure 7.7).

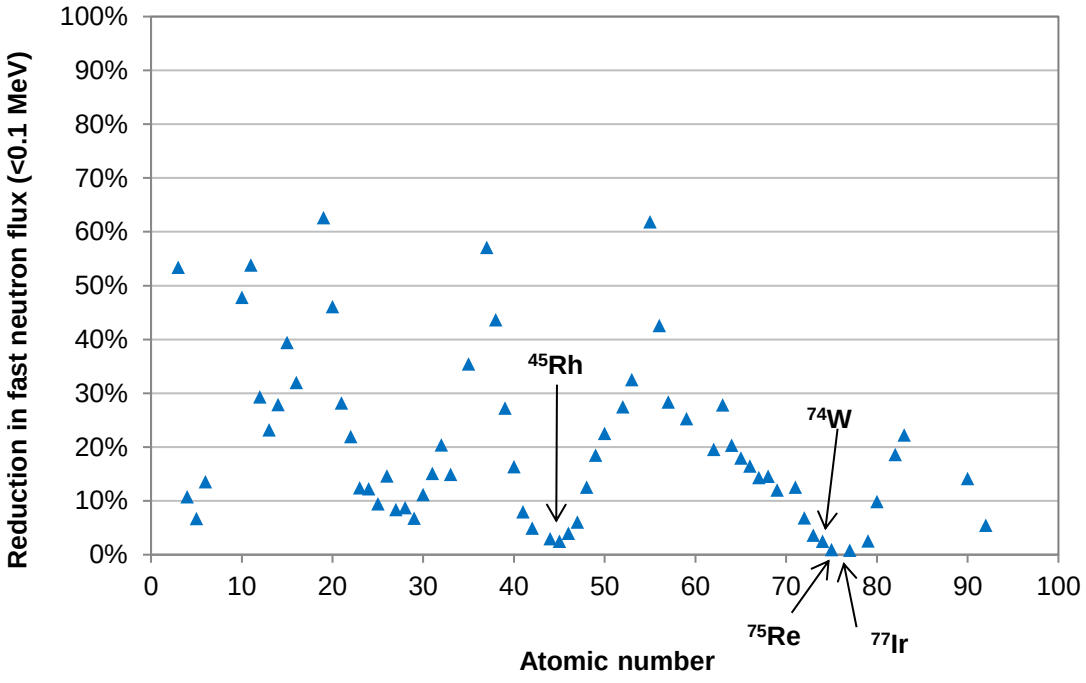

Figure 7.7 - Reduction in fast neutron flux (< 0.1 MeV) through a block of material.

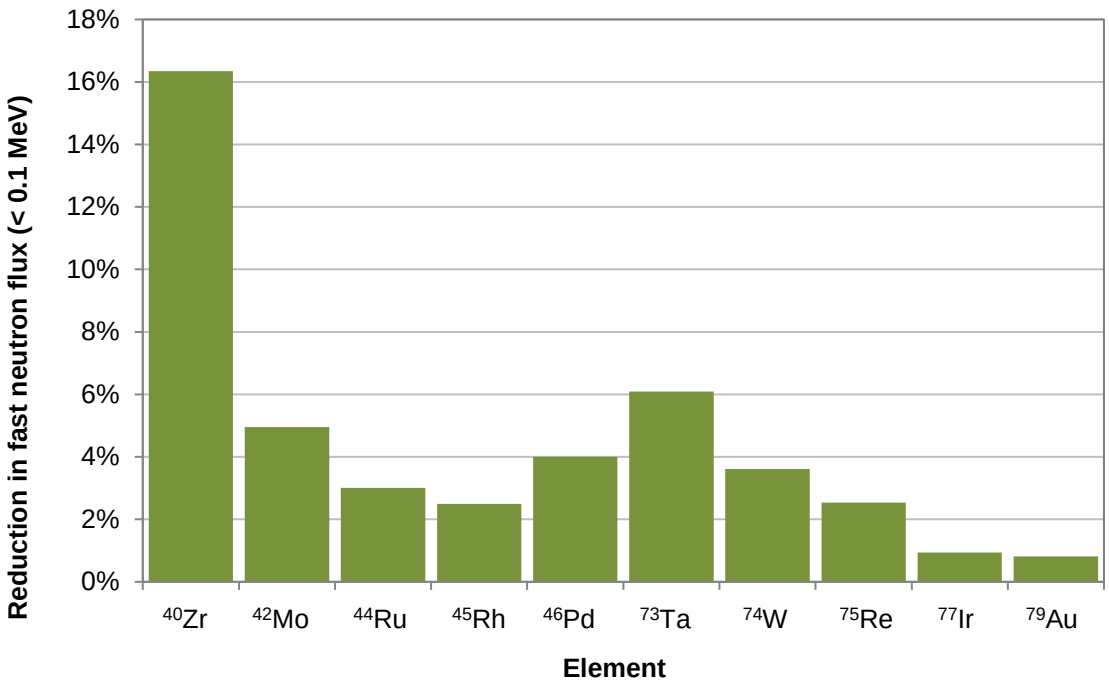

Figure 7.8 - Reduction in fast neutron flux for 10 of the elements.

The reduction in fast neutron flux for the 10 elements is shown in Figure 7.8. Of the ten elements tungsten is the most suitable, if not the only suitable, material for use as a shielding material within a fusion device. Within the literature [177], [178], however, other materials are considered such as: WC, B_4C, WB_4C, ZrH_2, $Zr(BH_4)_4$, TiH_2 and EUROFER. Tungsten itself is rarely used in its elemental form and would be used as a carbide (WC).

Shield material comparison

A comparison of some identified shielding materials, in terms of the fast neutron flux and magnet heating is given in Figure 7.9 and Figure 7.10, respectively. These calculations were performed with model B.

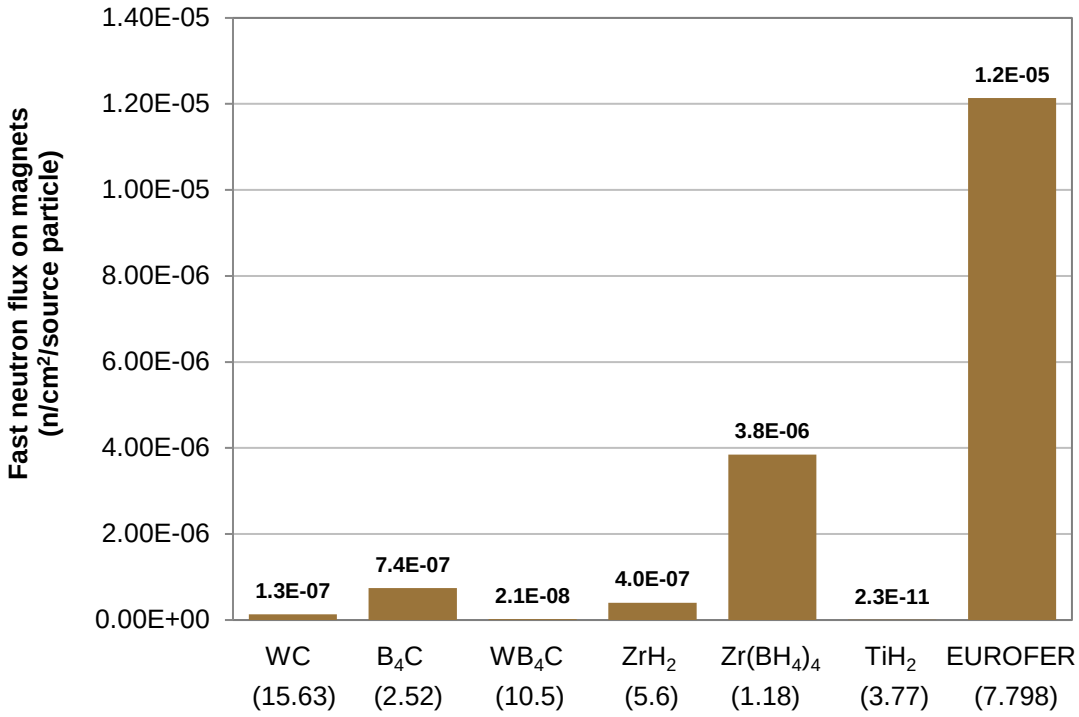

Figure 7.9 - Neutron fast flux on the magnet for different shielding materials. The mass density (g/cm^3) is given in parenthesis below the material name.

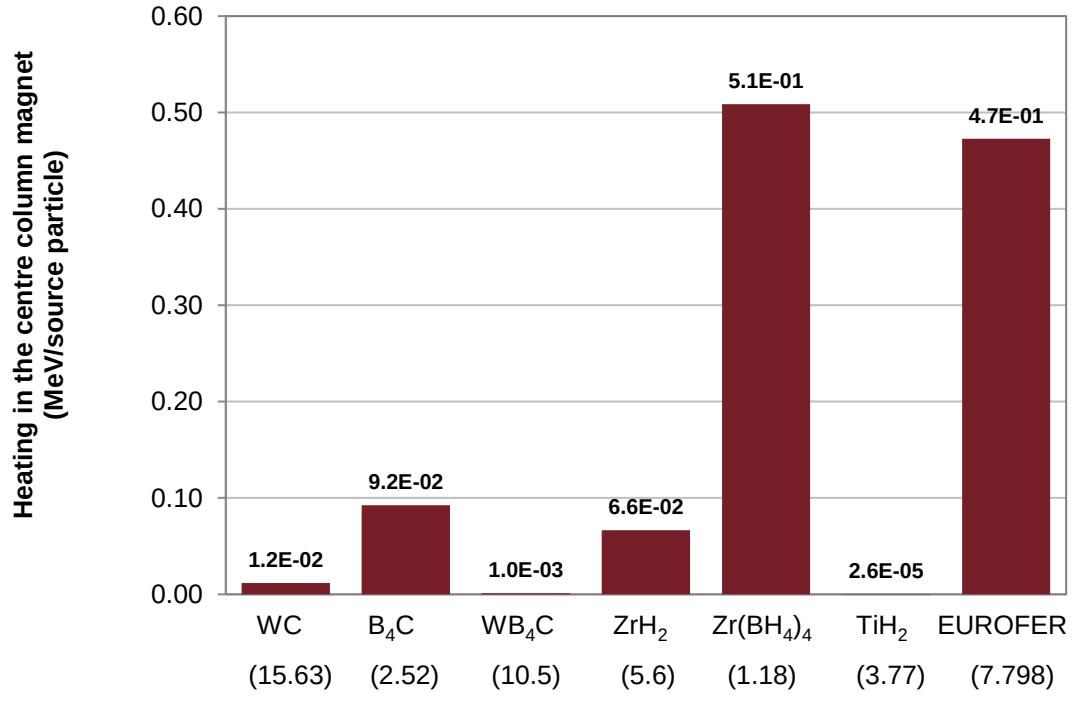

Figure 7.10 - Nuclear heating on the magnet for different shielding materials. The mass density (g/cm^3) is given in parenthesis below the material name.

Addition of coolant

Some form of cooling to the shield will be required, thereby water (H_2O) has been added with varying volume. The effect of adding coolant to the tungsten carbide is shown in the nuclear heating of the magnet (Figure 7.11).

A ratio of ~10 - 14 % coolant is the optimum for nuclear heating performance.

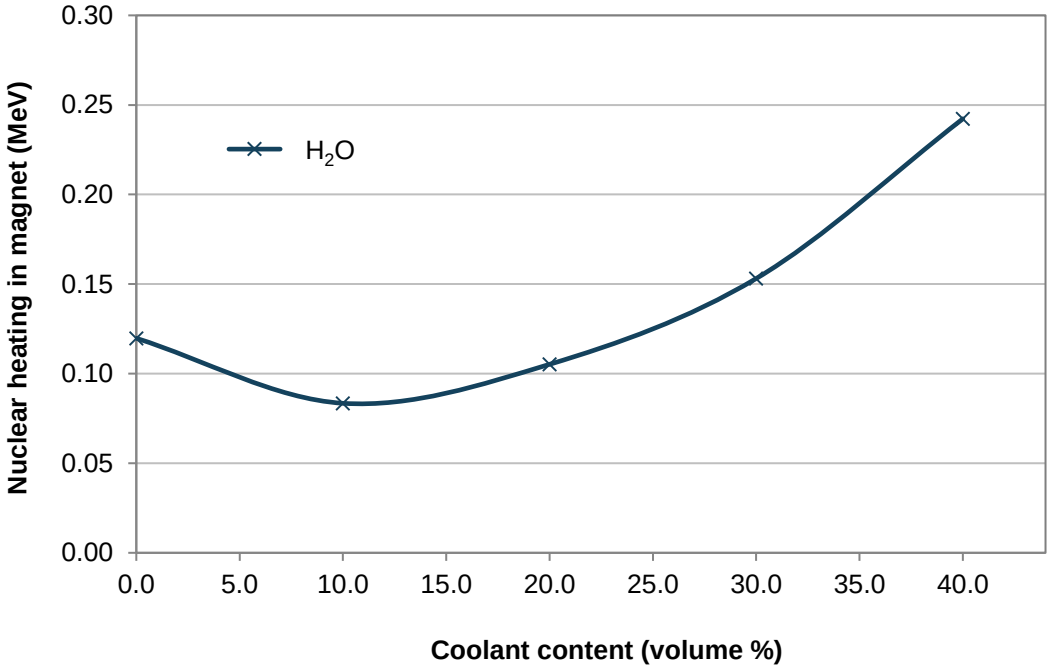

Figure 7.11 - Nuclear heating in magnet as a function of coolant volume using water (H_2O) with tungsten carbide shielding.

Conclusions

The following main conclusions were drawn from this shielding assessment:

- The comparison of fast flux reduction capabilities of a number of stable isotopes has reaffirmed the shielding selection of tungsten carbide. The few elements that could potentially perform better are not suitable either due to cost, availability or usability.
- The addition of boron, boron doping, could reduce the amount of tungsten and improve the shielding capabilities.
- A water volume fraction of 0.13 is the optimum for reducing nuclear heating in the copper conductors within the centre column magnet.

APPENDIX 5: RESULTS

APPENDIX 5.1: Results for spherical tokamak configurations

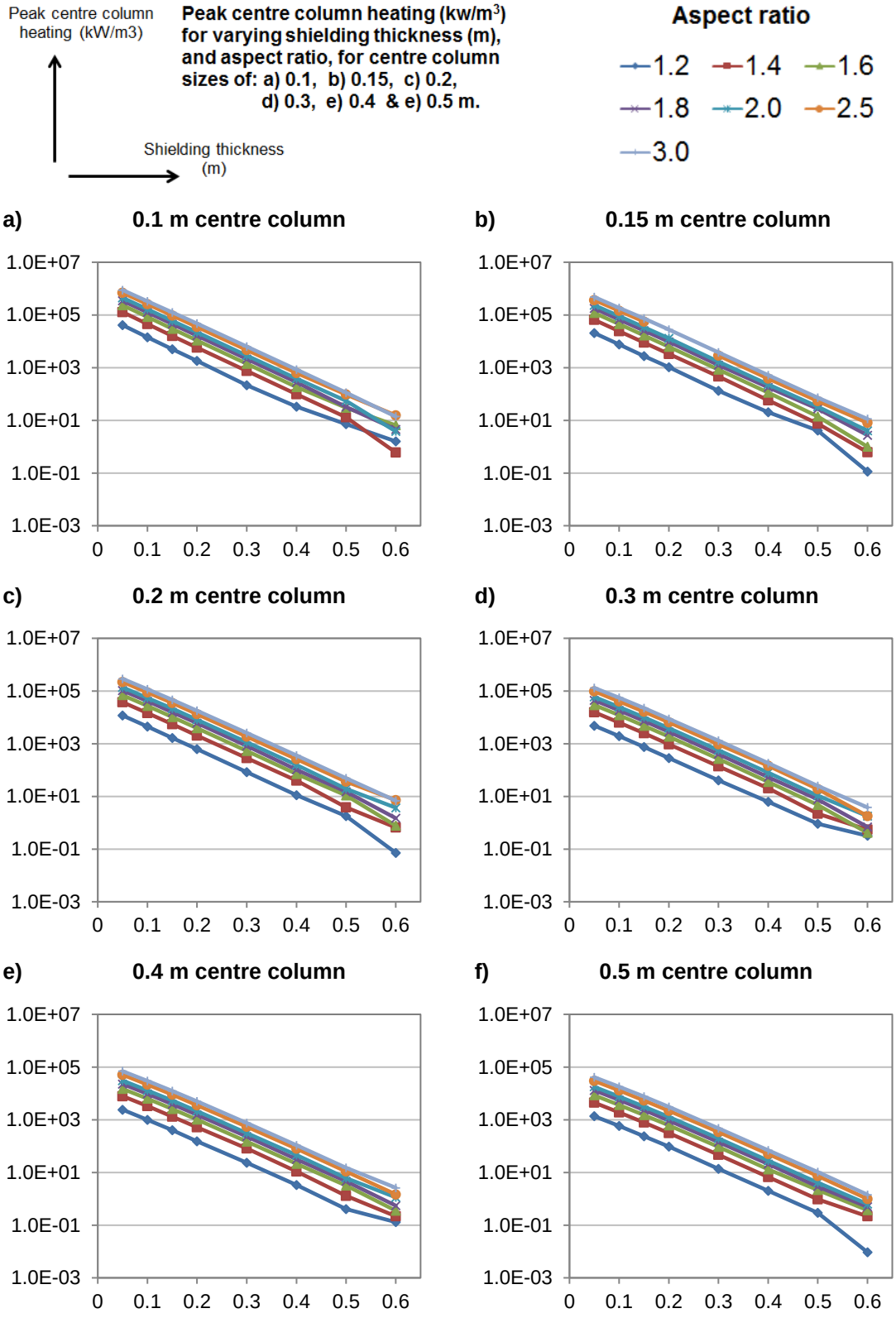

Figure 7.12 - Variation in peak nuclear heating with inboard shielding thickness for varying aspect ratio and centre column radius.

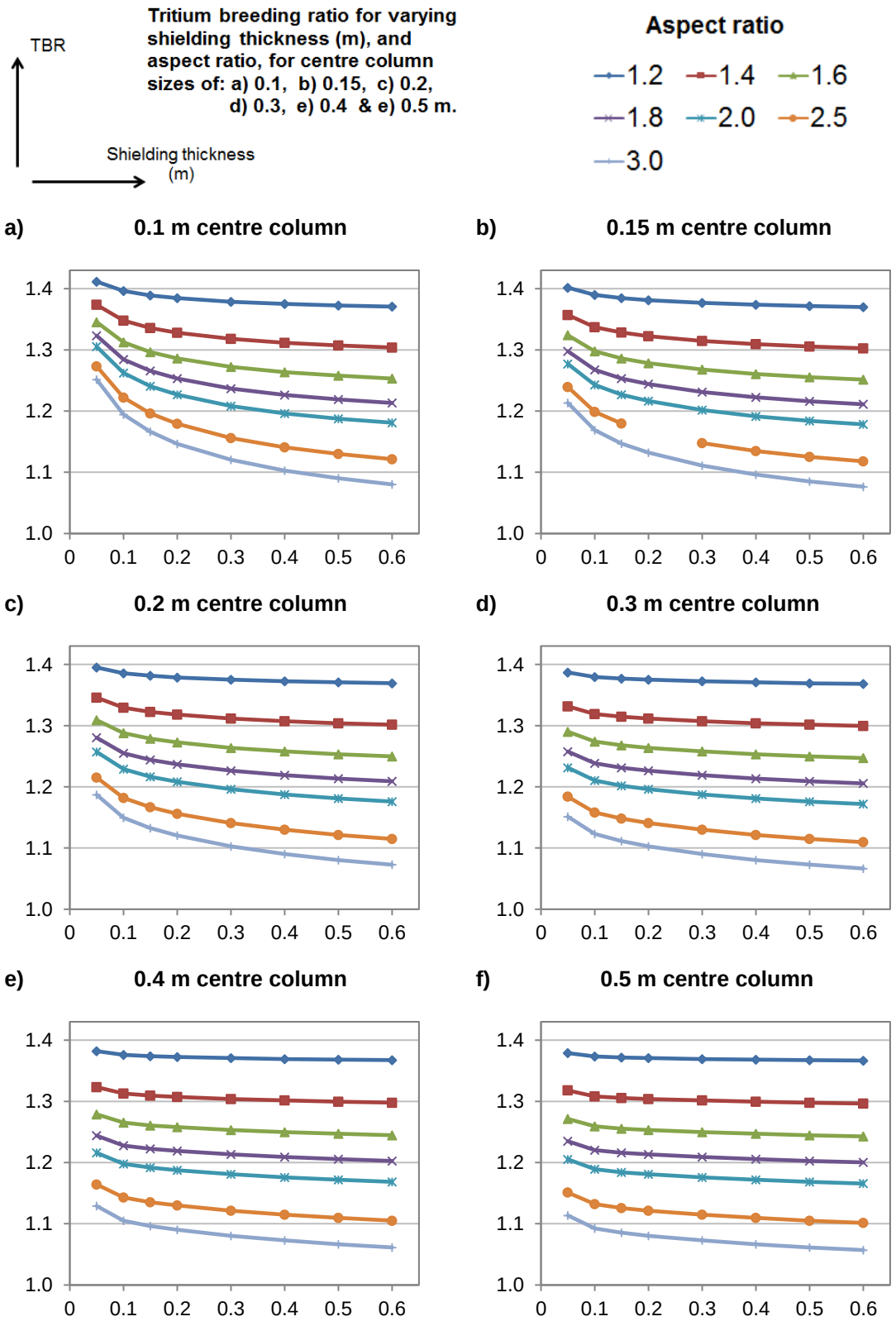

Figure 7.13 - Variation in TBR with inboard shielding thickness for varying aspect ratio and centre column radius.

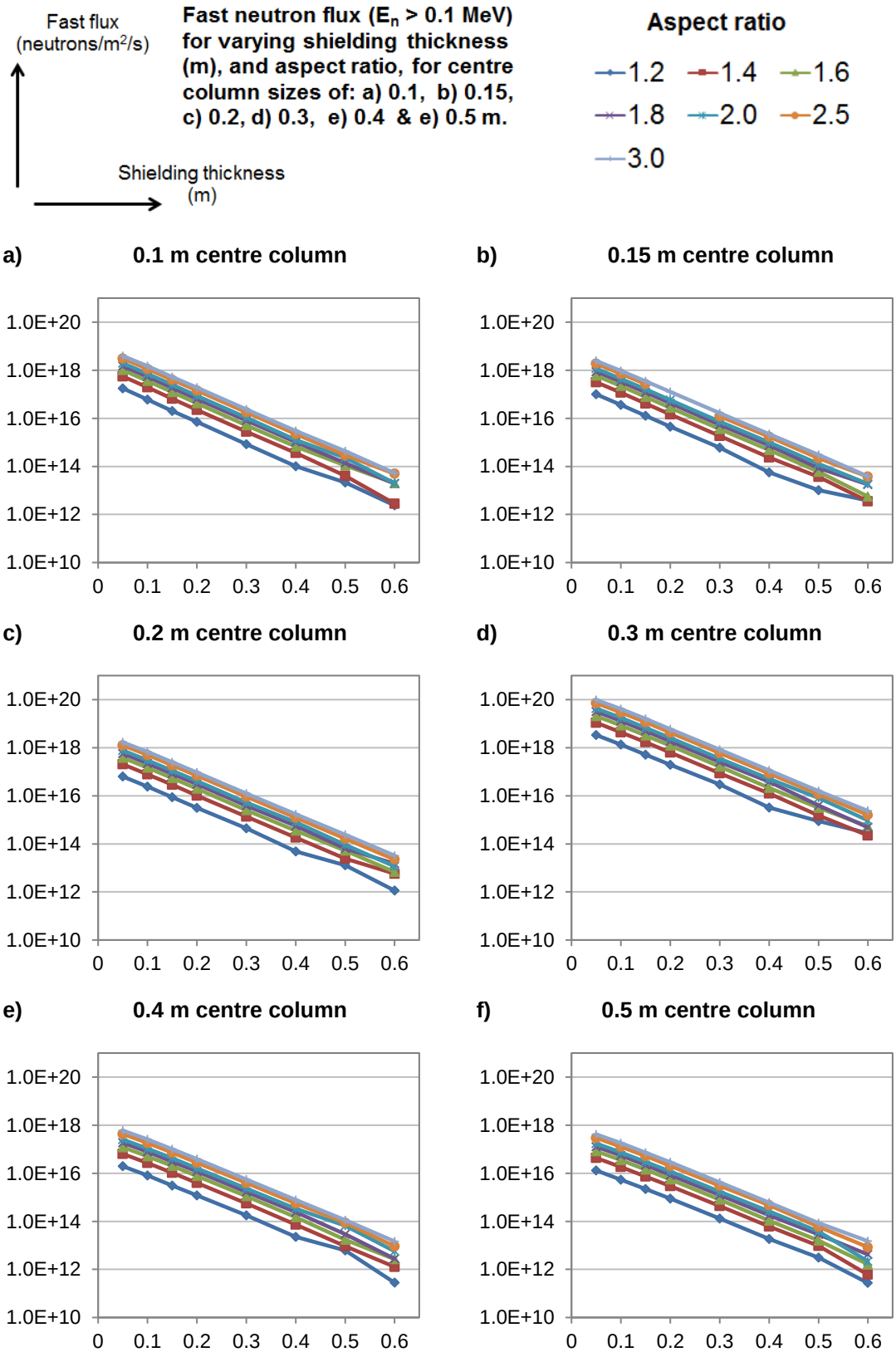

Figure 7.14 - Variation in peak fast flux with inboard shielding thickness for varying aspect ratio and centre column radius.

APPENDIX 5.2: Activation of breeder blanket materials

The following appendix (Figure 7.15 - Figure 7.20) provides the activity concentration results for the remaining six blanket mixtures activated. These results were used as part of the discussions in Section 4.5.6. The data is provided for a selection of dominant nuclides at 50 - 100 years cooling time.

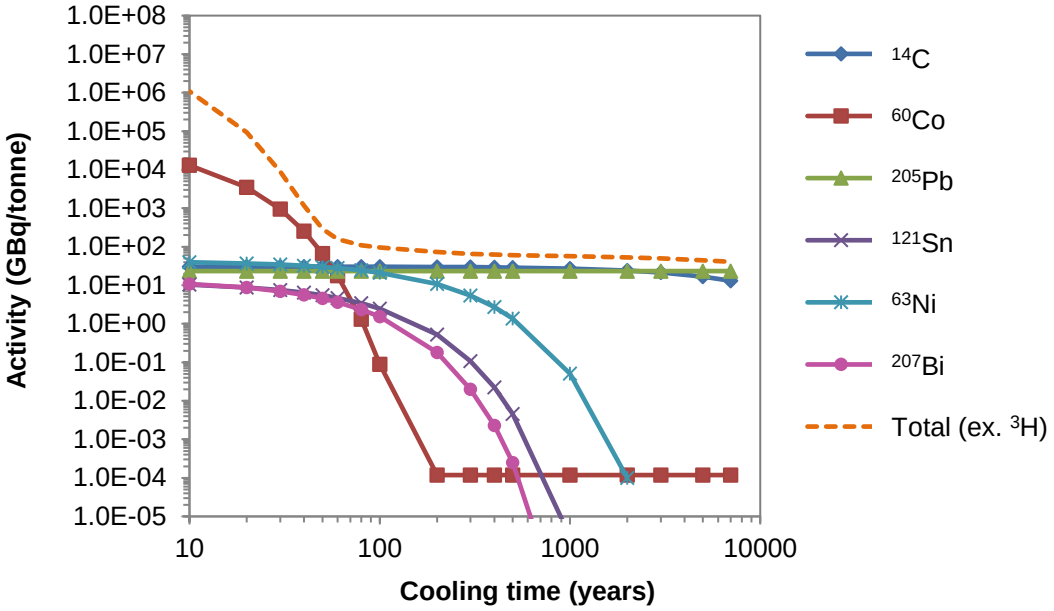

Figure 7.15- Dominant nuclides for blanket mix 2 using a LiPb breeder material.

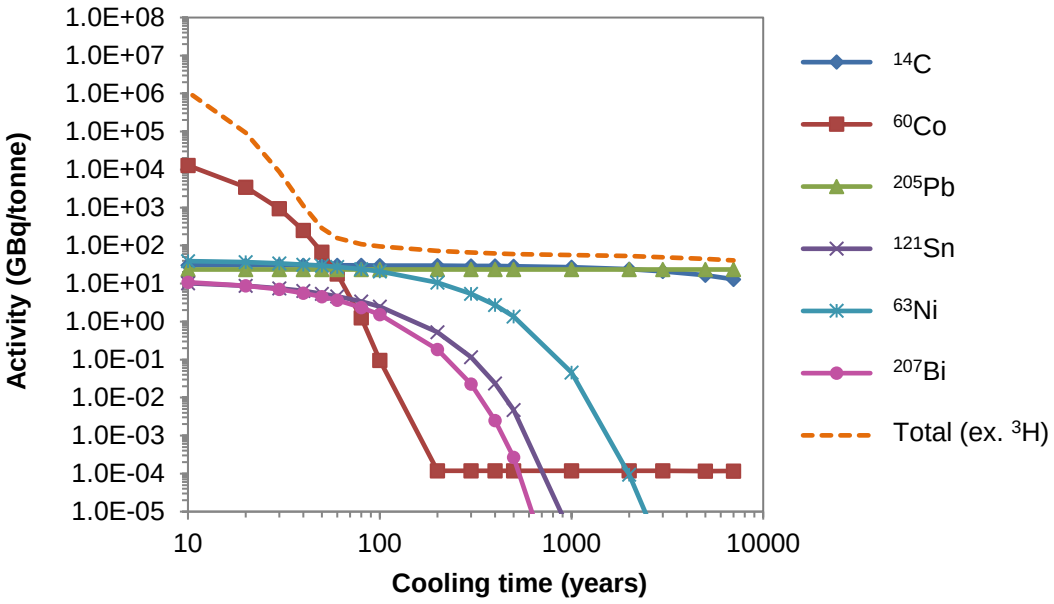

Figure 7.16 - Dominant nuclides for blanket mix 3 using a LiPb breeder material.

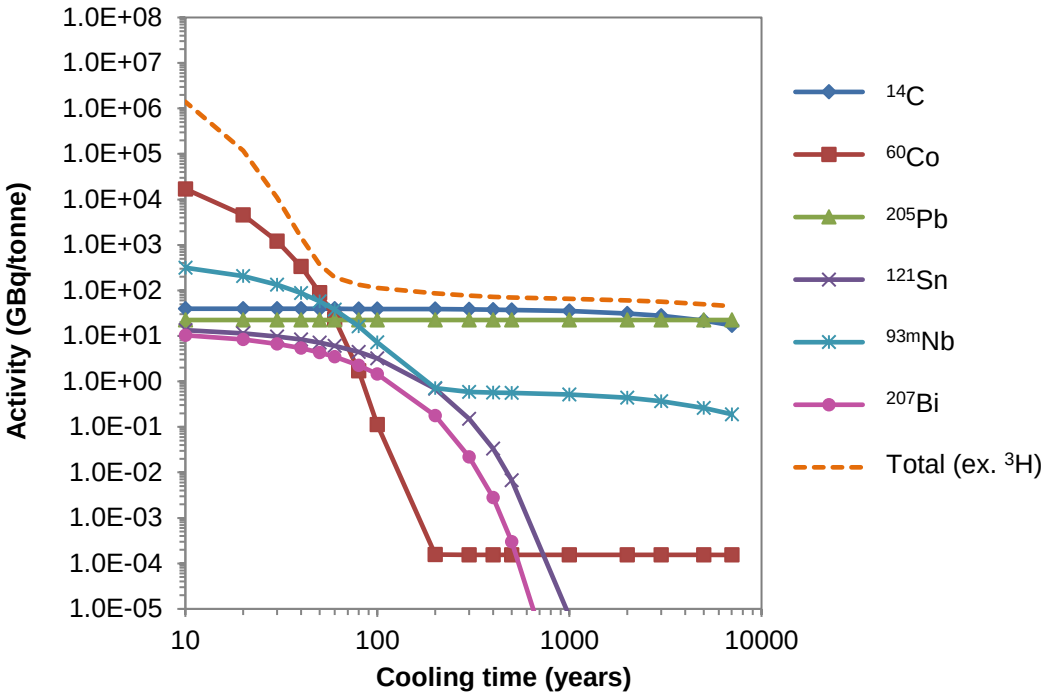

Figure 7.17 - Dominant nuclides for blanket mix 4 using a LiPb breeder material.

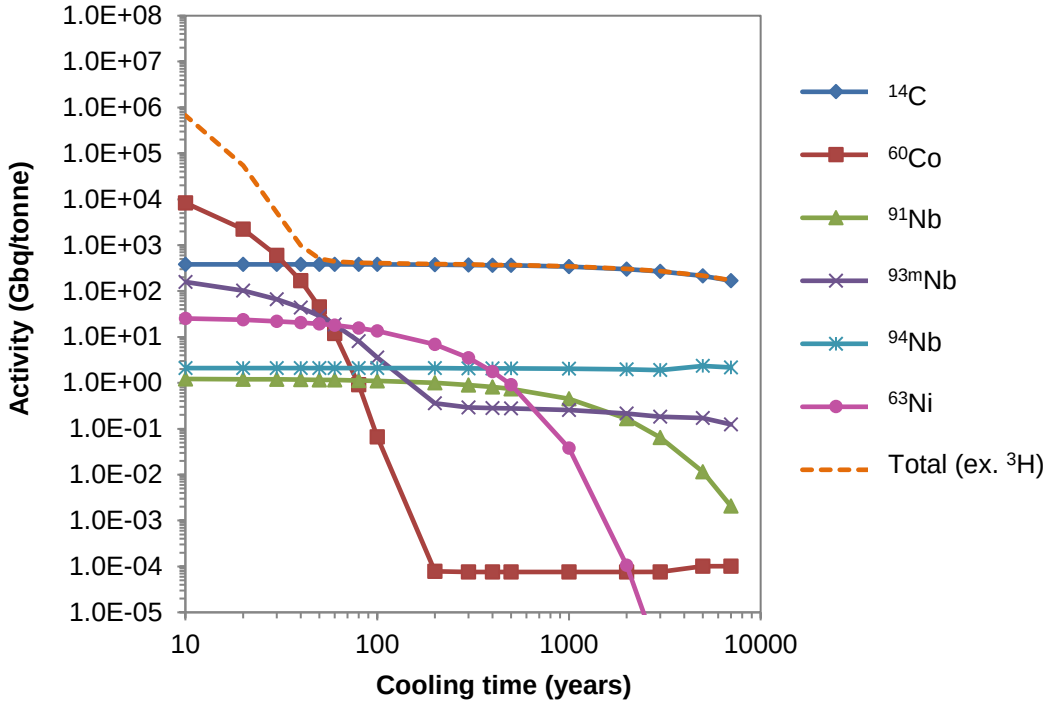

Figure 7.18 - Dominant nuclides for blanket mix 5 using a LiFBe breeder material.

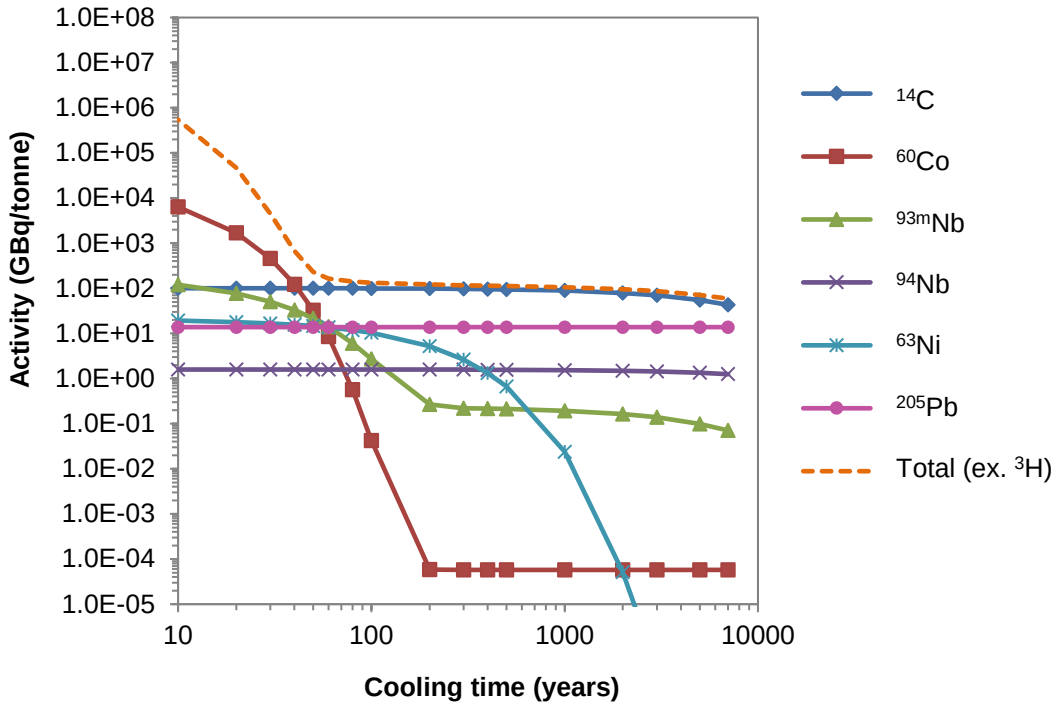

Figure 7.19 - Dominant nuclides for blanket 6 using a Li_8PbO_6 breeder material.

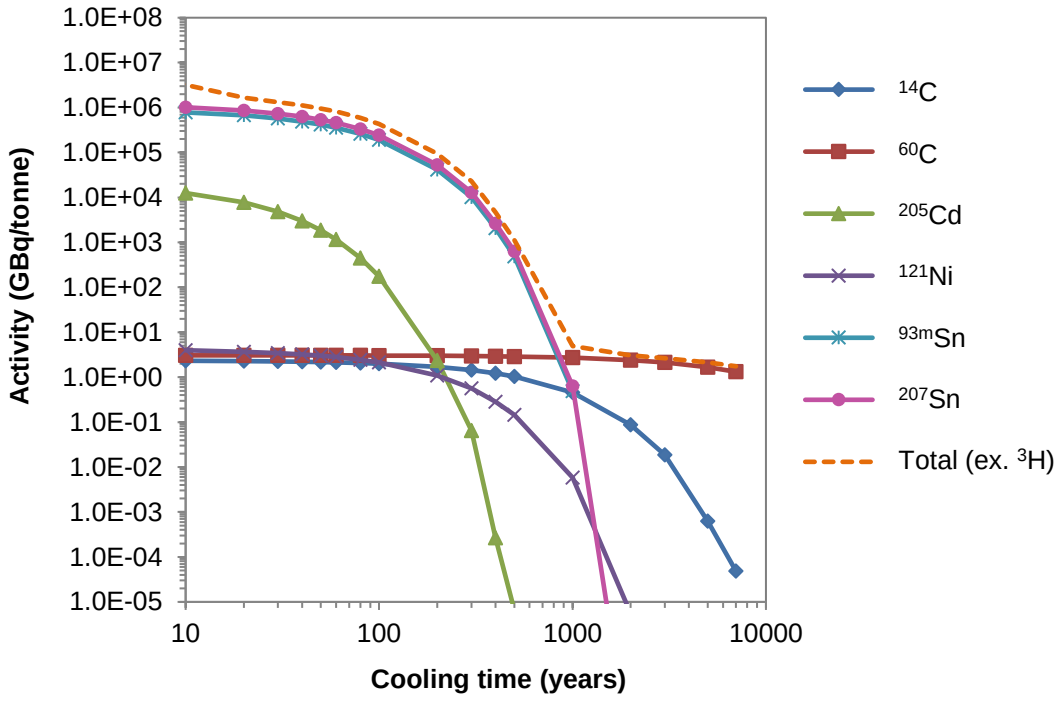

Figure 7.20 - Dominant nuclides for blanket 7 using a LiSn breeder material.

APPENDIX 5.3: Radioactive waste results

A summary of component contribution using a 9 cm structured mesh and an unstructured mesh approach is given in Table 7.13 - Table 7.14. The mass of material within each waste class, including the percentage for potential recycling, is given in Figure 7.21 to Figure 7.25, for the full model, blankets, vacuum vessel, divertors and toroidal field coils respectively. These figures show results using the 3 methods, cell based, structured mesh (both a 9 cm and 15 cm resolution) and an unstructured mesh. The mass data (in kilotonnes) is given in Table 7.15 to Table 7.19.

Table 7.13 - Material classification for each component after 100 years cooling (using method 2 – structured mesh 9 cm resolution).

	Mass (kt) (Percentage of component)			**Potential recycling (%)**	
	NAW	LLW	ILW	LLW-RM	ILW-RM
Divertor	0.0 (0%)	2.9 (74%)	1.0 (26%)	100%	100%
Blanket	0.0 (0%)	0.0 (0%)	8.8 (100%)		100%
Vacuum vessel	2.7 (20%)	5.6 (42%)	5.0 (37%)	100%	100%
TF coils	0.0 (1%)	2.1 (94%)	0.1 (3%)	100%	90%
Remaining materials	13.2 (57%)	8.3 (36%)	1.7 (7%)	100%	99%
Total	15.9 (31%)	19.0 (37%)	16.5 (32%)	100%	100%

Table 7.14 - Material classification for each component after 100 years cooling (using method 3 – unstructured mesh).

	Mass (kt) (Percentage of component)			**Potential recycling (%)**	
	NAW	LLW	ILW	LLW-RM	ILW-RM
Divertor	0.0 (0%)	3.2 (81%)	0.8 (19%)	100%	94%
Blanket	0.0 (0%)	0.0 (0%)	8.8 (100%)		100%
Vacuum vessel	2.2 (17%)	5.6 (43%)	5.2 (40%)	100%	100%
TF coils	0.1 (5%)	2.1 (92%)	0.1 (3%)	100%	94%
Remaining materials	9.1 (49%)	7.8 (42%)	1.9 (10%)	100%	99%
Total	11.5 (25%)	18.7 (40%)	16.6 (35%)	100%	100%

a) Mass of total NAW

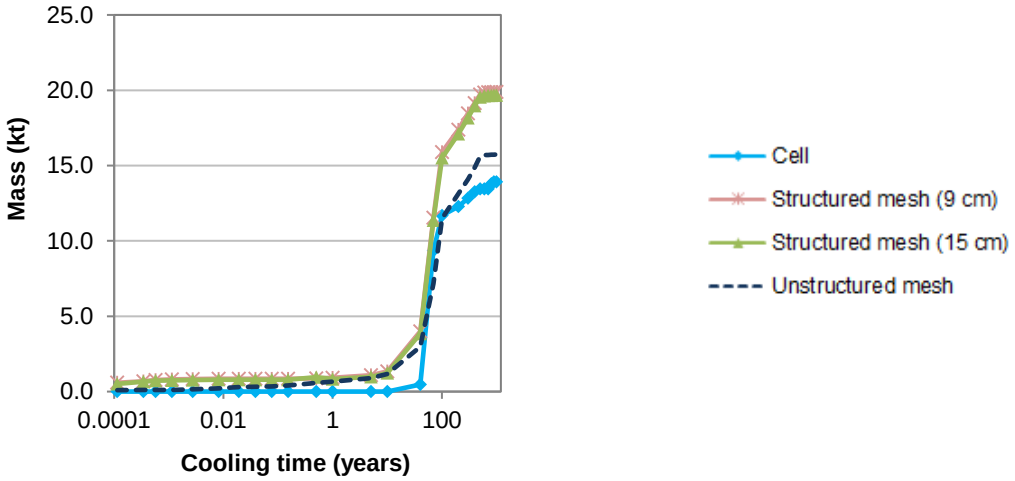

b) Mass of total LLW

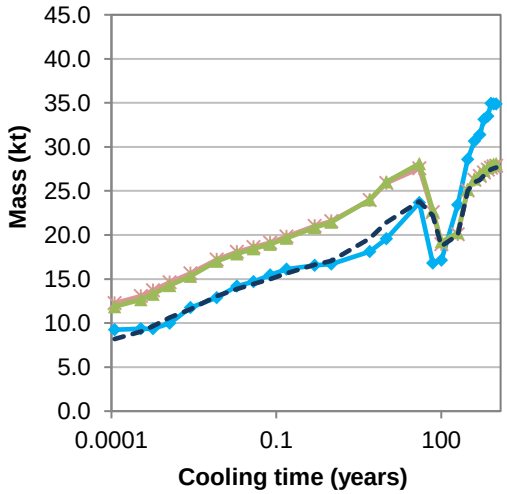

c) Potential for recycling (LLW-RM)

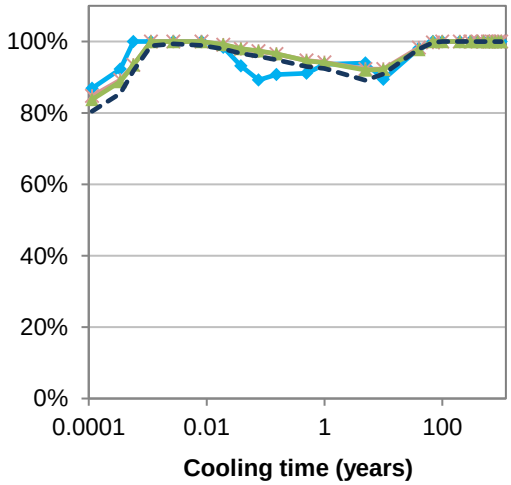

d) Mass of total ILW

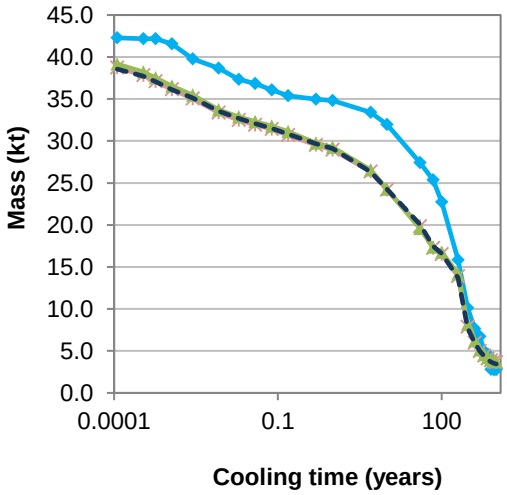

e) Potential for recycling (ILW-RM)

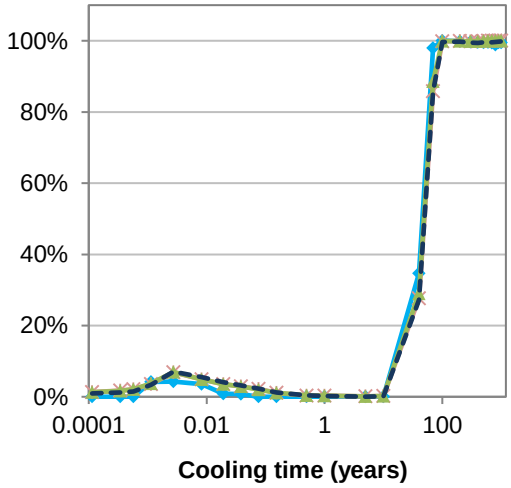

Figure 7.21 - Mass (kilotonne) of material comprising the whole model (EU DEMO 2015) within each waste class, including the percentage for potential recycling.

a) Mass of blanket NAW

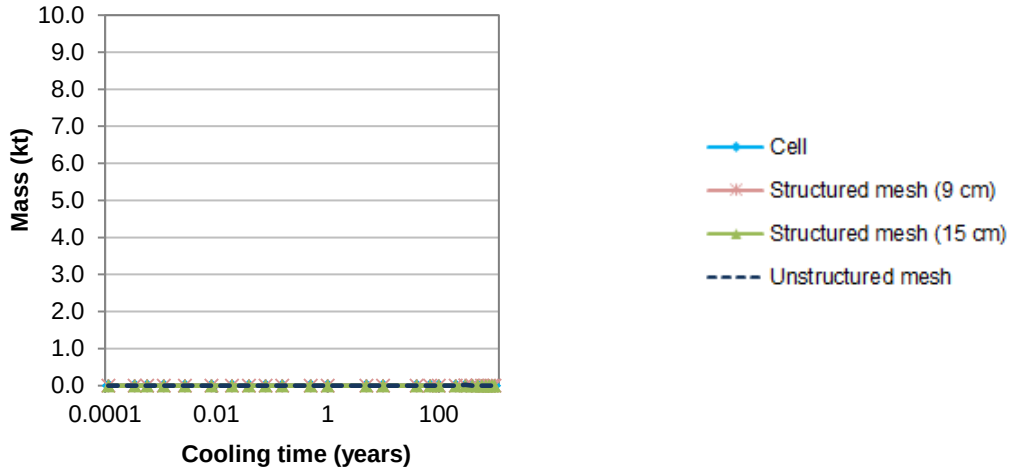

b) Mass of blanket LLW

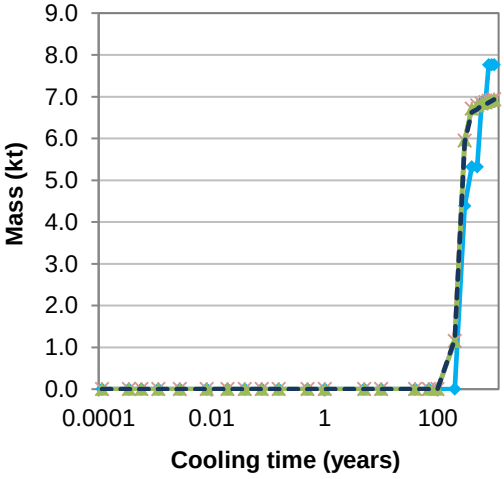

c) Potential for recycling (LLW-RM)

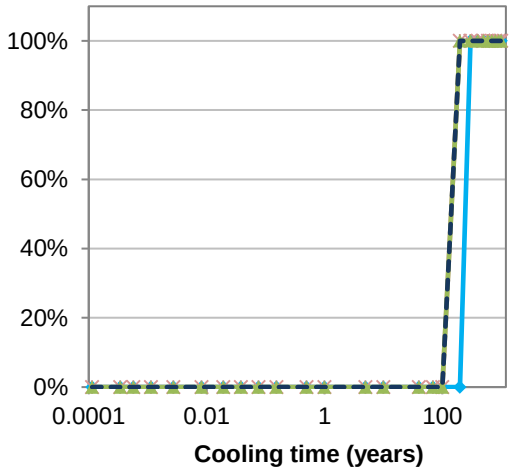

d) Mass of blanket ILW

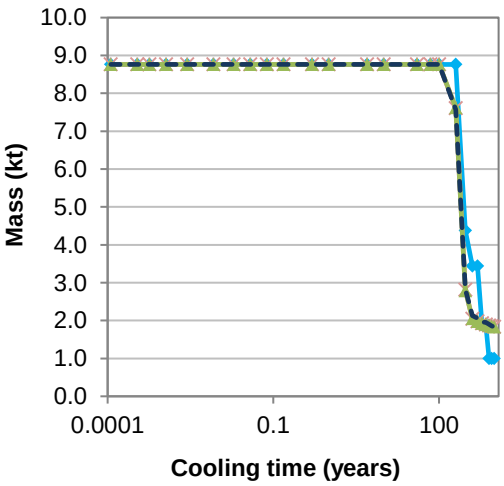

e) Potential for recycling (ILW-RM)

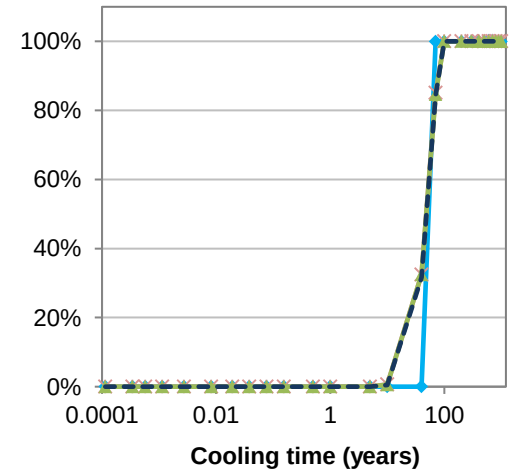

Figure 7.22 - Mass (kilotonne) of material comprising the blanket (EU DEMO 2015) within each waste class, including the percentage for potential recycling.

a) Mass of vacuum vessel NAW

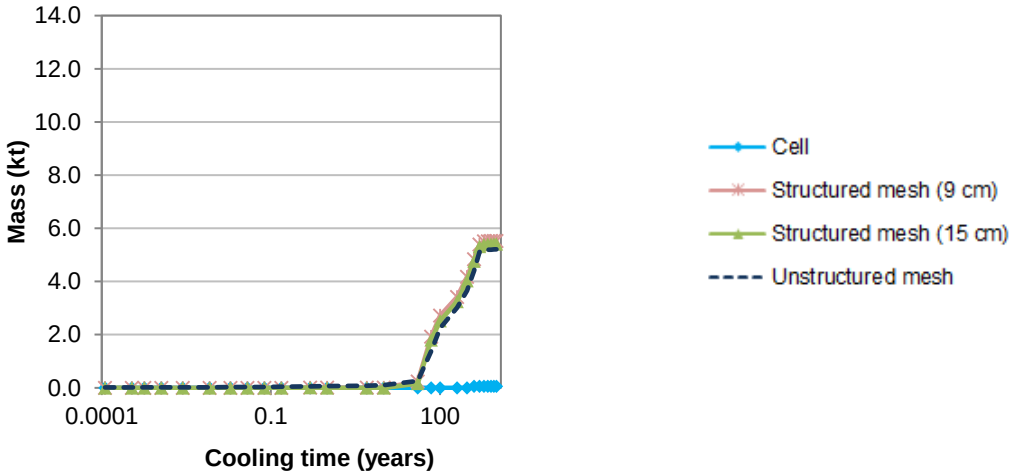

b) Mass of vacuum vessel LLW

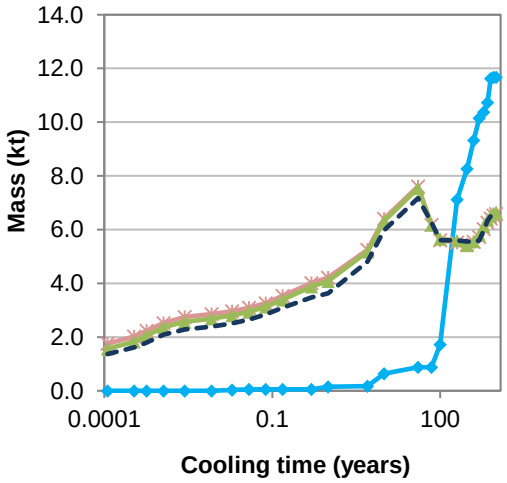

c) Potential for recycling (LLW-RM)

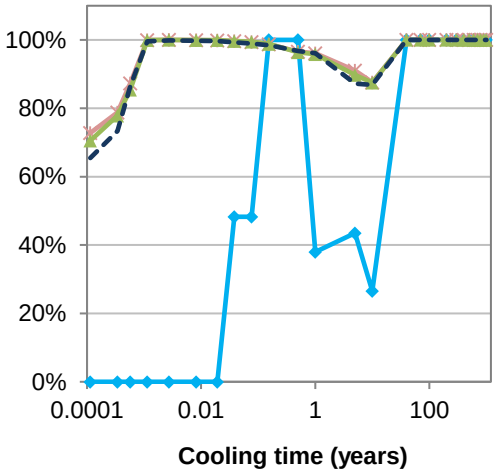

d) Mass of vacuum vessel ILW

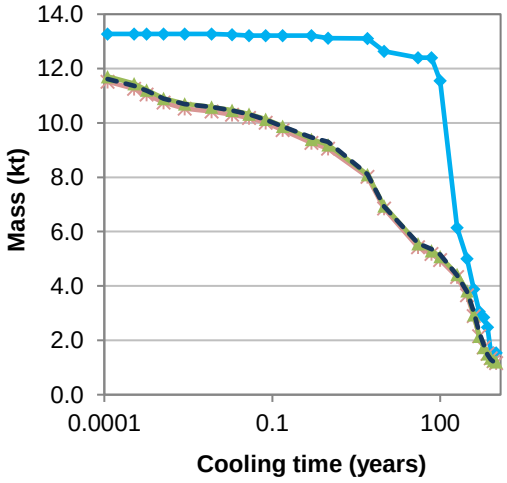

e) Potential for recycling (ILW-RM)

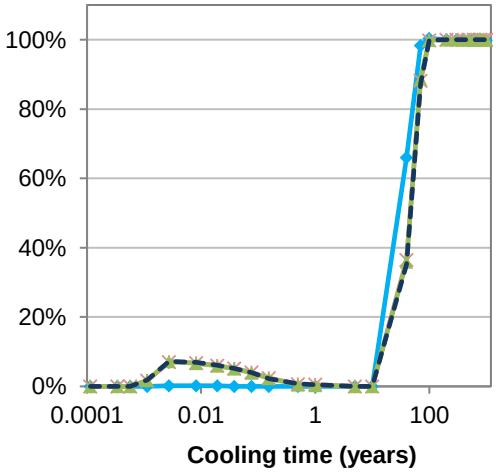

Figure 7.23 - Mass (kilotonne) of material comprising the vacuum vessel (EU DEMO 2015) within each waste class, including the percentage for potential recycling.

a) Mass of divertor NAW

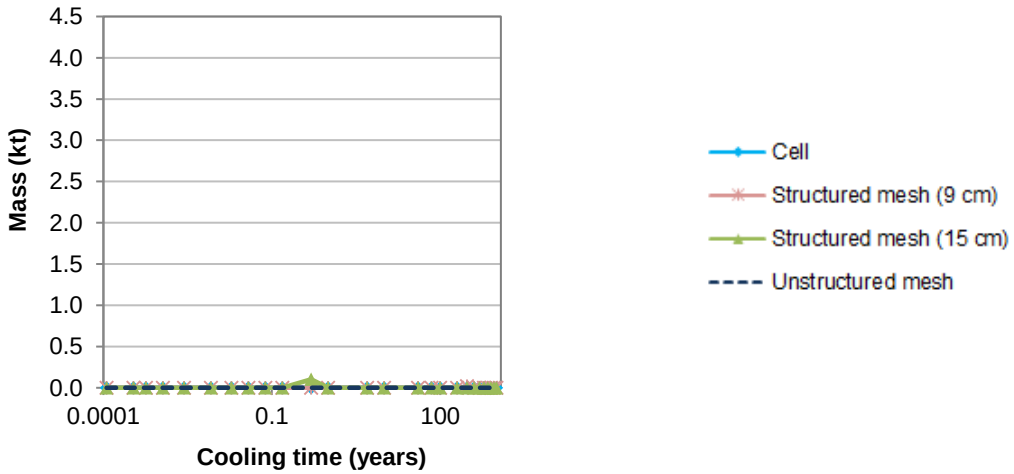

b) Mass of divertor LLW

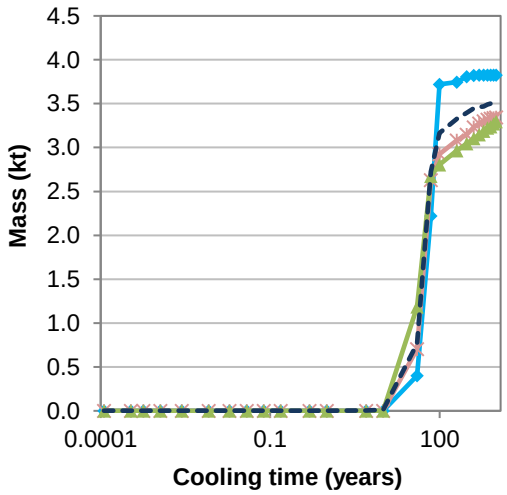

c) Potential for recycling (LLW-RM)

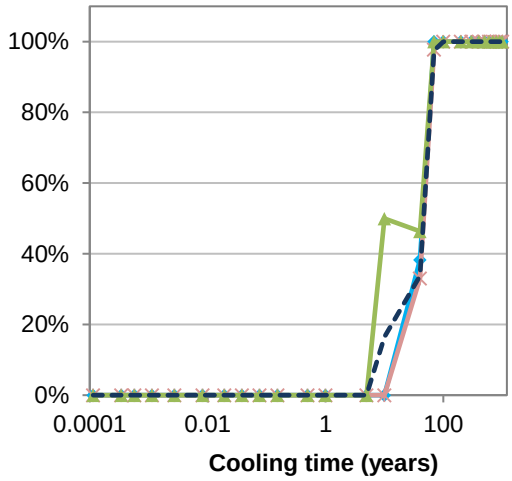

d) Mass of divertor ILW

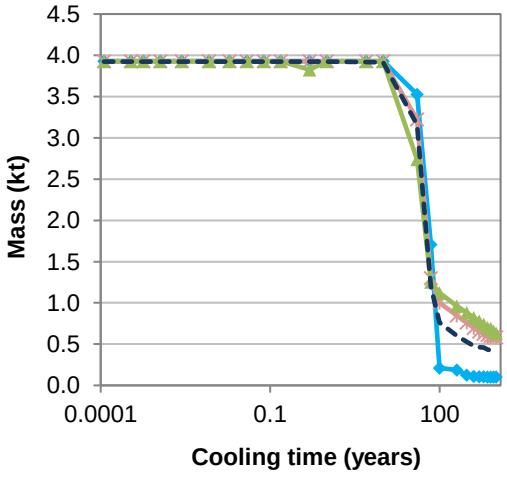

e) Potential for recycling (ILW-RM)

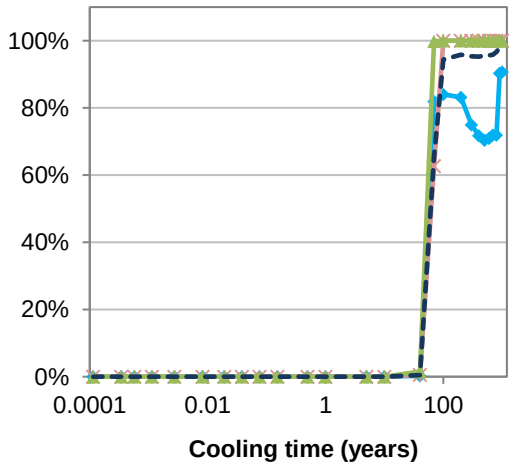

Figure 7.24 - Mass (kilotonne) of material comprising the divertor (EU DEMO 2015) within each waste class, including the percentage for potential recycling.

a) Mass of toroidal field coils NAW

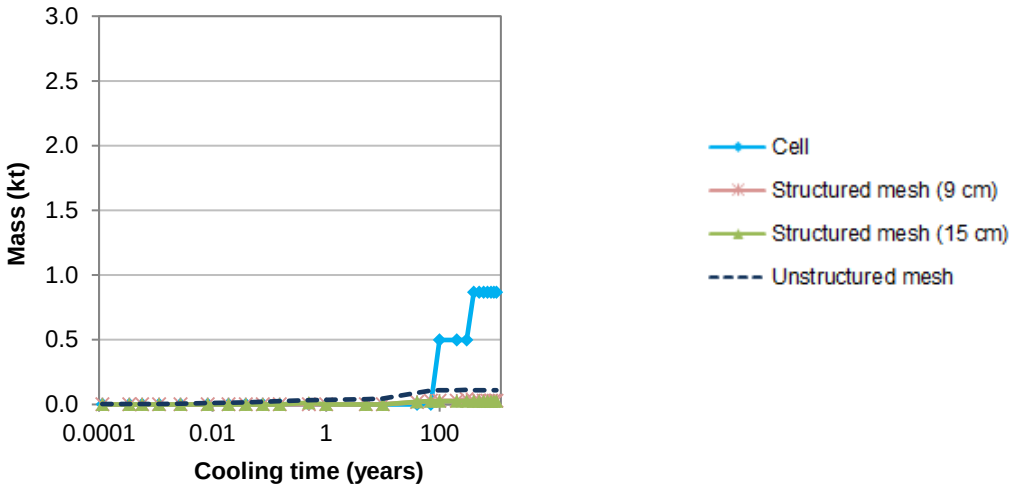

b) Mass of toroidal field coils LLW

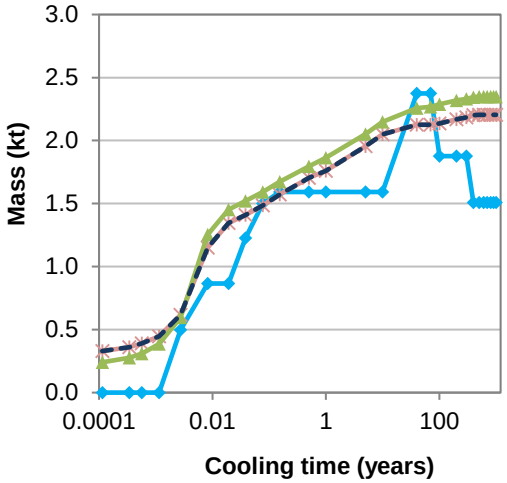

c) Potential for recycling (LLW-RM)

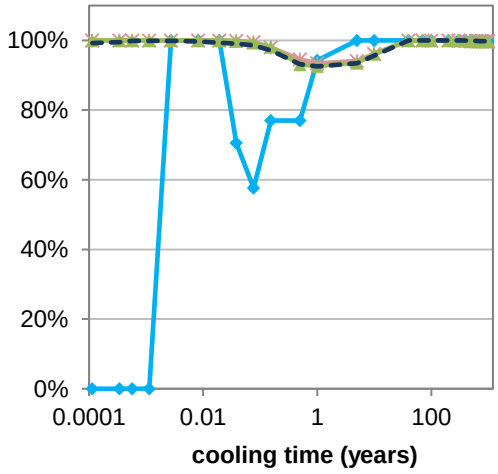

d) Mass of toroidal field coils ILW

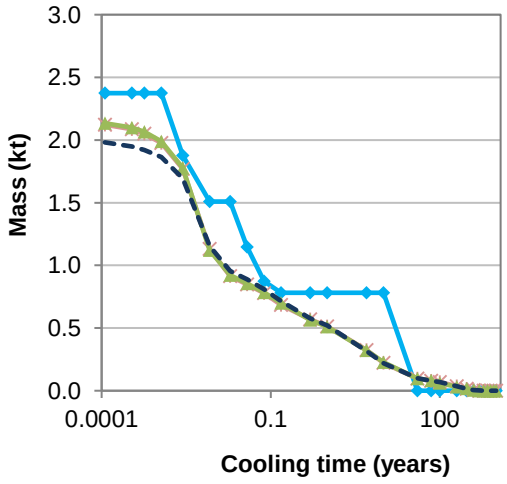

e) Potential for recycling (ILW-RM)

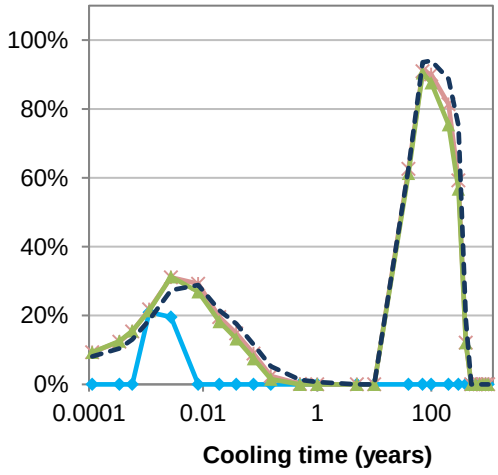

Figure 7.25 - Mass (kilotonne) of material comprising the toroidal field coils (EU DEMO 2015) within each waste class, including the percentage for potential recycling.

Table 7.15 - Mass of total model (EU DEMO 2015) material, in kilotonnes, within each waste class, for all methods used.

Time (years)	Cell					Structured mesh (9 cm)					Structured mesh (15 cm)					Unstructured mesh				
	NAW	LLW	ILW	LLW-RM	ILW-RM	NAW	LLW	ILW	LLW-RM	ILW-RM	NAW	LLW	ILW	LLW-RM	ILW-RM	NAW	LLW	ILW	LLW-RM	ILW-RM
1.1E-04	0.000	9.244	42.286	8.034	0.000	0.587	12.259	38.755	10.384	0.520	0.510	11.858	39.162	9.932	0.509	0.095	8.189	38.563	6.590	0.366
3.4E-04	0.000	9.350	42.179	8.627	0.000	0.688	13.069	37.839	11.654	0.655	0.654	12.663	38.212	11.238	0.645	0.107	9.036	37.704	7.722	0.461
5.7E-04	0.000	9.350	42.179	9.350	0.000	0.761	13.705	37.124	12.808	0.790	0.730	13.273	37.526	12.405	0.794	0.110	9.655	37.082	8.865	0.550
1.1E-03	0.000	9.966	41.564	9.966	1.728	0.803	14.621	36.146	14.614	1.292	0.755	14.257	36.517	14.246	1.352	0.117	10.621	36.109	10.493	1.227
2.7E-03	0.000	11.760	39.770	11.760	1.695	0.828	15.656	35.049	15.656	2.400	0.774	15.303	35.452	15.303	2.454	0.146	11.564	35.136	11.492	2.465
8.2E-03	0.000	12.870	38.660	12.870	1.358	0.842	17.218	33.370	17.215	1.648	0.785	17.014	33.730	17.012	1.666	0.210	13.061	33.576	12.922	1.856
1.9E-02	0.000	14.202	37.328	13.970	0.307	0.845	18.078	32.483	17.903	1.165	0.785	17.869	32.875	17.724	1.167	0.299	13.869	32.679	13.579	1.333
3.8E-02	0.000	14.693	36.837	13.683	0.279	0.848	18.619	31.939	18.229	0.941	0.785	18.431	32.313	18.070	0.929	0.325	14.445	32.077	13.967	1.029
7.7E-02	0.000	15.450	36.080	13.786	0.000	0.852	19.121	31.439	18.597	0.687	0.787	18.965	31.777	18.465	0.650	0.348	14.988	31.511	14.371	0.727
1.5E-01	0.000	16.129	35.401	14.633	0.000	0.860	19.824	30.721	19.121	0.335	0.791	19.623	31.115	18.957	0.345	0.410	15.629	30.808	14.831	0.370
5.0E-01	0.000	16.539	34.990	15.071	0.000	0.883	21.011	29.528	19.890	0.102	0.949	20.828	29.753	19.692	0.110	0.566	16.616	29.665	15.446	0.109
1.0E+00	0.000	16.712	34.818	15.639	0.000	0.910	21.557	28.953	20.299	0.101	0.821	21.456	29.252	20.174	0.102	0.667	17.073	29.107	15.783	0.068
5.0E+00	0.000	18.101	33.429	17.009	0.000	1.091	23.968	26.370	22.113	0.028	0.976	23.995	26.558	22.065	0.030	0.903	19.616	26.328	17.484	0.009
1.0E+01	0.000	19.552	31.978	17.473	0.000	1.341	25.905	24.174	23.904	0.060	1.232	26.017	24.281	23.980	0.063	1.164	21.423	24.260	19.473	0.041
4.0E+01	0.461	23.661	27.408	23.202	9.499	3.990	27.579	19.823	27.108	5.485	3.856	28.102	19.571	27.465	5.670	2.976	23.815	20.056	23.308	5.446
7.0E+01	9.350	16.814	25.366	16.814	24.850	11.532	22.581	17.266	22.523	14.819	11.361	22.806	17.363	22.806	15.378	7.165	22.211	17.471	22.142	14.974
1.0E+02	11.692	17.113	22.724	17.113	22.737	15.898	18.952	16.529	18.952	16.504	15.515	19.248	16.765	19.248	16.746	11.502	18.737	16.607	18.737	16.544
2.0E+02	12.290	23.409	15.831	23.409	15.799	17.390	20.092	13.897	20.092	13.881	17.099	20.261	14.168	20.261	14.152	13.142	19.994	13.711	19.994	13.672
3.0E+02	12.833	28.581	10.115	28.581	10.079	18.457	25.063	7.868	25.063	7.852	18.171	25.172	8.186	25.172	8.171	14.081	25.027	7.739	25.027	7.700
4.0E+02	13.259	30.641	7.630	30.641	7.597	19.137	26.258	5.985	26.253	5.974	18.976	26.344	6.208	26.338	6.199	14.877	26.011	5.958	26.011	5.921
5.0E+02	13.442	31.368	6.719	31.368	6.682	19.720	26.677	4.983	26.665	4.980	19.541	26.853	5.135	26.839	5.133	15.610	26.262	4.975	26.250	4.952
6.0E+02	13.442	33.132	4.955	33.132	4.933	19.846	27.104	4.430	27.089	4.430	19.630	27.334	4.565	27.319	4.564	15.698	26.779	4.371	26.765	4.350
7.0E+02	13.442	33.494	4.593	33.494	4.563	19.857	27.423	4.100	27.408	4.100	19.643	27.664	4.221	27.649	4.221	15.708	27.198	3.941	27.184	3.923
8.0E+02	13.785	34.941	2.804	34.941	2.771	19.864	27.634	3.882	27.619	3.882	19.655	27.878	3.996	27.864	3.995	15.717	27.446	3.684	27.432	3.670
9.0E+02	13.924	34.851	2.754	34.851	2.740	19.871	27.778	3.731	27.763	3.731	19.665	28.023	3.841	28.008	3.841	15.728	27.573	3.546	27.560	3.537
1.0E+03	13.924	34.851	2.754	34.851	2.740	19.882	27.865	3.633	27.850	3.633	19.680	28.115	3.735	28.100	0.000	15.739	27.662	3.445	27.649	3.439

Table 7.16 - Mass of blanket (EU DEMO 2015) material, in kilotonnes, within each waste class, for all methods used.

Time (years)	Cell					Structured mesh (9 cm)					Structured mesh (15 cm)					Unstructured mesh				
	NAW	LLW	ILW	LLW-RM	ILW-RM	NAW	LLW	ILW	LLW-RM	ILW-RM	NAW	LLW	ILW	LLW-RM	ILW-RM	NAW	LLW	ILW	LLW-RM	ILW-RM
1.1E-04	0.000	0.000	8.763	0.000	0.000	0.000	0.000	8.764	0.000	0.000	0.000	0.000	8.764	0.000	0.000	0.000	0.000	8.763	0.000	0.000
3.4E-04	0.000	0.000	8.763	0.000	0.000	0.000	0.000	8.764	0.000	0.000	0.000	0.000	8.764	0.000	0.000	0.000	0.000	8.763	0.000	0.000
5.7E-04	0.000	0.000	8.763	0.000	0.000	0.000	0.000	8.764	0.000	0.000	0.000	0.000	8.764	0.000	0.000	0.000	0.000	8.763	0.000	0.000
1.1E-03	0.000	0.000	8.763	0.000	0.000	0.000	0.000	8.764	0.000	0.000	0.000	0.000	8.764	0.000	0.000	0.000	0.000	8.763	0.000	0.000
2.7E-03	0.000	0.000	8.763	0.000	0.000	0.000	0.000	8.764	0.000	0.000	0.000	0.000	8.764	0.000	0.000	0.000	0.000	8.763	0.000	0.000
8.2E-03	0.000	0.000	8.763	0.000	0.000	0.000	0.000	8.764	0.000	0.000	0.000	0.000	8.764	0.000	0.000	0.000	0.000	8.763	0.000	0.000
1.9E-02	0.000	0.000	8.763	0.000	0.000	0.000	0.000	8.764	0.000	0.000	0.000	0.000	8.764	0.000	0.000	0.000	0.000	8.763	0.000	0.000
3.8E-02	0.000	0.000	8.763	0.000	0.000	0.000	0.000	8.764	0.000	0.000	0.000	0.000	8.764	0.000	0.000	0.000	0.000	8.763	0.000	0.000
7.7E-02	0.000	0.000	8.763	0.000	0.000	0.000	0.000	8.764	0.000	0.000	0.000	0.000	8.764	0.000	0.000	0.000	0.000	8.763	0.000	0.000
1.5E-01	0.000	0.000	8.763	0.000	0.000	0.000	0.000	8.764	0.000	0.000	0.000	0.000	8.764	0.000	0.000	0.000	0.000	8.763	0.000	0.000
5.0E-01	0.000	0.000	8.763	0.000	0.000	0.000	0.000	8.764	0.000	0.000	0.002	0.000	8.762	0.000	0.000	0.000	0.000	8.763	0.000	0.000
1.0E+00	0.000	0.000	8.763	0.000	0.000	0.000	0.000	8.764	0.000	0.000	0.000	0.000	8.764	0.000	0.000	0.000	0.000	8.763	0.000	0.000
5.0E+00	0.000	0.000	8.763	0.000	0.000	0.000	0.000	8.764	0.000	0.004	0.000	0.000	8.764	0.000	0.002	0.000	0.000	8.763	0.000	0.000
1.0E+01	0.000	0.000	8.763	0.000	0.000	0.000	0.000	8.764	0.000	0.057	0.000	0.000	8.764	0.000	0.054	0.000	0.000	8.763	0.000	0.041
4.0E+01	0.000	0.000	8.763	0.000	0.000	0.000	0.000	8.764	0.000	2.848	0.000	0.000	8.764	0.000	2.846	0.000	0.000	8.763	0.000	2.768
7.0E+01	0.000	0.000	8.763	0.000	8.760	0.000	0.000	8.764	0.000	7.459	0.000	0.000	8.764	0.000	7.419	0.000	0.000	8.763	0.000	7.396
1.0E+02	0.000	0.000	8.763	0.000	8.760	0.000	0.000	8.764	0.000	8.764	0.000	0.000	8.764	0.000	8.764	0.000	0.000	8.763	0.000	8.763
2.0E+02	0.000	0.000	8.763	0.000	8.760	0.000	1.154	7.610	1.154	7.610	0.000	1.143	7.621	1.143	7.621	0.000	1.191	7.572	1.191	7.572
3.0E+02	0.000	4.381	4.381	4.381	4.380	0.003	5.948	2.813	5.948	2.813	0.000	5.972	2.792	5.972	2.792	0.023	5.915	2.825	5.915	2.825
4.0E+02	0.000	5.320	3.443	5.320	3.440	0.000	6.717	2.047	6.717	2.047	0.000	6.714	2.050	6.714	2.050	0.000	6.630	2.133	6.630	2.133
5.0E+02	0.000	5.320	3.443	5.320	3.440	0.000	6.790	1.974	6.790	1.974	0.000	6.786	1.978	6.786	1.978	0.000	6.701	2.062	6.701	2.062
6.0E+02	0.000	6.867	1.896	6.867	1.900	0.000	6.835	1.929	6.835	1.929	0.000	6.833	1.931	6.833	1.931	0.000	6.798	1.965	6.798	1.965
7.0E+02	0.000	6.867	1.896	6.867	1.900	0.000	6.867	1.897	6.867	1.897	0.000	6.862	1.902	6.862	1.902	0.000	6.810	1.953	6.810	1.953
8.0E+02	0.000	7.762	1.001	7.762	1.000	0.000	6.894	1.870	6.894	1.870	0.000	6.891	1.873	6.891	1.873	0.000	6.861	1.902	6.861	1.902
9.0E+02	0.000	7.762	1.001	7.762	1.000	0.000	6.914	1.850	6.914	1.850	0.000	6.911	1.853	6.911	1.853	0.000	6.901	1.862	6.901	1.862
1.0E+03	0.000	7.762	1.001	7.762	1.000	0.000	6.934	1.830	6.934	1.830	0.000	6.932	1.832	6.932	1.832	0.000	6.933	1.830	6.933	1.830

Table 7.17 - Mass of vacuum vessel (EU DEMO 2015) material, in kilotonnes, within each waste class, for all methods used.

Time (years)	Cell					Structured mesh (9 cm)					Structured mesh (15 cm)					Unstructured mesh				
	NAW	LLW	ILW	LLW-RM	ILW-RM	NAW	LLW	ILW	LLW-RM	ILW-RM	NAW	LLW	ILW	LLW-RM	ILW-RM	NAW	LLW	ILW	LLW-RM	ILW-RM
1.1E-04	0.000	0.000	13.274	0.000	0.000	0.000	1.753	11.522	1.276	0.000	0.000	1.562	11.710	1.101	0.000	0.017	1.368	11.615	0.896	0.000
3.4E-04	0.000	0.000	13.274	0.000	0.000	0.000	2.022	11.252	1.594	0.000	0.000	1.825	11.447	1.421	0.000	0.017	1.615	11.368	1.185	0.000
5.7E-04	0.000	0.000	13.274	0.000	0.000	0.000	2.233	11.041	1.948	0.000	0.000	2.057	11.215	1.757	0.000	0.017	1.794	11.189	1.551	0.000
1.1E-03	0.000	0.000	13.274	0.000	0.000	0.001	2.522	10.751	2.521	0.185	0.000	2.365	10.907	2.365	0.196	0.017	2.089	10.894	2.081	0.201
2.7E-03	0.000	0.000	13.274	0.000	0.028	0.001	2.744	10.529	2.744	0.743	0.000	2.564	10.708	2.564	0.772	0.021	2.283	10.696	2.279	0.775
8.2E-03	0.000	0.000	13.274	0.000	0.028	0.001	2.851	10.422	2.851	0.699	0.000	2.689	10.583	2.689	0.705	0.024	2.387	10.590	2.381	0.734
1.9E-02	0.000	0.030	13.243	0.000	0.028	0.001	2.964	10.309	2.961	0.619	0.000	2.805	10.467	2.802	0.616	0.032	2.507	10.461	2.499	0.640
3.8E-02	0.000	0.059	13.215	0.028	0.000	0.001	3.092	10.182	3.082	0.529	0.000	2.940	10.332	2.931	0.528	0.036	2.651	10.314	2.631	0.536
7.7E-02	0.000	0.059	13.215	0.028	0.000	0.001	3.263	10.010	3.244	0.408	0.000	3.131	10.141	3.113	0.394	0.037	2.846	10.117	2.816	0.404
1.5E-01	0.000	0.059	13.215	0.059	0.000	0.001	3.534	9.738	3.490	0.234	0.000	3.389	9.883	3.351	0.233	0.042	3.096	9.862	3.047	0.221
5.0E-01	0.000	0.059	13.215	0.059	0.000	0.003	4.007	9.264	3.872	0.061	0.003	3.873	9.396	3.735	0.045	0.051	3.478	9.471	3.364	0.073
1.0E+00	0.000	0.155	13.119	0.059	0.000	0.004	4.211	9.059	4.048	0.049	0.000	4.077	9.195	3.906	0.028	0.068	3.632	9.301	3.489	0.044
5.0E+00	0.000	0.170	13.104	0.074	0.000	0.006	5.245	8.023	4.773	0.001	0.001	5.174	8.097	4.642	0.000	0.083	4.808	8.109	4.192	0.003
1.0E+01	0.000	0.641	12.633	0.170	0.000	0.009	6.407	6.859	5.614	0.000	0.001	6.326	6.945	5.538	0.000	0.100	5.975	6.926	5.186	0.000
4.0E+01	0.000	0.872	12.402	0.872	8.190	0.240	7.611	5.423	7.611	1.976	0.170	7.541	5.561	7.541	2.000	0.263	7.173	5.564	7.173	1.957
7.0E+01	0.000	0.872	12.402	0.872	12.200	1.924	6.174	5.176	6.174	4.565	1.797	6.181	5.293	6.181	4.698	1.378	6.265	5.356	6.265	4.679
1.0E+02	0.000	1.718	11.555	1.718	11.600	2.711	5.604	4.960	5.604	4.951	2.528	5.658	5.086	5.658	5.083	2.244	5.602	5.153	5.602	5.148
2.0E+02	0.000	7.125	6.148	7.125	6.150	3.414	5.523	4.337	5.523	4.337	3.250	5.594	4.428	5.594	4.428	3.011	5.599	4.389	5.599	4.389
3.0E+02	0.000	8.269	5.005	8.269	5.000	4.168	5.446	3.660	5.446	3.660	4.026	5.421	3.824	5.421	3.824	3.656	5.555	3.790	5.555	3.790
4.0E+02	0.059	9.326	3.889	9.326	3.890	4.830	5.549	2.895	5.549	2.895	4.765	5.560	2.947	5.560	2.947	4.404	5.543	3.053	5.543	3.053
5.0E+02	0.059	10.152	3.063	10.152	3.060	5.387	5.729	2.158	5.729	2.158	5.312	5.804	2.157	5.804	2.157	5.107	5.597	2.297	5.597	2.297
6.0E+02	0.059	10.369	2.846	10.369	2.850	5.505	6.023	1.746	6.023	1.746	5.394	6.133	1.745	6.133	1.745	5.186	5.969	1.845	5.969	1.845
7.0E+02	0.059	10.730	2.485	10.730	2.480	5.512	6.260	1.501	6.260	1.501	5.400	6.364	1.509	6.364	1.509	5.191	6.333	1.476	6.333	1.476
8.0E+02	0.059	11.622	1.593	11.622	1.590	5.515	6.414	1.345	6.414	1.345	5.404	6.514	1.355	6.514	1.355	5.199	6.502	1.300	6.502	1.300
9.0E+02	0.059	11.672	1.543	11.672	1.540	5.518	6.522	1.233	6.522	1.233	5.407	6.603	1.262	6.603	1.262	5.204	6.585	1.211	6.585	1.211
1.0E+03	0.059	11.672	1.543	11.672	1.540	5.523	6.582	1.168	6.582	1.168	5.411	6.650	1.210	6.650	1.210	5.210	6.636	1.153	6.636	1.153

Table 7.18 - Mass of divertor (EU DEMO 2015) material, in kilotonnes, within each waste class, for all methods used.

Time (years)	Cell					Structured mesh (9 cm)					Structured mesh (15 cm)					Unstructured mesh				
	NAW	LLW	ILW	LLW-RM	ILW-RM	NAW	LLW	ILW	LLW-RM	ILW-RM	NAW	LLW	ILW	LLW-RM	ILW-RM	NAW	LLW	ILW	LLW-RM	ILW-RM
1.1E-04	0.000	0.000	3.930	0.000	0.000	0.000	0.000	3.928	0.000	0.000	0.000	0.000	3.928	0.000	0.000	0.000	0.002	3.924	0.000	0.000
3.4E-04	0.000	0.000	3.930	0.000	0.000	0.000	0.000	3.928	0.000	0.000	0.000	0.000	3.928	0.000	0.000	0.000	0.002	3.924	0.000	0.000
5.7E-04	0.000	0.000	3.930	0.000	0.000	0.000	0.000	3.928	0.000	0.000	0.000	0.000	3.928	0.000	0.000	0.000	0.002	3.924	0.000	0.000
1.1E-03	0.000	0.000	3.930	0.000	0.000	0.000	0.000	3.928	0.000	0.000	0.000	0.000	3.928	0.000	0.000	0.000	0.002	3.924	0.000	0.000
2.7E-03	0.000	0.000	3.930	0.000	0.000	0.000	0.000	3.928	0.000	0.000	0.000	0.000	3.928	0.000	0.000	0.000	0.002	3.924	0.000	0.000
8.2E-03	0.000	0.000	3.930	0.000	0.000	0.000	0.000	3.928	0.000	0.000	0.000	0.000	3.928	0.000	0.000	0.000	0.002	3.924	0.000	0.000
1.9E-02	0.000	0.000	3.930	0.000	0.000	0.000	0.000	3.928	0.000	0.000	0.000	0.000	3.928	0.000	0.000	0.000	0.002	3.924	0.000	0.000
3.8E-02	0.000	0.000	3.930	0.000	0.000	0.000	0.000	3.928	0.000	0.000	0.000	0.000	3.928	0.000	0.000	0.000	0.002	3.924	0.000	0.000
7.7E-02	0.000	0.000	3.930	0.000	0.000	0.000	0.000	3.928	0.000	0.000	0.000	0.000	3.928	0.000	0.000	0.000	0.002	3.924	0.000	0.000
1.5E-01	0.000	0.000	3.930	0.000	0.000	0.000	0.000	3.928	0.000	0.000	0.000	0.000	3.928	0.000	0.000	0.000	0.002	3.924	0.000	0.000
5.0E-01	0.000	0.000	3.930	0.000	0.000	0.000	0.000	3.928	0.000	0.000	0.102	0.000	3.826	0.000	0.000	0.000	0.002	3.924	0.000	0.000
1.0E+00	0.000	0.000	3.930	0.000	0.000	0.000	0.000	3.928	0.000	0.000	0.000	0.000	3.928	0.000	0.000	0.000	0.002	3.924	0.000	0.000
5.0E+00	0.000	0.000	3.930	0.000	0.000	0.000	0.000	3.928	0.000	0.000	0.000	0.000	3.928	0.000	0.000	0.000	0.005	3.920	0.000	0.000
1.0E+01	0.000	0.000	3.930	0.000	0.000	0.000	0.000	3.928	0.000	0.000	0.000	0.000	3.927	0.000	0.000	0.000	0.009	3.916	0.002	0.000
4.0E+01	0.000	0.402	3.528	0.154	0.009	0.000	0.702	3.226	0.232	0.017	0.000	1.187	2.741	0.550	0.041	0.000	0.766	3.160	0.258	0.015
7.0E+01	0.000	2.222	1.708	2.222	1.400	0.000	2.630	1.299	2.571	0.814	0.000	2.674	1.254	2.674	1.252	0.000	2.725	1.200	2.657	0.786
1.0E+02	0.000	3.720	0.211	3.720	0.177	0.000	2.926	1.002	2.926	1.002	0.000	2.805	1.122	2.805	1.122	0.000	3.164	0.761	3.164	0.719
2.0E+02	0.000	3.745	0.185	3.745	0.154	0.000	3.082	0.847	3.082	0.847	0.000	2.964	0.964	2.964	0.964	0.000	3.325	0.601	3.325	0.576
3.0E+02	0.000	3.807	0.123	3.807	0.093	0.018	3.148	0.762	3.148	0.762	0.000	3.047	0.881	3.047	0.881	0.001	3.395	0.530	3.395	0.505
4.0E+02	0.000	3.821	0.109	3.821	0.078	0.000	3.231	0.697	3.231	0.697	0.000	3.106	0.822	3.106	0.822	0.000	3.448	0.477	3.448	0.455
5.0E+02	0.000	3.826	0.104	3.826	0.073	0.000	3.274	0.654	3.274	0.654	0.000	3.148	0.779	3.148	0.779	0.000	3.462	0.464	3.462	0.443
6.0E+02	0.000	3.826	0.104	3.826	0.074	0.000	3.301	0.627	3.301	0.627	0.000	3.186	0.742	3.186	0.742	0.000	3.467	0.458	3.467	0.438
7.0E+02	0.000	3.827	0.103	3.827	0.074	0.000	3.318	0.611	3.318	0.611	0.000	3.223	0.705	3.223	0.705	0.000	3.490	0.435	3.490	0.417
8.0E+02	0.000	3.827	0.103	3.827	0.074	0.000	3.329	0.599	3.329	0.599	0.000	3.238	0.690	3.238	0.690	0.000	3.503	0.423	3.503	0.409
9.0E+02	0.000	3.827	0.103	3.827	0.093	0.000	3.337	0.591	3.337	0.591	0.000	3.270	0.658	3.270	0.658	0.000	3.506	0.419	3.506	0.410
1.0E+03	0.000	3.827	0.103	3.827	0.093	0.000	3.345	0.583	3.345	0.583	0.000	3.296	0.632	3.296	0.632	0.000	3.512	0.413	3.512	0.407

Table 7.19- Mass of toroidal field coils (EU DEMO 2015) material, in kilotonnes, within each waste class, for all methods used.

Time (years)	Cell					Structured mesh (9 cm)					Structured mesh (15 cm)					Unstructured mesh				
	NAW	LLW	ILW	LLW-RM	ILW-RM	NAW	LLW	ILW	LLW-RM	ILW-RM	NAW	LLW	ILW	LLW-RM	ILW-RM	NAW	LLW	ILW	LLW-RM	ILW-RM
1.1E-04	0.000	0.000	2.374	0.000	0.000	0.000	0.330	2.123	0.330	0.199	0.000	0.240	2.134	0.240	0.200	0.003	0.330	1.981	0.327	0.161
3.4E-04	0.000	0.000	2.374	0.000	0.000	0.000	0.361	2.086	0.361	0.259	0.000	0.275	2.099	0.275	0.265	0.003	0.361	1.950	0.359	0.203
5.7E-04	0.000	0.000	2.374	0.000	0.000	0.000	0.391	2.051	0.391	0.316	0.000	0.310	2.064	0.310	0.321	0.003	0.391	1.920	0.391	0.250
1.1E-03	0.000	0.000	2.374	0.000	0.498	0.000	0.447	1.976	0.447	0.430	0.000	0.385	1.990	0.385	0.427	0.004	0.447	1.863	0.446	0.348
2.7E-03	0.000	0.498	1.876	0.498	0.367	0.000	0.616	1.769	0.616	0.551	0.000	0.597	1.777	0.597	0.556	0.005	0.616	1.692	0.616	0.464
8.2E-03	0.000	0.866	1.508	0.866	0.000	0.000	1.151	1.131	1.151	0.330	0.000	1.254	1.121	1.254	0.301	0.010	1.151	1.153	1.147	0.333
1.9E-02	0.000	0.866	1.508	0.866	0.000	0.000	1.345	0.914	1.345	0.179	0.000	1.453	0.921	1.453	0.169	0.014	1.345	0.955	1.336	0.206
3.8E-02	0.000	1.226	1.147	0.866	0.000	0.000	1.409	0.849	1.407	0.125	0.000	1.520	0.854	1.517	0.113	0.017	1.409	0.888	1.396	0.156
7.7E-02	0.000	1.501	0.873	0.866	0.000	0.000	1.486	0.779	1.479	0.070	0.000	1.591	0.783	1.581	0.059	0.020	1.486	0.808	1.465	0.094
1.5E-01	0.000	1.592	0.781	1.226	0.000	0.000	1.571	0.685	1.540	0.017	0.000	1.674	0.701	1.642	0.011	0.026	1.571	0.716	1.527	0.037
5.0E-01	0.000	1.592	0.781	1.226	0.000	0.000	1.704	0.570	1.611	0.001	0.013	1.796	0.565	1.672	0.000	0.033	1.704	0.577	1.588	0.008
1.0E+00	0.000	1.592	0.781	1.501	0.000	0.000	1.759	0.514	1.643	0.000	0.000	1.863	0.512	1.726	0.000	0.035	1.759	0.521	1.628	0.004
5.0E+00	0.000	1.592	0.781	1.592	0.000	0.000	1.956	0.325	1.841	0.000	0.000	2.052	0.322	1.919	0.000	0.040	1.956	0.318	1.828	0.000
1.0E+01	0.000	1.592	0.781	1.592	0.000	0.000	2.050	0.223	1.971	0.000	0.000	2.148	0.226	2.064	0.000	0.046	2.050	0.219	1.961	0.000
4.0E+01	0.000	2.374	0.000	2.374	0.000	0.019	2.126	0.097	2.126	0.061	0.020	2.257	0.097	2.257	0.060	0.089	2.126	0.099	2.126	0.062
7.0E+01	0.000	2.374	0.000	2.374	0.000	0.027	2.126	0.079	2.126	0.072	0.025	2.268	0.082	2.268	0.074	0.108	2.126	0.080	2.126	0.075
1.0E+02	0.498	1.876	0.000	1.876	0.000	0.027	2.137	0.068	2.137	0.061	0.025	2.287	0.063	2.287	0.055	0.109	2.137	0.069	2.137	0.065
2.0E+02	0.498	1.876	0.000	1.876	0.000	0.027	2.169	0.035	2.169	0.029	0.025	2.318	0.032	2.318	0.024	0.109	2.169	0.036	2.169	0.032
3.0E+02	0.498	1.876	0.000	1.876	0.000	0.041	2.185	0.015	2.184	0.009	0.026	2.332	0.017	2.332	0.010	0.113	2.185	0.016	2.185	0.012
4.0E+02	0.866	1.508	0.000	1.508	0.000	0.027	2.200	0.005	2.198	0.001	0.026	2.344	0.005	2.341	0.001	0.109	2.200	0.005	2.200	0.001
5.0E+02	0.866	1.508	0.000	1.508	0.000	0.028	2.204	0.001	2.199	0.000	0.026	2.348	0.001	2.341	0.000	0.109	2.204	0.001	2.201	0.000
6.0E+02	0.866	1.508	0.000	1.508	0.000	0.028	2.204	0.001	2.199	0.000	0.026	2.348	0.001	2.341	0.000	0.110	2.204	0.000	2.200	0.000
7.0E+02	0.866	1.508	0.000	1.508	0.000	0.028	2.204	0.000	2.199	0.000	0.026	2.348	0.000	2.341	0.000	0.110	2.204	0.000	2.200	0.000
8.0E+02	0.866	1.508	0.000	1.508	0.000	0.028	2.204	0.000	2.199	0.000	0.026	2.348	0.000	2.341	0.000	0.110	2.204	0.000	2.201	0.000
9.0E+02	0.866	1.508	0.000	1.508	0.000	0.028	2.204	0.000	2.199	0.000	0.026	2.348	0.000	2.341	0.000	0.110	2.204	0.000	2.201	0.000
1.0E+03	0.866	1.508	0.000	1.508	0.000	0.028	2.204	0.000	2.199	0.000	0.026	2.348	0.000	2.341	0.000	0.110	2.204	0.000	2.201	0.000

APPENDIX 6: VALIDATION OF PHOTON DATA LIBRARY

Introduction

During the course of the PhD documented in this thesis a newer version of MCNP became available. Earlier work, including that presented in Section 4.1, made use of MCNP version 5. The production version of MCNP6 was released in 2013 and is used in all other particle transport work presented in this thesis. The beta release MCNP6v1.1 was used for testing of the unstructured mesh capability, however as it did not fix problems regarding the use of weight windows for variance reduction, it was not used in any of the results presented.

MCNP uses nuclear cross-section data provided in data libraries. The neutron data libraries are specified on the material ZAID input using an extension which in turn matches an entry on the cross-section directory file 'xsdir'. This xsdir file contains the path to the cross-section data library. If no extension is present on the material ZAID then the first matching entry in the xsdir is used. The photon data library can also be specified using the PLIB keyword. If this is not explicitly defined then the default library is used. In MCNP5 and the extended MCNP version, MCNPx, the default photon library is PLIB 04. In MCNP6 the default is PLIB 84. These libraries, PLIB 04 and PLIB 84 contain exactly the same nuclear data but provided in different formats. The reason for this is discussed later in this appendix.

The neutron cross-section data used in all work presented in this thesis, is from the FENDL 2.1 data library, or where not available, the ENDF VII data library. The FENDL data library is preferred as this 'evaluated nuclear data' has been complied for use in fusion. The default photon data libraries have been used in this thesis research; in the case of MCNP5 this is now known to be incorrect.

A number of photon cross-section data libraries are available for use with MCNP for photon transport/heating calculations; 04, 05t, 84 and 12. MCNP also has a number of physics options available, including the ability to perform Doppler broadening to incorporate the effect of bound electrons on photon scattering. The PLIB 04 has been considered the standard and default library for photon calculations in MCNP. Since the release of MCNP5 it was found that there was a bug with Doppler broadening [95].

The format for the data provided in PLIB 04 for sampling which atomic shell the electron is bound, provided as a probability density function (PDF), does not match the format in which MCNP5 samples. MCNP5 samples assuming a cumulative density function (CDF). The official report on this MCNP bug is given in [107]. To enable users of MCNP5 to have corrected data sampling, a temporary library, PLIB 84, was created with the correctly formatted data. However this requires the end-user to specify it explicitly using the PLIB keyword in the MCNP input file. The sampling bug is not evident with MCNP6 which can determine what format the library data is, and sample accordingly.

A summary of investigations into the effect of using different photon libraries and the MCNP5 bug with Doppler broadening, along with a comparison of using MCNP5 and MCNP6 is documented in this appendix. This work was part funded by the RCUK Energy Programme [grant number EP/1501045] and the European Union's Horizon 2020 research and innovation programme. It was presented at the 2014 JEFF Meeting (the Joint Evaluated Fission and Fusion File project) at the Nuclear Energy Agency (NEA), Issy-les-Moulineaux, France.

Available photon nuclear data libraries and compatibility

As already mentioned, the standard photon data library for use with MCNP is PLIB 04/84, with PLIB 84 having a different format for use with MCNP5. MCNP6 determines the format of the library and samples accordingly, so using PLIB 04 or PLIB 84 would present the same result. A test library, PLIB 05t, was developed in order to include form factor data from ENDF/B-VII(rev. 0) as the incoherent and coherent form factors in MCNP5 and MCNPx were described as obsolete, affecting photon transport with energies greater than 74 KeV [179]. The PLIB 05t data is identical to that in the standard PLIB 04 apart from the inclusion of the updated form factor data. A version of MCNPx [180] was developed to identify and use the PLIB 05t data as it is not compatible with MCNP5. PLIB 12, is in a newly developed format that includes photon transport data from PLIB 04 and complete relaxation and electron interaction data [181]. The three main developments in this data library are: (1) the extension of photon transport to lower energies; 1 eV, (2) enhancement of the treatment of atomic relaxation processes, and (3) changes in electron transport methods to allow transport at lower energies.

It is important to consider the compatibility of the libraries with different versions of MCNP, namely MCNP5, MCNP6 and MCNPx. The versions of MCNP used are given in Table 7.20. A summary of the compatibility is given in Table 7.21. The reference case (MCNP6 + PLIB 04) is highlighted in light green; the use of PLIB 84 with MCNP6 should be identical to the reference case.

Table 7.20 - MCNP versions and default photon cross-section data libraries.

MCNP Version	Default Library and Sampling of Bound Electrons for Doppler Broadening
MCNP5 v1.6	The default library is PLIB 04, however MCNP5 assumes that the data provided as part of the Doppler broadening function is a CDF.
MCNP6 v1.1	The default library is PLIB 84, the data of which is identical to PLIB 04. MCNP6 can correctly sample from either PLIB 04 or PLIB 84, as the code will convert, where necessary, PDF to CDF.
MCNPx v2.7.0	This particular version of MCNPx has been developed to identify and use PLIB 05t, though the version also incorrectly samples the Doppler broadening data as CDF.

Table 7.21 - Summary of photon library and MCNP compatibility.

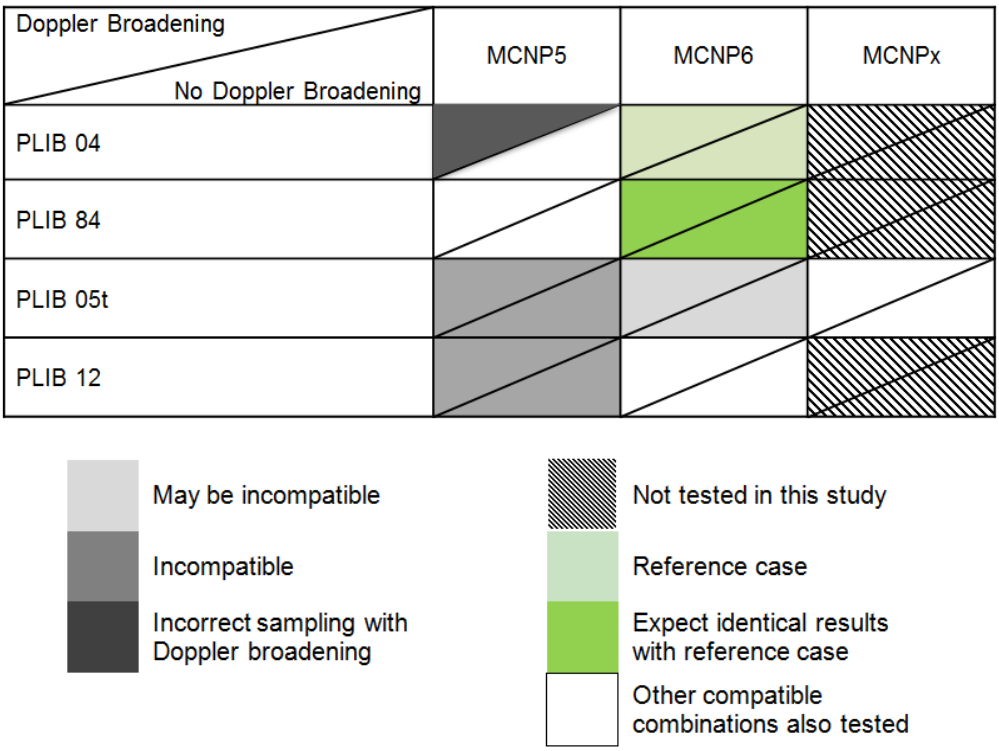

Photon physics in MCNP

The MCNP6 default photon physics options have been applied throughout the testing calculations (Table 7.22). Calculations were also performed with and without the Doppler broadening feature; this was changed through the use of '0' or '1' on the NODOP entry of the PHYS:P photon physics card in the MCNP input file. It should be noted that no photonuclear interactions were included.

Table 7.22 - Physics transport options in MCNP and default values.

Input Parameter	Description	Default
EMCPF	Upper energy limit for detailed photon physics treatment, photons with energy above this will be tracked using the simple physics treatment.	100 MeV
IDES	Controls generation of bremsstrahlung photons, when using MODE P only, with the thick-target bremsstrahlung model	Generation of bremsstrahlung photons turned on
NOCOH	Coherent scattering on/off	On
ISPN	Photonuclear particle production	No photonuclear particle production
NODOP	Doppler energy broadening on/off	On (note default is off in MCNPx)
J	Unused	
FISM	Photofission method	Sample from ACE libraries (no photofission prompt gammas)

Neutronics models

Simple physics test model

A simple spherical test case (see Figure 7.26) was used to compare the effect on the photon flux from the use of different photon libraries. Using a script, the 200 cm radius sphere was filled with each of the 100 elements featured in the photon data libraries and a separate photon transport calculation performed for each. The mass density of the material within the sphere has been kept constant at 1 g/cm^3. An 8 MeV photon point source was placed at the centre and the resulting photon flux tallied at 20 spherical surfaces through the material and in 175 energy bins. Each transport calculation was performed without variance reduction with 1 x 10^8 photon histories.

Table 7.23 summarises the combinations of MCNP and photon library used with the simple model.

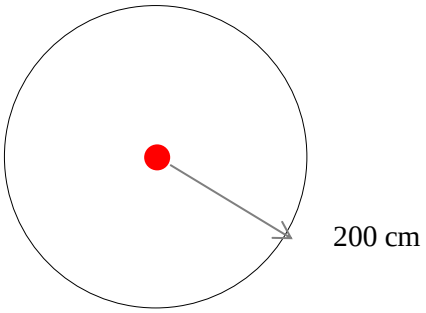

Figure 7.26 - Simple spherical test model geometry; a 200 cm sphere with a point source in the centre.

Table 7.23 - MCNP and photon library combinations used with simple test model.

Doppler Broadening / No Doppler Broadening	MCNP5	MCNP6	MCNPx
PLIB 04	✓ ✓	✓ ✓	
PLIB 84	✓ ✓	✓ ✓	
PLIB 05t	✓ ✓	✓ ✓	✓
PLIB 12		✓	

DEMO Baseline model

Further photon library comparisons, and a comparison of the use of MCNP5 and MCNP6, were made using a fusion relevant model; the benchmark EU HCLL DEMO 2012 model [182]. The materials used can be seen in Table 7.24. A D-T parametric plasma source was used (as previously referenced).

A summary of the combinations of MCNP and photon library used in simulations with the DEMO model can be seen in Table 7.26. The photon and neutron flux and heating have been tallied on a superimposed mesh (see Table 7.25 for the extents of the mesh). Global variance reduction was utilised to establish a weight window map and the simulations performed to 2 x 10^9 histories.

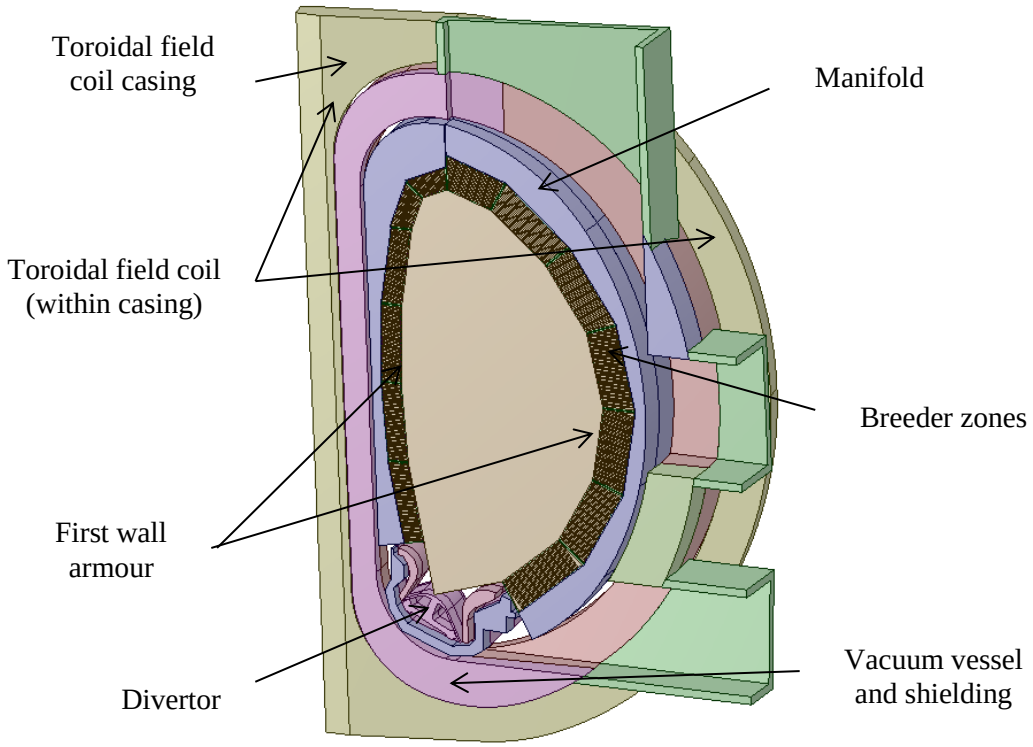

Figure 7.27 - The EU HCLL DEMO 2012 model [182], an 11.25º sector.

Table 7.24 - Summary of main materials used in the EU HCLL DEMO 2012 model [182].

Component	Material
First wall armour	Tungsten
First wall, side wall, back wall	EUROFER + 1w% tungsten
Breeding zone	
Cooling & Stiffening plates	EUROFER & helium
Breeder material	Pb-15.8Li, 90% ^{6}Li enrichment
Manifold	LiPb 5%, EUROFER 28% , helium 67%
Vacuum vessel/shielding	Tungsten carbide 30%, SS316-LN 37.46%, water 31.46%, boron 1.08%
Toroidal field casing	SS316-LN
Toroidal field coil	R-epoxy 18%, Nb_3Sn 2.895%, bronze 7,35%, copper 11.69%, helium 16.82%, SS-316 43.19%, void 0.055%
Divertor	EUROFER + 1w% tungsten

Table 7.25 - The X, Y & Z extents for mesh tallies used in EU HCLL DEMO 2012 model.

X min (cm)	X max (cm)	Y min (cm)	Y max (cm)	Z min (cm)	Z max (cm)	Resolution (cm)
200	1500	-4	286	-940	950	~10x10x10

Table 7.26 - MCNP and photon library combinations used with EU HCLL DEMO 2012 model.

Doppler Broadening / No Doppler Broadening	MCNP5	MCNP6	MCNPx
PLIB 04	✓	✓	
PLIB 84	✓	✓	
PLIB 05t		✓	
PLIB 12		✓	

Results

Doppler broadening

The use of Doppler broadening with MCNP5 and the standard PLIB 04 is compared with reference case results. The percentage difference in the total flux results for all 100 elements tested, at 160 cm from the source is given in Figure 7.28 along with results from the use of MCNP5 with the format corrected library PLIB 84. The majority of results are still within 1 standard deviation of the reference case (with Doppler broadening) as shown by the red line.

The differences observed with the use of Doppler broadening in Fe, with the standard library (PLIB 04) and the corrected format PLIB 84, can be seen in Figure 7.29. This shows the percentage difference in the total surface flux results at each surface through the sphere at radial distances from the centre source.

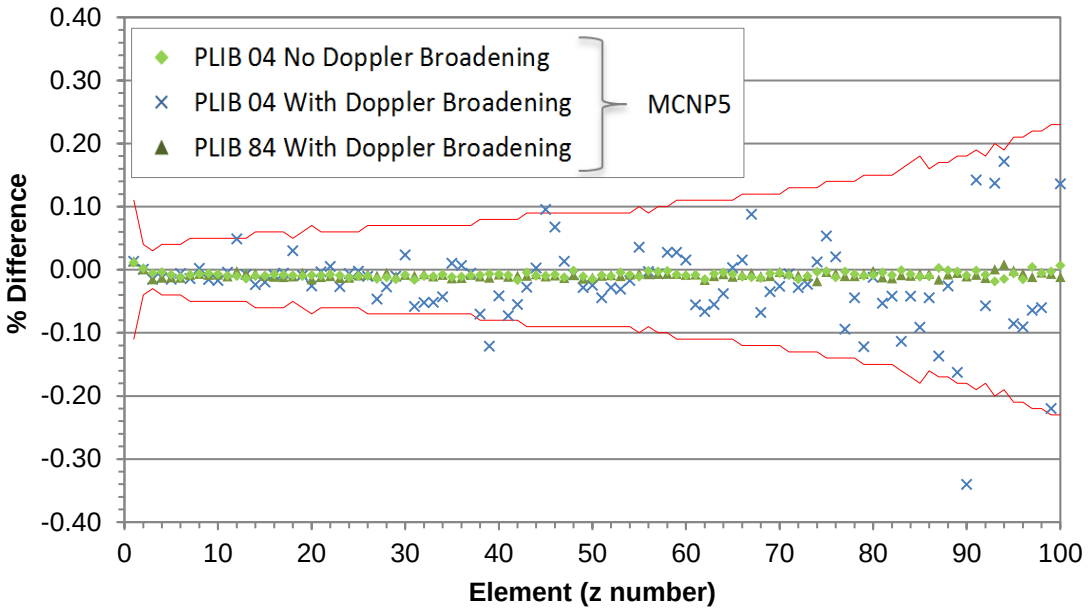

Figure 7.28 - Percentage difference of total surface flux for each element at 160 cm compared to the reference case. Using MCNP5 + PLIB 04 with and without the use of Doppler broadening and MCNP5 + PLIB 84 with Doppler broadening. The red lines show 1 standard deviation of the reference case with Doppler broadening.

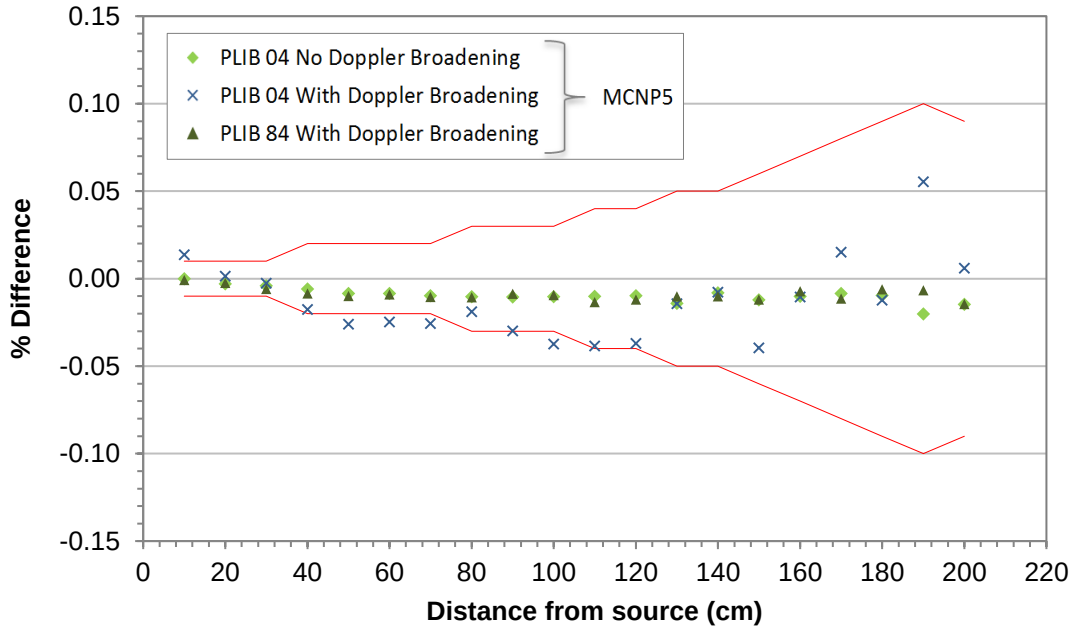

Figure 7.29 - Percentage difference of total surface flux for Fe at 160 cm compared to the reference case; using MCNP5 + PLIB 04/PLIB 84, with and without the use of Doppler broadening. The red lines show 1 standard deviation of the reference case with Doppler broadening.

Comparison of libraries

The libraries have been compared using default MCNP6 physics which includes the use of Doppler broadening. The percentage difference observed in the total surface flux (at 160 cm from the centre source) for each element tested and each MCNP and photon library combination is given in Figure 7.30.

The use of MCNP5 with PLIB 05t was not expected to be compatible. The plot is therefore given again in Figure 7.31 without the MCNP5 and PLIB 05t data. The difference in the total surface flux through Fe for the different MCNP and PLIB combinations is given in Figure 7.32.

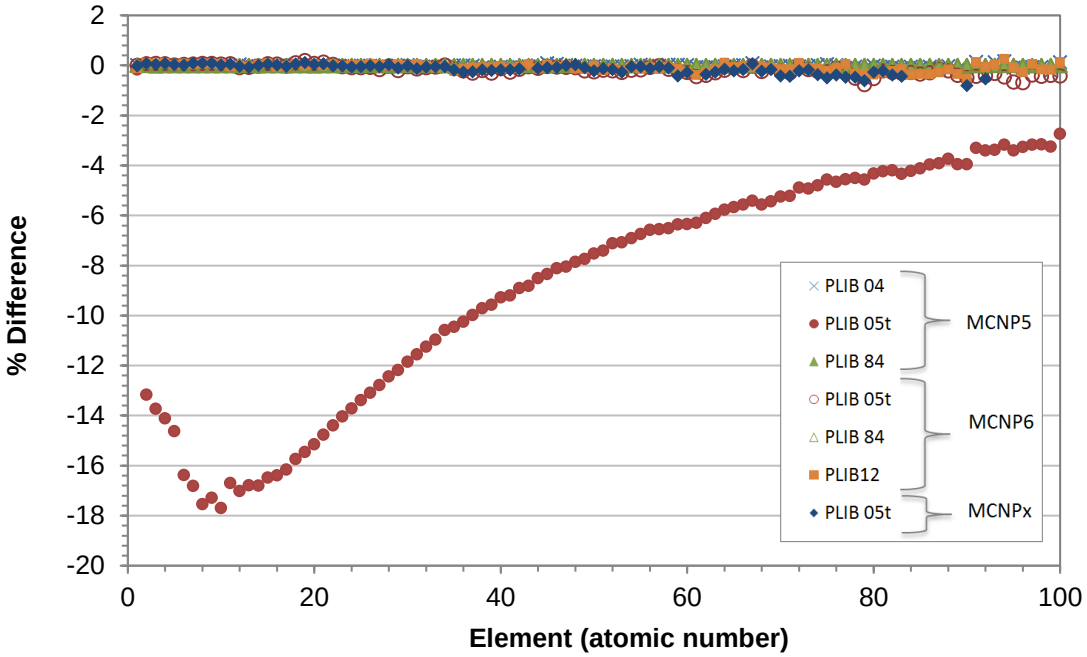

Figure 7.30 - Percentage difference in the total surface flux, when comparing the use of different PLIBs to the reference case (MCNP6 + PLIB 04).

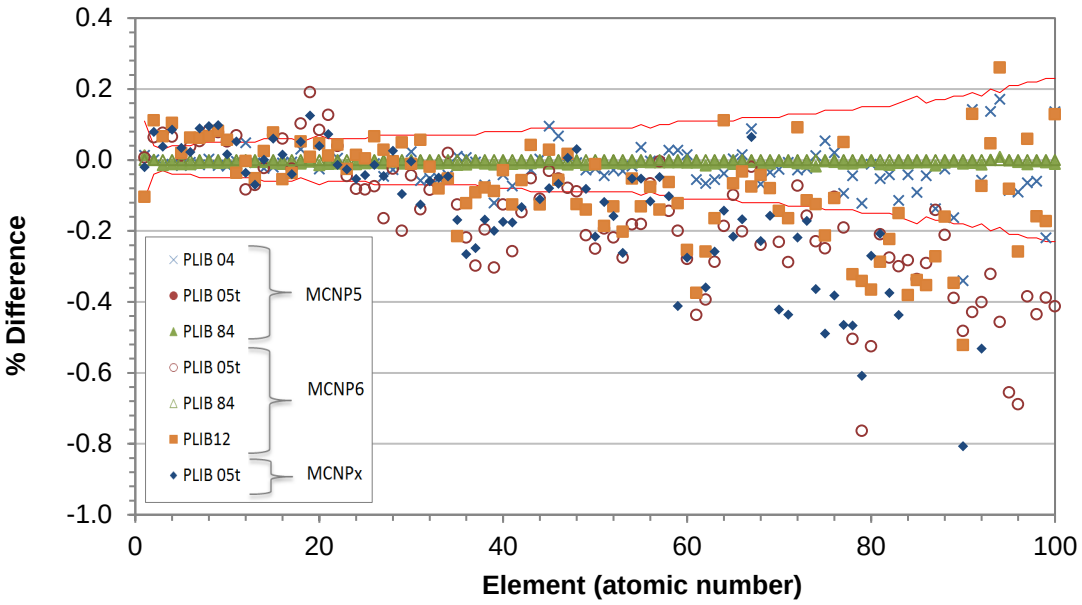

Figure 7.31 - Percentage difference in the total surface flux at 160cm from the source; comparing the use of different PLIBs to the reference case (MCNP6 + PLIB 04). This is the same as Figure 7.30 with data for MCNP5 + PLIB05t removed. The red lines show 1 standard deviation of the reference case with Doppler broadening.

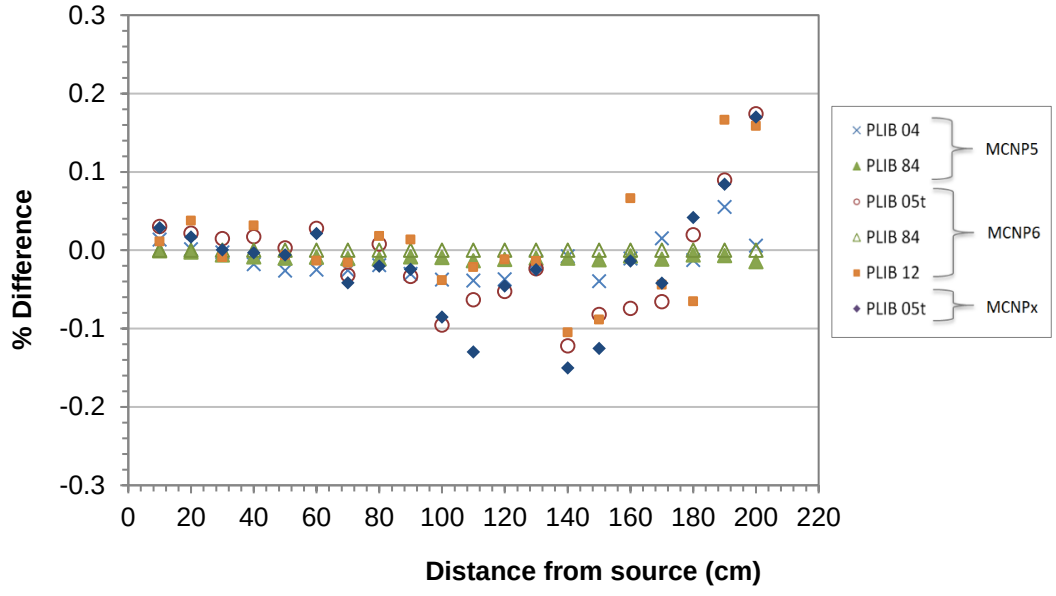

Figure 7.32 - Percentage difference in the total surface flux through Fe; comparing the use of different PLIBs to the reference case (MCNP6 + PLIB 04).

A comparison of the total surface flux at 160 cm from the centre source for different photon libraries is given in Figure 7.33, showing the percentage of results that fall within 1 standard deviation of the reference case. The combined error was calculated by adding the errors in quadrature. A summary of the data is given in Table 7.27 which includes the percentage of compared results that fall within 1-2, 2-3 and greater than 3 standard deviations. Only non-zero results, and those that have an associated statistical uncertainty less than 5%, have been compared.

Table 7.27 - A summary of the percentage of compared flux per energy bin results for all elements (at 160 cm from the source) that are within 1, 1 to 2, 2 to 3 and above 3 standard deviations of the reference case. Only non-zero values with a relative statistical uncertainty <5% are compared.

MCNP and PLIB	MCNP 5			MCNP 6			MCNPx
% of results within:	4	05t	84	05t	84	12	05t
1 standard deviation of the reference case	91.90	18.15	100.00	71.62	100.00	67.36	70.79
1-2 standard deviations of the reference case	7.63	11.02	0.00	24.50	0.00	27.01	24.82
2-3 standard deviations of the reference case	0.47	8.45	0.00	3.63	0.00	4.54	4.11
> 3 standard deviations of the reference case	0.00	62.39	0.00	0.25	0.00	1.08	0.29

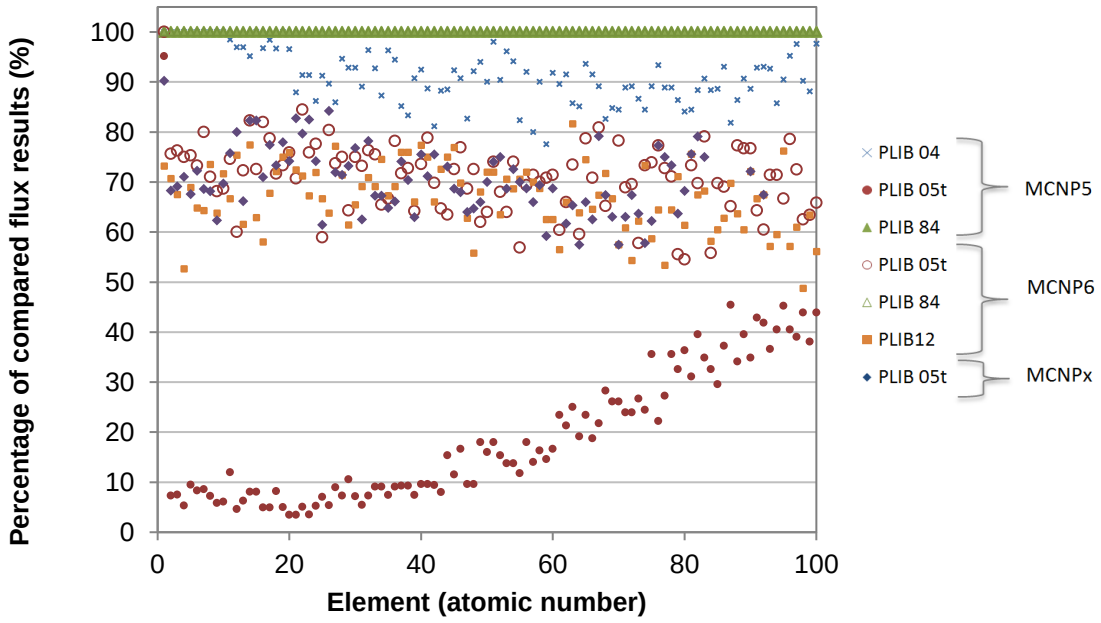

Figure 7.33 - Percentage of compared surface flux per energy bin results at 160 cm that fall with 1 standard deviation of the reference case. Only non-zero values with a relative statistical uncertainty <5% are compared.

Photon heating in DEMO

The reference case (MCNP6 + PLIB 04) photon heating is shown in Figure 7.34, normalised to a 2385 MW power plant (i.e. 8.468 x 10^{20} neutrons / second). A comparison of the resulting inboard and outboard (see Figure 7.35) photon heating using different data libraries is shown in Figure 7.36 and Figure 7.37, respectively.

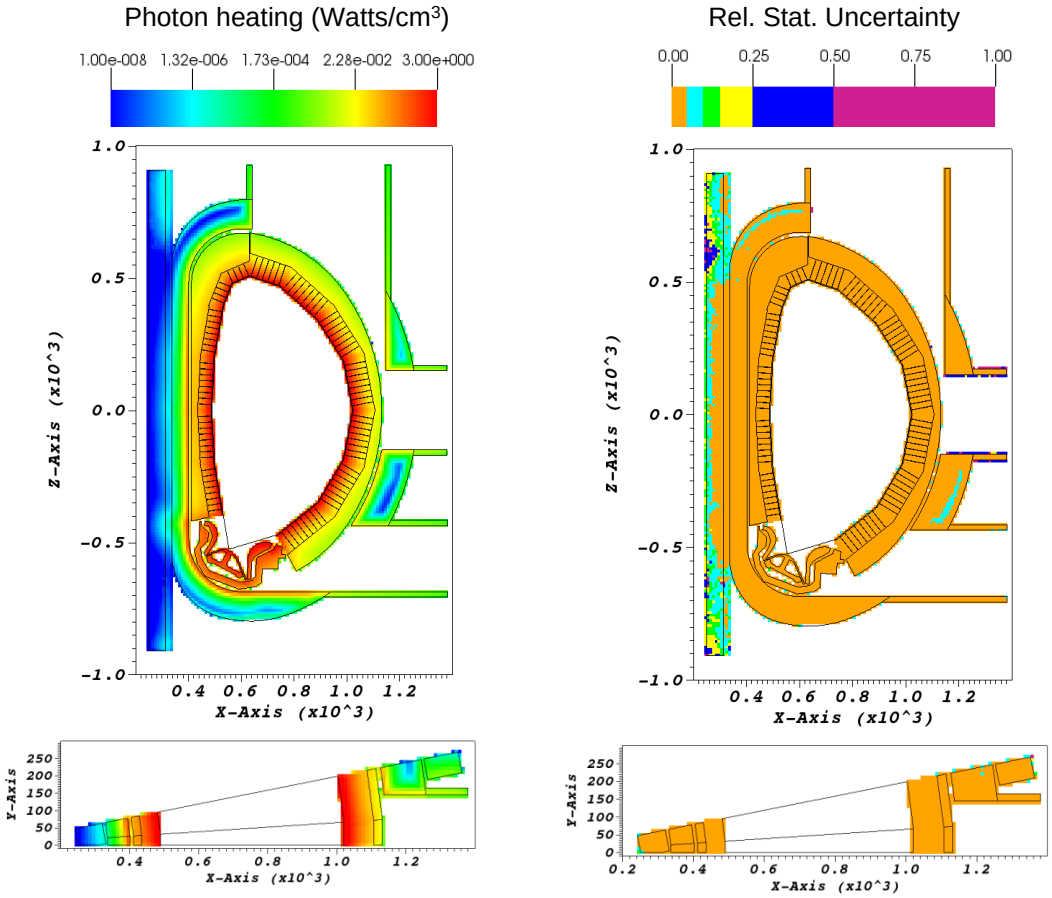

Figure 7.34 - A vertical elevation plot of the photon heating map (left) and relative statistical uncertainty (right) using the reference case (MCNP6 PLIB 04). (Scale in cm)

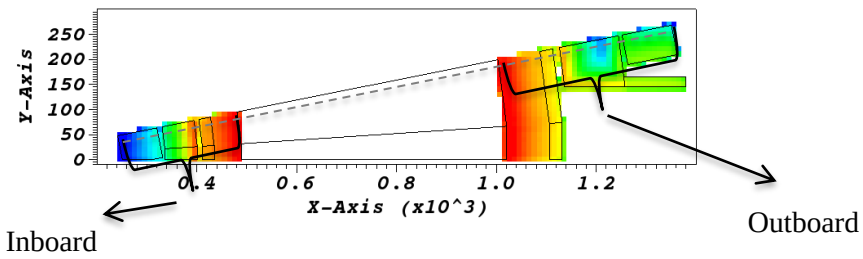

Figure 7.35 - A horizontal plot, at z = 0 cm, of the photon heating map using reference case (MCNP6 PLIB 04). The dotted line shows the location of the data for Figure 7.36 and Figure 7.37. (Scale in cm)

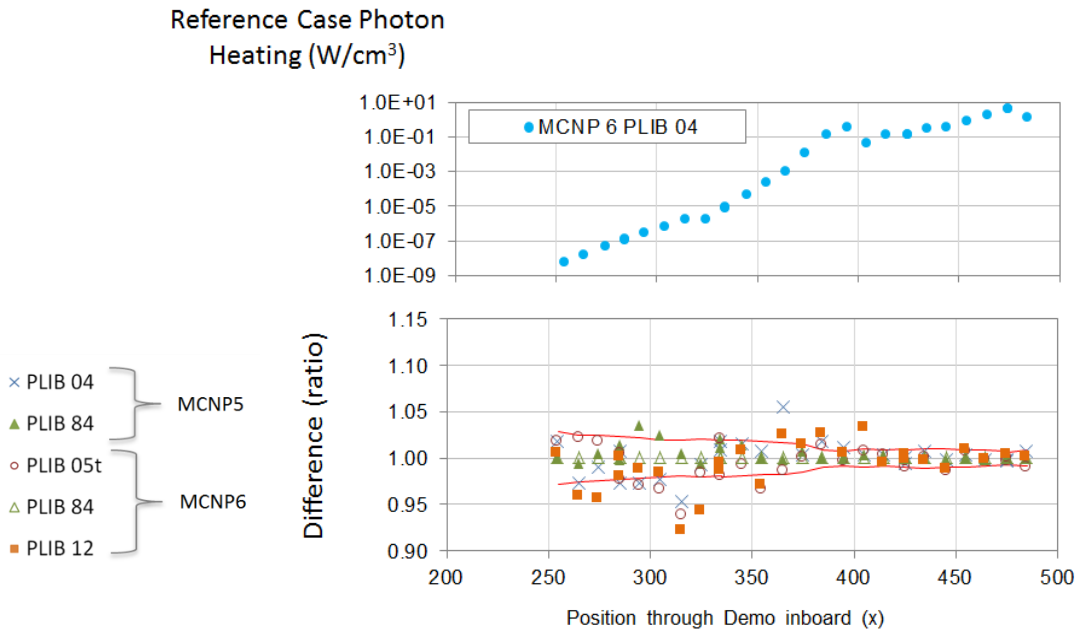

Figure 7.36 - Inboard reference case photon heating (location shown in Figure 7.35), and the difference, as a ratio, when using other PLIBs. The red lines show 1 standard deviation of the reference case with Doppler broadening.

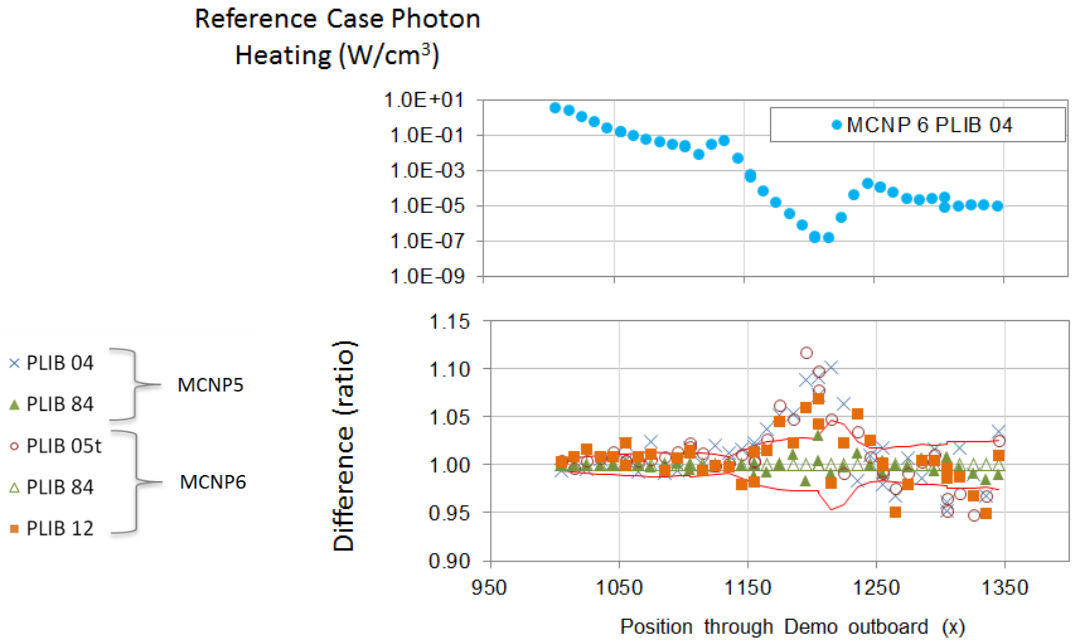

Figure 7.37 - Outboard reference case photon heating (location shown in Figure 7.35), and the difference, as a ratio, when using other PLIBs. The red lines show 1 standard deviation of the reference case with Doppler broadening.

Comparing each voxel of the superimposed mesh

The heating value in each voxel of the superimposed mesh has been compared to that of the reference case (MCNP6 + PLIB 04). Figure 7.39 shows vertical elevation plots through the centre of the EU HCLL DEMO 2012 benchmark model with each voxel of a mesh coloured depending on the comparison with the reference case; whether the value falls within 1, 1-3 or 2-3 standard deviations of the mean. Only non-zero values have been compared and those with an associated statistical uncertainty less than 25%. Figure 7.38 shows the difference in the use of the standard PLIB 04 and the corrected format PLIB 84 with MCNP5. Some differences are observed with PLIB 04, most of which are eliminated with the use of the corrected format PLIB 84, see Figure 7.38 (right). As expected the use of MCNP6 with PLIB 84 (Figure 7.40) gives identical results to the reference case (MCNP6 + PLIB 04).

A summary of the results comparing the heating results in each voxel against the reference case is given in Table 7.28.

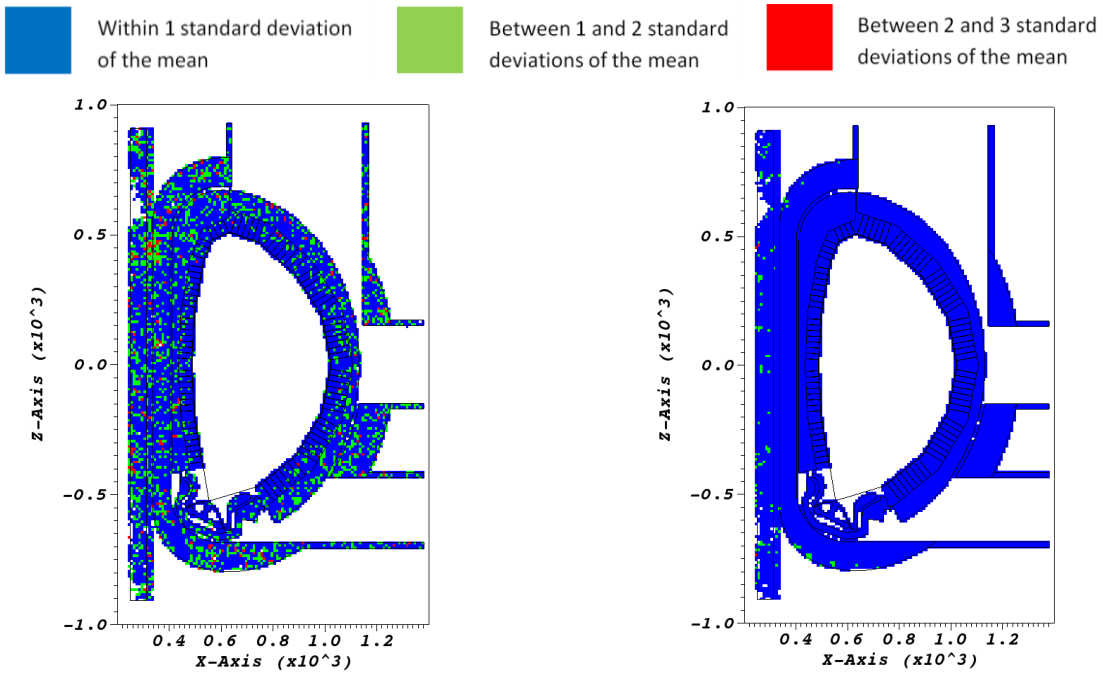

Figure 7.38 - Voxel values within 1, 1 to 2, and 2 to 3 standard deviations of the reference case; using MCNP5 + PLIB 04 (left) and MCNP5 + PLIB 84 (right).

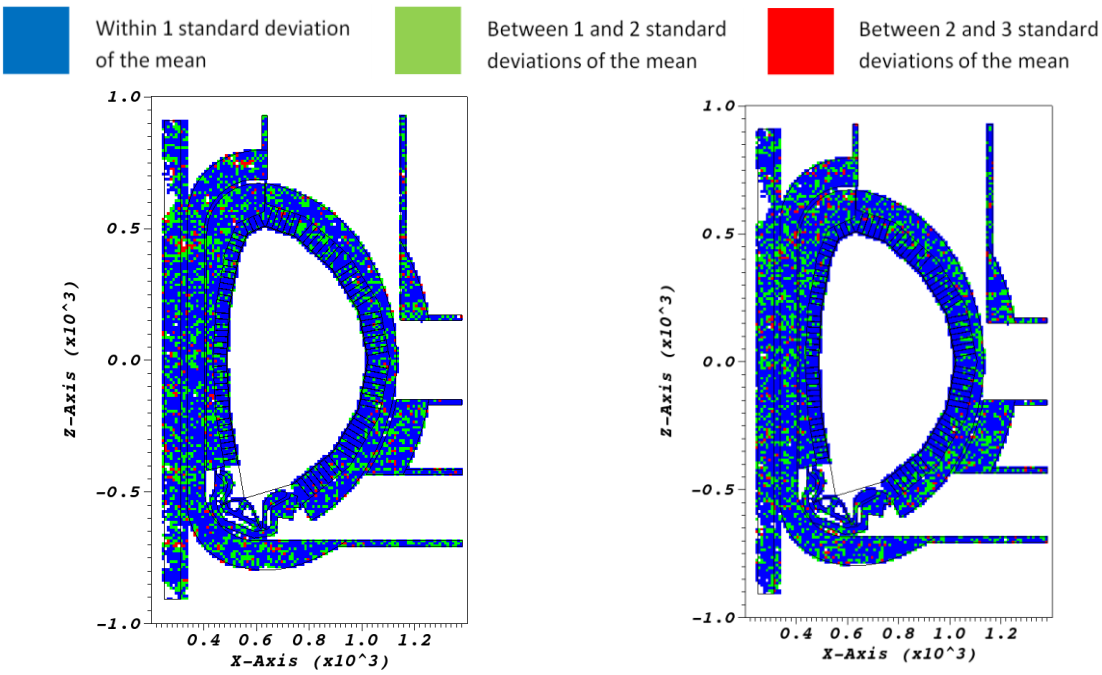

Figure 7.39 - Voxel values within 1, 1 to 2, and 2 to 3 standard deviations of the reference case; using MCNP6 + PLIB 05t (left) and MCNP6 + PLIB12 (right).

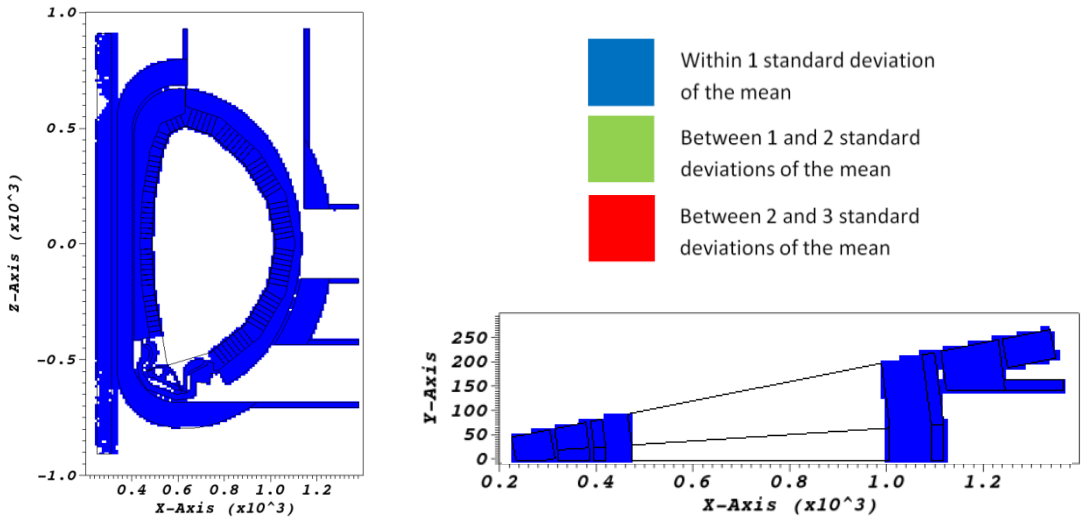

Figure 7.40 - Voxel values within 1, 1 to 2, and 2 to 3 standard deviations of the reference case; using MCNP6 + PLIB 84.

Table 7.28 - A summary of the percentage of compared voxel heating results that are within 1, 1 to 2, 2 to 3 and above 3 standard deviations of the reference case, for the combinations of MCNP and PLIB library used. Only non-zero values with a relative statistical uncertainty <25% are compared.

MCNP and PLIB	MCNP5		MCNP6		
% of results within:	04p	84p	84p	05t	12p
1 standard deviation of the reference case	74.46	99.06	100.00	68.83	70.61
1-2 standard deviations of the reference case	22.63	0.92	0.00	26.72	25.40
2-3 standard deviations of the reference case	2.73	0.02	0.00	4.04	3.70
> 3 standard deviations of the reference case	0.18	0.00	0.00	0.41	0.29

Discussion

The photon libraries PLIB 04 and PLIB 84 are identical in cross-section data and differ only in the format of the data provided. Results from both the simple test case and the DEMO benchmark model show this to be true, MCNP6 using PLIB 04 gives identical results to MCNP6 using PLIB 84, regardless of whether Doppler broadening is in use or not.

Differences are observed when comparing the use of MCNP5 with PLIB04 to the reference case, with Doppler broadening, as expected due to the known bug. For the majority of elements tested, ~92 %, the difference observed in the surface flux per energy bin of the simple test model is still within 1 standard deviation of the reference case. For the DEMO benchmark model, approximately 75 % of the total photon heating mesh tally values are within 1 standard deviation. Although values within 1 standard deviation are not strictly identical, one might expect ~68 % agreement.

The use of the corrected format library PLIB 84 with MCNP 5 gives results within 1 standard deviation of the reference case for the simple test case. Some slight differences observed are related to the use of the different MCNP versions.

The use of the testing library PLIB 05t was expected to be incompatible with MCNP5; results from the simple test case demonstrate this. Only approximately 18 % of the surface flux tally results were within 1 standard deviation of the reference case. The combination of PLIB 05t and MCNP5 gave the largest percentage difference to the reference case than all other combinations tested, including the use of MCNP5 with

the incorrectly formatted PLIB 04 when using Doppler broadening. The total surface flux results, at 160 cm from the source, using MCNP5 with PLIB 05t were up to 18 % lower than the reference case. Limited analysis was carried out on the resulting effect of using this combination of MCNP and photon library as it was already expected to be incompatible.

It was not clear from the literature review whether MCNP6 would be compatible with PLIB 05t, though results using the simple test case show that this may be the case. Good agreement in the results was observed between the use of MCNP6 and MCNPx with PLIB 05t, when comparing to the reference case (MCNP6 + PLIB 04). In both cases, approximately 71 % of the flux values for each element are within 1 standard deviation of the reference case.

The most recently developed photon library provided with MCNP6 is the PLIB 12 data. In the simple test case, PLIB 12 is shown to give similar photon flux results to PLIB 05t with approximately 67 % of the surface flux per energy bin values at 160 cm for each element, within 1 standard deviation of the reference case. In the DEMO benchmark model approximately 71 % of the photon heating mesh results using MCNP6 with PLIB 12 are within 1 standard deviation of the reference case, and 69 % for MCNP6 with PIB 05t. It can be seen in Figure 7.36 and Figure 7.37 that, although a similar amount of voxel results fall within 1 standard deviation of the reference case, the position of these differences vary.

Conclusions

The observed difference in results for a number of photon libraries (04, 84, 05t and 12) has been investigated. The key conclusions are:

- The majority of the results from the photon library comparison were as expected (see compatibility summary in Table 7.21).
- There is a difference observed in total surface flux due to incorrect sampling when using MCNP5 with PLIB 04, although this difference is < 0.4% in the simple model studies.
- The sampling bug with MCNP5 is shown to be corrected with the use of PLIB 84.

- Use of PLIB 05t with MCNP5 is shown to provide significantly different results to the reference case; total surface flux values were up to 18 % lower than the reference case in simple model studies. This is not unexpected as although MCNP5 will run with the PLIB 05t specified, it is not compatible. It is unclear from the literature whether PLIB 05t is compatible with MCNP6, results presented here show that there is little difference observed in the surface flux when comparing PLIB 05t with MCNP6 and MCNPX.
- The use of PLIB 05t (with MCNPx) gives up to 11 % difference in the DEMO model photon heating values when compared to the reference case, with approximately 69 % of the voxel values within 1 standard deviation of the reference case.
- The use of PLIB 12 gives up to ~7 % difference in the DEMO model photon heating values when compared to the reference case, with approximately 71 % of the voxel values within 1 standard deviation of the reference case.

APPENDIX 7: UNCERTAINTY AND ASSUMPTIONS

Dealing with uncertainties in the designing of a future fusion reactor is inherently difficult, DEMO will have many unknown challenges to address. The intrinsic complexity of the fusion tokamak due to numerous interdependent system parameters and the dependence of plasma physics on scaling results in significant technical uncertainties. The important uncertainties within the broader context of fusion reactor design development are discussed in [183].

Uncertainties regarding the results presented in this thesis arise from many areas including, but not limited to: statistical methods, cross-section data, resolution of result tallying and error propagation in the R2S method. Further uncertainties arise from the model itself: material definitions, location and design of components etc. Uncertainties regarding the computational methods and the main assumptions made are described in further detail in this appendix. The uncertainties regarding the model are not quantified and would require some computationally expensive sensitivity study in order to define such quantities.

Statistical uncertainty in Monte Carlo Calculations

The results obtained using MCNP, a Monte Carlo code, represent an average of the contributions made from many sampled histories. The result has an associated statistical error or uncertainty. The behaviour of this statistical error versus the number of histories is very important and provides insight into the quality of the results and statistical behaviour. If the tally is not ‘well behaved’ the statistical error associated with the result generally will not reflect the true confidence interval of the result. There are several checks performed in MCNP to provide the user with quantities to assess the quality of the confidence interval and ensure a well-behaved and properly converged tally result.

In a Monte Carlo calculation, precision is the uncertainty caused by the statistical fluctuations for the portion of physical phase space sampled by the Monte Carlo process [72]. Problem cutoffs (such as in time or energy), inappropriate use of variance reduction techniques or insufficient sampling of important low-probability events can result in important portions of the physical phase space not sampled. Accuracy is a measure of how close the expected value is to the true physical quantity

being estimated. The difference between this true value and the expected value is called the systematic error which is usually not known. The uncertainty estimates for the results of Monte Carlo calculations refer only to the precision of the result, not the accuracy. Care needs to be taken to ensure the problem is correctly modelled, as a highly precise result can be calculated that is far from the true result because the problem is incorrectly defined.

Uncertainties in FISPACT activation calculations

The uncertainty in the activation calculation is dominated by the associated cross-section uncertainties. Other uncertainties arise, such as from the propagation of statistical error on the neutron flux and uncertainty in decay data. The propagation of statistical errors cannot currently be accounted for in FISPACT and it is expected that in the majority of cases, provided the statistical uncertainty on the neutron flux is low, these errors will be much smaller than those associated with cross-section uncertainties. The uncertainties in the decay data are also not included in this assessment, but can be accounted for in FISPACT-II provided that the uncertainty data is available. Including decay data in uncertainty calculations can significantly increase computational time and is usually orders of magnitude smaller than cross-section uncertainties.

Blanket performance (Section 4.2 and 4.3)

For clarity in the results presented in Section 4.2 and 4.3, the uncertainty data was not included. Some examples are provided here.

The blanket performance calculations were conducted using either a spherical model or the rectangular cross-section tokamak model [127]. In the case of the spherical model it is assumed that the reactor can be simplified to a sphere and is symmetrical, only varying in one dimension. This is a significant simplification of a ‘real’ fusion tokamak, however for broad scoping studies this is sufficient. The spherical simplifications enable shorter computational time with reduced statistical uncertainties. It also facilitates the use of simple scripting routines to alter many geometric and material parameters.

The rectangular cross-section tokamak model introduces a more realistic geometry and includes a simple representation of the divertor region. This model assumes

symmetry around the tokamak and does not include any ports. Only the in-vessel components are modelled with the breeder blanket comprising of breeder and structural layers. The magnets and vacuum vessel are not included in the model. As this is used for a purely blanket analysis for comparison of breeder types these assumptions are appropriate.

An example of the 10 statistical check results from MCNP for a TBR calculation is given in Table 7.29. An example of the statistical uncertainty on the TBR calculations in each layer of a spherical model, using a blanket material composition with 40 % lithium, is given in Figure 7.41.

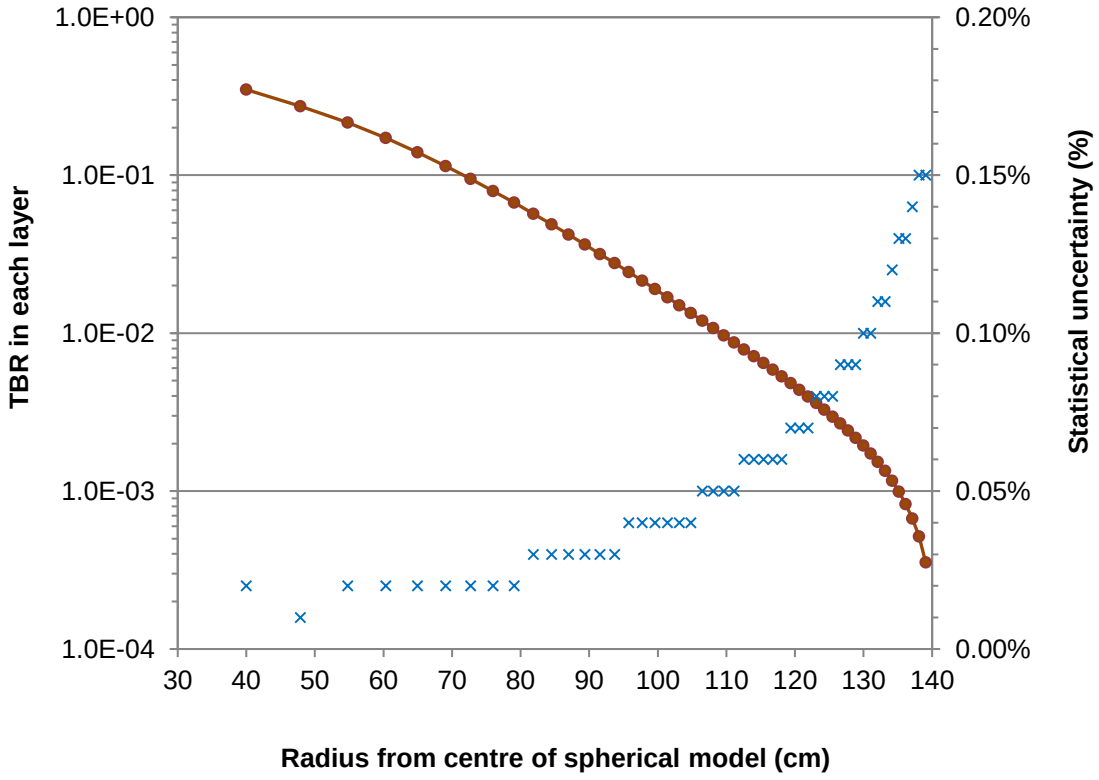

Figure 7.41 - The statistical uncertainty in the MCNP TBR calculation. An example for a material composition with 40% Li breeder, at natural lithium-6 enrichment using the neutronics model as detailed in Section 4.2.2.

An increase in statistical uncertainty with distance from the plasma is observed. This is to be expected. If the increase in statistical uncertainty was significant it could be reduced through the use of a variance reduction technique. However the uncertainties in these results are well below a level for concern and variance reduction would be inappropriate.

An example of the typical statistical uncertainty values associated with the solid and liquid breeding material comparison using the rectangular cross-section model is given in Figure 7.42. Similar to the spherical model, the uncertainties increase with radial distance from the plasma but are still below 1%.

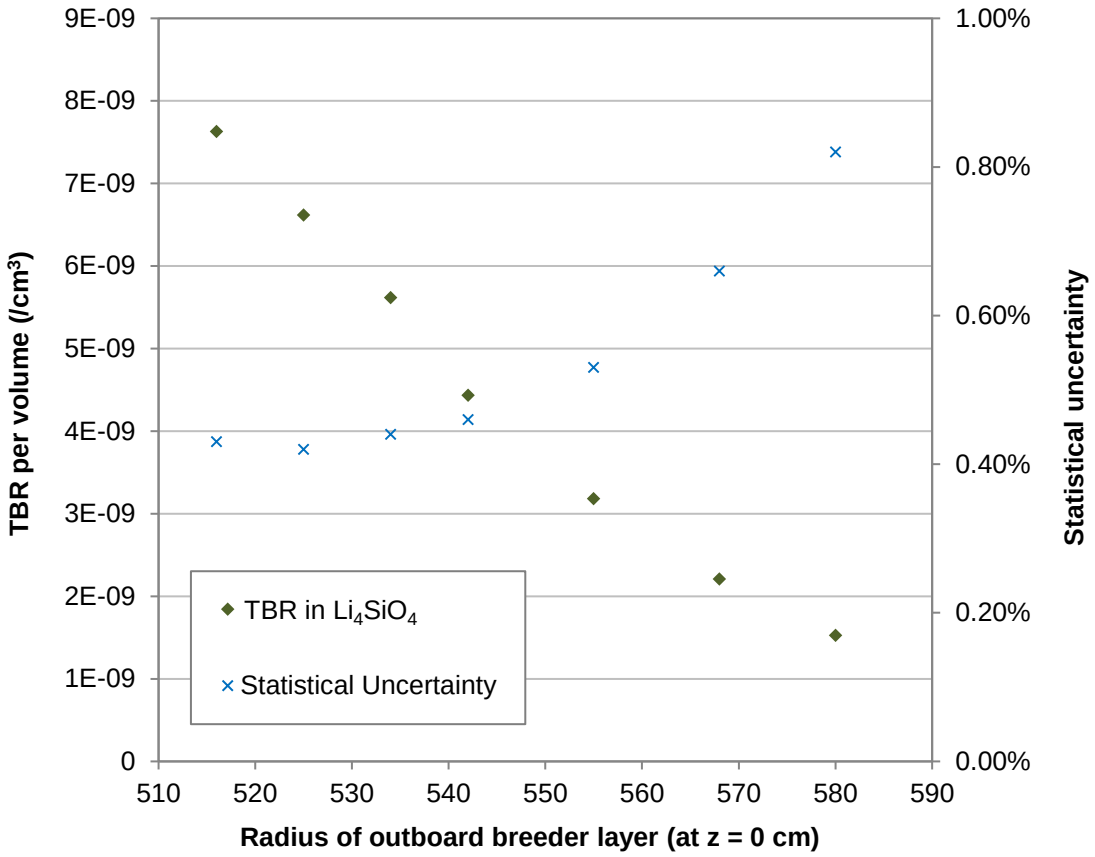

Figure 7.42 - The statistical uncertainty in the MCNP TBR calculation. An example for a material composition with 40% Li_4SiO_4 breeder, at natural lithium-6 enrichment using the neutronics model as detailed in Section 4.3.2.

Heating in superconducting magnet (Section 4.4)

Calculations performed on the spherical tokamak model assumed the model to be simplified to a sphere with a cylindrical centre column. The model was also assumed to be symmetrical and reflecting boundary planes used to reduce the geometry size (thus reducing computational effort for the same statistical uncertainty). No divertor or ports were included in the spherical model. As these calculations were focused on the heating in the centre column magnets, the energy deposition from both neutrons and photons was tallied. For this, MCNP is run in mode ‘n p’.

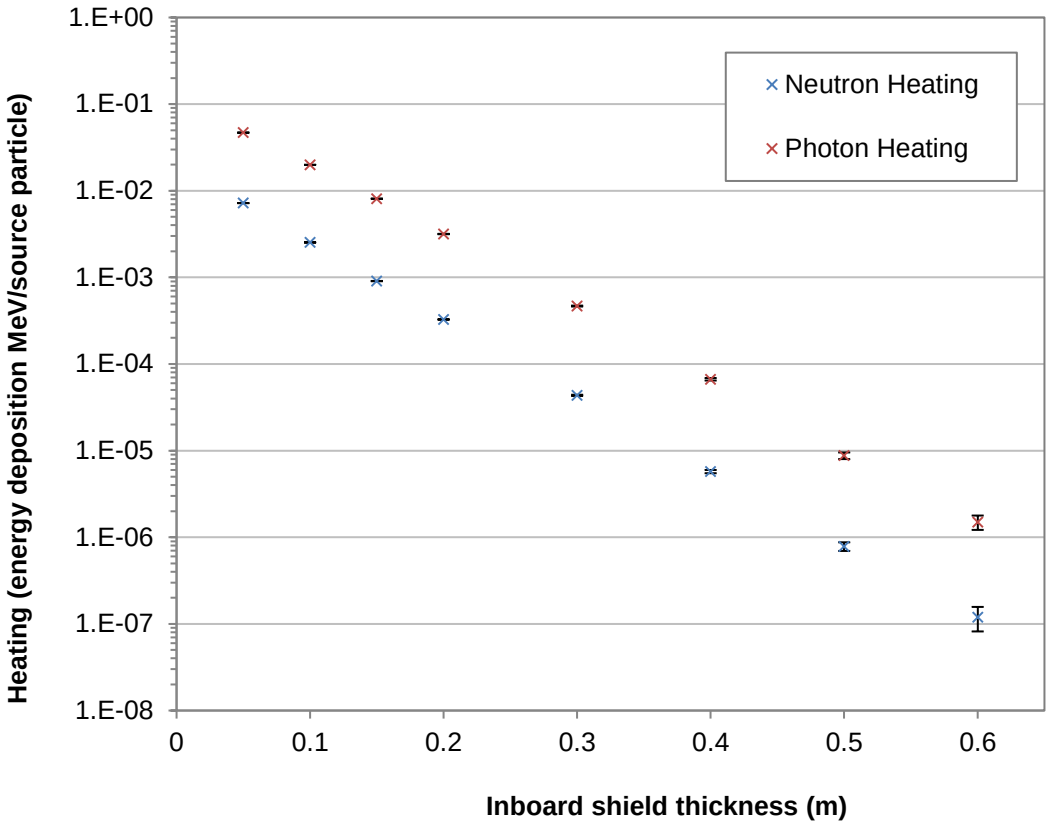

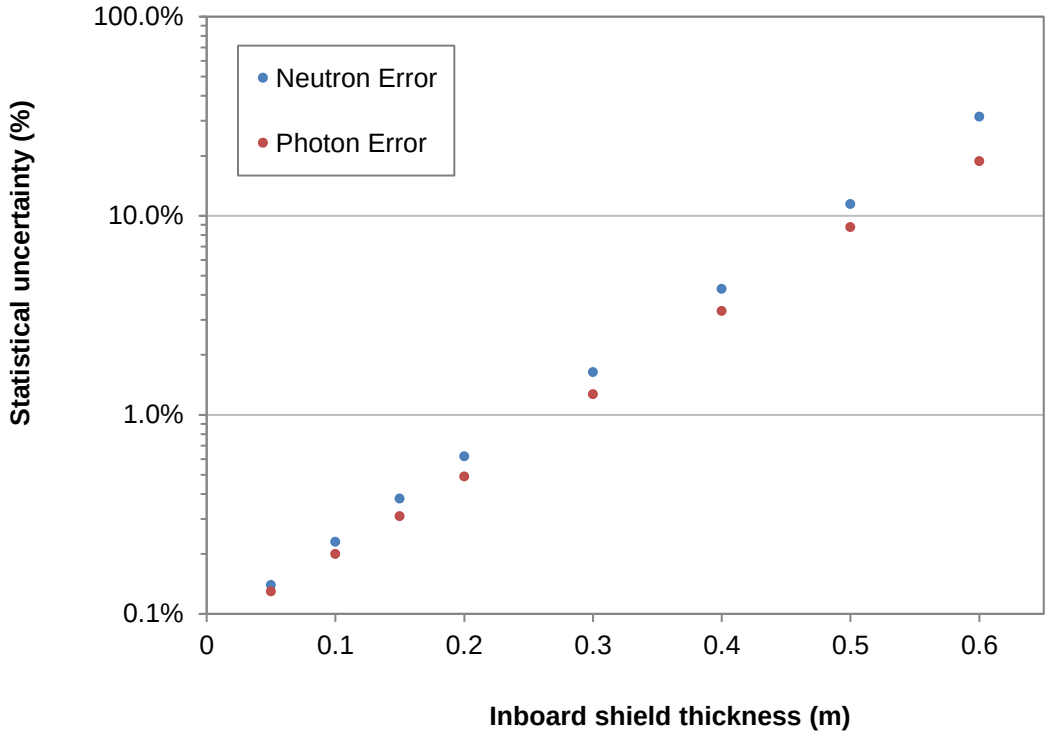

Figure 7.43 - Nuclear heating (energy deposition) for a 0.3 m centre column, aspect ratio 2 and varying shielding thickness. (Top) Statistical uncertainty (%) in the MCNP calculation. (Bottom)

Table 7.29 - Summary of the results from the statistical checks performed within the MCNP calculation; for a TBR calculation (F4 tally with FM 205 tally multiplier) using a blanket composition with 40% breeder material (Figure 4.3, Section 4.2).

tfc bin	--mean--	---------relative error---------			----variance of the variance----			--figure of merit--		-pdf-
behavior	behavior	value	decrease	decrease rate	value	decrease	decrease rate	value	behavior	slope
desired	random	<0.10	yes	1/sqrt(nps)	<0.10	yes	1/nps	constant	random	>3.00
observed	random	0.00	yes	yes	0.00	yes	yes	constant	random	10
passed?	yes	yes	yes	yes	yes	yes	yes	yes	yes	yes

Table 7.30 - Summary of the results from the statistical checks performed within the MCNP calculation; for a heating calculation (F6 tally for neutron and photon energy deposition) using a 30 cm centre column and 40 cm inboard shield (Section 4.4).

tfc bin	--mean--	---------relative error---------			----variance of the variance----			--figure of merit--		-pdf-
behavior	behavior	value	decrease	decrease rate	value	decrease	decrease rate	value	behavior	slope
desired	random	<0.10	yes	1/sqrt(nps)	<0.10	yes	1/nps	constant	random	>3.00
observed	random	0.03	yes	yes	0	yes	yes	constant	random	10
passed?	yes	yes	yes	yes	yes	yes	yes	yes	yes	yes

In a small number of cases where the models used a thick inboard shield (> 0.5 m) the statistical uncertainties in the peak heating (i.e. +- 5cm from the mid-plane) were 15 - 40 % (see Figure 7.43). In more detailed investigations assessing the profile of the heating and neutron flux through the shield, variance reduction through the use of user-defined importance's with cell splitting was performed. This requires the shield to be composed of a number of concentric cylinders with the cell importance increasing through the shield, away from the plasma. This causes increased particle splitting in the areas of importance i.e. through into the thick shield. To check the efficiency of this method the particle population table in the MCNP output file was used.

An example of the energy deposition results in the centre column magnets from neutron and photon interactions is given in Figure 7.43 with the associated statistical uncertainty included both as error bars, and below as a percentage. An example of the 10 statistical checks performed by MCNP for the heating/energy deposition tally is given in Table 7.30.

For the more complex model used in the neutronics analysis of the HTS-ST, global variance reduction was used. This was performed using the automated weight window generation tool WWiter (Weight Window iteration). The WWiter code uses an iterative approach to determining a suitable weight window and requires an initial analogue MCNP calculation to obtain an estimate of the neutron flux over the weight window mesh. WWiter uses a tool 'mesh2ww', also developed at CCFE, to apply Cooper's method for optimizing the weight window map. This is repeated in an iterative loop automatically using WWiter until a user specified optimisation is reached. The weight window has two energy bins 0 - 0.1 MeV and 0.1 - 20 MeV and a spatial resolution of approximately 10 cm (Figure 7.44).

The relative statistical uncertainty of the total flux in each voxel is shown in the error map of Figure 7.45. The majority of voxels have a total statistical uncertainty below 5 % with some voxels at 10 % in the lower region of the model. The important areas for the calculation show good statistical uncertainties. The 10 statistical checks within the MCNP calculation are not performed on mesh-based tallies. The checks have been assessed and passed for the cell tallies used for peak centre column heating and TBR in the blanket.

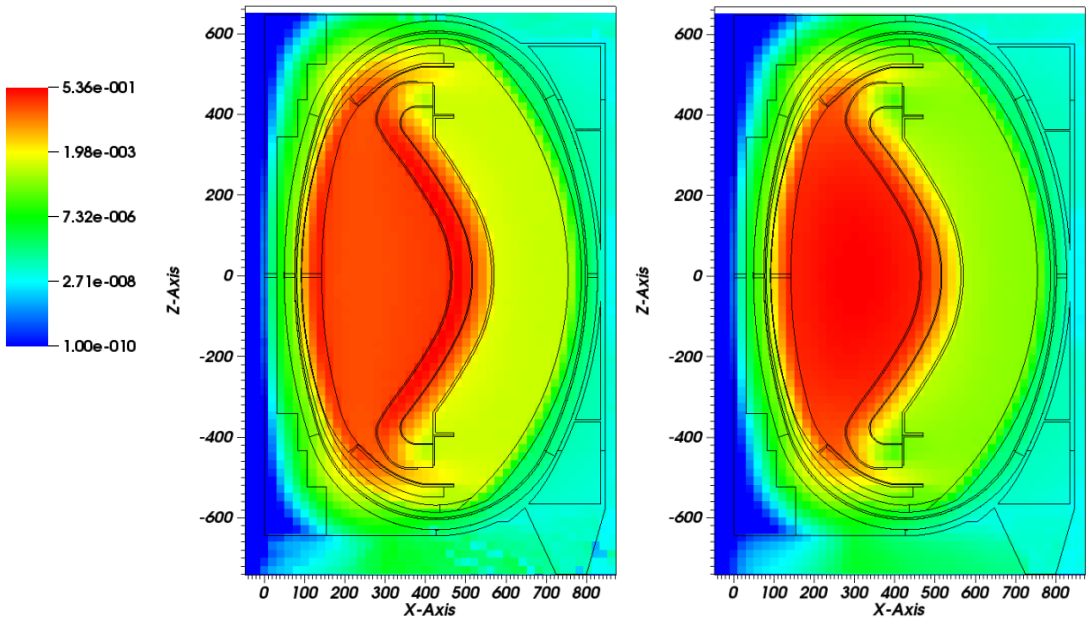

Figure 7.44 - An elevation plot through HTS-ST model, showing lower bound voxel weight in the 2 energy groups: 0 - 0.1 MeV (Left) and 0.1 - 20 MeV (Right).

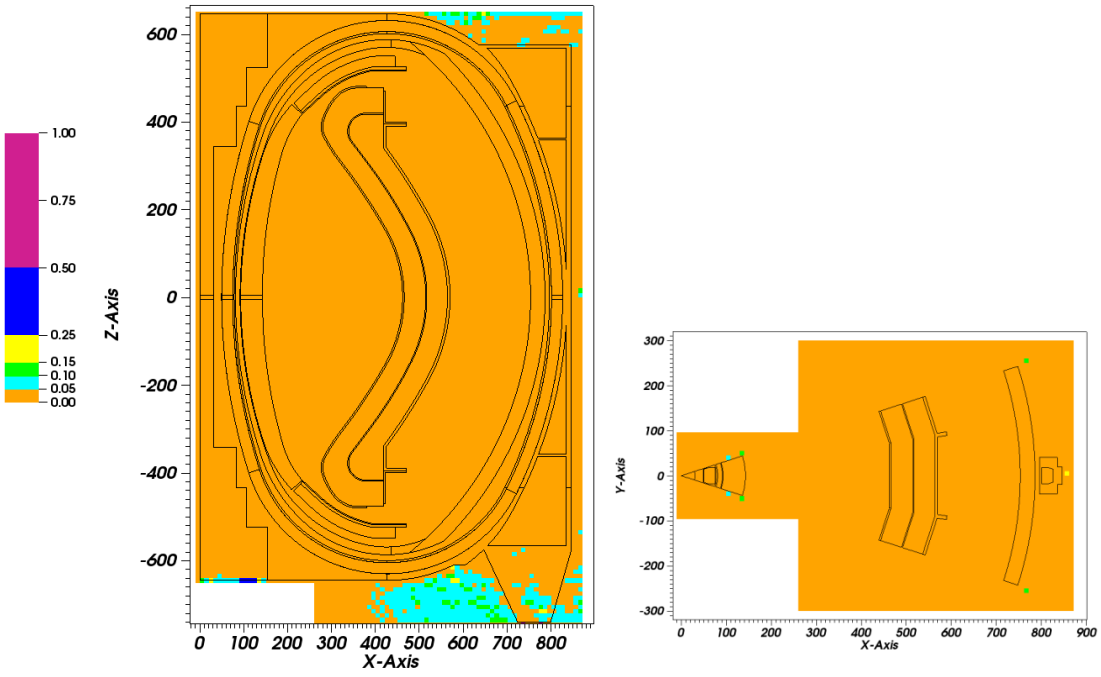

Figure 7.45 - Relative statistical uncertainty in total neutron flux maps using HTS-ST neutronics model. An elevation view through the centre of the model, Y = 0 cm (Left) and a plan view through the middle of the model at Z = 0 cm (Right).

Activation and radioactive waste inventory using MCR2S

It has already been mentioned that the propagation of errors through the neutron transport calculation and the activation with MCR2S is an area of continued research within the fusion community. The uncertainty is currently, therefore, assumed to be dominated by the statistical uncertainty in the neutron flux calculation and the cross-section data in activation calculations.

MCNP neutron flux calculation

To produce neutron flux results with sufficient statistical uncertainty, and within an acceptable time frame, global variance reduction was used with the DEMO-2015 neutronics model. During testing, the code WWiter was used to automatically generate neutron importance maps for global variance reduction. The produced weight window was shown to perform poorly and significantly increased computational time for the final neutron transport calculation. The recently released Automated Variance Reduction Parameter Generator (ADVANTG) software, a deterministic hybrid approach to variance reduction, was used instead and performed more efficiently.

The variance reduction parameters consisted of space and energy-dependent weight window bounds and a biased source distribution. In the simulation, the weight windows are used to split or roulette particles that move toward relatively more or less important regions of phase space, respectively. The biased source ensures that particles are preferentially started where they are likely to contribute to the tally of interest. To accelerate the process the Forward-Weighted CADIS (FW-CADIS) method [184] was developed. In this method a forward (as opposed to adjoint) deterministic calculation is initially performed and the results are used to construct an adjoint source that is weighted by the inverse of the forward flux in the regions of space and energy where the tallies are defined. Once the source has been computed, a deterministic adjoint calculation is performed and variance reduction parameters are computed using the CADIS methodology. ADVANTG uses the Denovo 3-D discrete ordinates package for discretization and generation of variance reduction parameters for a structured mesh grid.

An example of the forward and adjoint flux is shown in Figure 7.46 and Figure 7.47 respectively.

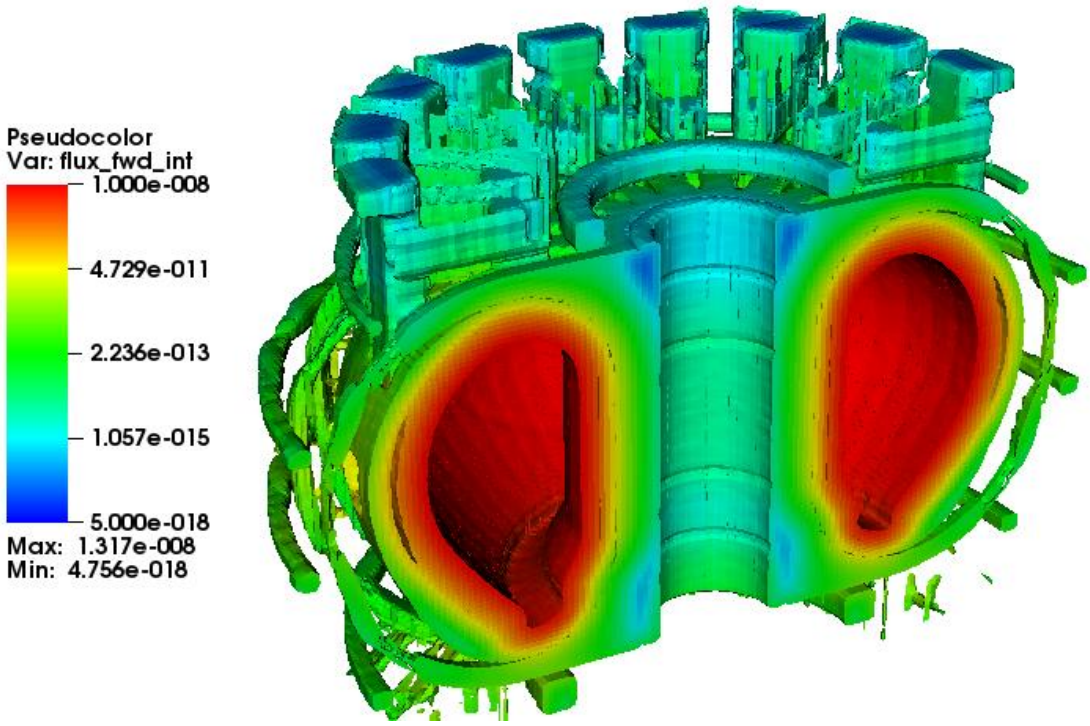

Figure 7.46 - The total (energy integrated) forward flux calculated using Denovo with ADVANTG.

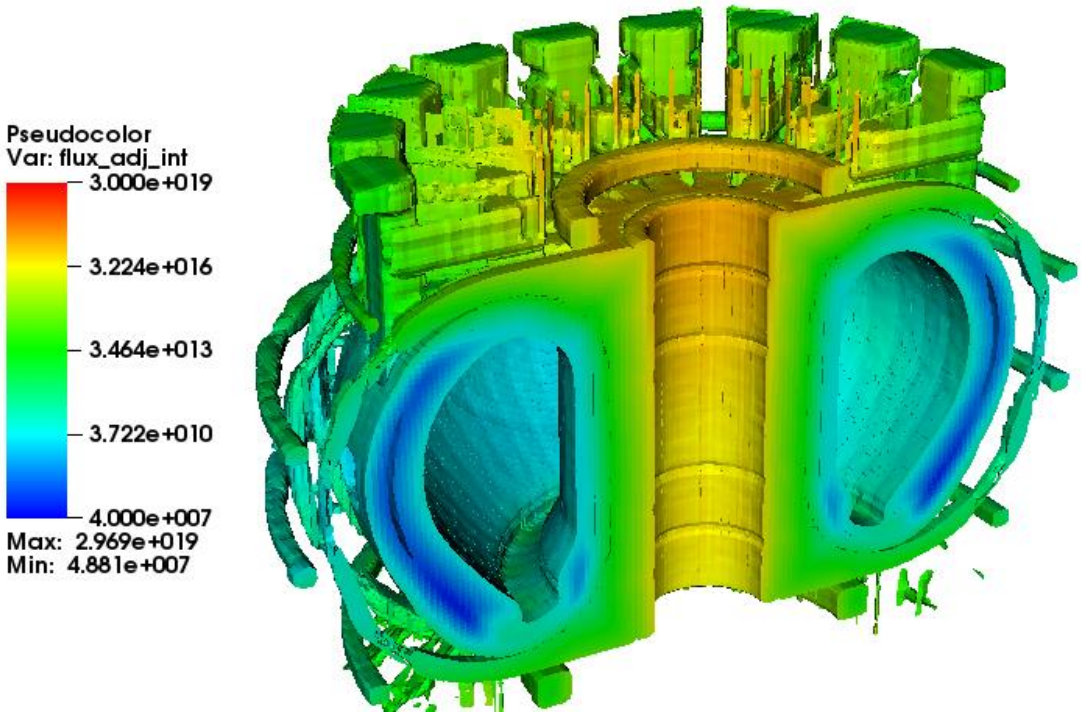

Figure 7.47 - The total (energy integrated) adjoint scalar flux calculated using Denovo with ADVANTG.

The statistical uncertainty in the total neutron flux is below 5 % in the majority of mesh voxels for the structured mesh methods used, with some higher errors in regions that present a 'deep shielding problem', such as along the manifold within the upper port. In MCNP, confidence in results with statistical uncertainties below 10 % is reasonable, provided that the 10 statistical checks are also passed. However, these checks are not performed by MCNP for mesh tallies. Reducing the statistical errors to 5 - 10 % is therefore assumed in this work to be adequate in providing reasonable results. The 10 statistical checks are provided for the cell tallies used in the cell-based method, and the results from this provide confidence in both the cell and mesh based results. (Examples are given for the toroidal field coil and breeder blanket in Table 7.31 and Table 7.32.)

Statistical uncertainties within the cell tallies, as used for the cell based methods, were in general significantly lower, as the result is a neutron flux averaged over a large volume, which will be based on more histories than the result in a relatively small mesh voxel volume. Global variance reduction using weight windows was not achievable with the unstructured mesh method, therefore long calculation time was required to increase the number of particle histories. The uncertainty information was not computed for each of the mesh elements comprising the unstructured mesh due to memory limitations and difficulties in interpreting and visualizing the data. A structure mesh computing total neutron flux and associated error was superimposed and included in the calculation. This showed that in-vessel components had reasonably good statistics, below 5 - 10 % in the majority of mesh elements apart from some within the vacuum vessel. Though there was poor uncertainty statistics in the majority of the surrounding components, and in the case of the centre coils there were no results at all. The relative statistical uncertainty maps can be seen in Section 5.9.

Figure 7.48 shows the neutron flux spectrum at point B, a mesh voxel located in the outboard blanket, estimated using the different calculation methods, with the percentage error plotted in Figure 7.49. The majority of the energy bins (over 70 % of the non-zero bins) within the cell-based method have an associated statistical error of less than 5 %. At lower energies (< 0.5 eV) the statistical uncertainties are higher and tend to be above 20 %. In the both the 15 cm and 9 cm resolution structured meshes, over 90 % of the energy bins have a statistical uncertainty less than 5 %.

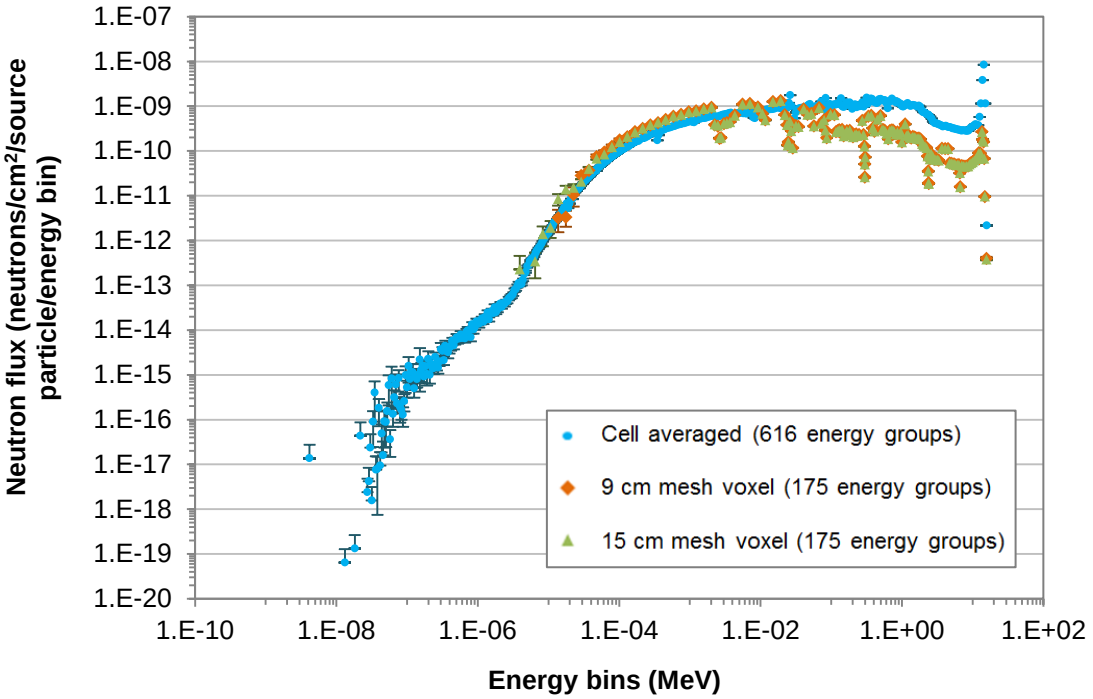

Figure 7.48 - Neutron flux spectra calculated in the cell, 9cm mesh voxel and 15 cm mesh voxel (at point B within the outboard blanket of the EU DEMO model).

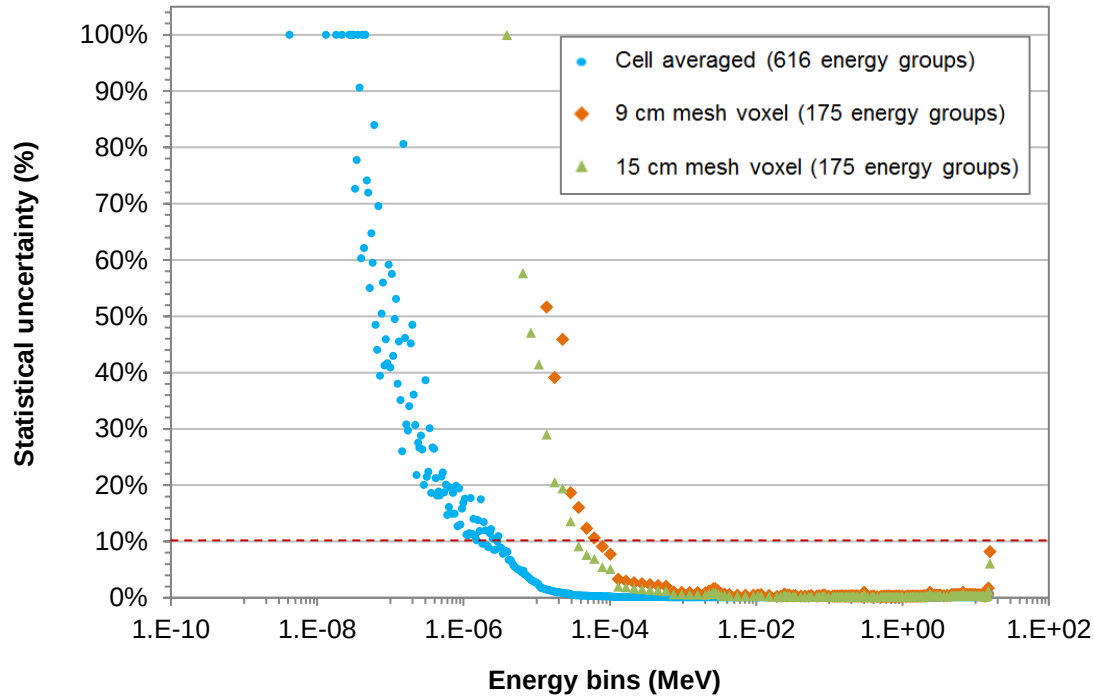

Figure 7.49 - Statistical uncertainty (%) in each energy bin of the neutron flux spectra calculated in the cell, 9cm mesh voxel and 15 cm mesh voxel (at point B within the outboard blanket of the EU DEMO model).

Table 7.31 - Summary of the results from the statistical checks performed within the MCNP calculation; neutron flux in toroidal field coil.

tfc bin	--mean--	---------relative error---------			----variance of the variance----			--figure of merit--		-pdf-
behavior	behavior	value	decrease	decrease rate	value	decrease	decrease rate	value	behavior	slope
desired	random	<0.10	yes	1/sqrt(nps)	<0.10	yes	1/nps	constant	random	>3.00
observed	random	0.00	yes	yes	0.00	yes	yes	constant	random	10.00
passed?	yes	yes	yes	yes	yes	yes	yes	yes	yes	yes

Table 7.32 - Summary of the results from the statistical checks performed within the MCNP calculation; TBR in breeder blanket.

tfc bin	--mean--	---------relative error---------			----variance of the variance----			--figure of merit--		-pdf-
behavior	behavior	value	decrease	decrease rate	value	decrease	decrease rate	value	behavior	slope
desired	random	<0.10	yes	1/sqrt(nps)	<0.10	yes	1/nps	constant	random	>3.00
observed	random	0.00	yes	yes	0	yes	yes	constant	random	6.66
passed?	yes	yes	yes	yes	yes	yes	yes	yes	yes	yes

Radioactive waste calculations

For activation, inventory and contact dose calculations, used to determine the waste class with MCR2S, FISPACT-II release 2.20 and release 3.00 were used. There are some differences in the structure of the output file, but there should be no difference in the results. Using the 9 cm structured mesh neutron flux from point B as a test case, it was shown that there was no difference observed in results between the 2 releases. This same test case, with FISPACT-II release 3.00 was used to assess the cross-section related uncertainties.

As detailed in Section 5.8.1, EAF-2010 nuclear data was used for the FISPACT calculations. Some uncertainty information is provided with the EAF data, however the methods for determining this uncertainty value do not include covariance. The TENDL data library includes complete covariance uncertainty and recent detailed validation and evaluations are available[11]. It is therefore useful to also consider the uncertainty information using TENDL data, even though the nuclear data used in the activation and/or waste calculation may not be identical.

The dominant nuclides within point B are shown in Table 7.33.

Table 7.33 - Primary pathways for dominant nuclides in the activation of a voxel at point B (within the outboard blanket of the EU DEMO 2015 model).

Nuclide	Half-life	Primary pathways	Pathway contribution
^{3}H	12.32 y	$^{6}\mathrm{Li}(n,\alpha)^{3}\mathrm{H}$	99.25%
^{14}C	5730 y	$^{14}\mathrm{N}(n,p)^{14}\mathrm{C}$	99.97%
^{63}Ni	9.90 y	$^{62}\mathrm{Ni}(n,\gamma)^{63}\mathrm{Ni}$	42.47%
		$^{63}\mathrm{Cu}(n,p)^{63}\mathrm{Ni}$	54.87%
^{93m}Nb	16.2 y	$^{93}\mathrm{Nb}(n,n)^{93m}\mathrm{Nb}$	100.00%
^{94}Nb	19986 y	$^{93}\mathrm{Nb}(n,\gamma)^{94}\mathrm{Nb}$	68.84%
		$^{93}\mathrm{Nb}(n,\gamma)^{94}\mathrm{Nb}$	31.09%
^{121m}Sn	43.9 y	$^{122}\mathrm{Sn}(n,2n)^{121m}\mathrm{Sn}$	75.66%
		$^{120}\mathrm{Sn}(n,\gamma)^{121m}\mathrm{Sn}$	21.11%
^{121}Sn	27.03 h	$^{120}\mathrm{Sn}(n,\gamma)^{121}\mathrm{Sn}$	97.58%
^{60}Co	5.27 y	$^{59}\mathrm{Co}(n,\gamma)^{60}\mathrm{Co}$	55.51%
		$^{59}\mathrm{Co}(n,\gamma)^{60}\mathrm{Co}$	44.40%

[11] See http://www.ccfe.ac.uk/fispact_validation.aspx for validation reports.

Activation variation with cooling time is given in Figure 7.50 with EAF error bars included. The percentage error is shown in Figure 7.51 and Figure 7.52 using TENDL data library. In order to use the TENDL data library the flux has been converted from 175 energy groups into 709.

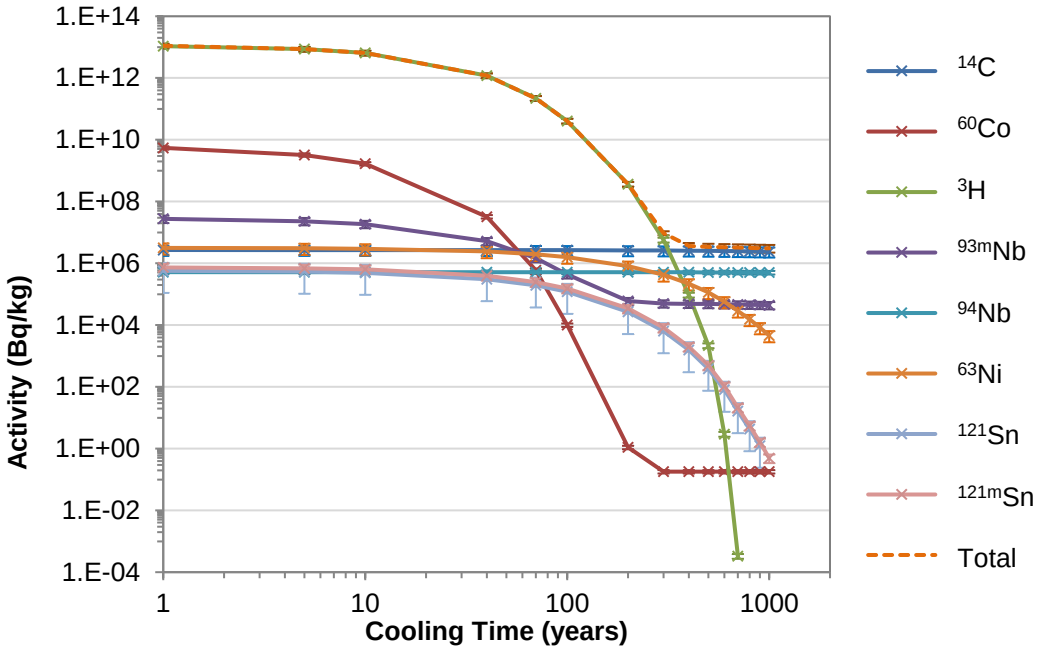

Figure 7.50 - Activity concentration (Bq/kg) with estimated nuclear data uncertainty (using EAF-2010 data). Dominant nuclides at 50-100 years for point B in the outboard blanket of the EU DEMO 2015.

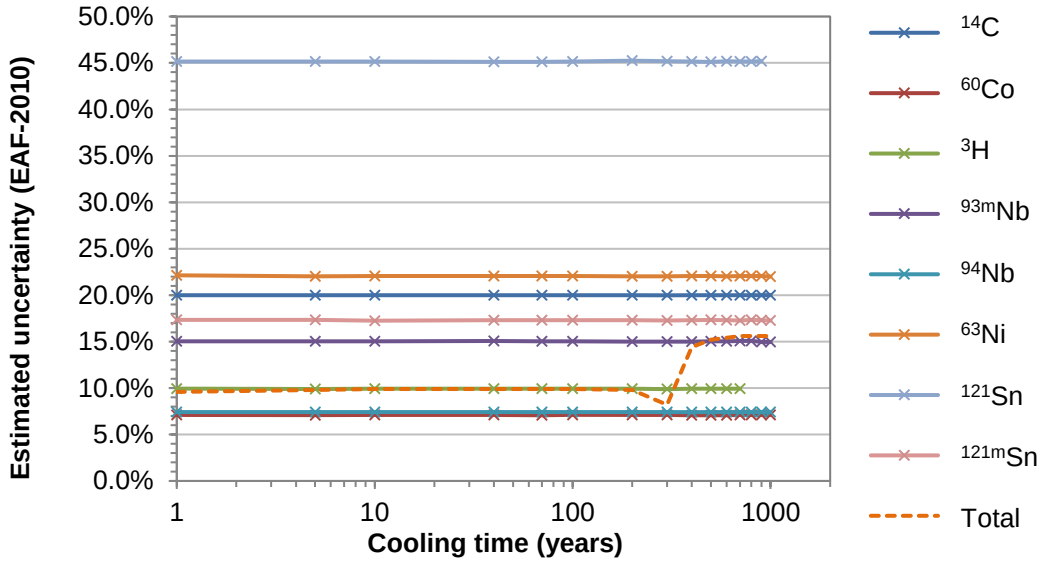

Figure 7.51 - Estimated nuclear data uncertainty for dominant nuclides using EAF-2010 uncertainty data. Dominant nuclides determined at 50-100 years for point B in the outboard blanket of the EU DEMO 2015.

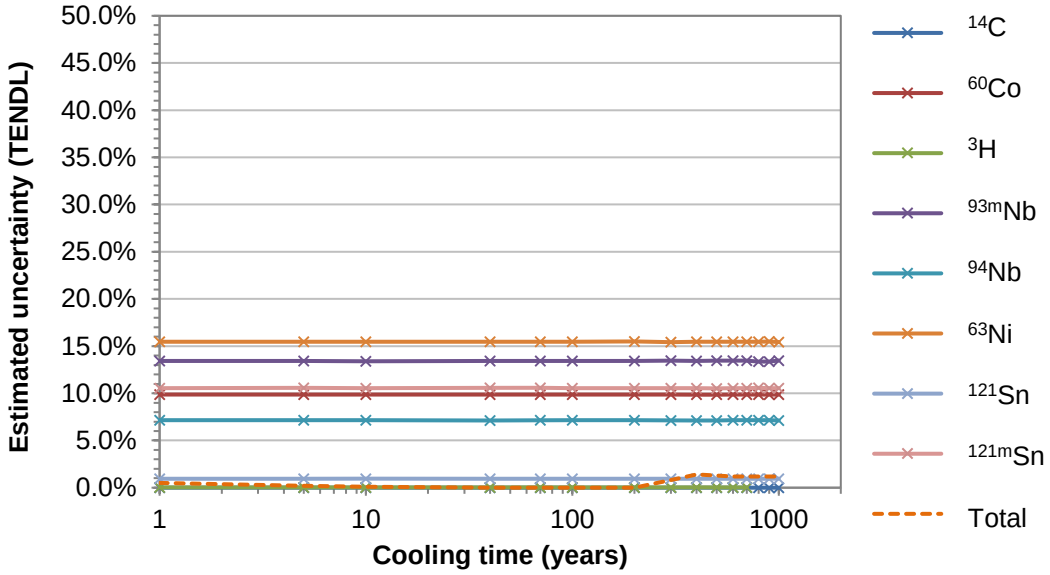

Figure 7.52 - As Figure 7.51 but using TENDL uncertainty data.

Activation calculations in HTS-ST

Activation calculations were performed for a number of breeder blanket materials using a neutron flux map calculated over the blanket of a HTS-ST model, see Section 4.4.5. The neutron flux with error bars corresponding to the statistical uncertainty is shown in Figure 7.53.

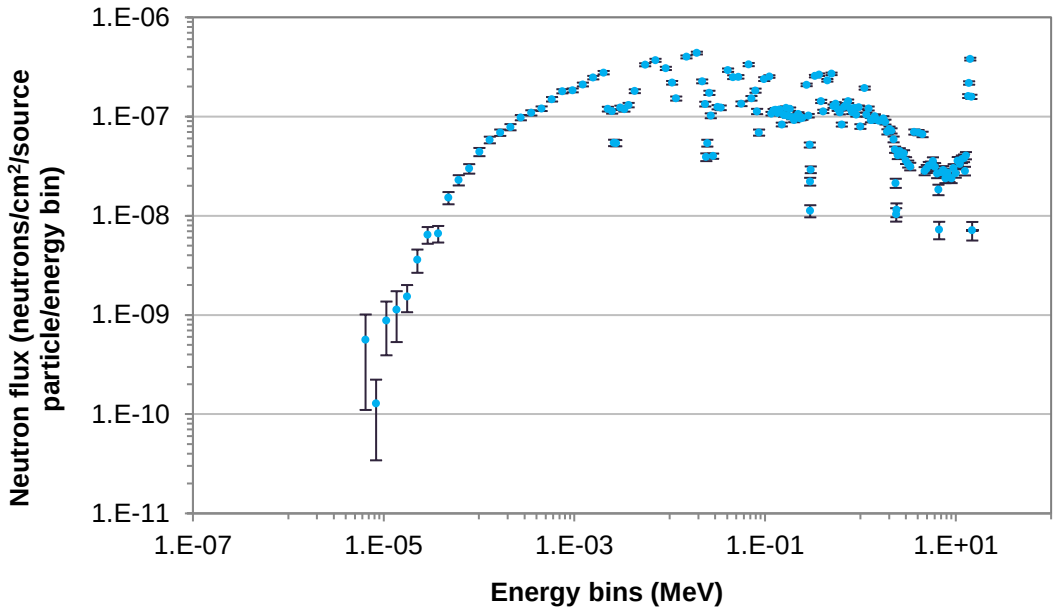

Figure 7.53 - Neutron flux spectrum within the outboard blanket of the HTS-ST model. Error bars correspond to MCNP neutron transport statistical uncertainty.

The dominant nuclides at 100 years cooling time were compared at a location in the first outboard blanket (the primary pathways are shown in Table 7.34 - Table 7.36). The uncertainties arising from the nuclear data are shown in Figure 7.54 to Figure 7.56 as activation with error bars, and the percentage uncertainty. The uncertainty estimations are from the TENDL data library, though the EAF-2010 data was used for the original activation calculations. The reason for using TENDL data to assess cross-section data uncertainties is provided earlier in this appendix.

Table 7.34 - Primary pathways for dominant nuclides in the activation of a LiPb blanket, based on the EU DEMO HCLL.

Nuclide	Half-life	Primary pathways	Pathway contribution
^{3}H	12.32 y	$^{6}\mathrm{Li}(n,\alpha)^{3}\mathrm{H}$	99.90%
^{14}C	5730 y	$^{14}\mathrm{N}(n,p)^{14}\mathrm{C}$	99.93%
^{205}Pb	1.73 x 10^{7} y	$^{206}\mathrm{Pb}(n,2n)^{205}\mathrm{Pb}$	93.26%
^{63}Ni	9.90 y	$^{63}\mathrm{Cu}(n,p)^{63}\mathrm{Ni}$	65.37%
		$^{62}\mathrm{Ni}(n,\gamma)^{63}\mathrm{Ni}$	22.57%
^{121m}Sn	43.9 y	$^{122}\mathrm{Sn}(n,2n)^{121m}\mathrm{Sn}$	56.94%
		$^{120}\mathrm{Sn}(n,\gamma)^{121m}\mathrm{Sn}$	32.19%
^{94}Nb	19986 y	$^{93}\mathrm{Nb}(n,\gamma)^{94m}\mathrm{Nb(IT)}^{94}\mathrm{Nb}$	64.75%
		$^{93}\mathrm{Nb}(n,\gamma)^{94}\mathrm{Nb}$	34.89%
^{53}Mn	3.74 x 10^{6} y	$^{54}\mathrm{Fe}(n,np)^{53}\mathrm{Mn}$	99.67%
^{60}Co	5.27 y	$^{59}\mathrm{Co}(n,\gamma)^{60m}\mathrm{Co}(IT)^{60}\mathrm{Co}$	55.77%
		$^{59}\mathrm{Co}(n,\gamma)^{60}\mathrm{Co}$	34.07%

Table 7.35 - Primary pathways for dominant nuclides in the activation of a LiFBe blanket.

Nuclide	Half-life	Primary pathways	Pathway contribution
^{3}H	12.32 y	$^{6}\mathrm{Li}(n,\alpha)^{3}\mathrm{H}$	97.52%
^{14}C	5730 y	$^{19}\mathrm{F}(n,n\alpha)^{15}\mathrm{N}(n,p)^{14}\mathrm{C}$ $^{19}\mathrm{F}(n,n\alpha)^{15}\mathrm{N}(n,d)^{14}\mathrm{C}$	61.85%
		$^{19}\mathrm{F}(n,t)^{17}\mathrm{O}(n,\alpha)^{14}\mathrm{C}$	18.02%
^{63}Ni	9.90 y	$^{63}\mathrm{Cu}(n,p)$ $^{63}\mathrm{Ni}$	65.39%
		$^{62}\mathrm{Ni}(n,\gamma)^{63}\mathrm{Ni}$	22.58%
^{121m}Sn	43.9 y	$^{122}\mathrm{Sn}(n,2n)^{121m}\mathrm{Sn}$	56.91%
		$^{120}\mathrm{Sn}(n,\gamma)^{121m}\mathrm{Sn}$	32.19%
^{94}Nb	19986 y	$^{93}\mathrm{Nb}(n,\gamma)^{94m}\mathrm{Nb}(IT)^{94}\mathrm{Nb}$	64.75%
		$^{93}\mathrm{Nb}(n,\gamma)^{94}\mathrm{Nb}$	34.89%
^{93m}Nb	16.2 y	$^{93}\mathrm{Nb}(n,n)^{93m}\mathrm{Nb}$	98.52%
^{121}Sn	27.03 h	$^{120}\mathrm{Sn}(n,\gamma)^{121}\mathrm{Sn}$	74.09%
^{60}Co	5.27 y	$^{59}\mathrm{Co}(n,\gamma)^{60m}\mathrm{Co}(IT)^{60}\mathrm{Co}$	55.78%
		$^{59}\mathrm{Co}(n,\gamma)^{60}\mathrm{Co}$	34.08%

Table 7.36 - Primary pathways for dominant nuclides in the activation of a LiSn blanket.

Nuclide	Half-life	Primary pathways	Pathway contribution
^{3}H	12.32 y	$^{6}\mathrm{Li}(n,\alpha)^{3}\mathrm{H}$	99.90%
^{121m}Sn	43.9 y	$^{122}\mathrm{Sn}(n,2n)^{121m}\mathrm{Sn}$	63.60%
		$^{120}\mathrm{Sn}(n,\gamma)^{121m}\mathrm{Sn}$	35.99%
^{121}Sn	27.03 h	$^{120}\mathrm{Sn}(n,\gamma)^{121}\mathrm{Sn}$	77.88%
^{113m}Cd	14.1 y	$^{116}\mathrm{Sn}(n,\alpha)^{113m}\mathrm{Cd}$	90.09%
^{14}C	5730 y	$^{14}\mathrm{N}(n,p)^{14}\mathrm{C}$	99.93%
^{63}Ni	9.90 y	$^{63}\mathrm{Cu}(n,p)^{63}\mathrm{Ni}$	65.37%
		$^{62}\mathrm{Ni}(n,\gamma)^{63}\mathrm{Ni}$	22.57%
^{108m}Ag	438 y	$^{112}\mathrm{Sn}(n,\alpha)^{109}\mathrm{Cd}(\beta+)^{109m}\mathrm{Ag}(IT)$	98.61%
		$^{109}\mathrm{Ag}\ (n,2n)^{108m}\mathrm{Ag}$	
^{60}Co	5.27 y	$^{59}\mathrm{Co}(n,\gamma)^{60m}\mathrm{Co}\ (IT)^{60}\mathrm{Co}$	55.79%

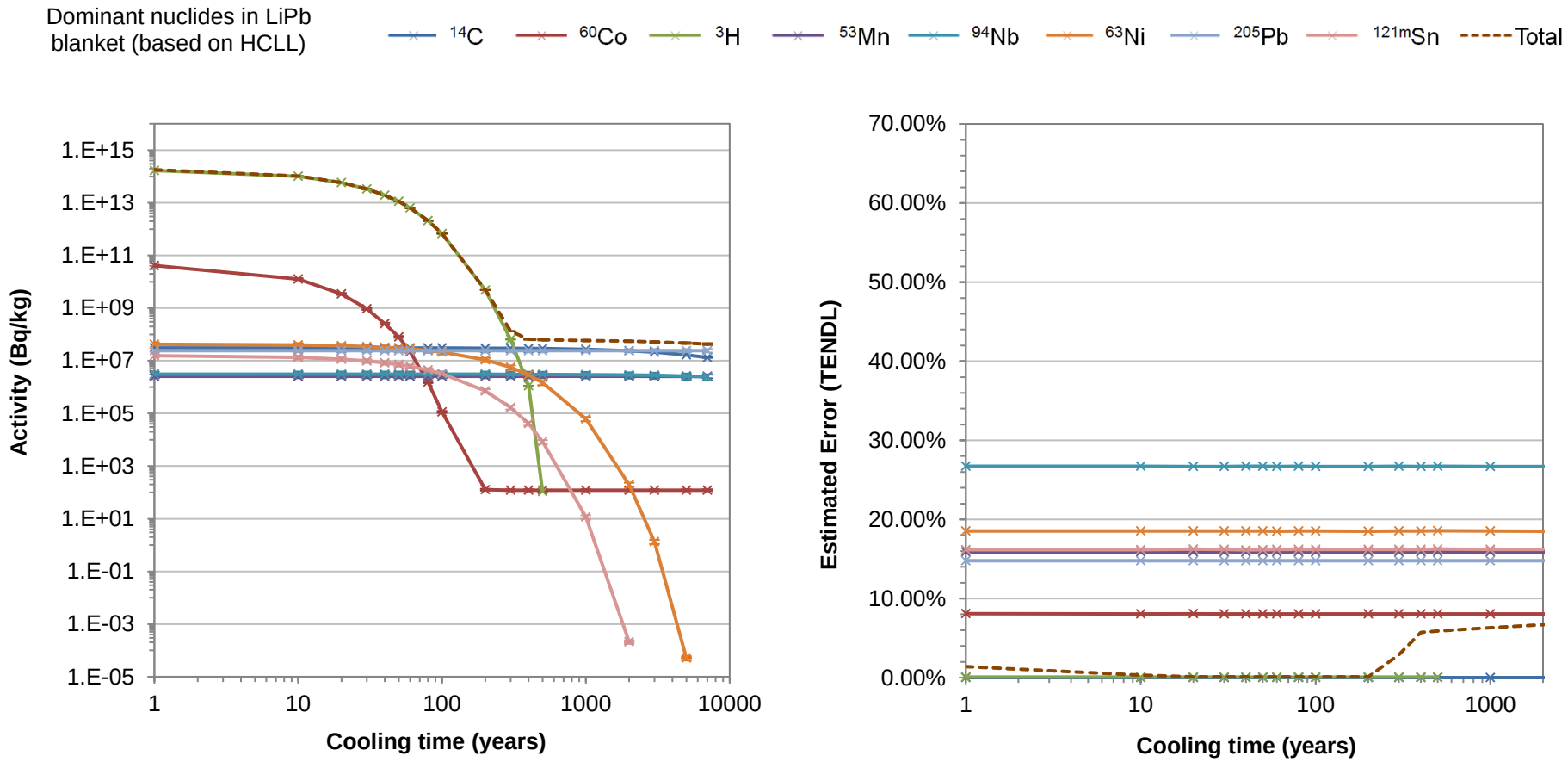

Figure 7.54 - Activity (Left) and uncertainty (Right) using TENDL data for a LiPb blanket (based on the EU DEMO HCLL concept).

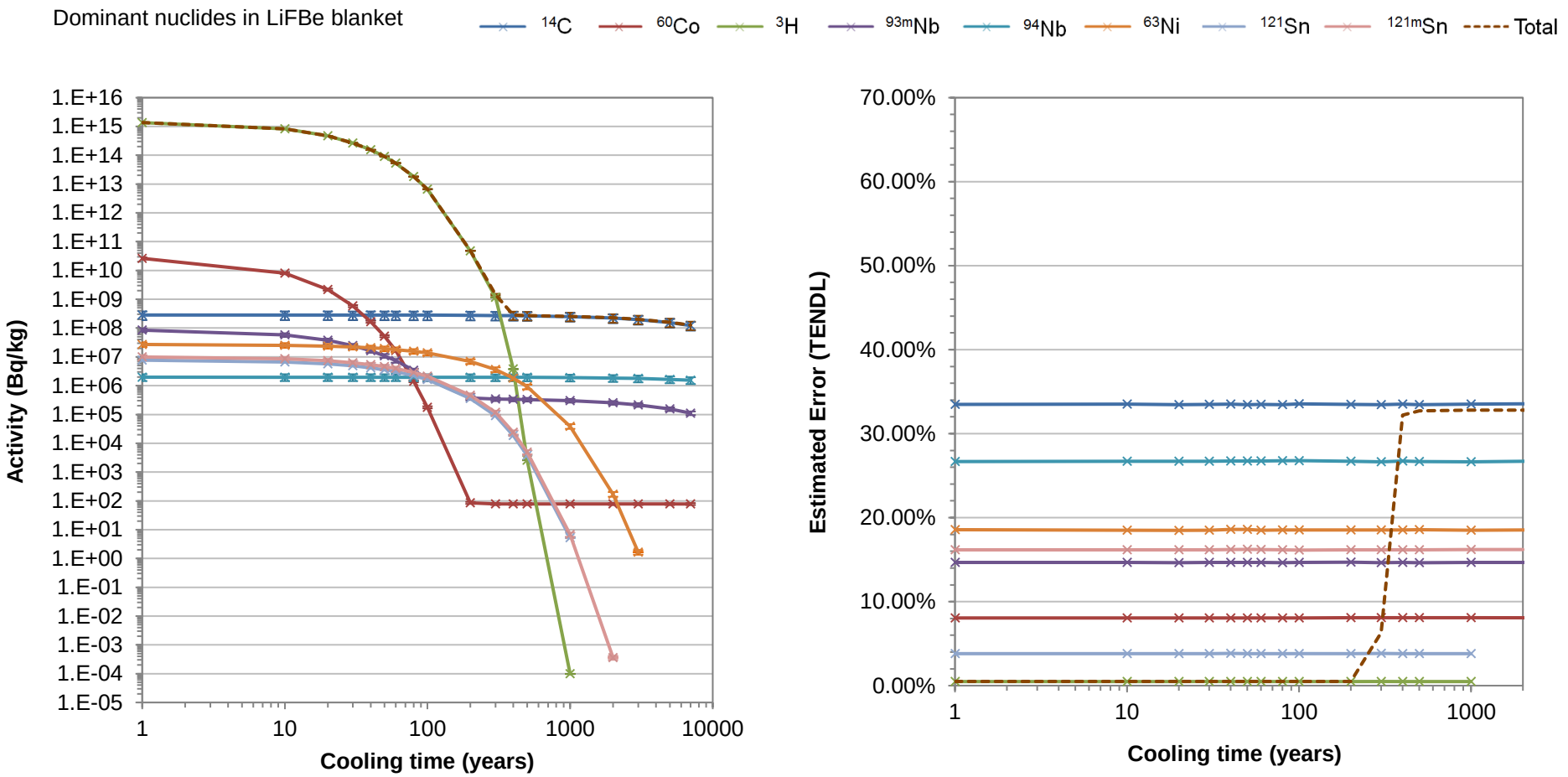

Figure 7.55 - Activity (Left) and uncertainty (Right) using TENDL data for LiFBe blanket.

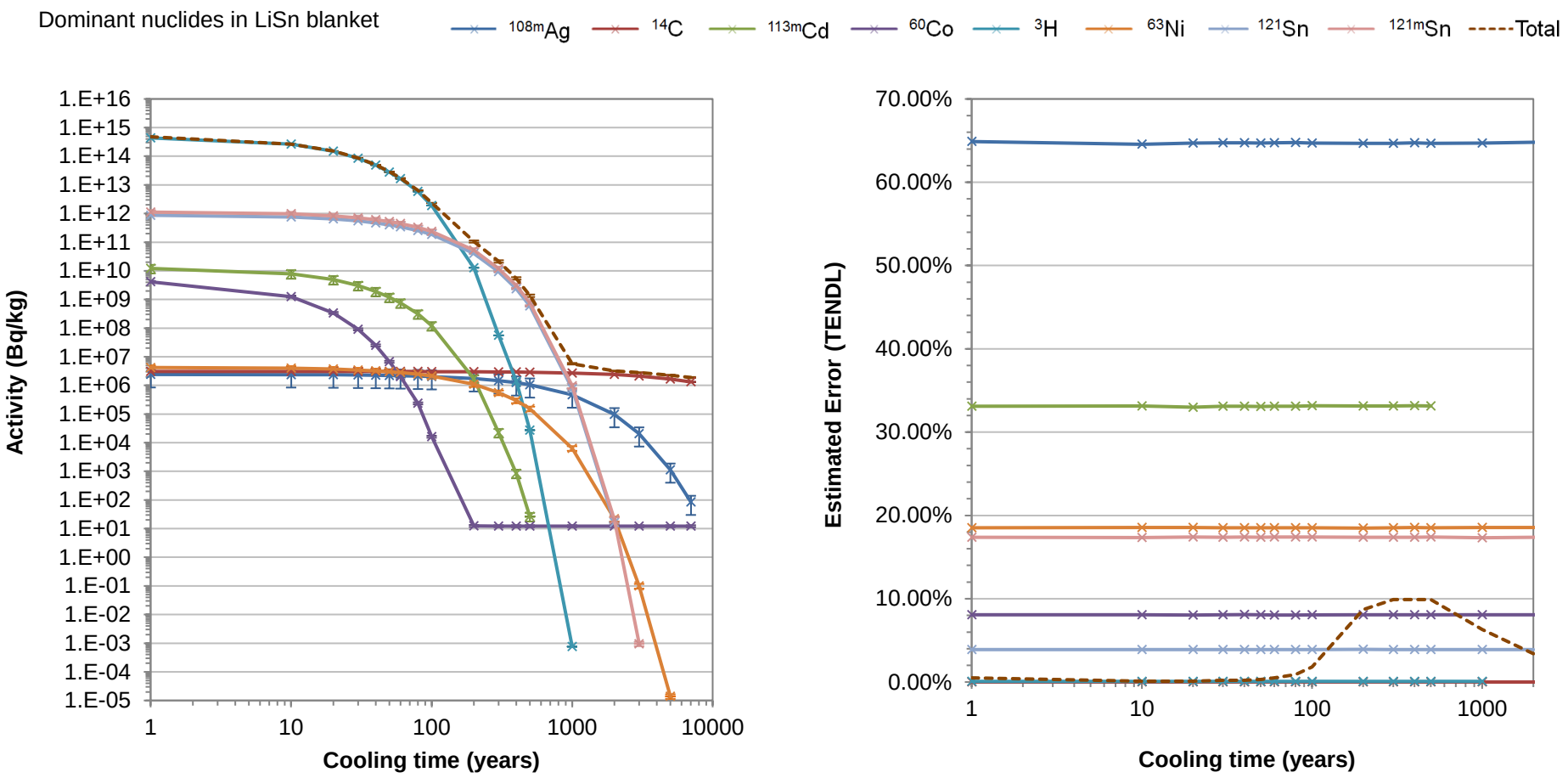

Figure 7.56 - Activity (Left) and uncertainty (Right) using TENDL data for LiSn blanket.